

Dynamic Performance of Heavy Vehicles Using Finite Element Method

Mahabubul Alam Chowdhury

A Thesis

In

The Department

of

Mechanical and Industrial Engineering

Presented in Partial Fulfillment of the Requirements
for the Degree of Master of Applied Science (Mechanical Engineering) at
Concordia University
Montreal, Quebec, Canada

April 2006

© Mahabubul Alam Chowdhury, 2006



Library and
Archives Canada

Bibliothèque et
Archives Canada

Published Heritage
Branch

Direction du
Patrimoine de l'édition

395 Wellington Street
Ottawa ON K1A 0N4
Canada

395, rue Wellington
Ottawa ON K1A 0N4
Canada

Your file Votre référence

ISBN: 0-494-14303-7

Our file Notre référence

ISBN: 0-494-14303-7

NOTICE:

The author has granted a non-exclusive license allowing Library and Archives Canada to reproduce, publish, archive, preserve, conserve, communicate to the public by telecommunication or on the Internet, loan, distribute and sell theses worldwide, for commercial or non-commercial purposes, in microform, paper, electronic and/or any other formats.

The author retains copyright ownership and moral rights in this thesis. Neither the thesis nor substantial extracts from it may be printed or otherwise reproduced without the author's permission.

AVIS:

L'auteur a accordé une licence non exclusive permettant à la Bibliothèque et Archives Canada de reproduire, publier, archiver, sauvegarder, conserver, transmettre au public par télécommunication ou par l'Internet, prêter, distribuer et vendre des thèses partout dans le monde, à des fins commerciales ou autres, sur support microforme, papier, électronique et/ou autres formats.

L'auteur conserve la propriété du droit d'auteur et des droits moraux qui protègent cette thèse. Ni la thèse ni des extraits substantiels de celle-ci ne doivent être imprimés ou autrement reproduits sans son autorisation.

In compliance with the Canadian Privacy Act some supporting forms may have been removed from this thesis.

Conformément à la loi canadienne sur la protection de la vie privée, quelques formulaires secondaires ont été enlevés de cette thèse.

While these forms may be included in the document page count, their removal does not represent any loss of content from the thesis.

Bien que ces formulaires aient inclus dans la pagination, il n'y aura aucun contenu manquant.


Canada

ABSTRACT

DYNAMIC PERFORMANCE OF HEAVY VEHICLES USING FINITE ELEMENT

METHOD

Mahabubul Alam Chowdhury

Although vehicles are made of flexible structures and components, they are typically modeled with the idealization of a rigid body. Furthermore, depending on the type of study, the models are simplified to planar models to carry out a wide range of dynamic studies. In recent years, non conventional applications of the finite element method (*FEM*) have been utilized to examine their effectiveness in the simulation of vehicle's dynamic performance. Such a validated model can provide a powerful and accurate tool for combined dynamic and structural performance of the vehicle in a wide range of environmental and operating conditions. In this study, a finite element model of a typical highway bus is developed with ANSYS, and is used to demonstrate its effectiveness in evaluating its dynamic performance in ride, handling and longitudinal modes. The number of degrees of freedom (DOF) of the developed highway bus model is 1848, and the model is validated by static weight balance check and frequency analysis. The major challenge and effort in this investigation was in the implementation of tire mechanics. Both linear and nonlinear tire models are incorporated in the *FEM* model in this study. Transient analyses have been carried out using mode superposition method. As such, determination of frequency range is essential, and the first twenty-two natural modes of the given bus are identified to be important in which the highest natural frequency is found to be 20.976 Hz. Ride quality of the bus model has been evaluated under two road surface irregularities (half sinusoidal and random input). The effects of the nonlinear tire

model and the corresponding linear tire model on simulation results are investigated using different amplitudes of half sinusoidal input. Transient analysis and Power Spectral Density (PSD) analyses have been carried out using realistic random road input. Pure cornering and combined cornering and braking analyses of the bus model have also been presented. Longitudinal tire forces, lateral tire forces and steering angle input on front wheels as external loads are applied on the designed bus to carry out the analyses. In both cases, in order to calculate the longitudinal and lateral forces, a proper four wheel mathematical model has been derived and simulated in MATLAB with the same model parameters. Moreover, in order to demonstrate the effectiveness and applicability of the developed large finite element model, comparison between elastic and rigid chassis performance is presented in this study for ride, handling and longitudinal analyses. When compared with rigid body model, the response at the center of gravity (c.g.) of FEM model is found to predict comparable performances under all excitations considered. The effect of body flexibility on the dynamic performance is also investigated and reported in this investigation. The effect of vertical input on bounce response of flexible model is negligible. However, for handling responses, there is a significant difference in the load shift when compared with the rigid body model. This in turn leads to some difference in the trajectory of the vehicle, which is further affected by the presence of combined braking input.

ACKNOWLEDGEMENTS

I am sincerely grateful to my erudite supervisors Dr. Waiz Ahmed and Dr. Ramin Sedaghati for their enthusiastic guidance and continuous encouragement throughout my thesis work almost for two years.

Also I would like to thank my colleagues and friends for their help and useful discussions during the course of this work.

Last but not the least I would like to thank my parents and brothers for their moral support throughout the research period.

TABLE OF CONTENTS

	PAGE No.
ABSTRACT	iii
ACKNOWLEDGEMENTS	v
TABLE OF CONTENTS	vi
LIST OF FIGURES	ix
LIST OF TABLES	xvii
CHAPTER 1 INTRODUCTION	1
1.1 MOTIVATION AND STATEMENT OF THE PROBLEM	1
1.2 STATE OF THE ART	4
1.2.1 Modeling of Bus Structure	4
1.2.2 Modeling of Suspension	6
1.2.3 Modeling of Tire	8
1.2.4 Ride Analysis of Vehicle	15
1.2.5 Handling and Longitudinal Analysis of Vehicle	17
1.3 SCOPE OF PRESENT WORK	21
1.4 THESIS ORGANIZATION	22
CHAPTER 2 FINITE ELEMENT MODELING OF HIGHWAY BUS AND ITS VALIDATION	24
2.1 INTRODUCTION	24
2.2 FINITE ELEMENT MODELING	28

2.2.1 Modeling of Highway Bus Structure	28
2.2.2 Modeling of Suspension Sets	29
2.2.3 Modeling of Tires	31
2.3 MODEL VALIDATION	41
2.3.1 Static Analysis	41
2.3.2 Modal Analysis	45
2.4 IDENTIFICATION OF FREQUENCY RANGE	49
CHAPTER 3 RIDE ANALYSIS OF VEHICLE	52
3.1 INTRODUCTION	52
3.2 RIDE ANALYSIS USING HALF SINUSOIDAL ROAD INPUT	53
3.3 RIDE ANALYSIS USING RANDOM ROAD INPUT	84
CHAPTER 4 HANDLING AND LONGITUDINAL ANALYSIS OF	
VEHICLE	102
4.1 INTRODUCTION	102
4.2 CORNERING ANALYSIS	103
4.2.1 Mathematical Modeling	104
4.2.2 Transient Response of the Bus with Rigid and Elastic Body	114
4.2.2.1 Extensive Cornering	114
4.2.2.2 Intensive Cornering	124
4.3 COMBINED CORNERING AND BRAKING ANALYSIS	132
4.3.1 Mathematical Modeling	134
4.3.2 Transient Response of the Bus with Rigid and Elastic Body	138

CHAPTER 5 CONCLUSIONS AND FUTURE WORK	149
5.1 CONCLUSIONS	149
5.2 FUTURE WORK	151
REFERENCES	153

LIST OF FIGURES

Fig. 1.1	Effect of tractive and breaking effort on the cornering characteristics of (a) a bias-ply and (b) a radial-ply car tire.	10
Fig. 1.2	The friction ellipse concept for predicting the cornering force available at specific slip angle in the presence of a tractive or braking force.	10
Fig. 1.3	Tire model in top and side view.	13
Fig. 1.4	Schematic view of tire model used.	14
Fig. 2.1	Complete highway-bus finite element model.	24
Fig. 2.2	Skeleton structure of the applied bus model with ground spring.	29
Fig. 2.3	Chassis with undercarriages and ground spring.	30
Fig. 2.4	Nonlinear damper characteristics.	31
Fig. 2.5	Linearization of nonlinear Damper characteristics.	31
Fig. 2.6	Finite element model of tires for handling analysis.	33
Fig. 2.7	Finite element model of tires with ground spring for ride analysis.	33
Fig. 2.8	Nonlinear characteristics of the elasticity of the front tire in radial direction.	34
Fig. 2.9	Linearization of nonlinear characteristics of the elasticity of the front tire in radial direction.	34
Fig. 2.10	Nonlinear characteristics of the elasticity of the rear tires in radial direction.	35
Fig. 2.11	Linearization of nonlinear characteristics of the elasticity of the rear tires in radial direction.	35
Fig. 2.12	Effect of vertical load on cornering stiffness of tire.	36
Fig. 2.13	Tire contact length.	39

Fig. 2.14	Longitudinal displacement of complete bus with ground spring due to the gravitational weight.	42
Fig. 2.15	Longitudinal displacement of complete bus without ground due to the gravitational weight.	42
Fig. 2.16	Vertical displacement of complete bus with ground spring due to the gravitational weight.	43
Fig. 2.17	Vertical displacement of complete bus without ground spring due to the gravitational weight.	43
Fig. 2.18	Lateral displacement of complete bus with ground spring due to the gravitational weight.	44
Fig. 2.19	Lateral displacement of complete bus without ground spring due to the gravitational weight.	44
Fig. 2.20	Rigid body mode shapes of the designed bus.	47
Fig. 2.21	Sprung mass mode shapes of the designed bus.	48
Fig. 2.22	Unsprung mass mode shapes of the designed bus.	49
Fig. 2.23	Vertical Displacements of node No. 69 for sweeping excitations.	50
Fig. 2.24	Vertical Displacements of node No. 216 for sweeping excitations.	51
Fig. 3.1	Vertical displacements of node No. 214 and node No. 264 for linear tire model (amplitude of bulge: 0.05 m).	59
Fig. 3.2	Vertical displacements of node No. 214 and node No. 264 for nonlinear tire model (amplitude of bulge: 0.05 m).	59
Fig. 3.3	Vertical displacements of node No. 215 and node No. 262 for linear tire model (amplitude of bulge: 0.05 m).	60
Fig. 3.4	Vertical displacements of node No. 215 and node No. 262 for nonlinear tire model (amplitude of bulge: 0.05 m).	60
Fig. 3.5	Bounce of the center of gravity (amplitude of bulge: 0.05 m).	61
Fig. 3.6	Pitch of the center of gravity (amplitude of bulge: 0.05 m).	61

Fig. 3.7	Vertical displacements of node No. 218 and node No. 234 for linear tire model (amplitude of bulge: 0.05 m).	62
Fig. 3.8	Vertical displacements of node No. 218 and node No. 234 for nonlinear tire model (amplitude of bulge: 0.05 m).	62
Fig. 3.9	Vertical displacements of node No. 221 and node No. 232 for linear tire model (amplitude of bulge: 0.05 m).	63
Fig. 3.10	Vertical displacements of node No. 221 and node No. 232 for nonlinear tire model (amplitude of bulge: 0.05 m).	63
Fig. 3.11	Rattle space at front right wheel (amplitude of bulge: 0.05 m).	64
Fig. 3.12	Rattle space at front right wheel (amplitude of bulge: 0.05 m).	64
Fig. 3.13	Bounce of the right hand side rear wheel for linear tire model (amplitude of bulge: 0.05 m).	65
Fig. 3.14	Bounce of the right hand side rear wheel for nonlinear tire model (amplitude of bulge: 0.05 m).	65
Fig. 3.15	Bounce of the right hand side front wheel for linear tire model (amplitude of bulge: 0.05 m).	66
Fig. 3.16	Bounce of the right hand side front wheel for nonlinear tire model (amplitude of bulge: 0.05 m).	66
Fig. 3.17	Bounce of the left hand side rear wheel for linear tire model (amplitude of bulge: 0.05 m).	67
Fig. 3.18	Bounce of the left hand side rear wheel for nonlinear tire model (amplitude of bulge: 0.05 m).	67
Fig. 3.19	Bounce of the left hand side front wheel for linear tire model (amplitude of bulge: 0.05 m).	68
Fig. 3.20	Bounce of the left hand side front wheel for nonlinear tire model (amplitude of bulge: 0.05 m).	68
Fig. 3.21	Vertical displacements of node No. 214 and node No. 264 for linear tire model (amplitude of bulge: 0.1 m).	69
Fig. 3.22	Vertical displacements of node No. 214 and node No. 264 for nonlinear tire model (amplitude of bulge: 0.1 m).	69

Fig. 3.23	Vertical displacements of node No. 215 and node No. 262 for linear tire model (amplitude of bulge: 0.1 m).	70
Fig. 3.24	Vertical displacements of node No. 215 and node No. 262 for nonlinear tire model (amplitude of bulge: 0.1 m).	70
Fig. 3.25	Bounce of the center of gravity (amplitude of bulge: 0.1 m).	71
Fig. 3.26	Pitch of the center of gravity (amplitude of bulge: 0.1 m).	71
Fig. 3.27	Vertical displacements of node No. 218 and node No. 234 for linear tire model (amplitude of bulge: 0.1 m).	72
Fig. 3.28	Vertical displacements of node No. 218 and node No. 234 for nonlinear tire model (amplitude of bulge: 0.1 m)	72
Fig. 3.29	Vertical displacements of node No. 221 and node No. 232 for linear tire model (amplitude of bulge: 0.1 m).	73
Fig. 3.30	Vertical displacements of node No. 221 and node No. 232 for nonlinear tire model (amplitude of bulge: 0.1 m).	73
Fig. 3.31	Rattle space at rear right wheel (amplitude of bulge: 0.1 m).	74
Fig. 3.32	Rattle space at front right wheel (amplitude of bulge: 0.1 m).	74
Fig. 3.33	Bounce of the right hand side rear wheel for linear tire model (amplitude of bulge: 0.1 m).	75
Fig. 3.34	Bounce of the right hand side rear wheel for nonlinear tire model (amplitude of bulge: 0.1 m).	75
Fig. 3.35	Bounce of the right hand side front wheel for linear tire model (amplitude of bulge: 0.1 m).	76
Fig. 3.36	Bounce of the right hand side front wheel for nonlinear tire model (amplitude of bulge: 0.1 m).	76
Fig. 3.37	Bounce of the left hand side rear wheel for linear tire model (amplitude of bulge: 0.1 m).	77
Fig. 3.38	Bounce of the left hand side rear wheel for nonlinear tire model (amplitude of bulge: 0.1 m).	77
Fig. 3.39	Bounce of the left hand side front wheel for linear tire model (amplitude of bulge: 0.1 m).	78

Fig. 3.40	Bounce of the left hand side front wheel for nonlinear tire model (amplitude of bulge: 0.1 m).	78
Fig. 3.41	Bounce of the Center of Gravity for linear tire model (amplitude of bulge: 0.1 m).	80
Fig. 3.42	Pitch of the Center of Gravity for linear tire model (amplitude of bulge: 0.1 m).	80
Fig. 3.43	Vertical displacement of node No. 214 for linear tire model (amplitude of bulge: 0.1 m).	81
Fig. 3.44	Vertical displacement of node No. 218 for linear tire model (amplitude of bulge: 0.1 m).	81
Fig. 3.45	Vertical displacement of node No. 191 for linear tire model (amplitude of bulge: 0.1 m).	82
Fig. 3.46	Vertical displacement of node No. 166 for linear tire model (amplitude of bulge: 0.1 m).	82
Fig. 3.47	Lateral displacement of node No. 12 for linear tire model (amplitude of bulge: 0.1 m).	83
Fig. 3.48	Lateral displacement of node No. 258 for linear tire model (amplitude of bulge: 0.1 m).	83
Fig. 3.49	Road profile (a) vertical displacement of node No. 218 (b) and node No. 214 (c).	88
Fig. 3.50	lateral displacement (a) and lateral acceleration (b) of node No. 304.	89
Fig. 3.51	Damping force in front-right suspension.	90
Fig. 3.52	Damping force in rear-right suspension.	90
Fig. 3.53	PSD of left track height.	91
Fig. 3.54	PSD of right track height.	91
Fig. 3.55	PSD of vertical acceleration of node No. 214.	92
Fig. 3.56	PSD of vertical acceleration of node No. 264.	92

Fig. 3.57	PSD of vertical acceleration of node No. 215.	93
Fig. 3.58	PSD of vertical acceleration of node No. 262.	93
Fig. 3.59	PSD of bounce acceleration of the center of gravity.	94
Fig. 3.60	PSD of pitch acceleration of the center of gravity.	94
Fig. 3.61	PSD of rear right wheel vertical acceleration.	95
Fig. 3.62	PSD of front right wheel vertical acceleration.	95
Fig. 3.63	PSD of rear left wheel vertical acceleration.	96
Fig. 3.64	PSD of front left wheel vertical acceleration.	96
Fig. 3.65	PSD of vertical load on front left tire.	97
Fig. 3.66	PSD of vertical load on front right tire.	97
Fig. 3.67	PSD of vertical load on rear left tire.	98
Fig. 3.68	PSD of vertical load on rear right tire.	98
Fig. 3.69	PSD of damping force in front right suspension.	99
Fig. 3.70	PSD of damping force in rear right suspension.	99
Fig. 3.71	PSD of damping force in front left suspension.	100
Fig. 3.72	PSD of damping force in rear left suspension.	100
Fig. 3.73	PSD of lateral acceleration of node No. 304.	101
Fig. 4.1	Current position of the vehicle in turning.	104
Fig. 4.2	Change of velocity component.	105
Fig. 4.3	Full Vehicle Model.	107
Fig. 4.4	Steering Geometry.	110
Fig. 4.5	Normal load on front tires (a) and rear tires (b).	112
Fig. 4.6	Velocity diagram of vehicle.	113

Fig. 4.7	Steering angle input (a), steering angle input distribution on inner front wheel (b) and on outer front wheel (c).	115
Fig. 4.8	Change in cornering stiffness at different tires.	116
Fig. 4.9	Change of developed cornering forces at different tires.	117
Fig. 4.10	Lateral velocity (a), lateral acceleration (b) and yaw velocity (c) of center of gravity.	118
Fig. 4.11	Normal load distribution on inner and outer front tires.	119
Fig. 4.12	Normal load distribution on inner and outer rear tires.	120
Fig. 4.13	Slip angle generation on inner and outer front tires.	122
Fig. 4.14	Slip angle generation on inner and outer rear tires.	123
Fig. 4.15	Trajectory of the bus.	124
Fig. 4.16	Steering angle input (a), steering angle input distribution on inner front wheel (b) and on outer front wheel (c).	126
Fig. 4.17	Change of cornering stiffness at different tires.	127
Fig. 4.18	Change of developed cornering force at different tires.	128
Fig. 4.19	Lateral velocity (a), lateral acceleration (b) and yaw velocity (c) of center of gravity.	129
Fig. 4.20	Slip angle generation on inner and outer front tires.	130
Fig. 4.21	Slip angle generation on inner and outer rear tires.	131
Fig. 4.22	Trajectory of the bus.	132
Fig. 4.23	Applied breaking moment on each wheel.	133
Fig. 4.24	Current position of the vehicle in combined turning and braking.	133
Fig. 4.25	Normal load on front tires (a) and rear tires (b).	136
Fig. 4.26	Load shift during braking.	137
Fig. 4.27	Breaking forces to different tires.	141

Fig. 4.28	Longitudinal slip of tires of the flexible body model.	142
Fig. 4.29	Change of developed cornering forces to different tires.	143
Fig. 4.30	Slip angle generation on inner and outer front tires.	144
Fig. 4.31	Slip angle generation on inner and outer rear tires.	145
Fig. 4.32	Longitudinal velocities (a) and longitudinal decelerations (b) of center of gravity.	146
Fig. 4.33	Lateral velocity (a), lateral acceleration (b) and yaw velocity (c) of center of gravity.	147
Fig. 4.34	Trajectory of the bus.	148

LIST OF TABLES

Table 1.1	Detailed specifications of Prévost–Car XLII intercity coach.	5
Table 2.1	Prévost–Car XLII–45 bus Components and Weights	26
Table 2.2	List of materials used in the model	27
Table 2.3	Important dimensions and weights of the candidate FE highway bus.	27
Table 2.4	Reaction load on different tire-ground contact.	43
Table 2.5	First fifty natural frequencies of the Candidate bus.	46

CHAPTER 1

INTRODUCTION

1.1 MOTIVATION AND STATEMENT OF THE PROBLEM

Nowadays a complete vehicle design process takes minimum 4 years, which requires the involvement of huge man-hour and manufacturing costs, and is composed of mainly three steps. First, designing of the vehicle structure with CAD tools like Pro-E, CATIA, AutoCAD; second, static and dynamic analysis of vehicle structure with finite element tools like ANSYS, COSMOS/M, NASTRAN and finally, the dynamic simulation of vehicle with multi-body computer codes (such as ADAMS, SIMPACK). Dynamic simulations of a vehicle are performed considering rigid body motions i.e. neglecting flexibility effects of structure during motions of vehicle. But in some cases flexibility can not be ignored as it plays an important role in both structural and dynamic performance. Recently ANSYS, Inc., developer of ANSYS, has also developed an ANSYS –ADAMS interface tool that is used to carry out the dynamic simulation of vehicle motions along with the consideration of the flexibility effect of vehicle structure. It is well known that the finite element method has been applied for a long time to the structural vibration analysis of vehicles using pre-determinate time varying external forces and kinematical excitations. However, the dynamic effects arising in vehicle structures are generated by means of the vehicle motions. Now if it possible to use the finite element technique in vehicle dynamic simulation, only two computer environments are needed for the whole design process. This will naturally reduce man-hours involved in the complete design of vehicles, and subsequently reduce the overall manufacturing

time and costs.

Dynamic performance of heavy vehicles is typically examined using rigid body models suspended through suspensions and tires. For heavy vehicles such as a bus, the structural properties including the damping, the distribution of stiffness (elasticity) and mass also play an important role on its dynamic response. Therefore, a well-detailed model utilizing Finite Element method can provide an efficient, practical accurate tool for evaluations of both local and global dynamic properties of the vehicle and its structure. Some recent studies have considered vehicles as multibody systems using multibody programs such as ADAMS, SIMPACK. to simulate the vehicle's motions. Some of the multibody programs, containing elastic bodies and substructures in addition to the rigid bodies, are capable of including elastic effects [1]. Commercial finite element programs (e.g. ANSYS, MSC/NASTRAN, and COSMOS/M) developed for general purposes can be applied not only for the structural dynamic analysis (computation of dynamic stresses and elastic deformations using predefined time dependent external forces and kinematical excitations) but also for the study of the mobility of vehicles. The objective of this thesis is to present examples of the non-conventional application of the finite element method, namely to predict the ride, handling and longitudinal performances of vehicles using efficient modeling. Examples of the non-conventional application of the finite element method are shown by the use of a highway bus finite element model. In the ride performance measurement, three dimensional vibrations of a candidate bus model are investigated under the action of vertical excitations through the consideration of different road inputs at a constant forward speed. The effects of linearity and nonlinearity in the case of radial tire stiffness have been investigated through parametric analyses under ride

performance measurements. Moreover, ride analysis has been conducted for both flexible and rigid body models in order to demonstrate the effectiveness and applicability of the large finite element model. Also pure turning and combined turning and braking analyses have been presented under the longitudinal and handling performances of the candidate bus. In order to demonstrate the effectiveness and applicability of the large finite element model, a comparison between elastic and rigid chassis performance is presented in this study for both types of analyses.

In this study, the dynamic analysis is carried out by a commercial finite element program (ANSYS). However, the application of the step-by-step numerical solution methods for the computation of dynamic responses of large finite element mechanical models with many degrees of freedom is computationally expensive, and thus the employment of any model reduction method becomes necessary. For this purpose, herein the mode superposition method is employed. In the study of vehicle dynamics, the natural modes up to 25-30 Hz are considered adequate for all practical purposes [2]. This makes it possible to reduce the size of the model significantly without any significant errors in the desired dynamic responses. It is well known in structural dynamics that the mode superposition method in its original form can only be applied to linear structures in case of small strains and displacements. However, a vehicle receives ground excitations during its large displacement (in longitudinal and lateral directions) and rotations about the vertical axis. In order to take these large motions into consideration, the corresponding (three) rigid body modes with zero natural frequencies have to be included in the considered set of mode shapes.

The following subsections present a state of the art review of relevant topics on



modeling and dynamic simulations in order to develop the scope of the present work.

1.2 STATE OF THE ART

1.2.1 Modeling of Bus Structure

In general, rigid body models are used to investigate the dynamic performances of heavy vehicles. However, the large finite element model is necessary for the dynamic simulations of heavy vehicles in order to get the more accurate responses. Moreover, an efficient finite element model of a heavy vehicle requires the consideration of detailed geometrical dimensions. With regard to the necessity of large finite element model, Kuti [2, 3] developed a finite element bus model containing more than 2200 degrees of freedom. The developed model is mainly comprised of structure, suspension sets and tires. The bus structure is a metallic frame covered with metallic and glass sheets, which are linked with different parts such as chassis, axles, power train, fuel tanks, and engine. Bus structure is mainly comprised of beam and shell elements. Balasa et al. [4] built a finite element (FE) model of the bus using beam elements for the metallic frame, shell elements for the sheets and linear spring elements for the suspensions and wheels. The other parts such as power train, engine, fuel tanks, luggage, and passengers were modeled as concentrated masses. At first, the bus was modeled without windows or adhesive between the window and the frame. Significant differences were noticed in the numerical simulation results when compared with the experimental data. So in the next step, the windows were modeled with shell elements, while the adhesive was represented with linear beam elements. The accuracy of the model response was greatly improved. The finite element model was then correlated by comparing the finite element analysis. Then the correlated model was subjected to time transient loads, and the results were

Table 1.1: Detailed specifications of Prevost-Car XLII intercitty coach [5].

 PREVOST <small>14001 800-86112800</small>		 PREVOST XLII MODEL 2005 BUS SHELLS FOR 'ULTIMATE' CLASS CONVERSION	
GENERAL		XLII-45	XLII-40
LENGTH, OVERALL		45.0 FT.	40.0 FT.
WHEELBASE		314.0 IN.	279.0 IN.
WIDTH, OVERALL		102.0 IN.	102.0 IN.
HEIGHT, OVERALL		140.0 IN.	140.0 IN.
FLOOR-TO-CEILING HEIGHT		86.0 IN.	86.0 IN.
CABIN FLOOR HEIGHT		48.5 IN.	48.5 IN.
USABLE CABIN FLOOR LENGTH		34.75 FT.	31.75 FT.
- (NO WHEEL HUBS)		40.7 CU.FT.	315 CU.FT.
UNDER-FLOOR STORAGE (W/DRIVER A/C)		60.5 IN.	53.5 IN.
UNDER-FLOOR COMPARTMENT DOORS WIDTH		30.0 IN.	30.0 IN.
ENTRANCE DOOR WIDTH		15.0 IN.	15.0 IN.
STEP HEIGHT		11.0 IN.	11.0 IN.
GROUND CLEARANCE		68.75 IN.	68.75 IN.
OVERHANG (INCL. BUMPER) — FRONT		107.75 IN.	82.75 IN.
(INCL. BUMPER) — REAR		41.8 FT.	38.4 FT.
TURNING RADIUS		STAINLESS STEEL AND RUST-PROTECTED HIGH TENSILE STEEL	
INTEGRAL BODY STRUCTURE (BOTH MODELS)			
INTEGRAL BODY OUTER SHELL (BOTH MODELS)			
FUEL TANK, STANDARD (U.S. GALLONS)		208.0	250.0
FUEL FILLER NECKS ON BOTH SIDES		STANDARD	STANDARD
GROSS VEHICLE WEIGHT RATING (LBS.)		54 500	51 400
AXLE LOAD CAPACITY (LBS.) - FRONT		18 000	18 000
AXLE LOAD CAPACITY (LBS.) - DRIVE		22 500	21 400
AXLE LOAD CAPACITY (LBS.) - TAG		14 000	12 000
WET WEIGHT, W/DRIVER A/C (LBS.)		30 150	29 020
WET WEIGHT, W/FULL A/C (LBS.)		30 850	29 720
DRIVER-ONLY A/C		STANDARD	STANDARD
FULL A/C		OPTIONAL	OPTIONAL
A/C BLOWER W/FULL A/C		2-SPEED	2-SPEED
A/C CONDENSER W/COOPER FINS		OPTIONAL	OPTIONAL
A/C REFRIGERANT		134A	134A
COOLING CAPACITY W/FULL A/C (BTU)		90 000	90 000
TIRES AND WHEELS			
MICHELIN 315/80R22.5 (DRIVE)		STANDARD	STANDARD
MICHELIN 365/70R22.5 (FRONT & TAG)		STANDARD	STANDARD
ALUMINUM RIMS 22.5X10.5 IN. (FRONT & TAG)		OPTIONAL	OPTIONAL
ALUMINUM RIMS 22.5X9 IN. (DRIVE)		OPTIONAL	OPTIONAL
DURA-BRIGHT COATING (ALUMINUM WHEELS)		OPTIONAL	OPTIONAL
POWERTRAIN		XLII-45	XLII-40
DOEC V SERIES 60 W/ECR 14L (515 HP)		STANDARD	N/A
DDEC V SERIES 60 W/ECR 12.7L (455 HP)		N/A	STANDARD
3-SPEED ENGINE COOLING: FAN		STANDARD	STANDARD
ALUMINUM W/CRUISE 4000W/11, 6-SPEED AUTOM.		STANDARD	STANDARD
ALUMINUM W/CRUISE 8500, 6-SPEED AUTOM.		OPTIONAL	OPTIONAL
- (5-YEAR WARRANTY)		STANDARD	STANDARD
CRUISE CONTROL		OPTIONAL	OPTIONAL
JACOR ENGINE BRAKE (ON ALL CYLINDERS)		OPTIONAL	OPTIONAL
ALUMINUM HYDRAULIC TRANS. RETARDER		OPTIONAL	OPTIONAL
TURBO-BOOST GAUGE		STANDARD	STANDARD
PNEUMATIC DRIVE BELTS TENSIONERS		STANDARD	STANDARD
ENGINE COOLANT FILTER		STANDARD	STANDARD
RACOR FUEL FILTER		OPTIONAL	OPTIONAL
FUEL/PARK FUEL FILTER		OPTIONAL	OPTIONAL
ELECTRICAL FUEL PUMP/PRIMER PUMP		OPTIONAL	OPTIONAL
BRAKES		XLII-45	XLII-40
AIR-DRIVE BRAKES WITH ABS		STANDARD	STANDARD
FRONT WHEELS BRAKE BOOSTERS		TYPE 27	TYPE 27
DRIVE WHEELS BRAKE BOOSTERS		TYPE 24-24	TYPE 24-24
TAG WHEELS BRAKE BOOSTERS		TYPE 14-16	TYPE 14-16
PARKING BRAKE BOOSTER ON TAG WHEELS		STANDARD	STANDARD
STEERING & SUSPENSION		XLII-45	XLII-40
INDEPENDENT SUSPENSION SYSTEM		STANDARD	STANDARD
STEERING SLAVE CYLINDER		STANDARD	STANDARD
FRONT & DRIVE AXES SWAY BARS		STANDARD	STANDARD
TILT & TELESCOPIC STEERING WHEEL		STANDARD	STANDARD
ZF-SERVOCOM CONSTANT POWER STEERING		STANDARD	STANDARD
ZF-SERVOCOM VARIABLE POWER STEERING		OPTIONAL	OPTIONAL
PNEUMATIC LEVEL-LOW SYSTEM (IN STATION)		OPTIONAL	OPTIONAL
LEAFABLE TAG AXLE		STANDARD	STANDARD
ELECTRICAL SYSTEM		XLII-45	XLII-40
12V EXT. LIGHTING/24V AMB. SYSTEM		STANDARD	STANDARD
SHIELD ALTERNATOR (W/FULL A/C)		DELCO 24V/270A	DELCO 24V/270A
- 12V/145A ADD'L. HOUSE SYSTEM ALTERNATOR		OPTIONAL	OPTIONAL
- 24V/100A ADD'L. HOUSE SYSTEM ALTERNATOR		OPTIONAL	OPTIONAL
SHIELD ALTERNATOR (W/DRIVER A/C)		DELCO 24V/75A	DELCO 24V/75A
- 12V/300A ADD'L. HOUSE SYSTEM ALTERNATOR		OPTIONAL	OPTIONAL
- 24V/270A ADD'L. HOUSE SYSTEM ALTERNATOR		OPTIONAL	OPTIONAL
- 24V/100A ADD'L. HOUSE SYSTEM ALTERNATOR		OPTIONAL	OPTIONAL
FACTORY-INSTALLED EQUIPMENT		XLII-45	XLII-40
FACTORY SIDE-CUTS (1-2, ALL ELECTRICAL)		OPTIONAL	OPTIONAL
PREVOST FRAMELESS SIDE WINDOWS		OPTIONAL	OPTIONAL
CHOICE OF SIDE WINDOW ARRANGEMENT & TYPE		OPTIONAL	OPTIONAL
- SINGLE/DUAL PANE, FIXED, SLIDING, EJECT, WINING		STANDARD	STANDARD
XENON HIGH INTENSITY HEADLIGHTS		OPTIONAL	OPTIONAL
FOG LIGHTS		OPTIONAL	OPTIONAL
UPPER SIDE WINDOW (FRONT ON)		STANDARD	STANDARD
LEFT/RIGHT WINDSHIELD ROLLER BLINDS		OPTIONAL	OPTIONAL
REMOTE CONTROLLED WINDSHIELD ROLLER BLINDS		OPTIONAL	OPTIONAL
DRIVER'S WINDOW BLIND		OPTIONAL	OPTIONAL
PANOIC REMOTE HEATED REARVIEW MIRRORS		OPTIONAL	OPTIONAL
- W/SEPARATE CONTEX TOP (WHITE BLACK)		STANDARD	STANDARD
- W/SEPARATE CONTEX TOP (CHROME)		OPTIONAL	OPTIONAL
- W/SEPARATE CONTEX INSERT (CHROME)		OPTIONAL	OPTIONAL
CENTRAL DOOR LOCKING SYSTEM		STANDARD	STANDARD
REMOTE KEYLESS LOCKING (ENTRANCE DOOR)		STANDARD	STANDARD
REMOTE KEYLESS LOCKING (COMPARTMENT DOORS)		STANDARD	STANDARD
TRAILER HITCH PACKAGE (20 000 LBS.)		OPTIONAL	OPTIONAL
TRAILER AIR BRAKE CONNECTION		OPTIONAL	OPTIONAL
LOW FUEL WARNING LIGHT		STANDARD	STANDARD
TURN SIGNAL LIGHTS (4 EXTRA)		OPTIONAL	OPTIONAL
SIDE-MARKER LIGHTS (4 EXTRA)		OPTIONAL	OPTIONAL
COURTESY LIGHTS BURNER SWITCH		STANDARD	STANDARD
ENGINE & COMPARTMENTS LIGHTING		STANDARD	STANDARD
DRIVER DELIVERY SEAT		STANDARD	STANDARD
ISRI PNEUMATIC ADJUSTABLE SEAT (6800)		OPTIONAL	OPTIONAL
ISRI POWER SEAT (WITHOUT MIRROR)		OPTIONAL	OPTIONAL
EXTERIOR GRAPHICS DESIGN ASSISTANCE		OPTIONAL	OPTIONAL
FACTORY PAINT W/SPECIAL EFFECTS		OPTIONAL	OPTIONAL
BACK-UP SOUND ALARM		OPTIONAL	OPTIONAL

PREVOST.
THE 'ULTIMATE' CLASS

WWW.PREVOSTCAR.COM

THESE SPECIFICATIONS ARE BASED ON THE LATEST PRODUCT INFORMATION AVAILABLE AT THE TIME OF PRINTING (04/07/2005) AND ARE SUBJECT TO CHANGE. CONTACT THE PREVOST V.P. BUS SELLER DIVISION OR YOUR PREVOST-APPOINTED INTERIOR DESIGNER AND SYSTEMS MANUFACTURER FOR FULL DETAILS ON STANDARD FEATURES, PACKAGES AND OPTIONS.

SALES INQUIRIES: USA: (866) 637-4355 | CANADA: (416) 893-3391

verified again against the time transient experimental data. In this investigation, the detailed specification of Prévost–Car XLII–40 intercity coach shown in Table 1.1 is considered as a candidate vehicle for the simulations. Some structural cross-sections and parameters were taken from other sources to realize as detailed a model as possible.

1.2.2 Modeling of Suspension

Design of suspension for a heavy vehicle requires careful selection of the suspension parameters such as the stiffness and damping properties. It is important to achieve a compromise among the ride, handling and control performance characteristics. Enhancement of ride quality requires soft and lightly damped suspensions. However, the soft vehicle suspensions cause poor roll stability and handling performance. Soft suspensions also increase the suspension rattle space requirements. On the basis of experimental and analytical results, a number of guidelines have been developed for the design of suspension systems. Natural frequency of the sprung mass should be approximately 1 Hz to ensure ride quality with adequate rattle space and it should not be greater than 1.5 Hz for passenger road vehicles. Since forces due to wheel motions and unbalance are transmitted to the sprung mass through the suspension and the human body is very sensitive in the range of 4-6 Hz, the bounce frequency of the unsprung mass should not be less than 8 Hz. On the contrary, larger frequencies requires stiff tire which affects the ride quality. Practically, the value of unsprung mass natural frequency is around 10 Hz. Pitch and bounce frequencies should be close together. The bounce natural frequency less than 1.2 times the pitch frequency gives good results. When a vehicle goes over a bump, the front axle is subjected to the impact before the rear axle. This excites the pitch resonance, which is more annoying than the vertical motion. For this purpose,

the rear suspension should be assigned 20-30 percent larger ride rate, or the center of gravity should be closer to the rear axle than the front. Designing rear suspension with slightly larger ride rate than the front introduces higher frequency of oscillation for the rear than the front so that front and rear end moves in phase within half a cycle after the bump is passed [6].

In reality, the characteristics of suspension system components, namely springs and dampers, are nonlinear and require nonlinear analysis. For comparative and qualitative studies, the nonlinear characteristics of suspension components can be linearized to take the advantage of the linear analytical tools. Some common type of springs such as coil, leaf and air springs are used in ground transportation suspension systems. Coil springs exhibit linear relationships, while the leaf springs exhibit hardening characteristics and hysteresis due to interleaf and bushing friction. Leaf springs are useful for vehicles that may have large variation in load. The vertical motions of such suspension are often small in amplitude as the effective ride stiffness of leaf springs is significantly larger than the nominal stiffness under small deflections. However, air springs are mostly used for commercial vehicles as they exhibit hardening characteristics and provide adaptive ride height control and improved ride quality and pavement load performance [6].

Since the vehicle ride quality and tire-load are strongly influenced by the suspension damping, it is important to include adequate damping characteristics in the vehicle model. Practically, hydraulic multi-stage dampers are used in vehicle suspension systems. Hydraulic multi-stage damper is asymmetric in compression and rebound. However, typical vehicle models, irrespective of their application, consider linear

damping characteristics. The damping forces in rebound are considerably larger than those in compression. The dampers exhibit high coefficients at low speeds and lower coefficient at higher speeds [6].

A physical arrangement and modeling of suspension components of a FEM bus model have been presented by Kuti [2]. In the suspension systems of the developed finite element bus model, leaf springs have been applied with linear characteristics at the extremities of the rigid spring arms. The elasticity of these leaf springs has been approximated by linear finite spring elements. The concentrated dampers of suspension systems have been positioned between the chassis and the axles at the midpoint of the rigid spring arms. The damping characteristics have been approximated by linear or nonlinear damping characteristics in order to carry out the analysis with linear model or nonlinear model, respectively. The linearization of non-linear damper characteristics has been done on the basis that both of them absorb the same given energy at a given nominal frequency and stroke. Rubber bumpers have been applied just next to the suspensions between axles and chassis with highly non-linear characteristics; however, these rubber bumpers are in operations only when the undercarriages are about to hit the chassis. An anti-roll torsion bar has been introduced in between the chassis and rear axle.

1.2.3 Modeling of Tire

All major forces and moments except gravitational and aerodynamic forces are applied through the tire-ground contact to control the motion of a ground vehicle. An understanding of the tire dynamics is, therefore, necessary to the study of longitudinal performance, ride quality, and handling behavior of ground vehicles. For that purpose different kinds of tire models such as pure mathematical tire model, functional tire model,

and finite element tire model are being used according to specific type of vehicle simulation (e.g. pure cornering, asymmetric braking and braking-in-a-turn) [7].

Julien developed mathematical model of tire for the relationship between pure tractive or braking effort and longitudinal slip or skid. But this requires considerable effort and elaborated experiments. In view of this, a simplified theory has been developed. But both theories are not valid for combined slip condition [8].

A significant attempt has been made by Temple and Schlippe to develop mathematical model for the pure cornering behavior of pneumatic tires [8]. But the theory proposed by them is restricted to small slip angles. It assumes that there is no sliding between the tread and the ground occurs; consequently, the lateral force and the aligning torque increase linearly with the slip angle. Moreover, this theory is only capable to capture the steady-state response of a tire, not the transient response of a tire. In view of this, a simplified theory has been proposed by Segel [9]. This theory is capable to capture the transient response of tire to large slip angle, but it is limited to pure side slip condition.

For pure cornering analysis the longitudinal tire force can be neglected as vehicle forward speed is constant during the maneuver. However, both longitudinal and lateral tire forces are present during braking-in-a-turn. In general, longitudinal tire force reduces the lateral tire force that can be generated at a given slip angle under free rolling condition, as shown in Fig. 1.1. The effect of acceleration or braking on lateral tire force can be considered by the help of *friction ellipse*. In *friction ellipse* it is assumed that the tire may slide on the ground in any direction if the resultant of the longitudinal tire force and lateral tire forces reaches the maximum value defined by the fictional

coefficient of road surface and the vertical load on the tire. However, the longitudinal and lateral tire force components can not be greater than their respective maximum values F_{xmax} and F_{ymax} , as shown in Fig 1.2. The available cornering force F_y at a given slip angle α , for any given longitudinal tire force F_x can be calculated from the following equation [8]:

$$\left(\frac{F_y}{F_{y\alpha}} \right)^2 + \left(\frac{F_x}{F_{xmax}} \right)^2 = 1$$

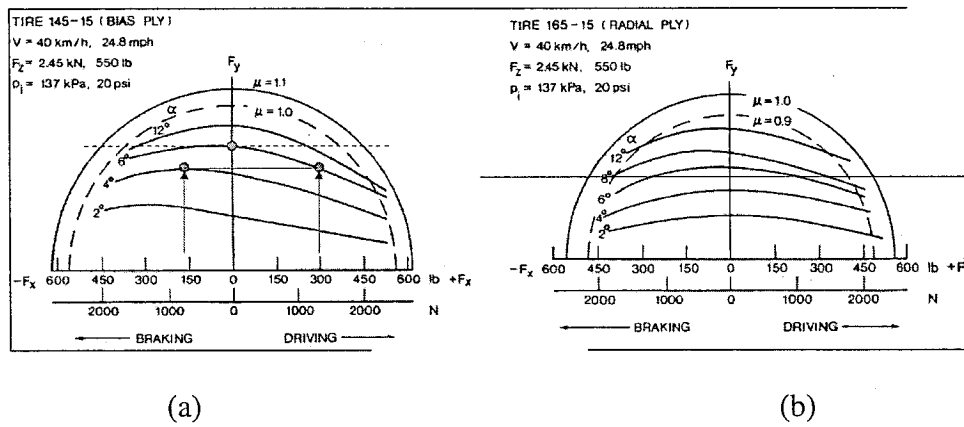


Fig. 1.1 Effect of tractive and braking effort on the cornering characteristics of (a) a bias-ply and (b) a radial-ply car tire [8].

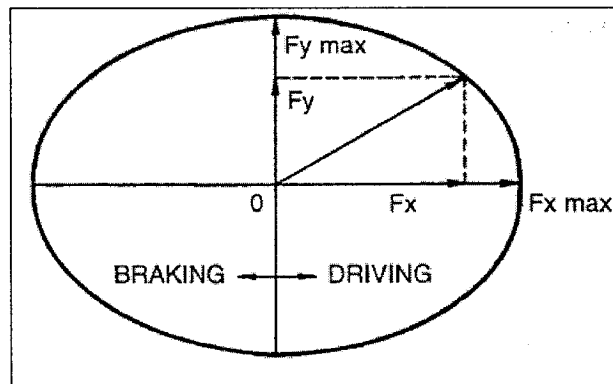


Fig. 1.2 The friction ellipse concept for predicting the cornering force available at specific slip angle in the presence of a tractive or braking force [8].

Segel [9] also proposed a semi-empirical method to predict the braking force and cornering force in the presence of both the longitudinal skid and slip angle. Following the same approach, a method for predicting the tractive force and cornering force as functions of combined longitudinal slip and slip angle can be formulated. To achieve more accurate predictions, the effects of normal load and speed on the values of coefficient of road adhesion, longitudinal stiffness of tire during braking or accelerating and other tire parameters should be properly taken into account.

In recent years, an empirical method for characterizing steady-state tire behavior at pure slip condition, known as the *magic formula*, has been developed by Pacejka [10] and widely used in vehicle handling simulations. The Magic Formula Tire Model requires a set of parameters to predict the tire force characteristics. Michelin [7] developed a purely empirical method based on *magic formula* to calculate the tire force generation at combined slip condition. This is called *cosine version of magic formula*, which is described with 13 coefficients or parameters as well as 4 coupling model coefficients for longitudinal tire force and for lateral tire force 15 coefficients as well as 10 coupling coefficients. A set of *magic formula* parameters are calculated from tire measurement data. One procedure, called regression method, to find these parameters is described in [11]. A main characteristic of this technique is that it requires starting values for the parameters to begin the optimization process. In case of pure slip conditions, most *magic formula* parameters have a physical meaning. Consequently, a good approximation of starting values can be made. However, good starting values for the combined slip conditions can be difficult. As a result, considerable time is needed to calculate the suitable parameters. Cabrera et al. [12] presented a different method with genetic

algorithms to determine the *magic formula* parameters. The main advantage of this method is that the optimization process to find the value of the parameters can be started with any initial values.

Both version of *magic formula* tire model mentioned above are inadequate for characterizing the transient response of the tire. In view of this, Pacejka [13] proposed a relatively simple model for longitudinal and lateral transient responses restricted to relatively low time and path frequencies, as shown in Fig. 1.3. The non-steady state behavior of the tire is important in transient simulations. The transient and oscillatory properties of the tire-wheel combination have been improved in this model. The model was able to capture the dynamic behavior as long as the frequency of the wheel motion remains less than 15 Hz and the wavelength of motion and road undulation is larger than 1.5m. Relaxation length approach was not included in the model since the computations would be critical due to possible instabilities at combined slip. Therefore, a contact patch was defined, which could deflect in both longitudinal and lateral directions with respect to the lower part of the rim. Only translations were allowed with respect to the wheel plane. A mass was attached to the moving contact patch to determine the longitudinal and lateral forces and the self-aligning moment acting on the tire-road contact as a response to the slip velocity of the contact patch mass and to the camber angle. The turn slip has not been considered. It was reported that the carcass compliance together with the contact patch slip model automatically takes care of the wheel load dependent lag and also of the decrease in lag at increased combined slip. In addition, the contribution of important gyroscopic effects related with belt distortions were taken into account. Moreover, the non-lagging part of the camber force was modeled to act directly on the wheel rim.

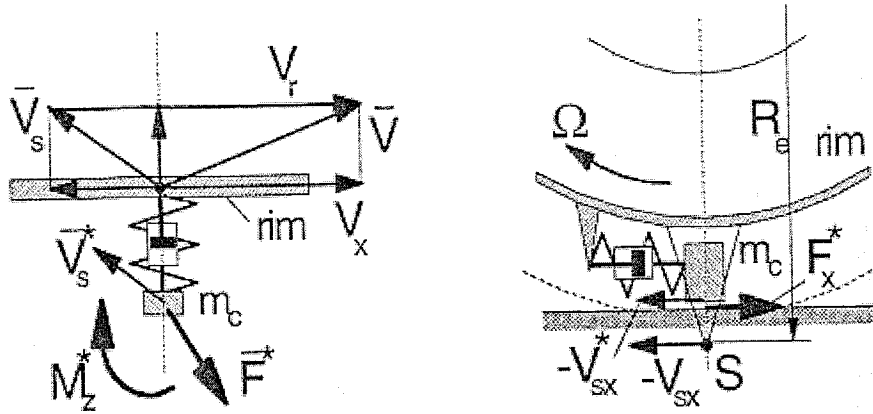


Fig. 1.3 Tire model in top and side view [13].

Mastinu [14] presented a physical tire model with semi-analytical formulation which is capable to calculate the tire forces generated at the tire-ground interface, i.e. the longitudinal force, the lateral force and the self-aligning torque. At steady-state condition, the consistency between computed and measured contact area size and between computed and measured longitudinal force, lateral force and aligning moment was satisfactory. However, at transient-state, the model, based on the present formulation, was capable to compute lateral force and aligning moment up to 10-15 Hz. A reasonable time was needed for the computation of tire forces.

Maurice [15] developed a rigid ring model for both lateral and longitudinal tire dynamics up to approximately 60 Hz, where the tire belt is modeled as rigid body with 6 degrees of freedom as shown in Fig. 1.4. The tire-road interface is modeled using a steady state tire model in conjunction with the relaxation length concept to describe the longitudinal and lateral tire force and the self-aligning moment. The relaxation length approach, however, is valid for low frequencies only as the inertia properties of the tire cannot be neglected at higher frequencies. Residual compliances were introduced to account for the large carcass deformations near the tire contact patch. The measured

frequency response functions of forces and moments with respect to the applied steering angle or braking moment were used to estimate the tire parameters. The total tire relaxation length was calculated as function of slip and the normal load. This model has been used to study the in-plane tire responses on uneven roads and to brake torque variations, and the out-of-plane tire responses due to side slip and yaw angle variations. The rigid ring model has been validated by experiments carried out on a rotating drum test stand. The tire dynamics were investigated by high frequency steer angle and brake torque variations, while the lateral transient behavior was studied by side slip variations. Although the model incorporates the three dimensional dynamic aspects of the tire tread band, only pure lateral and pure longitudinal slip situations were investigated. The theoretical stationary tire characteristic of the brush type tire model was used for the simplicity. Based on the investigation, it was concluded that the *magic formula* tire model, a better stationary tire characteristic, could be used to the improvement of the model behavior, especially for the self aligning moment [15].

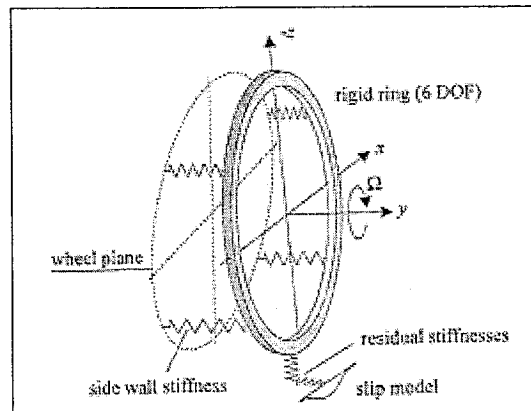


Fig. 1.4 Schematic view of tire model used [15].

Some other finite element models of tire, which are possible representation of the tire model proposed by Pacejka [13] are seen in the papers [1, 3, 16]. In those papers the

longitudinal tire forces, lateral tire forces and self-aligning moments have been determined by the *cosine version of magic formula* developed by Michelin [7].

1.2.4 Ride Analysis of Vehicle

Ride analysis of a vehicle refers to its vibration response during its motion. Ride quality is mainly concerned with the comfort of the passenger of moving vehicle, and the control of the intensity of dynamic loads transmitted to pavement. The performance measures related to ride quality has been the subject of considerable analytical and experimental evaluations. Ride quality can be assessed in terms of preservation of health, comfort and performance. The ride vibration environment of a vehicle could be expressed in terms of displacement, velocity, acceleration or jerk of the sprung mass. Many studies have shown a reasonably good correlation between the vertical acceleration and the subjective discomfort. The acceleration response of the sprung mass has thus been widely used as a measure of the vehicle ride quality [6].

Vehicle ride vibration and tire forces are strongly related to various vibration modes of the vehicle. Vehicle vibrations and thus the dynamic tire loads are dependent on the restoring and dissipative properties of the suspension and tires. Extensive studies reported on ride dynamics of road vehicles, however, have concluded that suspension damping affects the vehicle vibration behavior in a significant manner. Vibration absorbers mounted on vehicle axles have also been suggested for reducing the dynamic pavement loads in the range of wheel hop frequencies [17].

Ride dynamics of heavy vehicles are typically examined using rigid body models suspended through suspensions and tires. A number of ride dynamics models of vehicles ranging from two-DOF quarter vehicle models to comprehensive many-DOF three-

dimensional models have been reported in the literature [6]. Two DOF quarter-vehicle models have been extensively used to gain a fundamental understanding of the effect of suspension parameters on the vehicle performance characteristics subjected to deterministic or random road disturbances. A study performed by Oueslati [17] presented comprehensive attempt to evaluate the effects of suspension stiffness and damping on the root mean square (RMS) values and frequency response characteristics of the vehicle. The study [17] further presented the relative response characteristics of passive and ideal active suspensions using a seven DOF, three-dimensional car model, subjected to periodic and transient excitations arising from a chuck-hole type road disturbance.

In the research and design of vehicles, the accurate simulation of their dynamic behavior is often of interest. Moreover, failures of vehicles, due to dynamic excitations, originating either from huge transient loads or material fatigue always have local occurrence. Consequently the accurate knowledge of local dynamic behavior of vehicles is often interesting. Therefore, the application of large mechanical models is necessary in order to get correct information about the local dynamic behavior of critical parts of vehicles. In addition to, because of the required accuracy, the non-linear character of suspensions and tires usually may not be neglected. With regard to these requirements, Kuti [2] presented a special computational procedure for the nonlinear dynamic analysis of vehicles using large finite element models. This procedure consisted of two phases. In the first phase the mechanical model of linearized and undamped part of the given structure was elaborated and the natural mode calculation was carried out. Then, in the second phase, having considered the necessary model data, external excitations, and local nonlinearities, the step-by-step numerical solution of equilibrium equations was

performed. For this, a computer program had been written in FORTRAN. Correctness, in comparison to COSMOS/M commercial finite element program, and applicability of the presented procedure was shown by the use of a bus finite element model containing 2214 degrees of freedom. To reduce the solution time, the mode superposition method was successfully applied as the dynamic analysis of large finite element models by numerical methods is fairly time consuming, while the forces arising from these local nonlinearities (spring and damper forces) were taken into account by the pseudoforce method. Heavy vehicle vibration predominates in the 1-20 Hz range. It is important to note that this computational procedure was particularly developed for the three dimensional vibration analyses of vehicles under the action of vertical excitations when the vehicle forward speed was constant. Moreover, the slips between tires and road surface were neglected. The springs and dampers representing the elasticity and damping of tires were attached to the ground. However, this approach produced few undesirable low natural frequencies, which ultimately causes inaccurate result as the mode superposition method works on the basis of the participation of modes.

1.2.5 Handling and Longitudinal Analysis of Vehicle

The handling characteristics of a road vehicle usually refer to its response to steering commands and to environmental inputs. On the other hand, longitudinal characteristics of a road vehicle refer to its capability to accelerate, decelerate, and negotiate grades in a straight line motion. In general, vehicle lateral dynamics has been studied using rigid body models. To describe a vehicle's yaw, and lateral motions at a constant velocity, where the roll motions are ignored, a simpler model is obtained that is known as the bicycle model. The bicycle model has been widely used for control

purposes [8]. A comprehensive three-dimensional simulation program, referred to as Yaw/ Roll model, was developed by the Road and Transport Association of Canada (RTAC) and University of Michigan Transportation Research Institute (UMTRI). The simulation program incorporated nonlinear cornering characteristics of tires and nonlinear suspension force, while forward speed was assumed to be constant and the road is perfectly smooth. The above model was further improved to study the vehicle response to braking-in-a-turn [18]. Moreover, the above model was further enhanced by incorporating the road roughness [19].

Moreover, as mentioned before, Kuti [1, 3, 16] introduced large finite element vehicle model for bus and truck in order to carry out the handling and longitudinal performances measurement. The objective of these papers were to present examples of the non-conventional application of the finite element method, namely to the three dimensional dynamic analysis of the motions of road vehicles. The application of large finite element models, on the one hand, makes the accurate consideration of the elasticity and mass distribution of the structure of vehicles possible. The mode superposition method was applied since only a few low mode shapes to the structural dynamic analysis is enough to use. It also reduces the solution time. The vehicles carry out different maneuvers during their motions with large horizontal displacements (in longitudinal and lateral directions) and rotations about the vertical axis. In order to take these large motions into consideration by the help of the mode superposition method, the corresponding (three) rigid body modes with zero natural frequencies have to be included in the considered set of mode shapes. A detailed theoretical description of vehicle motions on the basis of the finite element method is given in paper [1]. It is well known

that these mode shapes do not contain any damping and non-linear effects; therefore, the pseudoforce method was applied to calculate the forces arising from dampers, springs and elastic deformation of other structural elements with nonlinear characteristics. The material damping of the vehicle has been approximated by the application of Rayleigh and/or modal damping. Considering that the vehicles perform large rotations about the vertical axis, the longitudinal and lateral tire forces as external excitations have been applied carefully to the instantaneous positions of the wheels.

In the paper [1] the dynamic behavior of the three dimensional semi rigid ring tire structural model (NDOF=306) was studied during cornering, braking and μ -split cornering, using a truck finite element model of 1874 degrees of freedom. This tire structural model contains the first natural modes of the tire belt in vertical, lateral, yaw, camber and rotational directions and in addition it can predict the large carcass deformations near the contact patch. The *cosine version of the magic formula* was used to the computation of the transient tire forces. Here, the transient behaviors of two versions of the truck model are compared with rigid and elastic chassis.

Another article written by Kuti [16], cornering, combined cornering and braking, μ -split cornering and wheel locking during asymmetric braking on symmetric frictional road processes were studied using a truck finite element model of 1064 degrees of freedom. In this study, the simpler contact patch tire model was applied. Tire springs and dampers were attached to the contact patches of tires. The motion of contact patches was constrained only in vertical direction so that the truck bus model could move and rotate freely in horizontal directions and about the vertical axis, respectively. The magnitudes of the contact patch masses were approximated in relation to the tire frequency considered.

Considering a single contact patch, different mass magnitudes in different directions and moments of inertia about different axes is defined. In this study, the natural frequency of the (undamped) camber mode of tires was 46 Hz, and that of the rotational mode was 41 Hz. The yaw mode was not considered. Finally, the transient behaviors of two versions of the truck model were compared with rigid and elastic chassis. The transient tire forces were computed using the *cosine version of the magic formula*.

In the article written by Kuti [3], two examples were presented in order to investigate the effectiveness and applicability of the elaborated method and finite element program written in FORTRAN for the step-by-step numerical solution of the given equations of motions. The first problem was related to an asymmetric braking when the path of the vehicle was corrected by steering the front wheels. In the second example, the right hand side wheels locking were studied. In both examples, the same finite element bus model containing 2294 degrees of freedom was applied. The simpler contact patch tire model with some modifications was used to predict the dynamic response of the tire belt. A rigid wheel model was applied to the considerations of the rotations of wheels by introducing a differential equation of motion for each wheel. A simple approximation was considered to determine the effective rolling radius as a function of the time varying vertical tire force. These effective rolling radii of wheels were calculated by the square of the ratio of the instantaneous and initial angular velocities in such a way that their magnitudes was equal to the corresponding deformed radii in case of zero angular velocities. The *cosine version of the magic formula* is used to the computation of the transient tire force characteristics.

1.3 SCOPE OF PRESENT WORK

This thesis includes a comprehensive study on ride, handling and longitudinal performance of heavy vehicles using the finite element model. Although the application of the finite element method in dynamic simulation of the motions of road vehicles is non-conventional, it provides more accurate response than traditional method. As discussed in the literature review, Kuti [1–3, 16, 20] recently carried out an extensive investigation of FEM model to address the issue of accuracy in simulation. However, still there are some issues which have not been addressed in the literature. Mostly the tire model used in ride analysis is not adequate to capture accurate response and the application of *cosine version of magic formula* tire model in handling and longitudinal performance has still made the analysis very costly. The present study, therefore, focuses on a finite element tire model which is capable to capture the response of vehicle on uneven road has been developed. Furthermore, an efficient mathematical model for a four wheel vehicle which is useful to analyze the combined slip conditions as well as pure slip conditions is proposed. More importantly, the *friction ellipse* tire model has been implemented instead of *cosine version of magic formula* tire model. In summary, the main contribution of this thesis can be itemized as follows:

1. To implement *friction ellipse* tire model in order to carry out efficient vehicle handling and longitudinal performance analysis.
2. To develop mathematical model for four-wheel rigid body vehicle which is well capable of capturing the responses to combined slip conditions (braking-in-a-Turn) as well as pure slip conditions.

3. To integrate load shift due to cornering and braking-in-a-turn in the mathematical model.
4. To define longitudinal and lateral slips for the finite element tire model based on the tire contact length, and to justify the proposed definition by comparing elastic body response with rigid body response.
5. To validate the finite element model by static weight balance check and frequency analysis.
6. To employ the mode superposition method in linear finite element model analysis, by which solution time can be reduced drastically.
7. To introduce ground spring with tire in ride analysis. This provides effective means to give the road excitations on the tire ground contact patch, especially when mode superposition method is employed.

1.4 THESIS ORGANIZATION

In Chapter 2, detailed finite element modeling of a highway bus, namely modeling of bus structure, suspension sets and tire, has been presented. Validations of model by static weight balance check and frequency response (modal) analysis have been illustrated. Moreover, prediction of low natural modes has been done by conducting transient analysis using kinematic harmonic sine sweep excitation. These modes are necessary to apply mode superposition method in transient analyses. This method is computationally very efficient compared to full method.

In Chapter 3, ride quality of the bus modeled in chapter 2 has been evaluated using ANSYS considering only surface irregularities or vertical excitations, namely half sinusoidal road input like a bulge and random road input like a city road. The effects of

nonlinear tire model and the corresponding linear tire model on ride quality have been investigated considering different maximum heights of the bulge. Moreover, in order to demonstrate the effectiveness and applicability of the large finite element model, ride analysis has been conducted for both flexible and rigid body models using linear tire model. This chapter also presents responses of the FEM model with linear tire model for a typical random rough road excitation.

The handling analysis of the candidate bus model is presented in Chapter 4. It includes pure cornering and combined cornering and braking analysis in order to simulate the handling and longitudinal performance of the candidate bus. Moreover, in order to demonstrate the effectiveness and applicability of the large finite element model, comparison between elastic and rigid chassis performance is presented in this study for both types of analyses. Mathematical four-wheel rigid body model is thus also developed to facilitate the analysis and comparison.

Chapter 5 presents the conclusions of the work undertaken and recommendations for the future work.

CHAPTER 2

FINITE ELEMENT MODELING OF HIGHWAY BUS AND ITS VALIDATION

2.1 INTRODUCTION

For a heavy vehicle, a well-detailed finite element model is necessary instead of using a typical rigid body model in order to attain more accurate dynamic responses and to examine the combined integrity of structural and dynamic performances. A highway bus is a perfect example of heavy vehicle. In this study, the finite element model of a typical highway bus shown in Fig. 2.1 is created in ANSYS, and is used to demonstrate the examples of the non-conventional application of the finite element method in measuring dynamic performances of heavy vehicles.

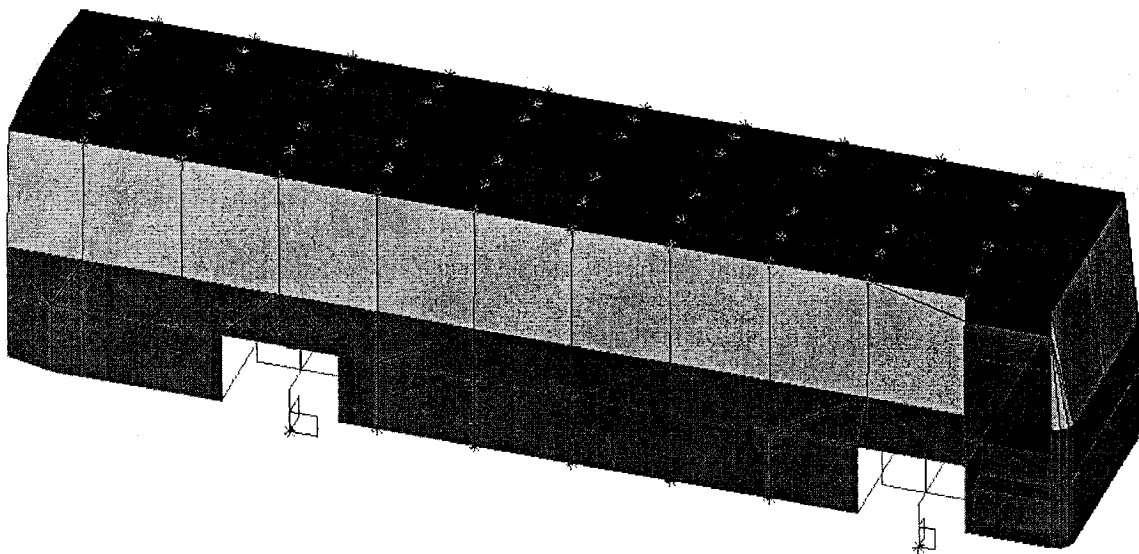


Fig. 2.1 Complete highway-bus finite element model.

Four types of elements, namely BEAM4, SHELL63, MASS21 and COMBIN14 (linear spring-damper element) have been used to construct the linear finite element highway bus model. In addition to those four types of element, COMBIN39 (nonlinear

spring element) element has been used to model nonlinear elements of the highway bus. The nonlinear model includes only the nonlinearity of radial (vertical) tire stiffness. Important information regarding the linear finite element highway bus model is summarized as follows:

Total Number of nodes:	325
Number of degrees of freedom:	1848
Total Number of beam elements:	522
Total Number of shell elements:	343
Total Number of mass elements:	115
Total Number of spring-damper elements:	46

Highway buses are considered commercial vehicles in both Canada and the United States. As such, they are subject to provincial weight and dimension limit regulations; for example, if overall length (including bumpers) is greater than 12.5 m, a minimum of 3 axles is required according to the original 1988 Memorandum of Understanding (MOU). Moreover, weight and dimension of vehicle play an important role on its dynamic performances. So, in this study to carry out the dynamic performances of a highway bus, a representative highway bus has to be chosen. The candidate bus chosen for this study is the Prévost-Car LeMirage XLII-40 model- a 12.2 m (40 ft) long two-axle highway bus. In order to build the finite element model of Prévost-Car LeMirage XLII-40, weights of different bus components are approximately taken according to Table 2.1 [21] since Table 2.1 is for model XLII-45, and model XLII-45 is five feet longer than model XLII-40. Moreover, material selection for different bus components has been accomplished on the basis of paper [21] as type of material dominates the weight of a component. However, the required properties of the selected materials (Table 2.2) to build the model are taken from the website of Automation Creations, Inc. [22]. Finally, gross weight of

the candidate bus becomes 17735 kg (Table 2.3). Several important dimensions of the candidate bus in Table 2.3 are approximately taken on the basis of the data given for model XLII-40 in Table 1.1 [5]. The remaining dimensions in Table 2.3, such as the distance of front tire center from c.g. (b), the distance of rear tire center from c.g. (c), and the location of c.g. are determined through self-weight analysis and precise mass calculation of the candidate highway bus model.

Table 2.1 Prévost Car XLII-45 Bus Components and Weights [21].

Component Name & Parts	Weight (kg)	Total (kg)	Percentage of Total Component	Percentage of Total Bus
Exterior Finish		1409.5		6.6
Doors, front bumper, front face	323.7		1.5	
Windows	686.2		3.2	
Baggage doors	163.3		0.8	
Rear face	29.9		0.1	
Motor cover	81.2		0.4	
Rear bumper	25.9		0.1	
Evaporator door, service doors	99.3		0.5	
Interior Finish		6077.7		28.4
Dashboard	89.8		0.4	
Defrost unit	45.8		0.2	
Drivers seat	115.7		0.5	
Parcel compartment	531.5		2.5	
Passengers	4382.1		20.5	
Passenger seats	881.9		4.1	
Toilet	30.8		0.1	
Baggage Compartment		2423.8		11.3
A/C ventilation	172.4		0.8	
Gas tank	93.4		0.4	
Fuel	661.1		3.1	
Luggage	1496.9		7.0	
Motor Compartment		2582.0		12.1
Motor and mechanicals	2582.0		12.1	
Spare Tire Compartment		169.6		0.8
Spare tire, gear box, Pitman arm	169.6		0.8	
Suspension		2953.8		
Differential	1360.8		6.4	
Tag axle	680.4		3.2	
Rigid axle	912.6		4.3	
Structure	3628.7	3628.7	17.0	17.0
Body & Accessories		2120.8		9.9
Miscellaneous body parts	2120.8		9.9	
TOTAL	21368.6	21368.6	100.0	100.0

Table 2.2 List of materials used in the model.

No. of Material	Name of Material	Properties		
		Young's Modulus (N/m ²)	Density (kg/m ³)	Poisson Ratio
1	AISI 1005 Steel, Subcategory: AISI 1000 Series Steel; Carbon Steel; Low Carbon Steel; Metal	0.20000E+06	7872	0.29
2	Aluminum 7005-W, Subcategory: 7000 Series Aluminum Alloy; Aluminum Alloy; Metal; Nonferrous Metal	72000	2780	0.33
3	Conventional LEXAN polycarbonate sheet, Subcategory: Polycarbonate; Polymer; Thermoplastic	2550	1200	0.10

Table 2.3 Important Dimensions and Weights of the candidate FE highway bus.

Name of Parameter	Value of Parameter
Overall Length	12.20 m
Overall Width	2.6 m
Overall Height	3.46 m
Cabin Floor Height	1.16 m
Floor-To-Ceiling Height	2.15 m
Ground Clearance	0.32 m
Wheel Base, L	7.25 m
Front Track Width, t_f	2.098 m
Rear Track Width, t_r	1.94 m
Front Overhang Length	1.825 m
Rear Overhang Length	3.125 m
Moment of Inertia about Vertical Axis	$I_{yy} = 0.24496\text{E}+06 \text{ kg}\cdot\text{m}^2$
Distance Front Tire to Center of Mass, b	5.2719 m
Distance Rear Tire to Center of Mass, c	1.9781 m
Center of Mass (X, Z) from Rear Right Corner Point of Bus Body	(5.1031 -1.2952) m
Height of Center of Gravity from the Ground, h	1.11184 m
Tires (Rear)	MICHELIN 315/70R×22.5
Tires (Front)	MICHELIN 365/70R×22.5
Chassis Frame	4.5 mm thick \square section steel profile
Gross Vehicle Weight Rating, m	17735 kg
Gross Weight on Front Tires, m_f	4838.84 kg
Gross Weight on Rear tires, m_r	12896.16 kg

2.2 FINITE ELEMENT MODELING

2.2.1 Modeling of Highway Bus Structure

The structural components of the bus shown in Fig. 2.2 have been modeled with beam and shell elements. Beam and shell parts of the structure are meshed using BEAM4 and SHELL63, respectively. BEAM4 is a uniaxial element with tension, compression, torsion, and bending capabilities. The element has six degrees of freedom at each node: translations in the nodal x, y, and z directions and rotations about the nodal x, y, and z-axes. BEAM4 is chosen for meshing chassis, floor-beam, side-post, side-truss and roof-beam. Chassis, floor-beam, side-post and side-truss are made of steel, material no. 1 in Table 2.2. Roof-beam is made of aluminum, material no. 2 in Table 2.2 as aluminum provides a very high potential for weight reductions. SHELL63 has both bending and membrane capabilities and both in-plane and normal loads are permitted. The element has six degrees of freedom at each node: translations in the nodal x, y, and z directions and rotations about the nodal x, y, and z-axes. SHELL63 is used for meshing floor, sidewall, ceiling and window. Floor and sidewall are made of steel, whereas ceiling is made of aluminum skin and window is of polycarbonate (Lexan) sheet, material no. 3 in Table 2.2. Polycarbonate (Lexan) windows offer high weight savings potential; however, scratch resistance, UV protection and static charge resistance are concerns [21]. All non-structural mass such as passengers, passenger seats, fuel, parcel compartment, engine, toilet, defrost unit, A/C ventilation, gas tank, driver seat, dashboard and luggage are represented by mass elements concentrated at the centroid of the actual equipment mass. MASS21 is used to represent the mass elements. MASS21 is a point element having up to six degrees of freedom: translations in the nodal x, y, and z directions and rotations about

the nodal x, y, and z-axes. A different mass and rotary inertia may be assigned to each coordinate direction. Material damping of structural elements can be approximated by the application of Rayleigh or modal damping.

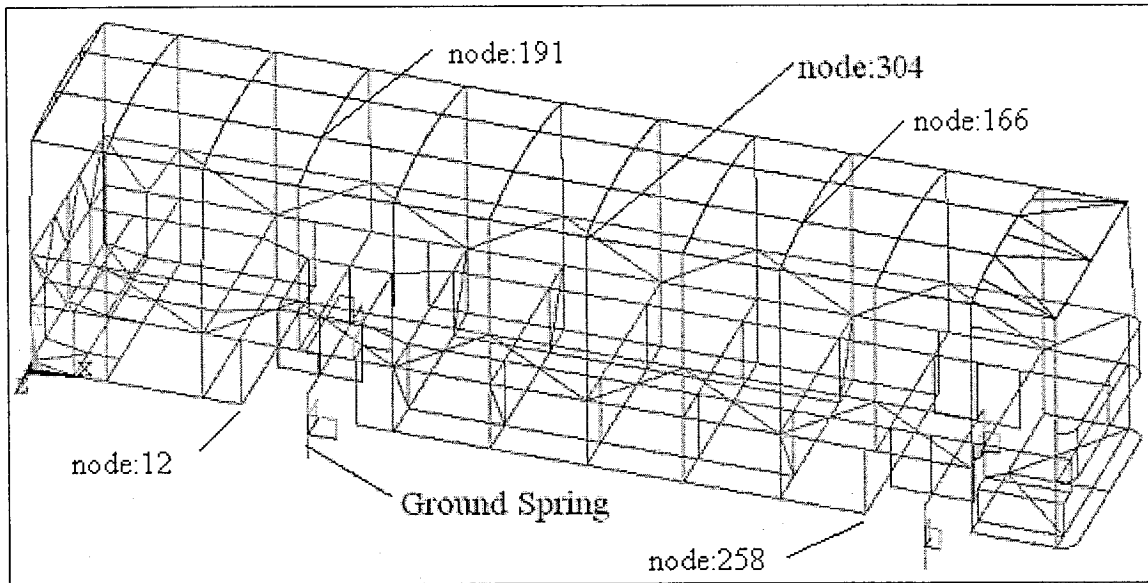


Fig. 2.2 Skeleton structure of the applied bus model with ground spring.

2.2.2 Modeling of Suspension Sets

The main frame of the chassis including the front and rear undercarriages are shown in Fig. 2.3. In the suspension sets, leaf springs are applied with linear characteristics at the extremities of the rigid spring arms, while the linear dampers are positioned at the midpoint of the rigid spring arms just above the axles. The stiffness of leaf springs on each side of rear axle is 468000 N/m, while that of leaf springs on each side of front axle is 156000 N/m. The characteristics of a real damper used in the suspension sets of a typical highway bus are nonlinear as shown in Fig. 2.4. However, linear damper characteristics are considered in this study. The applied linearized damper characteristics used in the suspension sets are shown in Fig. 2.5, and the linearization of

the non-linear damper characteristics is done by linear curve fitting for the positive part (extension of damper) of the curve shown in Fig. 2.4. However, that fixed damping coefficient is considered in both extension and compression of the applied damper. An anti-roll torsion bar is built in between the chassis and rear axle. Rigid spring arms and anti-roll torsion bar have been modeled using beam elements and meshed with BEAM4. Leaf springs and dampers have been modeled with linear spring-damper element COMBIN14. COMBIN14 has longitudinal or torsional capability in one, two, or three-dimensional applications. The longitudinal spring-damper option is a uniaxial tension-compression element with up to three degrees of freedom at each node: translations in the nodal x, y, and z directions. No bending or torsion is considered. The torsional spring-damper option is a purely rotational element with three degrees of freedom at each node: rotations about the nodal x, y, and z-axes. No bending or axial loads are considered. The spring or the damping capability may be removed from the element.

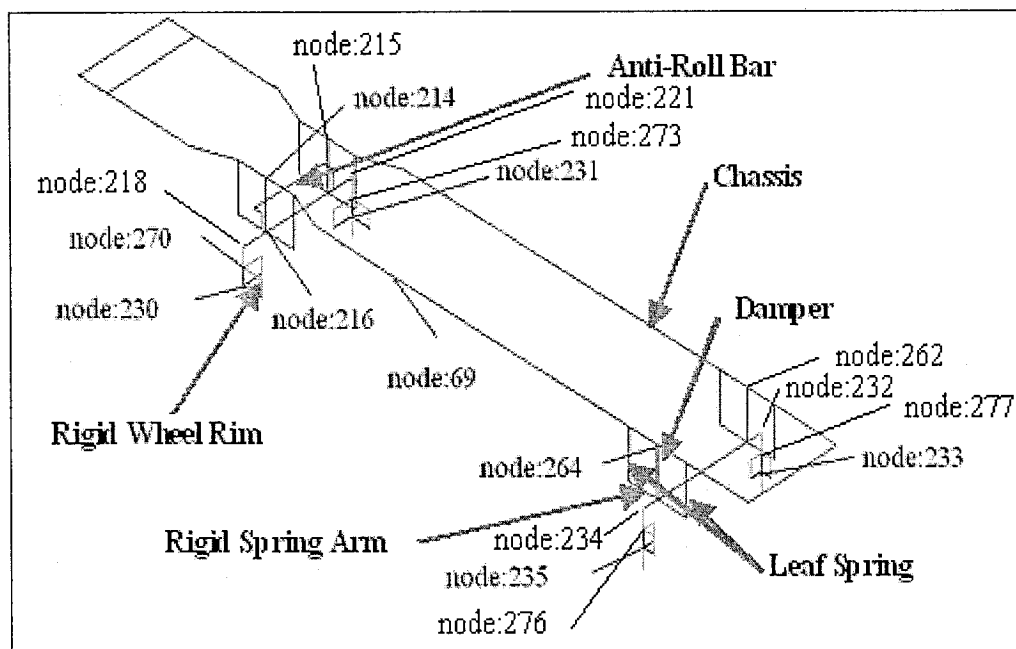


Fig. 2.3 Chassis with undercarriages and ground spring.

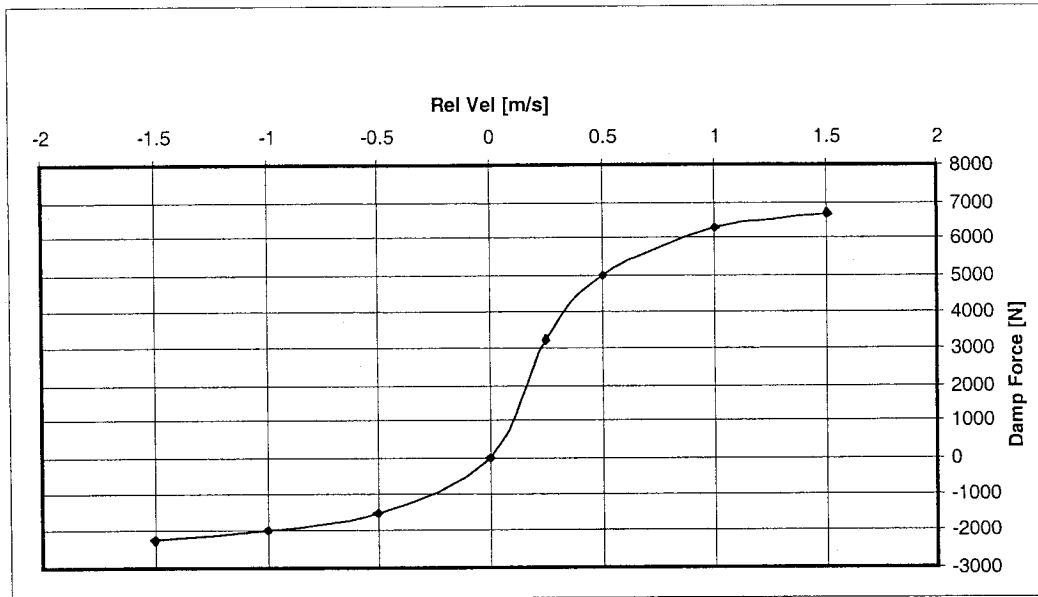


Fig. 2.4 Nonlinear damper characteristics.

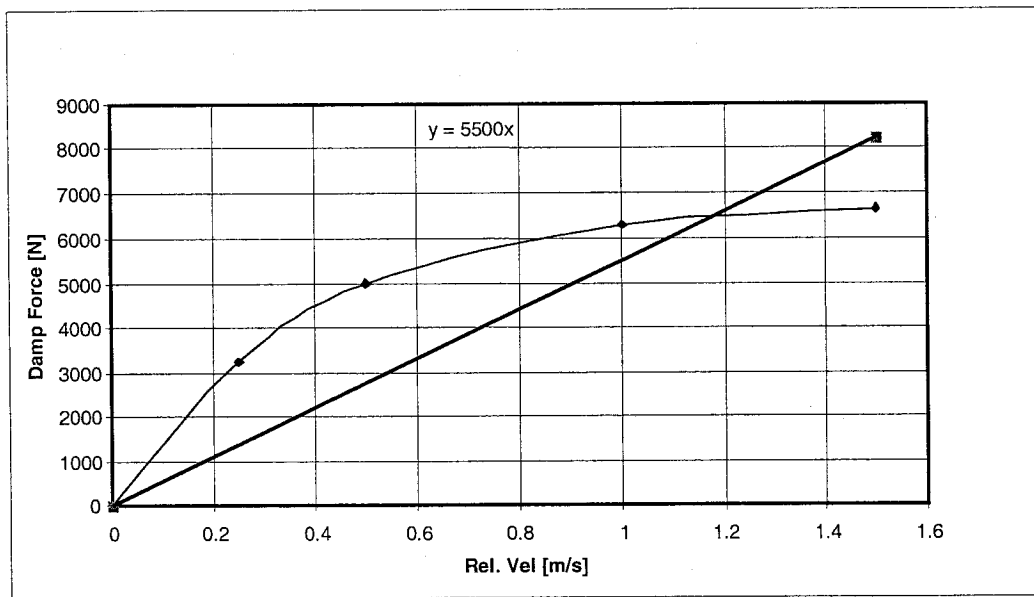


Fig. 2.5 Linearization of nonlinear damper characteristics.

2.2.3 Modeling of Tires

The most important aspect of this study is to develop a rigid ring tire model. Kuti [2] used a tire model with the springs and dampers representing the elasticity and damping of tires were attached to the ground. But this approach produced few

undesirable low natural frequencies, which ultimately causes inaccurate results as the mode superposition method works on the basis of the participation of modes. Now, these extremities of the springs and dampers are connected to the contact patches of tires as shown in Fig. 2.6. The motion of contact patches is constrained only in vertical direction using either boundary conditions or heavy stiffer springs ($k_{gr}=200e9$ N/m) that represents the ground; hence the complete bus model can move and rotate freely in horizontal directions and about the vertical axis, respectively. Boundary conditions are used in order to constrain the contact patches vertically as shown in Fig. 2.6 in case of longitudinal and handling analysis, while ground springs are modeled to constrain the contact patches as shown in Fig. 2.7 in case of ride analysis only. Moreover, these ground springs provide effective means to give the road excitations on the tire ground contact patch. Linear spring element (COMBIN14) is used to represent the ground spring in case of ride analysis with linear finite element bus model. On the contrary, nonlinear spring element (COMBIN39) is used to represent the ground spring in case of ride analysis with nonlinear finite element bus model as ground shows only compressive strength in fact. COMBIN39 is a unidirectional element with nonlinear generalized force-deflection capability that can be used in any analysis. The element has longitudinal or torsional capability in one, two, or three-dimensional applications. The longitudinal option is a uniaxial tension-compression element with up to three degrees of freedom at each node: translations in the nodal x, y, and z directions. No bending or torsion is considered. The torsional option is a purely rotational element with three degrees of freedom at each node: rotations about the nodal x, y, and z-axes. No bending or axial loads are considered.

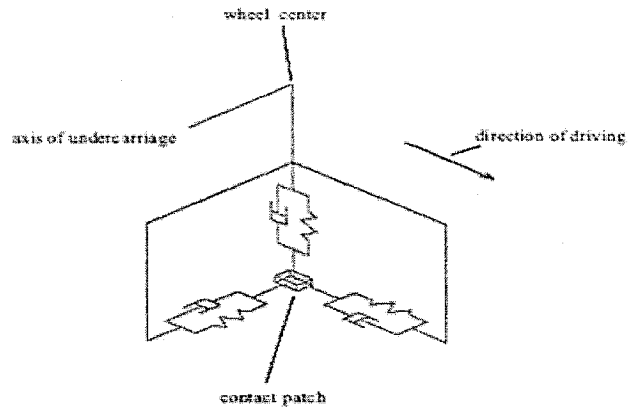


Fig. 2.6 Finite element model of tires for handling analysis.

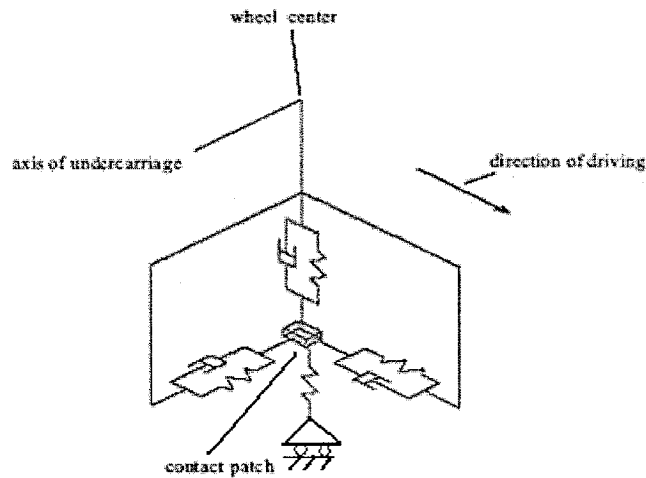


Fig. 2.7 Finite element model of tires with ground spring for ride analysis.

Tire is a complex mechanical system, and it is difficult to model precisely its elasticity and damping. The elasticity of a tire in the radial (vertical) direction is non-linear, but it can be represented by linear spring characteristics [23, 24]. Figs. 2.8-2.11 show the applied non-linear and linearized tire spring characteristics, in radial direction, of the front and rear wheels. The linearization of radial tire stiffness is done by linear curve fitting for the compressive zone shown in Figs. 2.9 and 2.11. However, the fixed radial tire stiffness is considered for both compression and tension in case of linear tire

model. It should be noted that on each side of rear axle two tires are considered. In lateral and longitudinal directions linear spring characteristics are applied. The damping coefficients of tires in each direction are selected on the basis of published measured data [6]. The damping coefficient of a tire in each direction is taken as 4000 N-s/m.

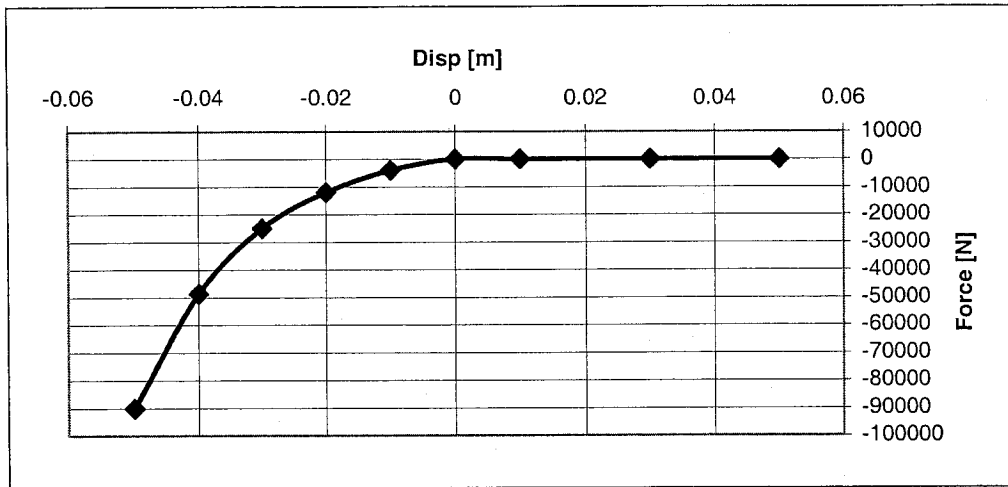


Fig. 2.8 Nonlinear characteristics of the elasticity of the front tire in radial direction.

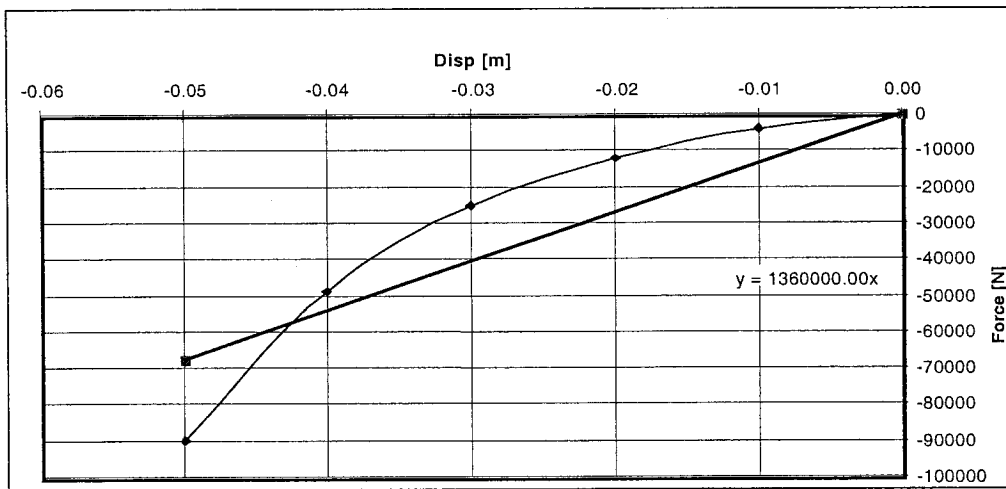


Fig. 2.9 Linearization of nonlinear characteristics of the elasticity of the front tire in radial direction.

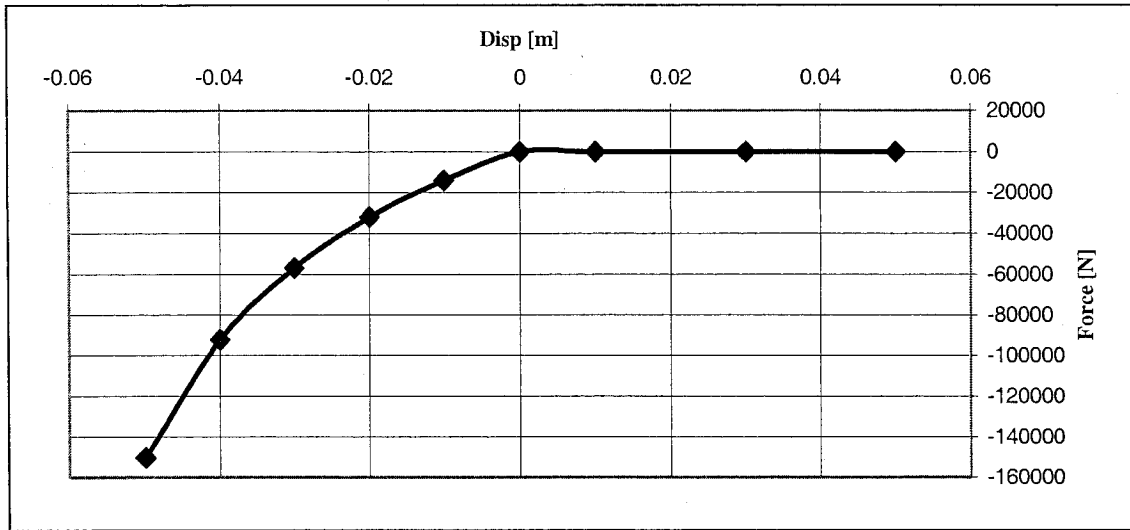


Fig. 2.10 Nonlinear characteristics of the elasticity of the rear tires in radial direction.

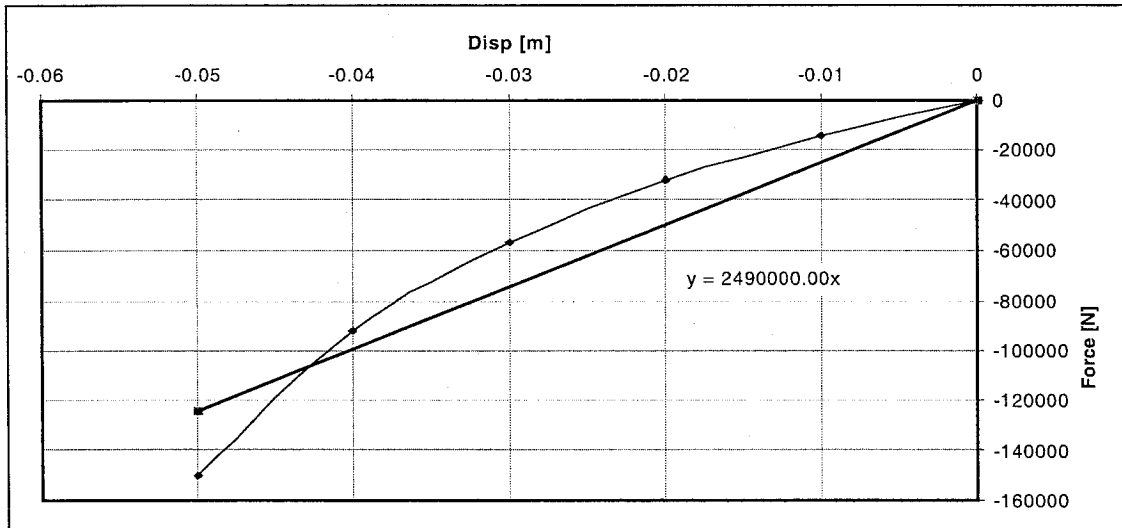


Fig. 2.11 Linearization of nonlinear characteristics of the elasticity of the rear tires in radial direction.

Longitudinal stiffness of a tire is calculated on the basis of the experimental value of longitudinal slip stiffness (211896 N/unit slip) and longitudinal relaxation length (0.1524 m) taken from Fancher et al. [25] with respect to the same vertical load (26487 N) on that tire. Longitudinal stiffness of a tire is calculated from the following relation:

$$\text{Long. tire stiffness} = \text{Long. Slip Stiffness} / \text{Long. Relaxation Length}$$

The effect of vertical load on longitudinal slip stiffness and longitudinal relaxation length of a tire is measurable through experiment. According to the experiment conducted by Maurice et al. [15], the characteristics of longitudinal slip stiffness and longitudinal relaxation length with respect to the vertical load are nonlinear, but the ratio of them is approximately unique. So, linear spring characteristics can be approximated for the longitudinal tire stiffness. The calculated longitudinal stiffness of a tire is 1390037.76 N/m.

Lateral stiffness of a tire is calculated on the basis of the experimental value of cornering stiffness (277610 N/rad) taken from the Fig. 2.12 and lateral relaxation length (0.3354 m) taken from Fancher et al. [25] with respect to the same vertical load (26487 N) on that tire. Lateral stiffness of a tire is calculated from the following relation:

$$\text{Lateral tire stiffness} = \text{Cornering Stiffness} / \text{Lateral Relaxation Length}$$

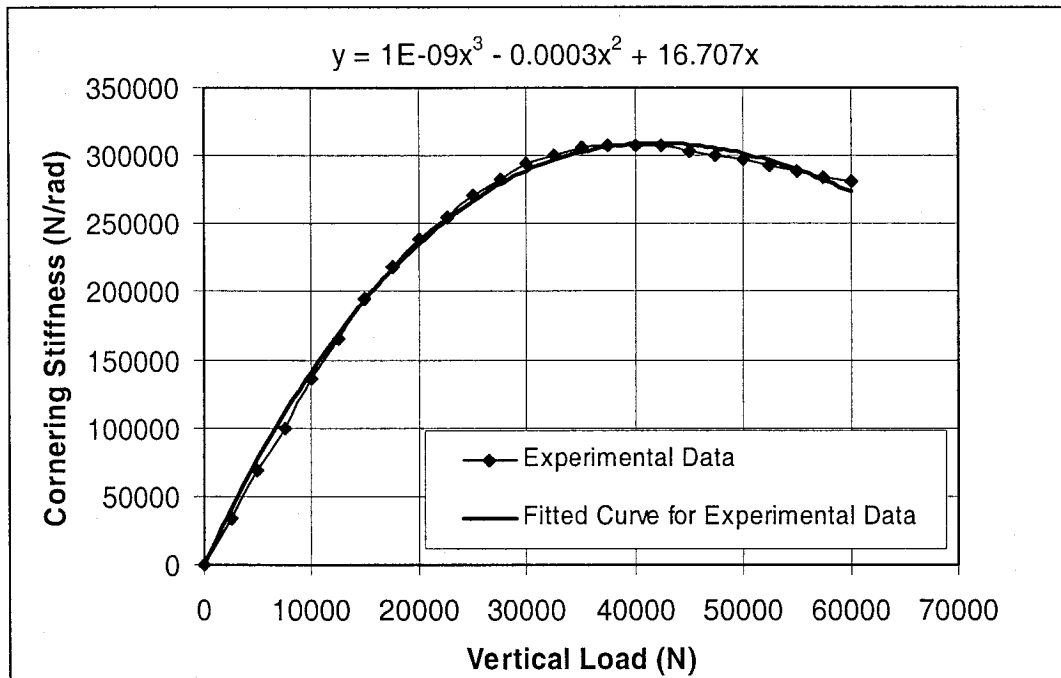


Fig. 2.12 Effect of vertical load on cornering stiffness of tire.

The effect of vertical load on cornering stiffness and lateral relaxation length of a tire is measurable through experiment. According to the experiment conducted by Maurice et al. [15], the characteristics of cornering stiffness and lateral relaxation length with respect to the vertical load are nonlinear, but the ratio of them is approximately unique. So, linear spring characteristics can be approximated for the lateral tire stiffness. The calculated lateral stiffness of a tire is 827698.27 N/m.

First rotational, camber and yaw modes of the developed rigid ring tire model can be taken into account, considering different mass magnitudes in different directions and moment of inertia about different axes for the contact patch of a tire. In this study, the natural frequency (undamped) of the camber mode of a tire is taken 46 Hz, and that of rotational mode is taken 41 Hz on the basis of the Kuti [16]. The yaw mode has not been considered yet. The magnitudes of a contact patch masses in different directions are calculated in relation to the corresponding included tire frequency. The following formula is used to calculate the contact patch masses in different directions:

$$f_n = 1/(2 \times \pi) \times \sqrt{k / m_c} ;$$

where: f_n = *Natural Frequency in Hz*,

k = *longitudinal or lateral tire stiffness in N / m*,

m_c = *tire contact patch mass in kg*

The calculated contact patch mass of a tire in the longitudinal direction is 20.95 kg as rotational frequency of the applied tire is taken 41 Hz, and the longitudinal stiffness of a tire is 1390037.76 N/m. Similarly, the calculated contact patch mass of a tire in the lateral direction is 9.91 kg as camber frequency of the applied tire is taken 46 Hz, and the lateral stiffness of a tire is 827698.27 N/m.

The construction of contact patches can be taken into account as a possible finite element representation of the tire model as presented by Pacejka et al. [13]. But in this study, the longitudinal and lateral tire forces arising between tires and road surfaces are determined by the *friction ellipse* instead of using the *cosine version of magic formula* tire model developed by Michelin [7]. The application of *friction ellipse* tire model over *cosine version of magic formula* tire model is found to be extremely useful and efficient for vehicle handling and longitudinal performance analysis as Magic Formula tire model requires the determination of increased number of parameters, around 42. On the contrary, *friction ellipse* tire model requires only a few numbers of experimental data sets. Moreover, the determination of increased number of parameters raises the total percentage of errors.

According to the Julien's theory, the tire tread is regarded as an elastic band, and the longitudinal strain of the tire tread is a measure of the longitudinal slip [8]. On the other hand, a simplified theory proposed by Segel [9] relates the slip angle with lateral tire tread deformation at a longitudinal distance measured from the front of the contact patch and along the wheel plane. But in this study, contact length approach, with the slight modifications of the concepts used by Julien and Segel [8, 9], is introduced to measure the longitudinal slip and the slip angle of tire. Consequently, the longitudinal slip and slip angle are defined as follows:

$$i = \frac{D_{cpx} - D_{cwx}}{l_t} \quad (2.1)$$

$$\alpha = \frac{D_{cpy} - D_{cwy}}{l_t} \quad (2.2)$$

where: i is the longitudinal slip,

α is the slip angle,

D_{cpx} is the longitudinal displacement of the contact patch,

D_{cwx} is the longitudinal displacement of the wheel center,

D_{cpy} is the lateral displacement of the contact patch,

D_{cwy} is the lateral displacement of the wheel center,

l_t is the tire contact length,

Referring to Fig. 2.13, the tire contact length can be calculated from the following equation:

$$l_t = R_o \times A(t) \quad (2.3)$$

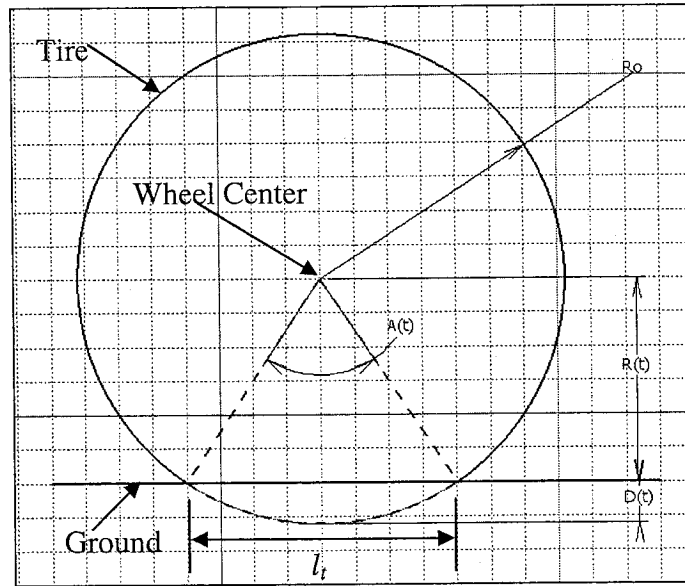


Fig. 2.13 Tire contact length.

where R_o is the unloaded tire radius, and $A(t)$ is the angle produced by the tire contact length with respect to the wheel center. t between the parentheses represents the time function. Referring to Fig. 2.13, $A(t)$ can be calculated from the following relation:

$$A(t) = 2 \times \cos^{-1}(R(t)/R_o) \quad (2.4)$$

where $R(t)$ is the dynamic loaded radius of tire and it can be calculated using the following equation:

$$R(t) = R_o - D(t) \quad (2.5)$$

where $D(t)$ is the vertical tire deformation and it can be readily found from the output of FEM model simulation.

There is also an alternative way to calculate the tire contact length, l_t as indicated in Eq. 2.6, but it requires the experimental data for the longitudinal slip stiffness, C_i versus vertical tire load.

$$(k_t \times l_t) / 2 = C_i; \text{ where } k_t \text{ is the longitudinal tire stiffness} \quad (2.6)$$

Linear spring-damper element COMBIN14 (uniaxial tension-compression element) is used to represent radial tire stiffness and damping in case of ride analysis with linear finite element bus model. On the contrary, nonlinear spring element COMBIN39 and COMBIN14 are used to represent radial tire stiffness and damping, respectively in case of ride analysis with nonlinear finite element bus model since a tire has no springing action when it lifts off the ground. Tire stiffness and damping in longitudinal and lateral directions are modeled with COMBIN14. Rigid wheel rims are modeled with COMBIN14 having heavy stiffer spring constant ($k_{wr}=200e9$ N/m). Contact patches are modeled with MASS21. An extra one dimensional torsional spring is used in each front tire to receive the steering input. COMBIN14 is used to model that torsional spring. It is important to mention that twenty constraint equations have been written for merging the

nodes used in the tire modeling, because all nodes in a tire does not have same degrees of freedom.

2.3 MODEL VALIDATION

Vehicles always are in motion and follow different shapes of path running over from smooth highways to extremely rough off-road terrains. So, static weight balance checks and frequency analyses are of primary concern in the effective design of vehicles. To validate the developed finite element highway bus model, first weight balance is checked by conducting static analysis due to the self weight of the bus. Then modal analysis is performed to obtain the natural frequencies and to compare those with the available experimental data of a real bus, since designing of a bus is followed by a number of guidelines and rules of thumb in view of the ride quality, human comfort and handling performance. It is important to note that natural frequency plays a major role on the dynamic performance of a system.

2.3.1 Static Analysis

Static weight balance of the candidate bus with or without ground spring has been checked considering self-weight of the bus. It should be noted that linear tire model is used in both cases, and the sprung mass, rear unsprung mass, and front unsprung mass are 15411.99 Kg, 1410.41 Kg, and 912.6 Kg, respectively. Figs. 2.14 and 2.15 show the longitudinal displacement of the candidate bus with or without ground spring due to the gravitational weight, respectively. The maximum longitudinal displacements of the candidate bus with or without ground spring are 8 mm and 13 mm, respectively.

Reaction loads due to the gravitational weight on different positioned tires are listed in Table 2.4. Figs. 2.16 and 2.17 show the vertical displacement of the candidate

bus with or without ground spring due to the gravitational weight, respectively. In both cases, the vertical displacements of the bus body along the length and width are almost same. Static suspension deflection and rattle space are found approximately 155.4 mm and 0.635m, respectively. In addition, the vertical deflections of front and rear tires are 17.6 mm and 25.6 mm, respectively, which are same as those found based on static load and radial tire stiffness.

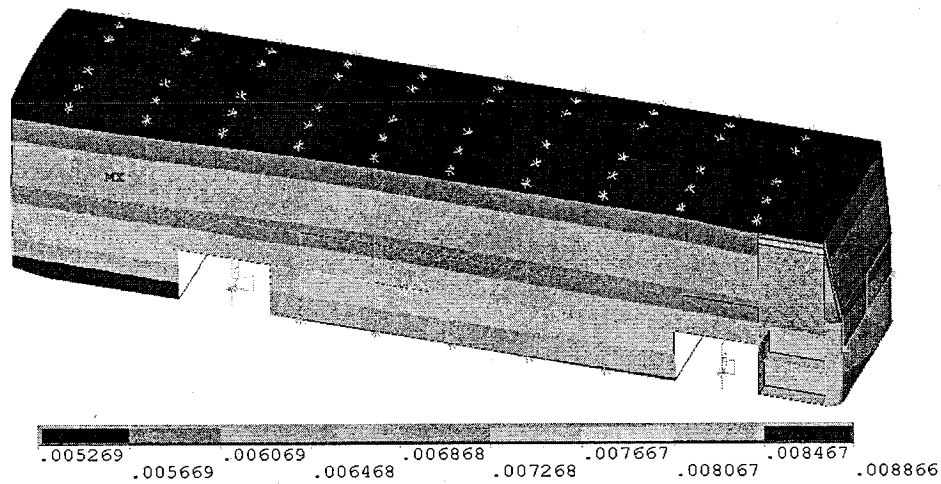


Fig. 2.14 Longitudinal displacement of complete bus with ground spring due to the gravitational weight.

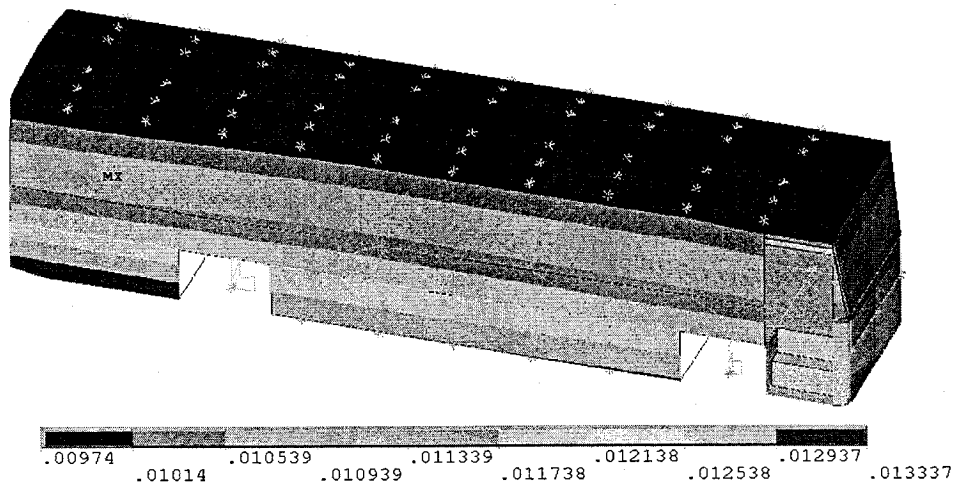


Fig. 2.15 Longitudinal displacement of complete bus without ground spring due to the gravitational weight.

Table 2.4 Reaction load on different tire-ground contact.

Position of Tire-Ground Contact	Reaction Load (N)
Rear Right	63538
Rear Left	63036
Front Right	23873
Front Left	23538

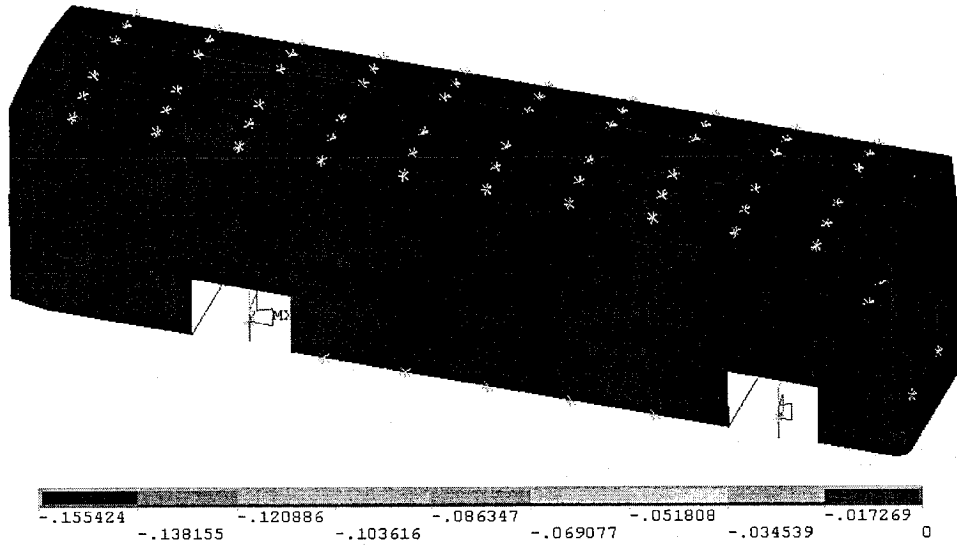


Fig. 2.16 Vertical displacement of complete bus with ground spring due to the gravitational weight.

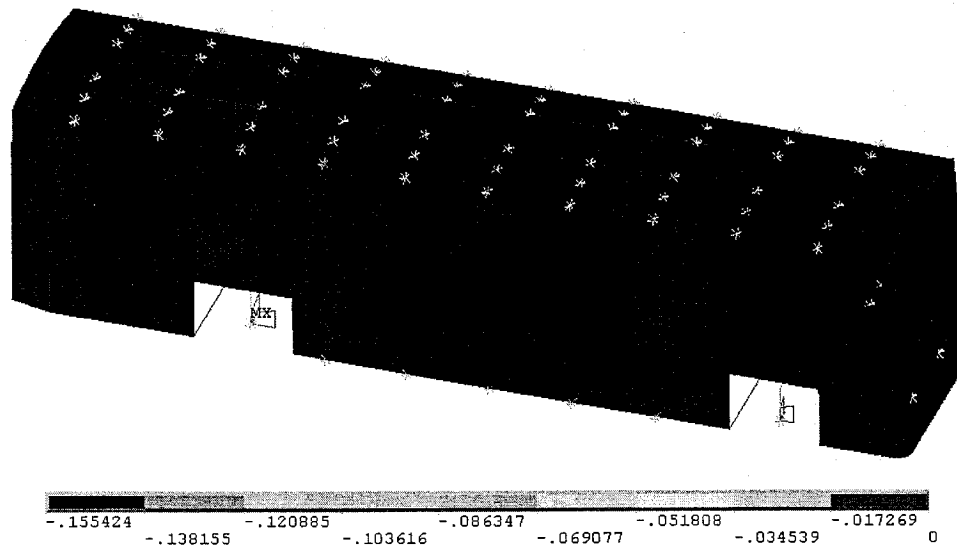


Fig. 2.17 Vertical displacement of complete bus without ground spring due to the gravitational weight.

Figs. 2.18 and 2.19 show the lateral displacement of the candidate bus with or without ground spring due to the gravitational weight, respectively. Both models show maximum lateral deflections of 4 mm at the roof.

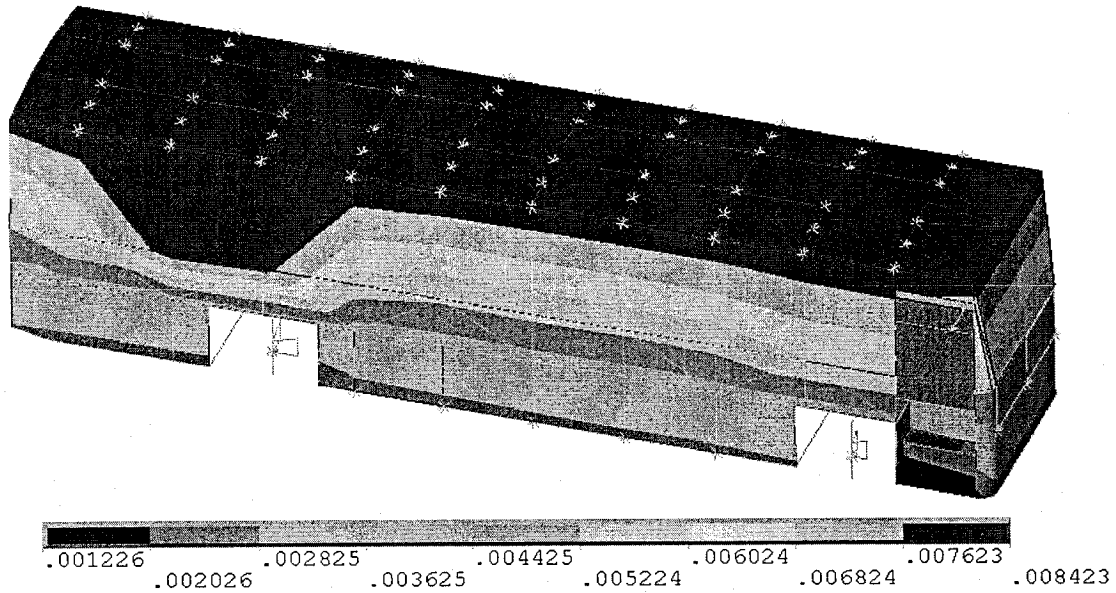


Fig. 2.18 Lateral displacement of complete bus with ground spring due to the gravitational weight.

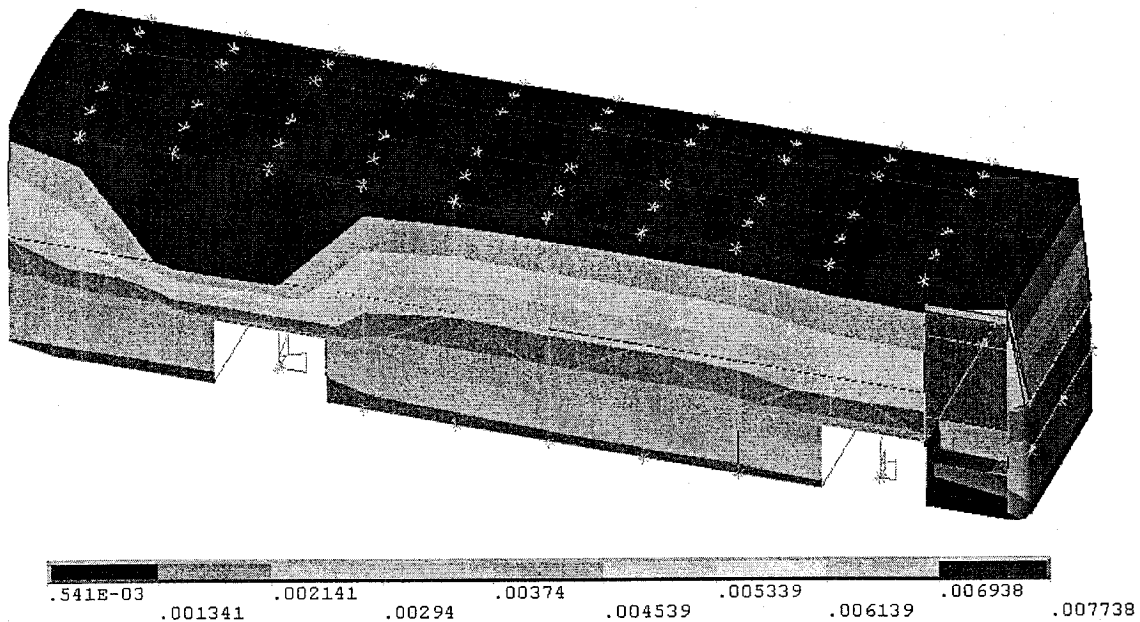


Fig. 2.19 Lateral displacement of complete bus without ground spring due to the gravitational weight.

2.3.2 Modal Analysis

Modal analysis is carried out for linear undamped bus model with or without ground spring. Table 2.5 summarizes the first fifty natural frequencies of the designed bus for both cases and it shows good correlation with the natural frequencies of a real bus. First three frequencies are rigid body frequencies which have been found due to the applied boundary conditions. Corresponding rigid mode shapes are shown in Fig. 2.20. Fig. 2.21 shows the rolling, pitch and bounce mode shapes, and corresponding to those natural frequencies. These sprung mass frequencies are less than 1.5 Hz, and the bounce natural frequency is less than 1.2 times the pitch natural frequency. The unsprung mass frequencies and corresponding mode shapes are shown in Fig. 2.22. These unsprung mass frequencies are well above 8 Hz. These predicted sprung and unsprung mass frequencies are typical design frequencies for such road vehicles.

Table 2.5 First fifty natural frequencies of the candidate bus.

Natural Frequency of Linear Undamped Bus Model with Ground Spring	Natural Frequency of Linear Undamped Bus Model without Ground Spring
<div>SET TIME/FREQ</div> <div>1 0.13922E-04</div> <div>2 0.51057E-04</div> <div>3 0.71642E-02</div> <div>4 0.72781</div> <div>5 1.1413</div> <div>6 1.3144</div> <div>7 9.1620</div> <div>8 9.3166</div> <div>9 10.960</div> <div>10 11.229</div> <div>11 13.041</div> <div>12 13.896</div> <div>13 13.910</div> <div>14 14.720</div> <div>15 15.097</div> <div>16 15.239</div> <div>17 15.303</div> <div>18 16.757</div> <div>19 17.265</div> <div>20 19.061</div> <div>21 19.746</div> <div>22 20.976</div> <div>23 22.102</div> <div>24 23.710</div> <div>25 23.981</div> <div>26 24.638</div> <div>27 26.381</div> <div>28 26.514</div> <div>29 26.794</div> <div>30 28.328</div> <div>31 28.670</div> <div>32 28.762</div> <div>33 29.107</div> <div>34 29.440</div> <div>35 29.884</div> <div>36 31.182</div> <div>37 31.820</div> <div>38 32.288</div> <div>39 32.858</div> <div>40 33.394</div> <div>41 33.572</div> <div>42 33.738</div> <div>43 33.869</div> <div>44 34.157</div> <div>45 34.222</div> <div>46 34.889</div> <div>47 35.336</div> <div>48 35.711</div> <div>49 35.904</div> <div>50 36.273</div>	<div>SET TIME/FREQ</div> <div>1 0.18578E-04</div> <div>2 0.72516E-04</div> <div>3 0.71642E-02</div> <div>4 0.72781</div> <div>5 1.1413</div> <div>6 1.3144</div> <div>7 9.1620</div> <div>8 9.3166</div> <div>9 10.960</div> <div>10 11.229</div> <div>11 13.041</div> <div>12 13.896</div> <div>13 13.910</div> <div>14 14.720</div> <div>15 15.097</div> <div>16 15.240</div> <div>17 15.303</div> <div>18 16.757</div> <div>19 17.265</div> <div>20 19.061</div> <div>21 19.746</div> <div>22 20.976</div> <div>23 22.102</div> <div>24 23.710</div> <div>25 23.981</div> <div>26 24.638</div> <div>27 26.381</div> <div>28 26.514</div> <div>29 26.794</div> <div>30 28.328</div> <div>31 28.670</div> <div>32 28.762</div> <div>33 29.107</div> <div>34 29.440</div> <div>35 29.884</div> <div>36 31.182</div> <div>37 31.820</div> <div>38 32.288</div> <div>39 32.858</div> <div>40 33.394</div> <div>41 33.572</div> <div>42 33.738</div> <div>43 33.869</div> <div>44 34.157</div> <div>45 34.222</div> <div>46 34.889</div> <div>47 35.336</div> <div>48 35.711</div> <div>49 35.904</div> <div>50 36.273</div>

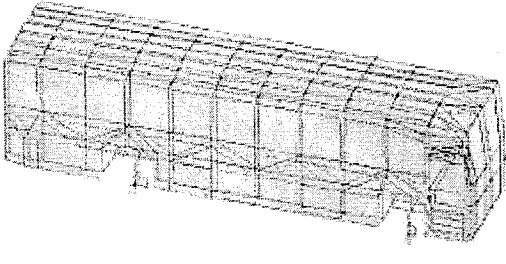
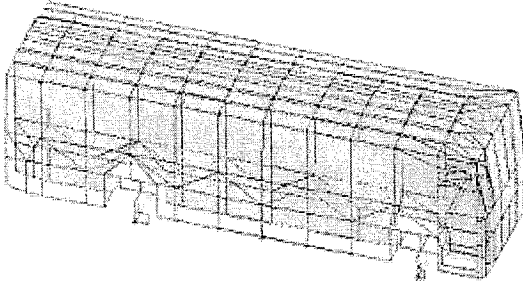
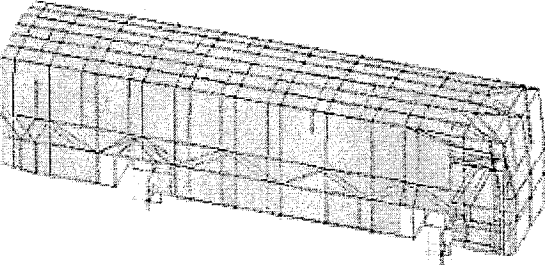
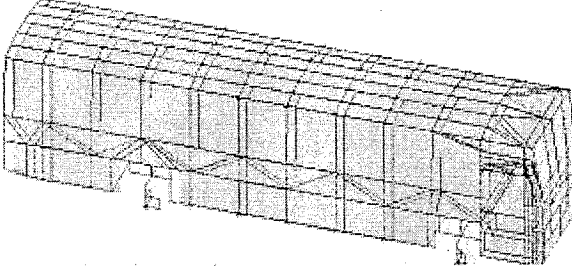
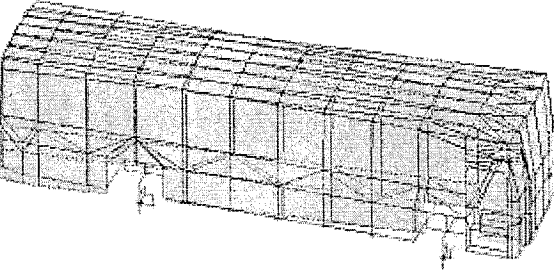
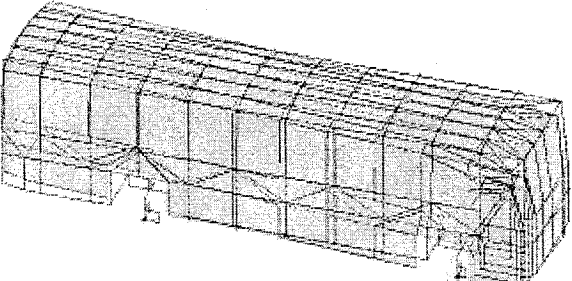
1 st Rigid Body Mode Shape	
 <p>Freq:0.139e-04Hz Max. Dsp:0.007493 m Tire Model with Ground Spring</p>	 <p>Freq:0.186e-04 Hz Max. Dsp:0.007493 m Tire Model without Ground Spring</p>
2nd Rigid Body Mode Shape	
 <p>Freq:0.511e-04 Hz Max. Dsp:0.007488 m Tire Model with Ground Spring</p>	 <p>Freq:0.725e-04 Hz Max Dsp:0.007488 m Tire Model without Ground Spring</p>
3rd Rigid Body Mode Shape	
 <p>Freq:0.007164 Hz Max. Dsp:0.01451 m Tire Model with Ground Spring</p>	 <p>Freq:0.007164 Hz Max. Dsp:0.03452 m Tire Model without Ground Spring</p>

Fig. 2.20 Rigid body mode shapes of the designed bus.

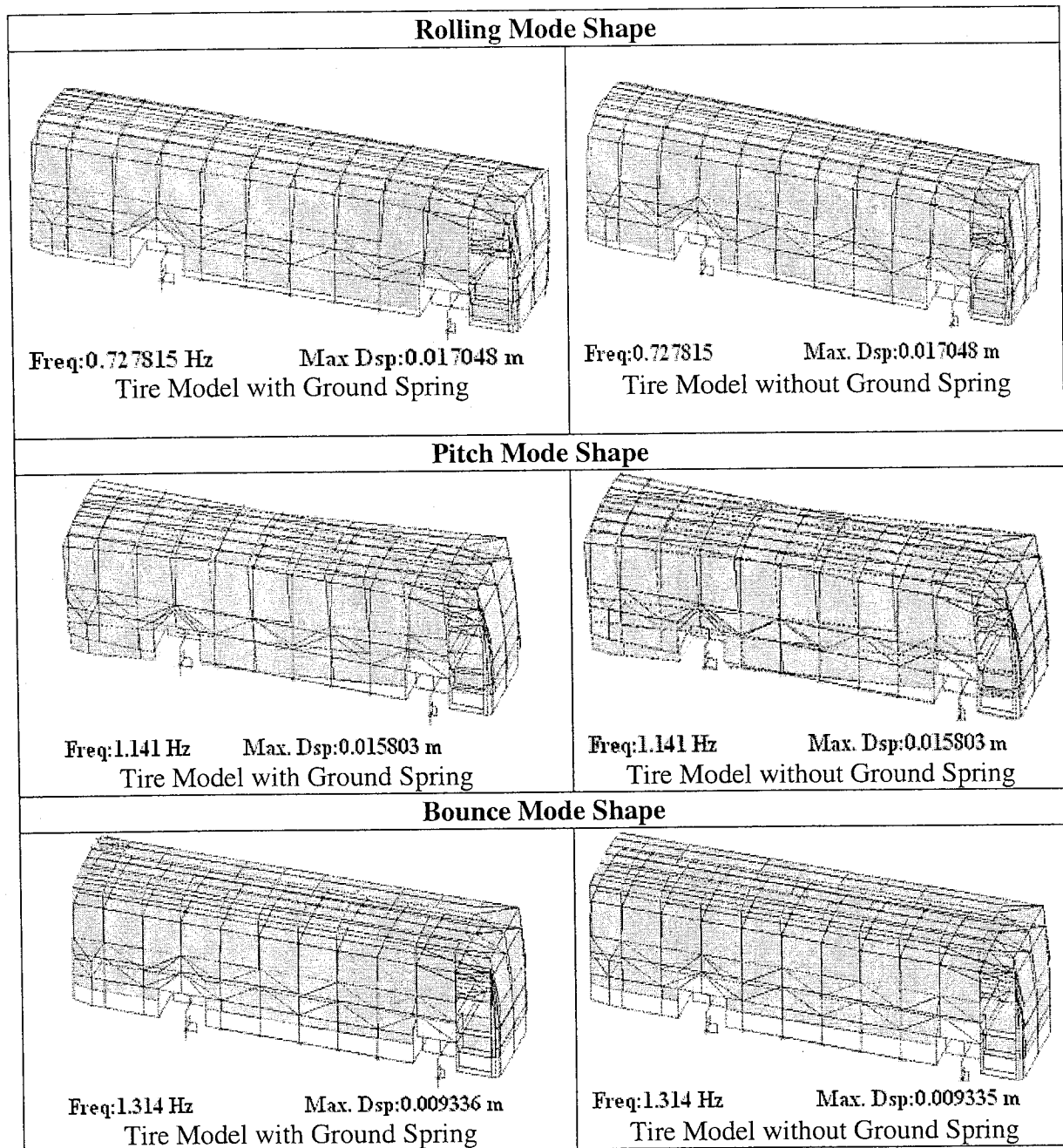


Fig. 2.21 Sprung mass mode shapes of the designed bus.

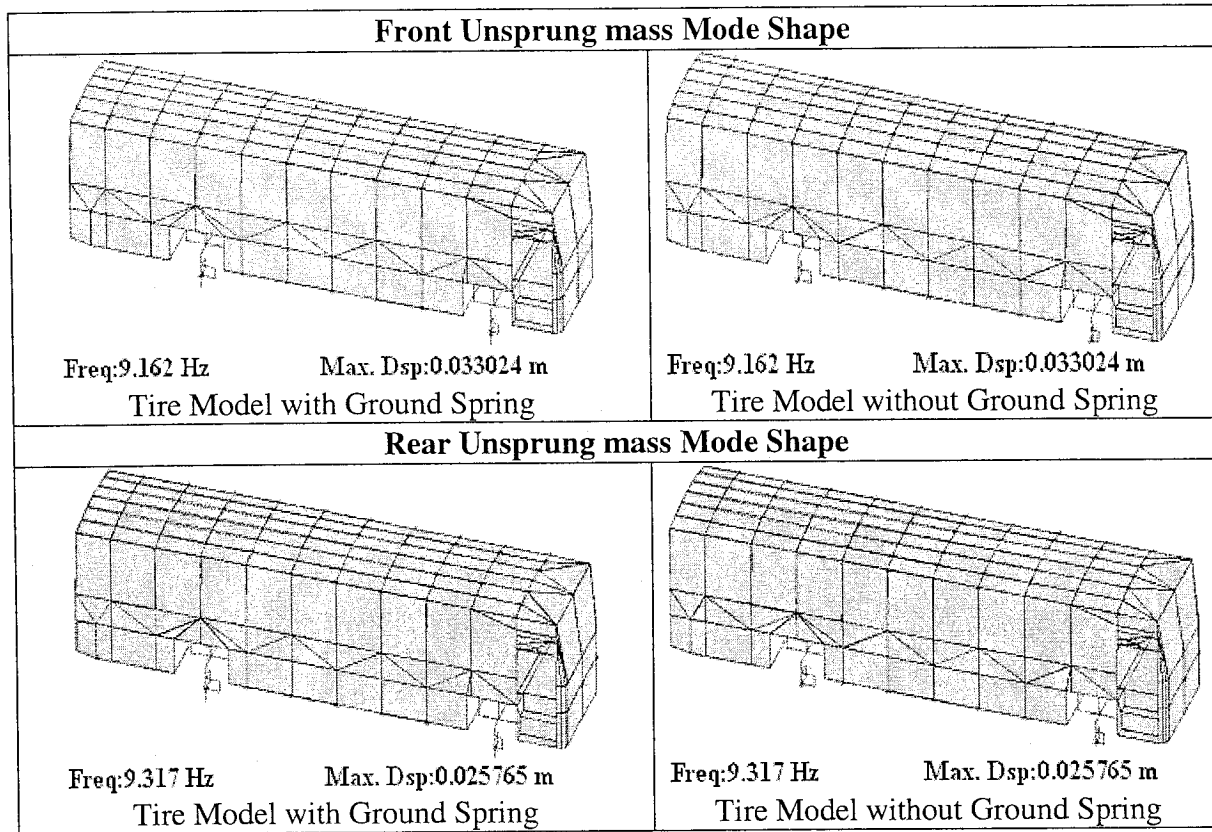


Fig. 2.22 Unsprung mass mode shapes of the designed bus.

2.4 IDENTIFICATION OF FREQUENCY RANGE

In this study, some transient analyses have been carried out using mode superposition method instead of using the full method, since mode superposition method was more efficient over the full method in analysis of model with large numbers of degrees of freedom. However, the identification of frequency range is essential in case of mode superposition method. The first twenty-two natural modes of the given bus are identified to be important in which the highest natural frequency is found to be 20.976 Hz. This implies that the number of the utilized second order differential equations in modal space is equal to twenty-two, which is only the 1.2 % of the number of original differential equations. The low natural modes have been predicted with the observation of

vertical responses of node No. 69 (Fig. 2.23) and 216 (Fig. 2.24) due to the application of harmonic sine sweeping kinematic excitation (amplitude: 0.05 m and frequency, being proportional to time, is swept from 0 Hz to 20 Hz) on both tires of rear wheels in vertical direction. At 0.8 sec the excitation frequency is 1.28 Hz and at that frequency node No. 69 being on the chassis (Fig. 2.3) representing sprung mass exhibits large amplitude response (Fig. 2.23), as expected. On the other hand, at 3 sec excitation frequency is 9 Hz and at that frequency the node No. 216 being on the rear axle (Fig. 2.3) representing unsprung mass shows large amplitude response (Fig. 2.24), as expected. The vertical vibration of node No. 69 above 10 Hz decreases very quickly, while the magnitudes of vibration of node No. 216 at around 20 Hz are very small. Consequently, in order to get more accurate response for the motion of the applied bus, the low natural modes up to 20.976 Hz can be considered.

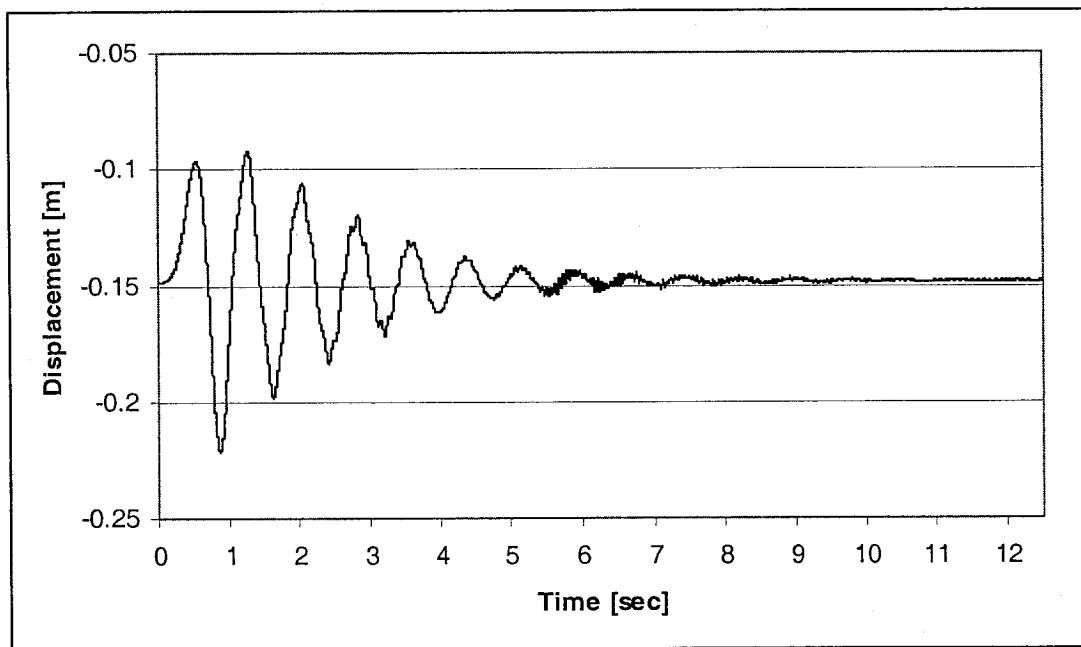


Fig. 2.23 Vertical Displacements of node No. 69 for sweeping excitations.

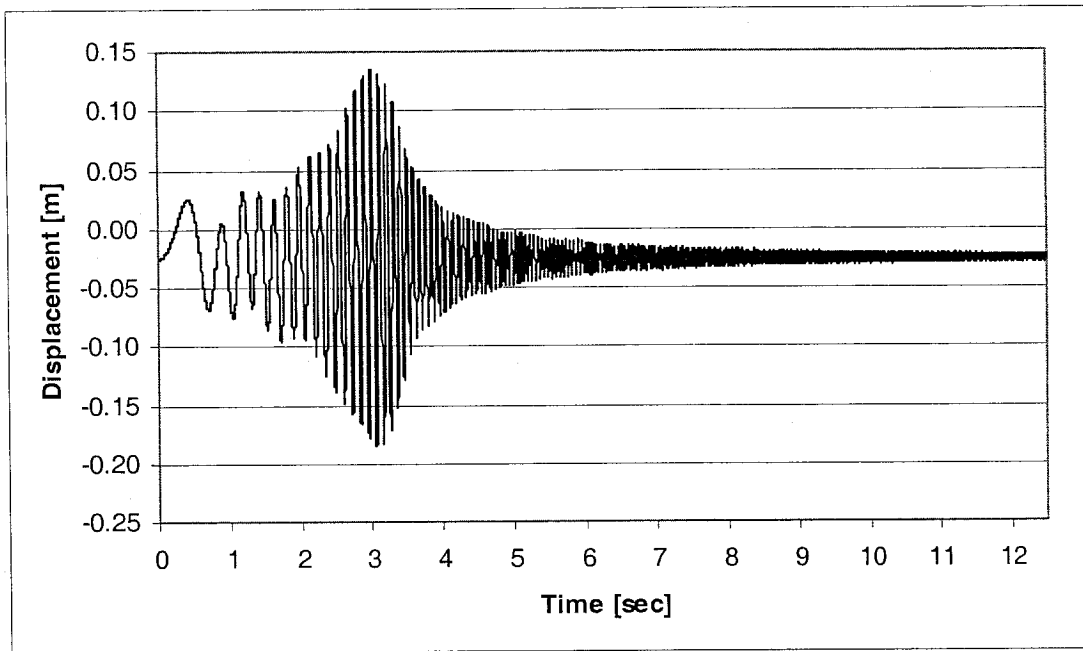


Fig. 2.24 Vertical Displacements of node No. 216 for sweeping excitations.

CHAPTER 3

RIDE ANALYSIS OF VEHICLE

3.1 INTRODUCTION

The vehicle body vibration or the ride quality is one of the primary concerns for the vehicle engineers. Ride quality deals with the sensation or feel of the passenger in the environment of a moving vehicle, and the control of the magnitudes of dynamic loads transmitted to the pavement [6]. It is thus important to evaluate the ride quality of a vehicle in design process utilizing a set of performance measures, and to establish appropriate suspension and tire properties for a given vehicle. Vehicle vibrations are induced by a variety of sources including vibrations of the engine and driveline, aerodynamic forces, unbalance of tire and wheel assembly, and most importantly the surface irregularities, ranging from the potholes to random variations of the surface elevation profile, which excites the vehicle body through the tire wheel assembly and the suspension system. In this study, ride quality of the candidate bus has been analyzed under only surface irregularities using both rigid body and flexible body (based on FEM) approaches. Two types of surface irregularities, namely: half sinusoidal road input like bulge and random road input representing city road, are taken into account for this purpose. The influences of nonlinear and the corresponding linear tire model along with the effects of rigid body and flexible body on simulation results are investigated. Mode superposition method is used in order to simulate the transient response due to half sinusoidal road input and linear tire model. However, full method is used in case of nonlinear tire model and random road input as any nonlinearity and table load data, for

instance, track height corresponding to time are not applicable with mode superposition method in ANSYS.

3.2 RIDE ANALYSIS USING HALF SINUSOIDAL ROAD INPUT

In this section, ride analysis of the candidate bus model for the case of half sinusoidal road input is presented for both nonlinear and the corresponding linear tire modes and the results are compared. Moreover, in order to demonstrate the effectiveness and applicability of the large finite element model, ride analysis has been conducted for both flexible and rigid body models using linear tire model only and results are compared. For this purpose, the bulge is considered as half sinusoidal input positioned in lateral direction on the surface of a perfectly smooth horizontal road and can be described as,

$$Z = A \times \sin \{(\pi \times V / \lambda) \times (t - t_0)\}$$

where: A is the maximum amplitude of the bulge,

V is the forward velocity of the bus, $V = 20$ m/s,

λ is the length of the bulge, $\lambda = 1.5$ m,

t is the time, $t_0 \leq t \leq t_0 + \lambda/V$,

t_0 is the time instant at which the bulge is reached by the corresponding wheel

It is assumed that the velocity of the bus is 20 m/s, and left and right hand side wheels mounted on the same axle pass over the bulge simultaneously. Time delay between the excitations of front and rear wheels is taken into consideration. The developed FEM model is also able to simulate the initial displacements due to the weight of the bus. Thus the motions due to excitation are defined from the initial position of the nodes.

As discussed in section 2.2.3, tire stiffness in vertical direction is nonlinear and can be approximated by a fixed stiffness for both in compression and tension (Figs. 2.8-2.11). Simulation of vehicle response over a bulge is a good opportunity to examine the influence of tire nonlinearity. Hence, two sets of responses are obtained for amplitudes of $A=0.05$ m and 0.1 m. Since FEM model is utilized, the response can be obtained at any location of the vehicle. To examine the responses that reflect both bounce and pitch behavior of the vehicle, several nodes on the chassis are selected. The selected nodes are nodes No. 214 (located on the chassis at the right side of the rear axle), 264 (located on the chassis at the right side of the front axle), 215 (located on the chassis at the left side of the rear axle), and 262 (located on the chassis at the left side of the front axle). Moreover, the bounce and pitch responses of the center of gravity of the candidate bus is investigated. Similarly, to examine the bounce behavior of the wheel, several nodes located on the wheels centers and the wheels rims are selected. The selected nodes are nodes No. 218 (located on the rear right wheel center), 234 (located on the front right wheel center), 221 (located on the rear left wheel center), 232 (located on the front left wheel center), 270 (located on the rear right wheel rim), 276 (located on the front right wheel rim), 273 (located on the rear left wheel rim), and 277 (located on the front left wheel rim) shown in Fig. 2.3.

The right hand side chassis bounce responses for 0.05 m bulge using linear tire model is shown in Fig. 3.1. The same responses for the nonlinear tire model are presented in Fig. 3.2. Similarly, Figs. 3.3 and 3.4 present the left hand side chassis bounce responses for 0.05 m bulge using linear and nonlinear tire models, respectively. As the results indicate, the static deflections of the chassis at the front and rear and left and right

are slightly different for the two models and there is insignificant difference between the responses for the linear and nonlinear tire models when amplitude of bulge is 0.05 m. It should be noted that the magnitudes of the vibration for nonlinear tire model are slightly larger than those of the vibration for linear tire model. This can be attributed to the fact that nonlinear tire model is less stiff than the linear tire model due to the methodology used (section 2.2.3) in the linearization of nonlinear vertical stiffness of a tire. Moreover, the vibration magnitude for the front chassis is slightly larger than that of rear chassis for both linear and nonlinear tire models since the equivalent spring stiffness of front suspensions are less than that of rear suspensions as discussed in section 2.2.2. It is interesting to note that front end and rear end of the chassis starts moving in phase (i.e., the bus body is merely bouncing) after approximately 3.4 seconds for both linear and nonlinear tire models. Thus, the passengers will feel the annoying pitch motion for 3.4 seconds. From the point of view of passenger ride comfort, pitching is more annoying than bouncing. The bounce response of the center of gravity shown in Fig. 3.5 also demonstrates the different static deflections for the two linear and nonlinear tire models. Also there are small differences between linear and nonlinear tire models response when amplitude of the bulge is 0.05 m. It is again noted that the magnitudes of the vibration for nonlinear tire model are slightly larger than that of the vibration for linear tire model. Consequently, the responses for nonlinear tire model takes a little more time to become steady compared to that of the linear tire model. The pitch response of the center of gravity shown in Fig. 3.6 also reveals that there is no significant difference between the responses for linear and nonlinear tire models. However, it should be noted that due to the long wheel base (7.25 m) the pitch angle is very small, less than 0.5 degree

for both models. The nonzero initial pitch angle indicates the front end of the chassis is few millimeters up compared to the rear end of the chassis.

The right hand side wheels bounce responses for 0.05 m bulge using linear tire model is shown in Fig. 3.7. The same responses for the nonlinear tire model are presented in Fig. 3.8. Similarly, Figs. 3.9 and 3.10 present the left hand side wheels bounce responses for 0.05 m bulge using linear and nonlinear tire models, respectively. As the results indicate, the static deflections of the wheels at the front and rear are slightly different for the two models and there is small effect on the responses when the amplitude of bulge is 0.05 m. In Figs. 3.7-3.10 the magnitudes of the responses for nonlinear tire model are slightly larger than that of the responses for linear tire model. It should be noted that wheel bounce is quickly damped out for both tire models compared to the bus body because of the damping effect of suspension and tire itself. As discussed in section 2.2.2 and 2.2.3, damping co-efficient value is the same for both front and rear suspension, and there are two tires on each side of the rear axle and one tire on each side of front axle. So equivalent damping capacity acting on rear axle is larger than that acting on the front axle. As a result, the bounce of rear wheels becomes steady faster than that of front wheels for both linear and nonlinear tire models even though the rear wheels are excited by the bulge after fractional second of the front wheels excitation.

Fig 3.11 demonstrates the rattle space or the relative distance between the axle at rear right wheel and chassis for 0.05 m bulge using linear and nonlinear tire model, while Fig. 3.12 presents the rattle space between the axle at front right wheel and chassis for both linear and nonlinear tire model. Fluctuation of rattle space for nonlinear tire model is slightly larger than that of linear tire model. However, rattle space for both tire models

become steady at the same time. Moreover, rattle space at the front axle takes slightly more time to become steady than that of the rear axle.

Figs. 3.13 and 3.14 illustrate the bouncing of the right hand side rear wheel for 0.05 m bulge using linear and nonlinear tire model, respectively, where the lower thick black line represents the shape of the bulge (max. amplitude: 0.05 m, wavelength: 1.5 m). The upper thin gray line being parallel with the lower one shows the hypothetical position of node No. 270 when the tire is not loaded i.e. is not deformed, and the thick gray line demonstrates the calculated vertical position of node No. 270 when the rear wheels pass over the bulge. Since thick gray line goes over the thin gray line, the corresponding wheel is bouncing i.e. wheel lift off occurs. It is important to note that tires would be in stretched condition in this case. However, in reality each spring and damper representing the elasticity and damping of the given tires is switched off when the tires are about to lift off the ground. As the results indicate, rear right wheel tires lose the contact with the ground twice for linear tire model, whereas for nonlinear tire model rear right wheel tires lift-off once, and those are in about to lift-off for the second time. The rear left wheel shows the same behaviors like rear right wheel for both linear and nonlinear tire models as shown in Figs. 3.15 and 3.16. According to the Figs. 3.17 and 3.18, front right wheel tire also loses the contact with the ground twice for linear tire model, whereas for nonlinear tire model front right wheel tire lifts-off once. The front left wheel shows the same behaviors similar to front right wheel for both linear and nonlinear tire models as shown in Figs. 3.19 and 3.20.

Alike the first case ($A = 0.05$ m), the same type of responses for the second case ($A = 0.1$ m) are given in Figs. 3.21-3.40. Although the patterns of the responses are identical

for both cases, significant differences have been observed between the magnitudes of the responses for linear and nonlinear tire models in the second case.

In conclusion, it can be realized that the linear tire model can provide reasonable results for small amplitude of excitations and moderately high forward velocity of the candidate bus. .

CASE 1:

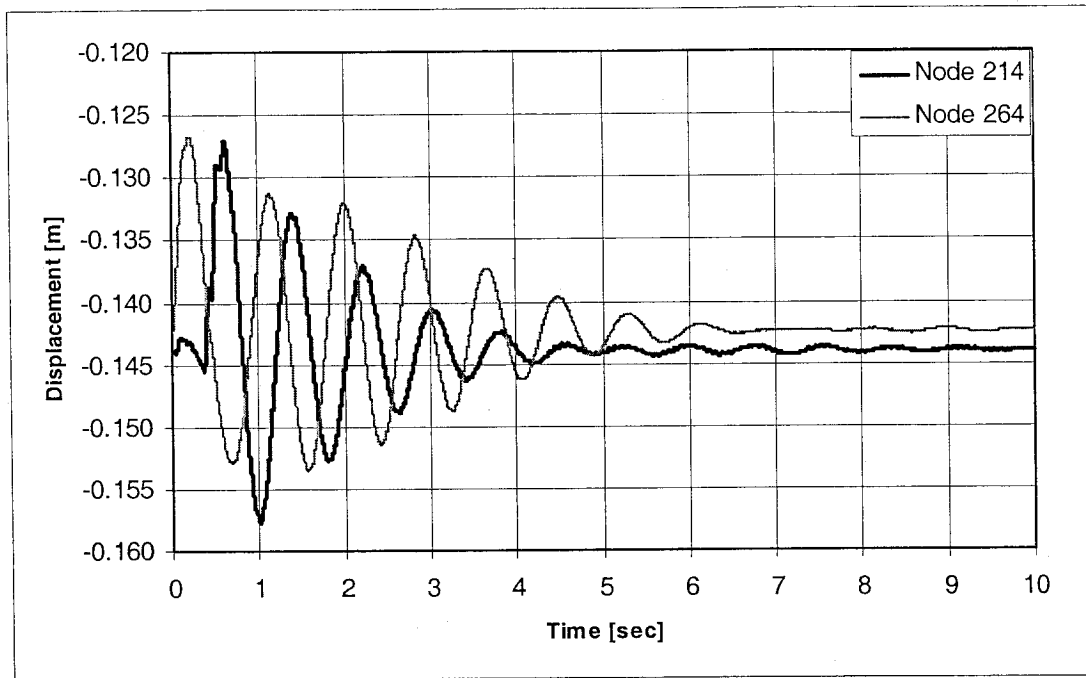


Fig. 3.1 Vertical displacements of node No. 214 and node No. 264 for linear tire model (amplitude of bulge: 0.05 m).

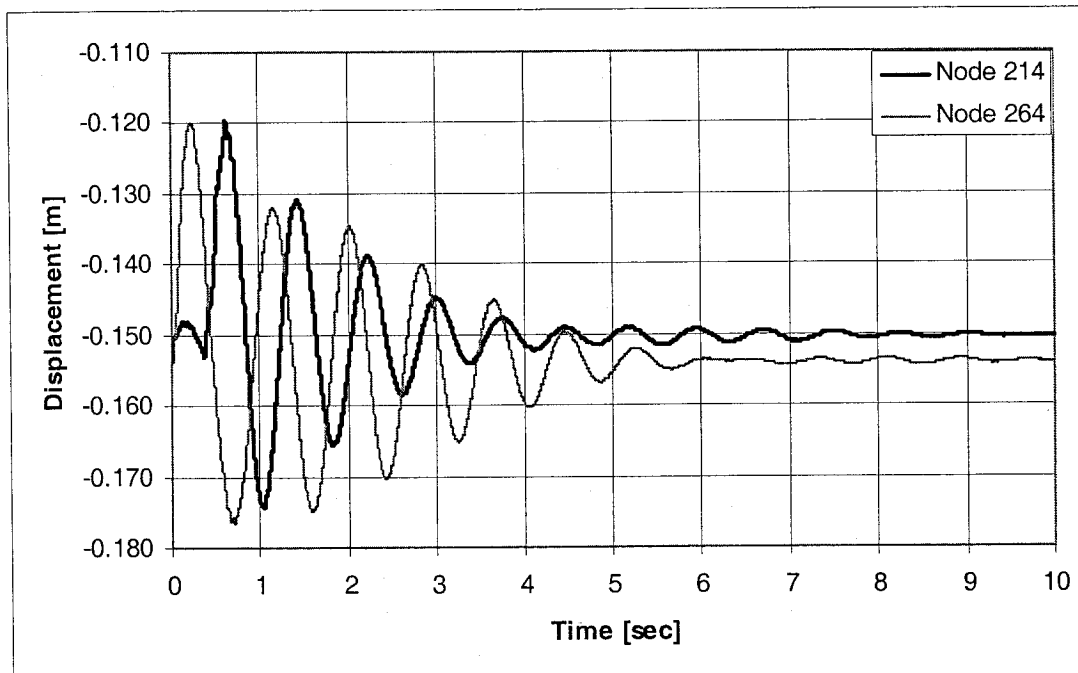


Fig. 3.2 Vertical displacements of node No. 214 and node No. 264 for nonlinear tire model (amplitude of bulge: 0.05 m).

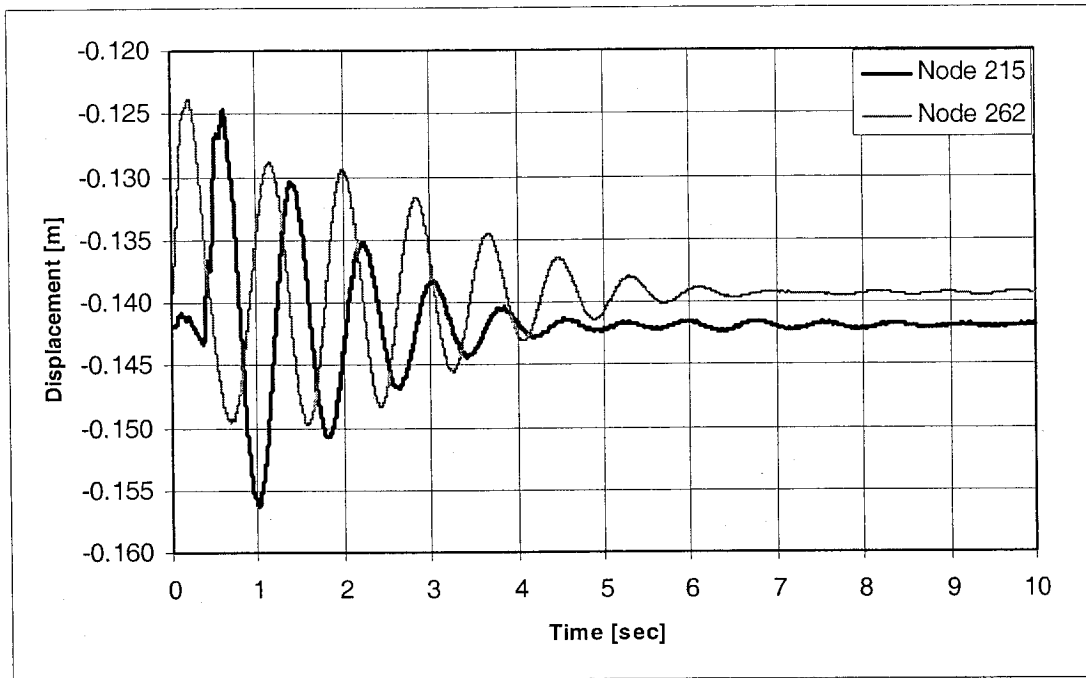


Fig. 3.3 Vertical displacements of node No. 215 and node No. 262 for linear tire model (amplitude of bulge: 0.05 m).

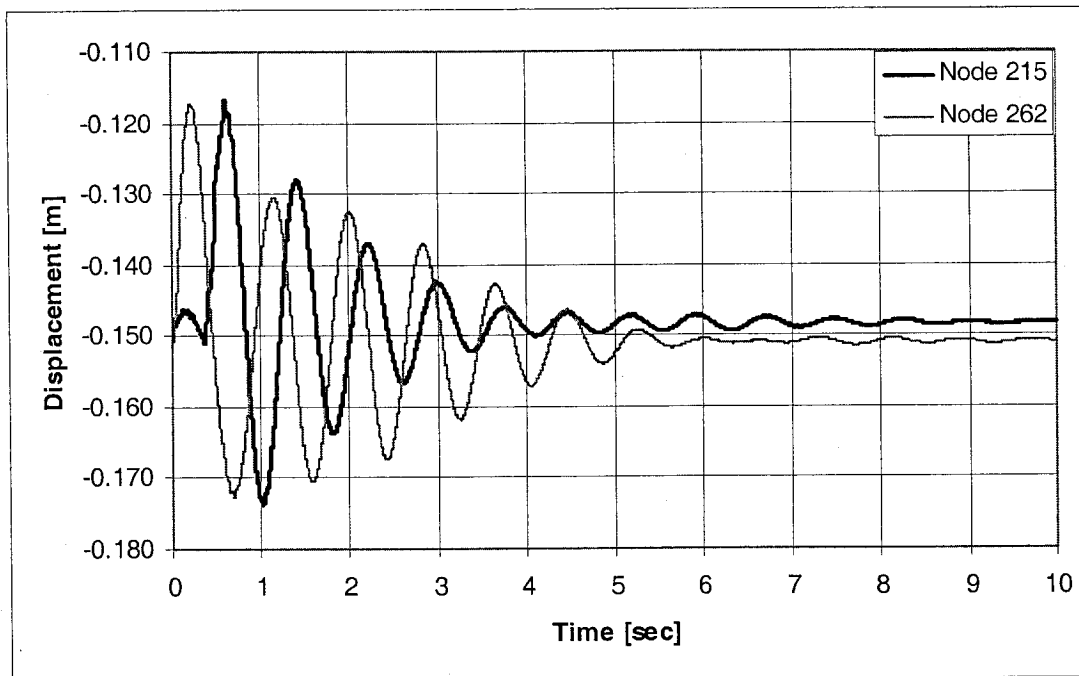


Fig. 3.4 Vertical displacements of node No. 215 and node No. 262 for nonlinear tire model (amplitude of bulge: 0.05 m).

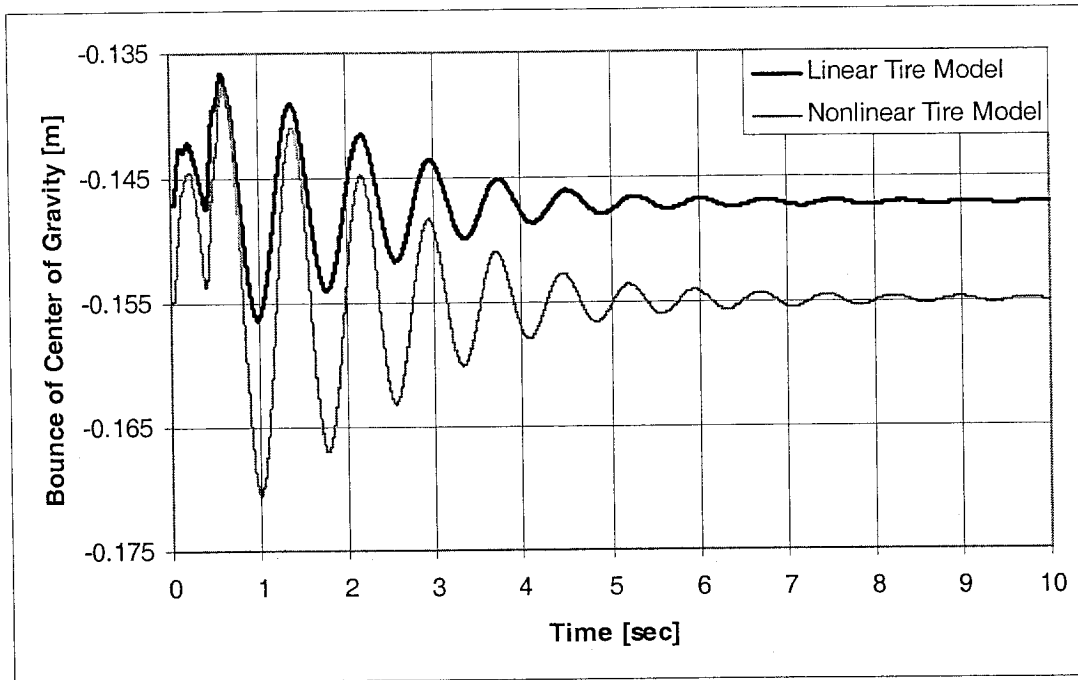


Fig. 3.5 Bounce of the center of gravity (amplitude of bulge: 0.05 m).

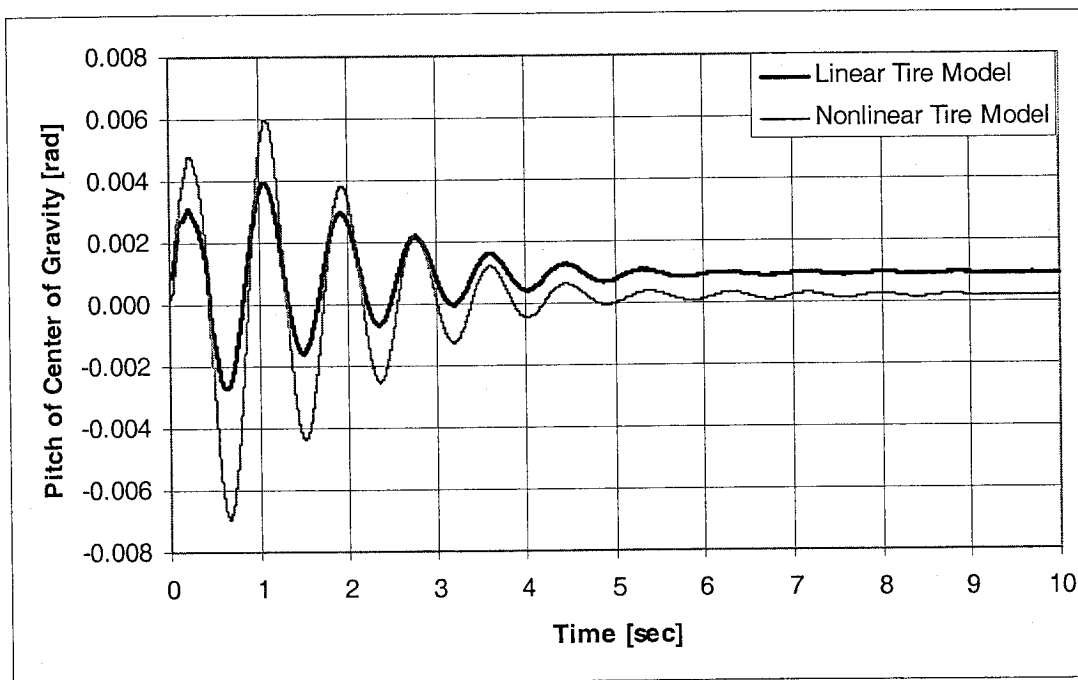


Fig. 3.6 Pitch of the center of gravity (amplitude of bulge: 0.05 m).

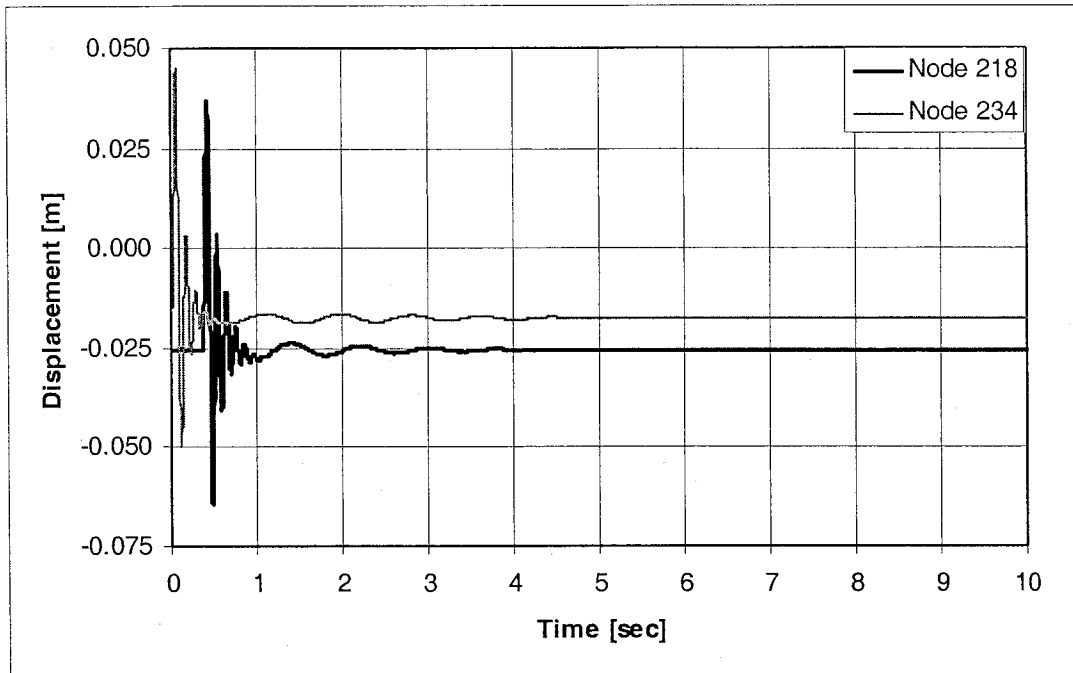


Fig. 3.7 Vertical displacements of node No. 218 and node No. 234 for linear tire model (amplitude of bulge: 0.05 m).

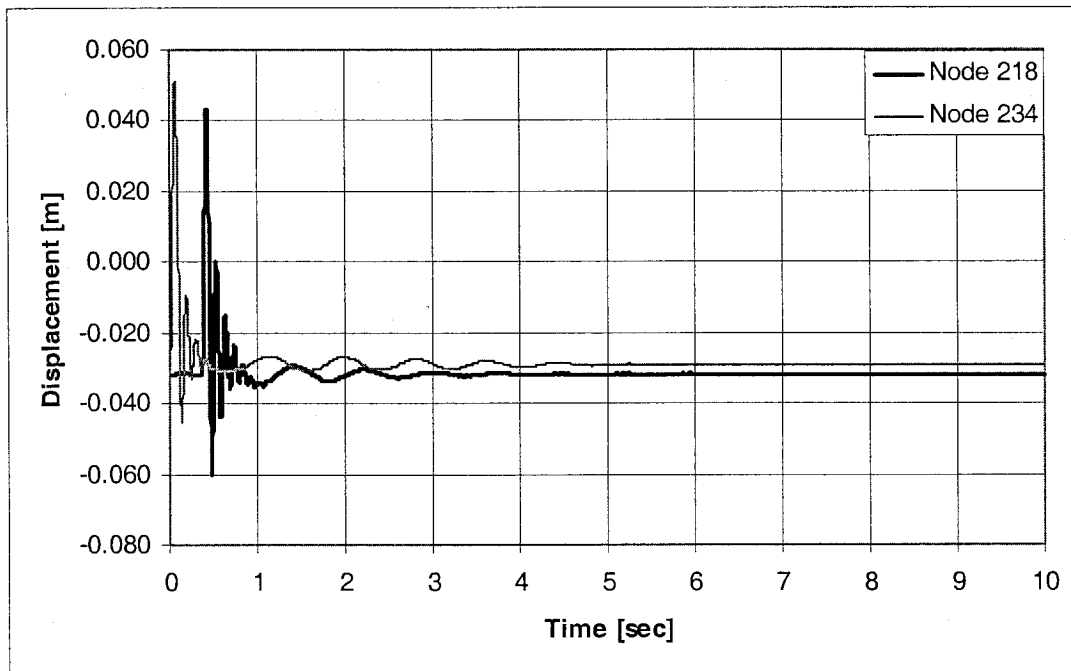


Fig. 3.8 Vertical displacements of node No. 218 and node No. 234 for nonlinear tire model (amplitude of bulge: 0.05 m).

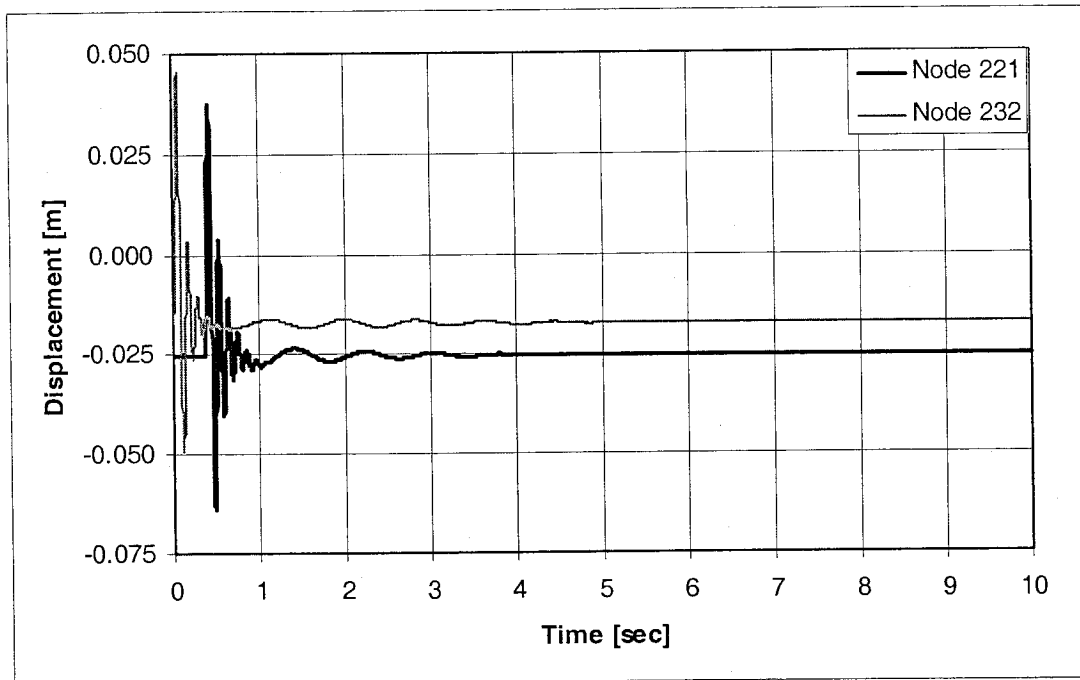


Fig. 3.9 Vertical displacements of node No. 221 and node No. 232 for linear tire model (amplitude of bulge: 0.05 m).

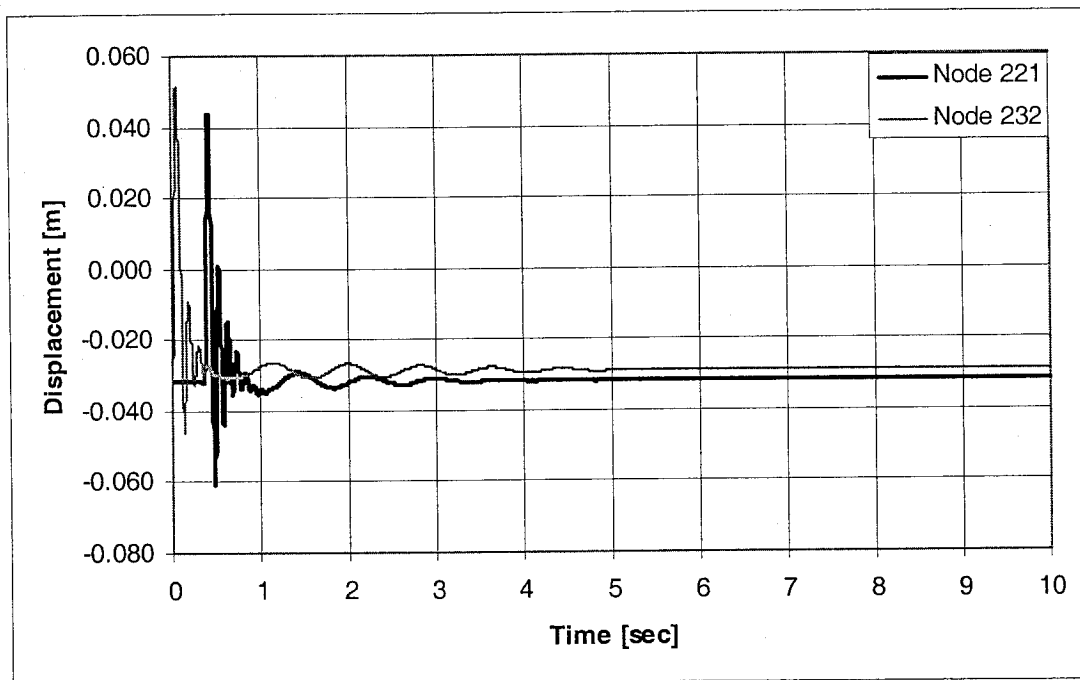


Fig. 3.10 Vertical displacements of node No. 221 and node No. 232 for nonlinear tire model (amplitude of bulge: 0.05 m).

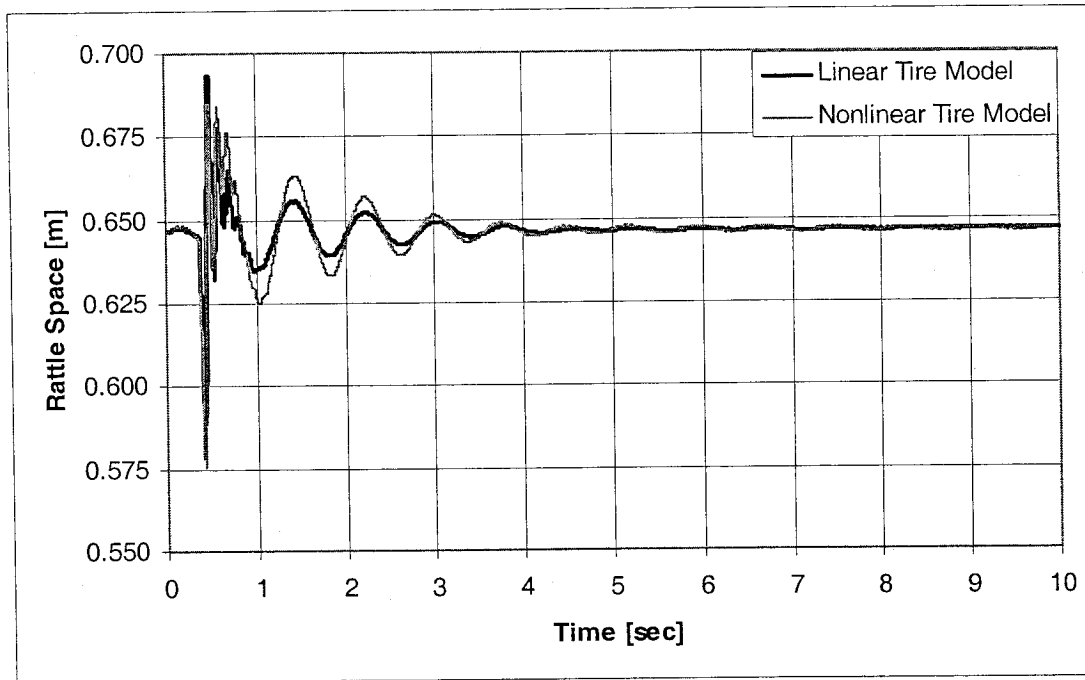


Fig. 3.11 Rattle space at rear right wheel (amplitude of bulge: 0.05 m).

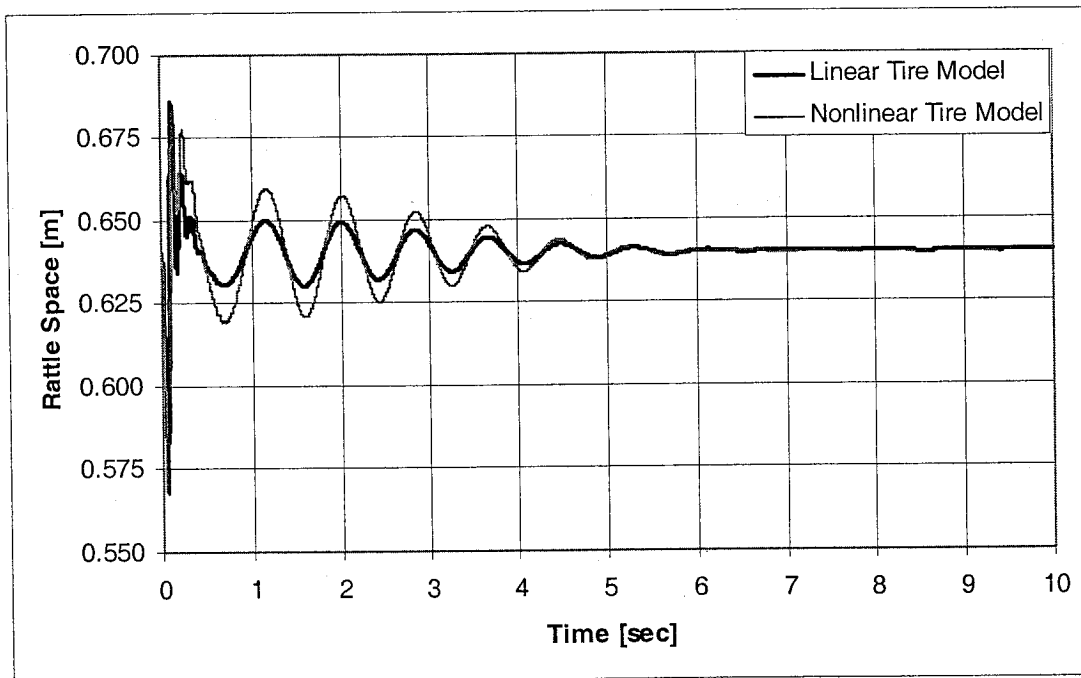


Fig. 3.12 Rattle space at front right wheel (amplitude of bulge: 0.05 m).

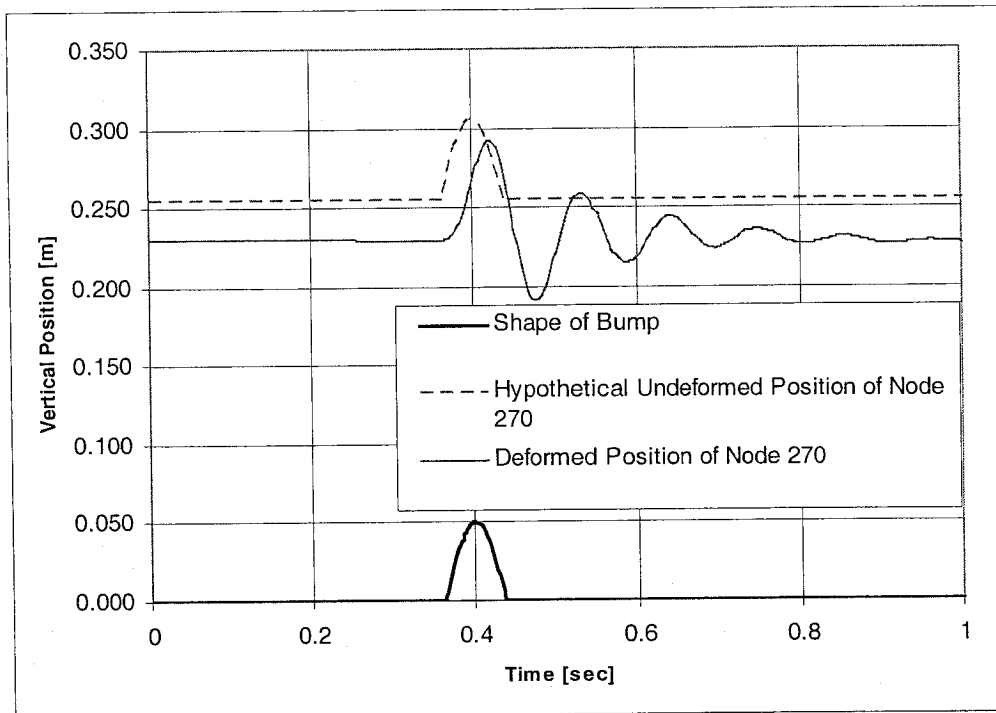


Fig. 3.13 Bounce of the right hand side rear wheel for linear tire model (amplitude of bulge: 0.05 m).

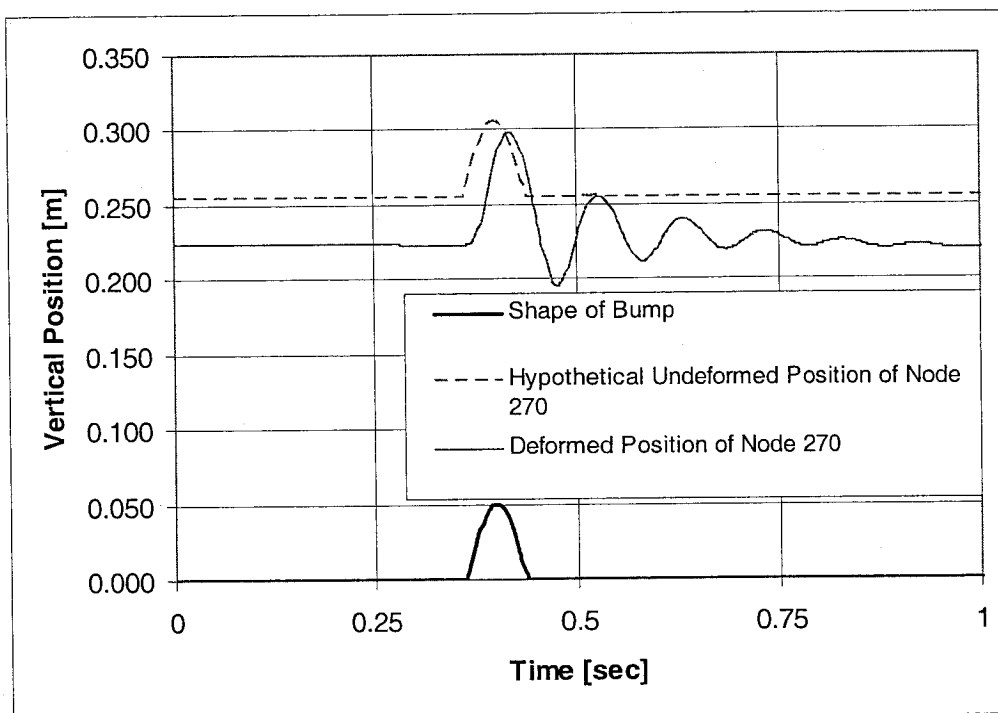


Fig. 3.14 Bounce of the right hand side rear wheel for nonlinear tire model (amplitude of bulge: 0.05 m).

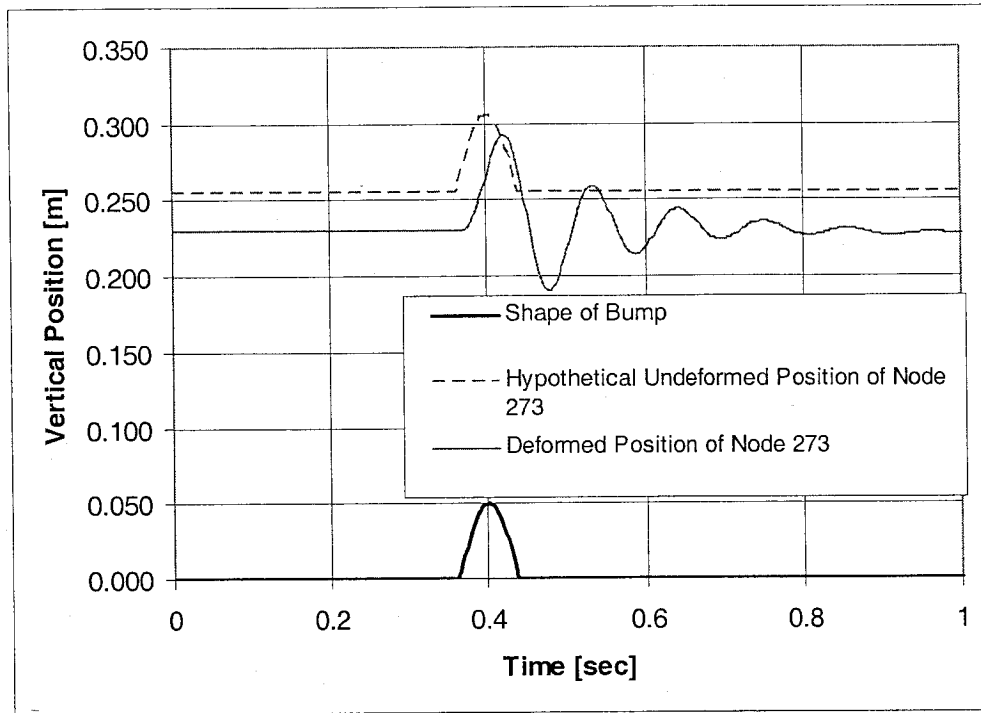


Fig. 3.15 Bounce of the left hand side rear wheel for linear tire model (amplitude of bulge: 0.05 m).

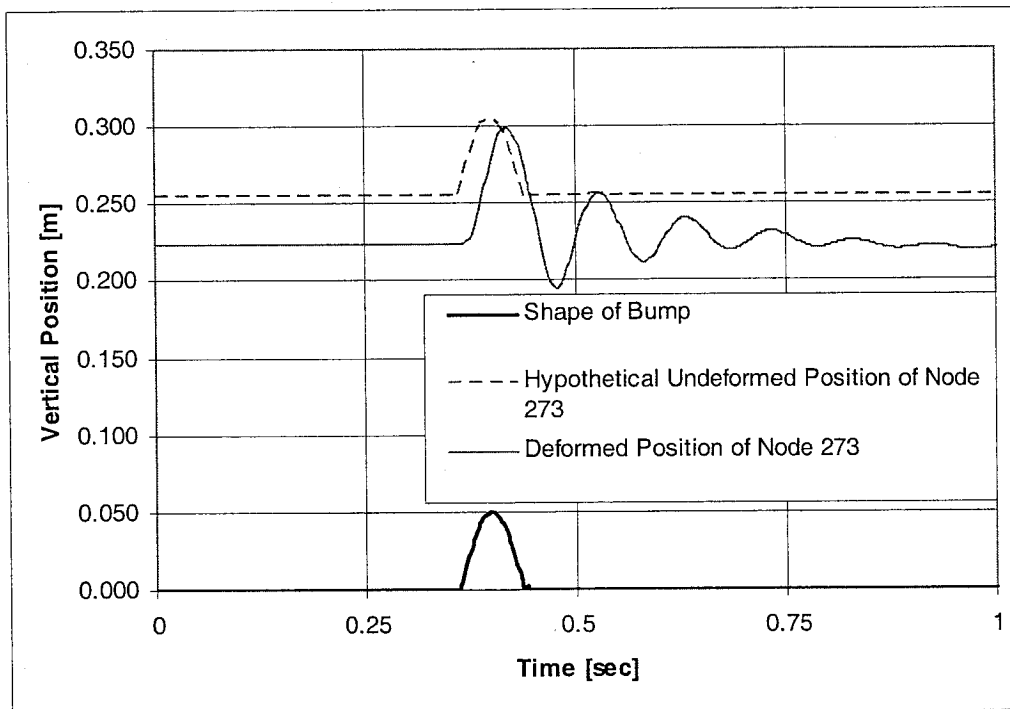


Fig. 3.16 Bounce of the left hand side rear wheel for nonlinear tire model (amplitude of bulge: 0.05 m).

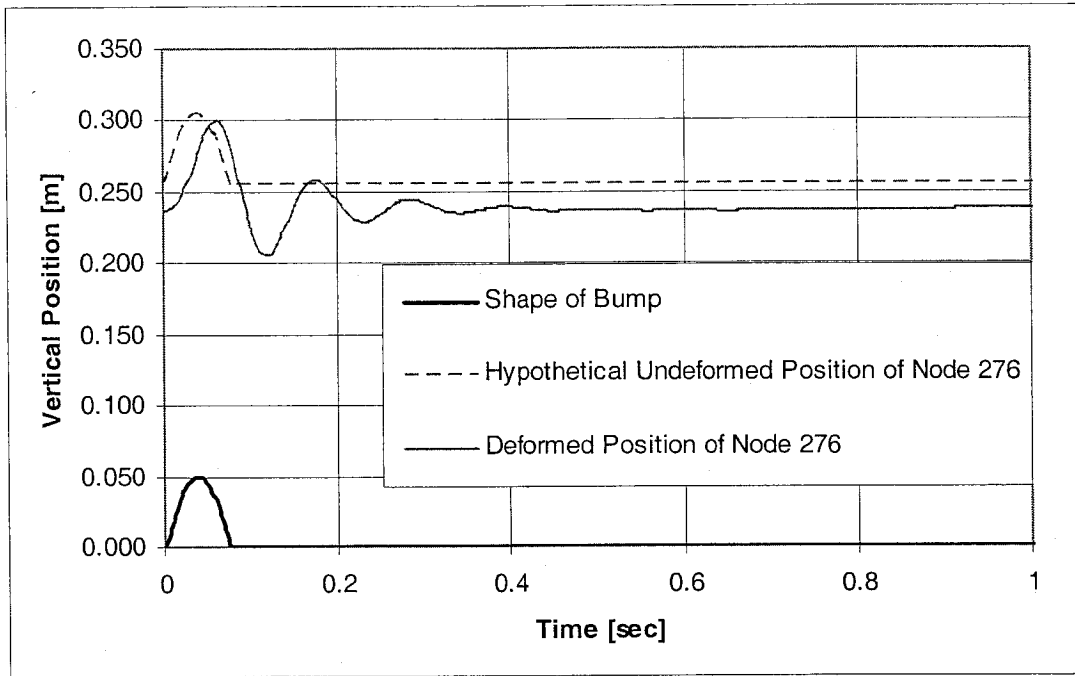


Fig. 3.17 Bounce of the right hand side front wheel for linear tire model (amplitude of bulge: 0.05 m).

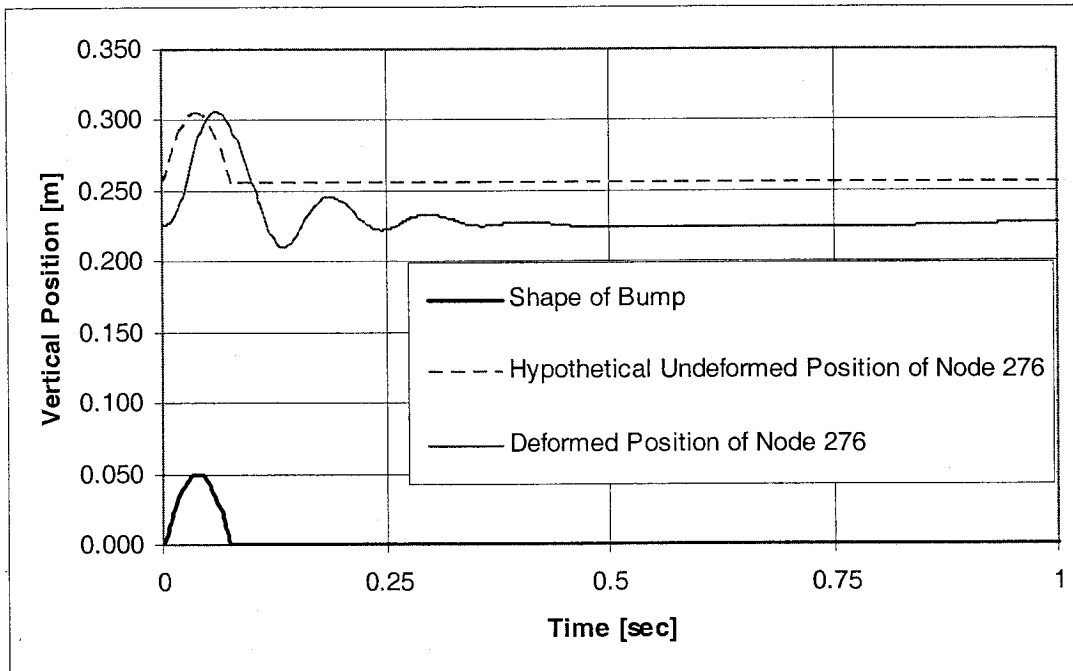


Fig. 3.18 Bounce of the right hand side front wheel for nonlinear tire model (amplitude of bulge: 0.05 m).

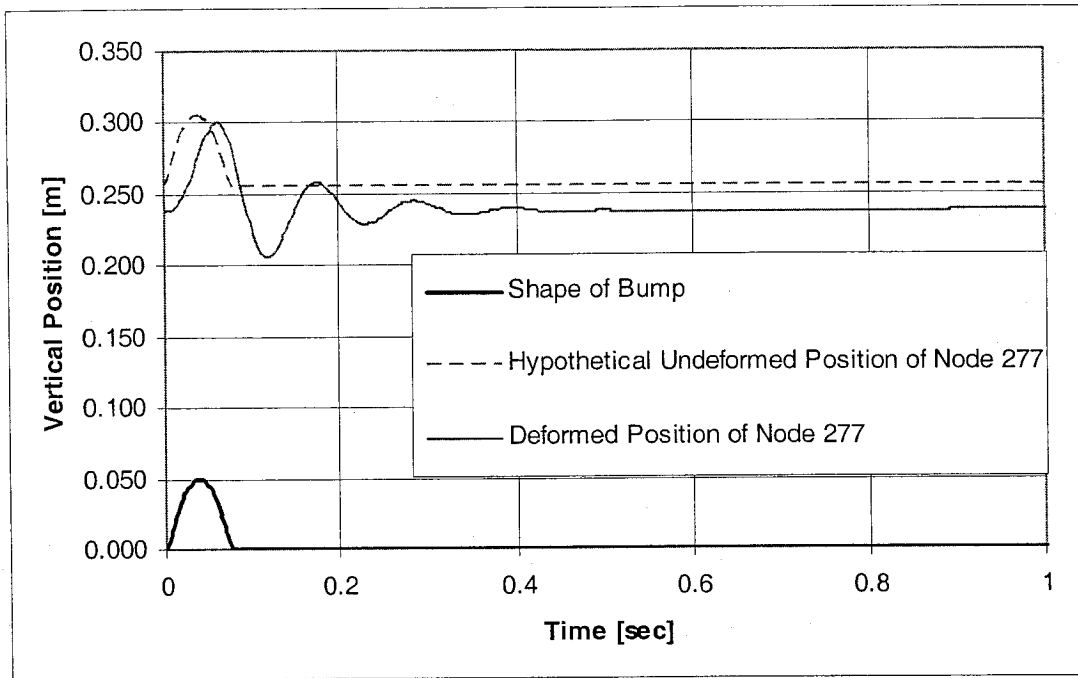


Fig. 3.19 Bounce of the left hand side front wheel for linear tire model (amplitude of bulge: 0.05 m).

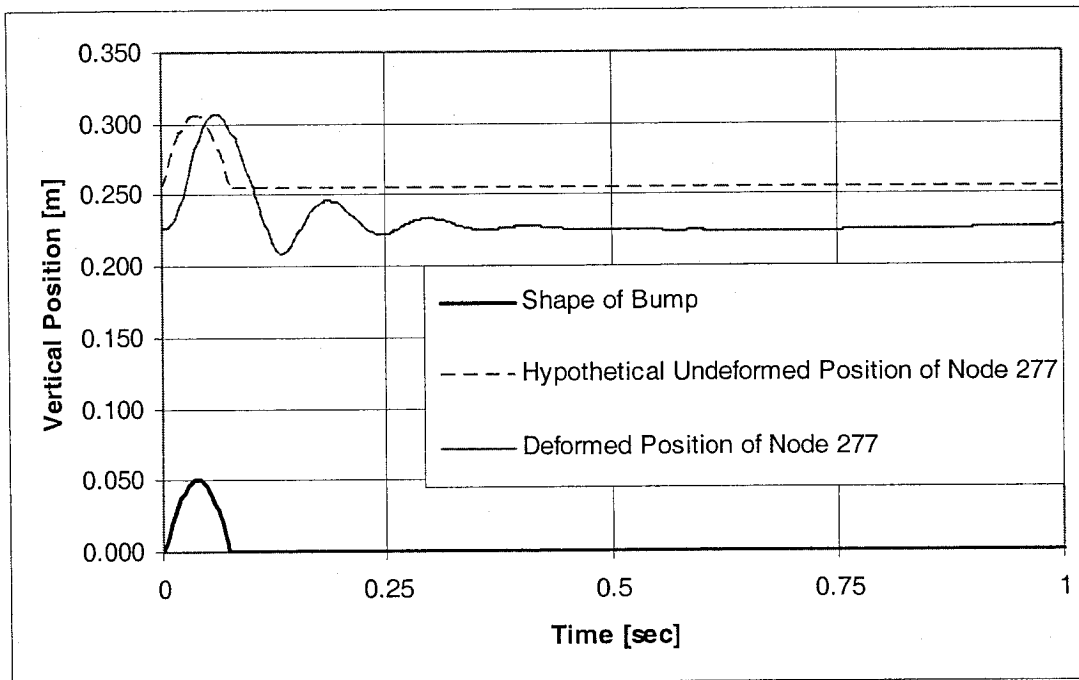


Fig. 3.20 Bounce of the left hand side front wheel for nonlinear tire model (amplitude of bulge: 0.05 m).

CASE 2:

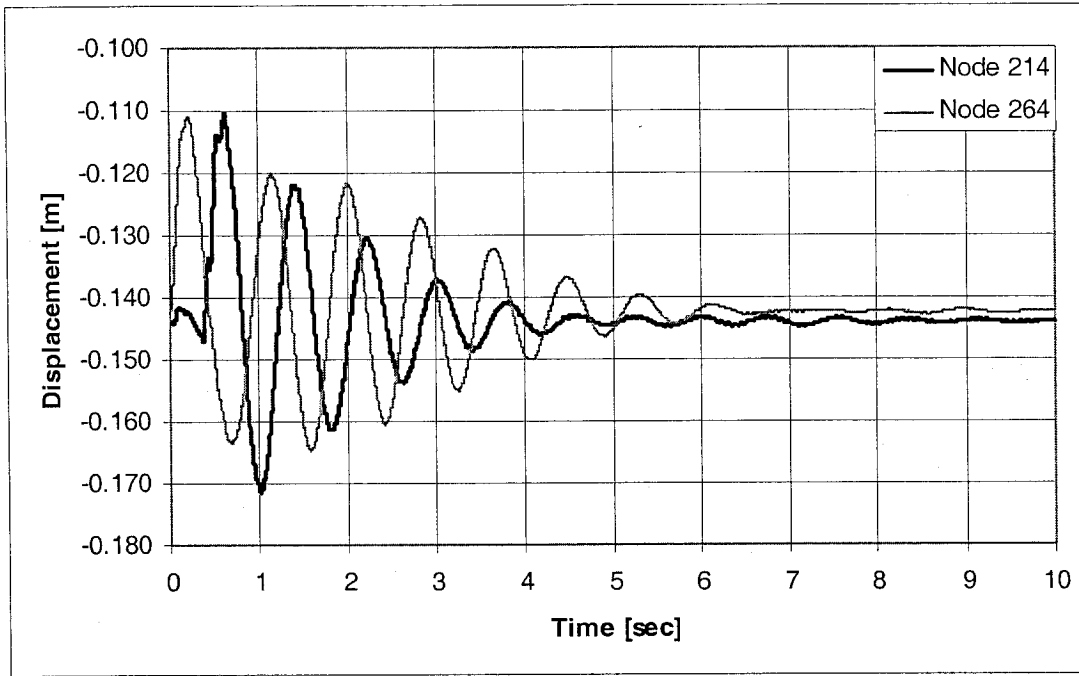


Fig. 3.21 Vertical displacements of node No. 214 and node No. 264 for linear tire model (amplitude of bulge: 0.1 m).

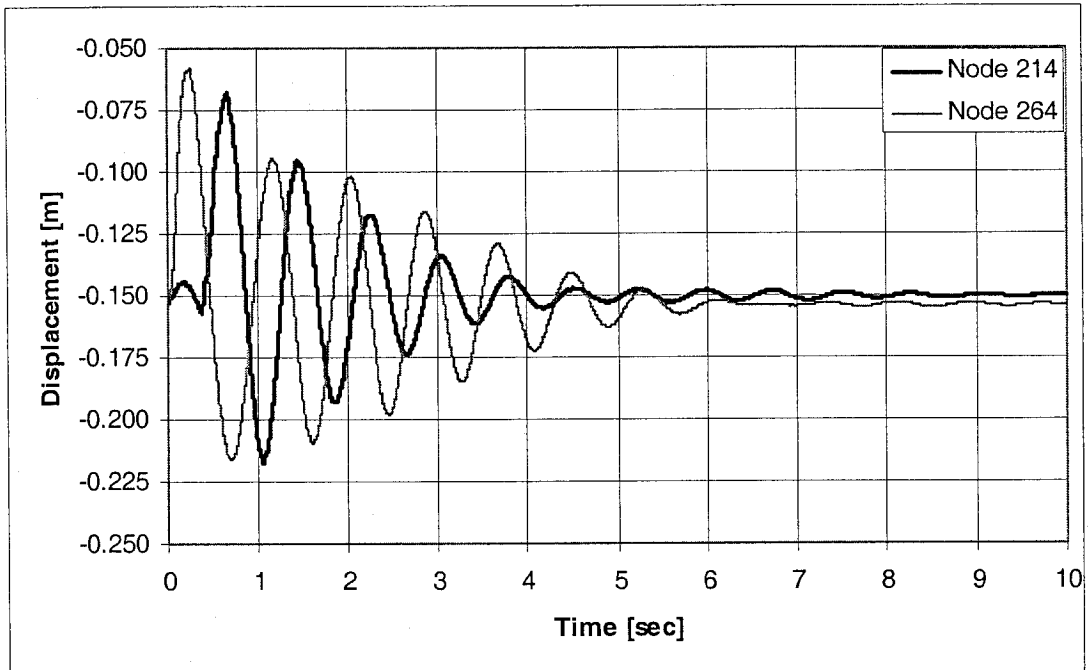


Fig. 3.22 Vertical displacements of node No. 214 and node No. 264 for nonlinear tire model (amplitude of bulge: 0.1 m).

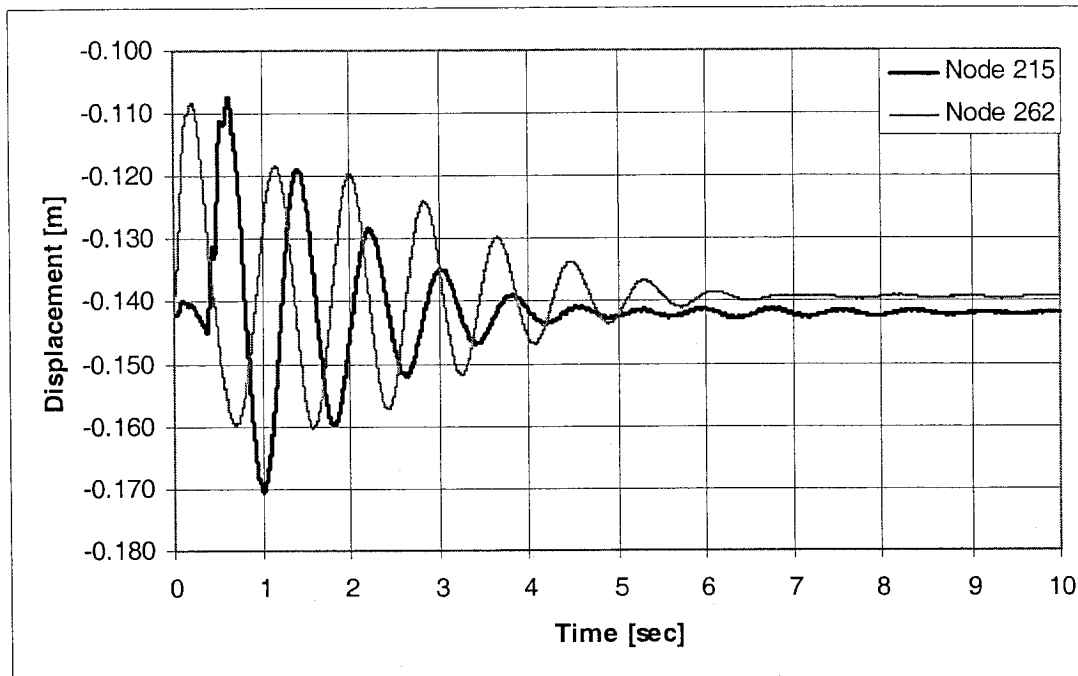


Fig. 3.23 Vertical displacements of node No. 215 and node No. 262 for linear tire model (amplitude of bulge: 0.1 m).

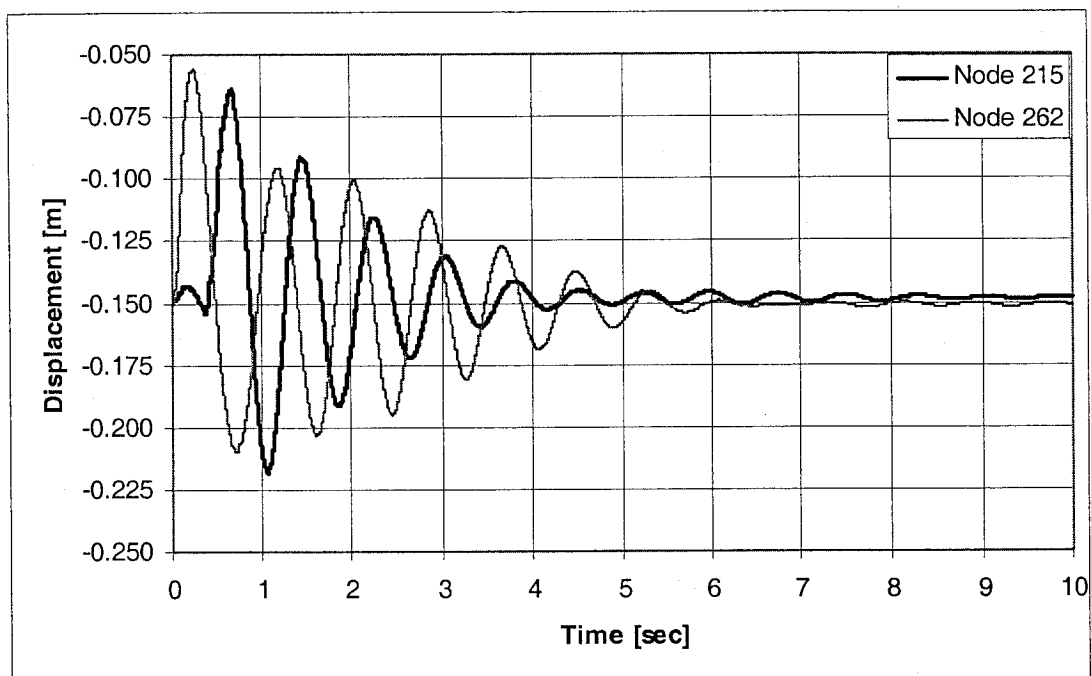


Fig. 3.24 Vertical displacements of node No. 215 and node No. 262 for nonlinear tire model (amplitude of bulge: 0.1 m).

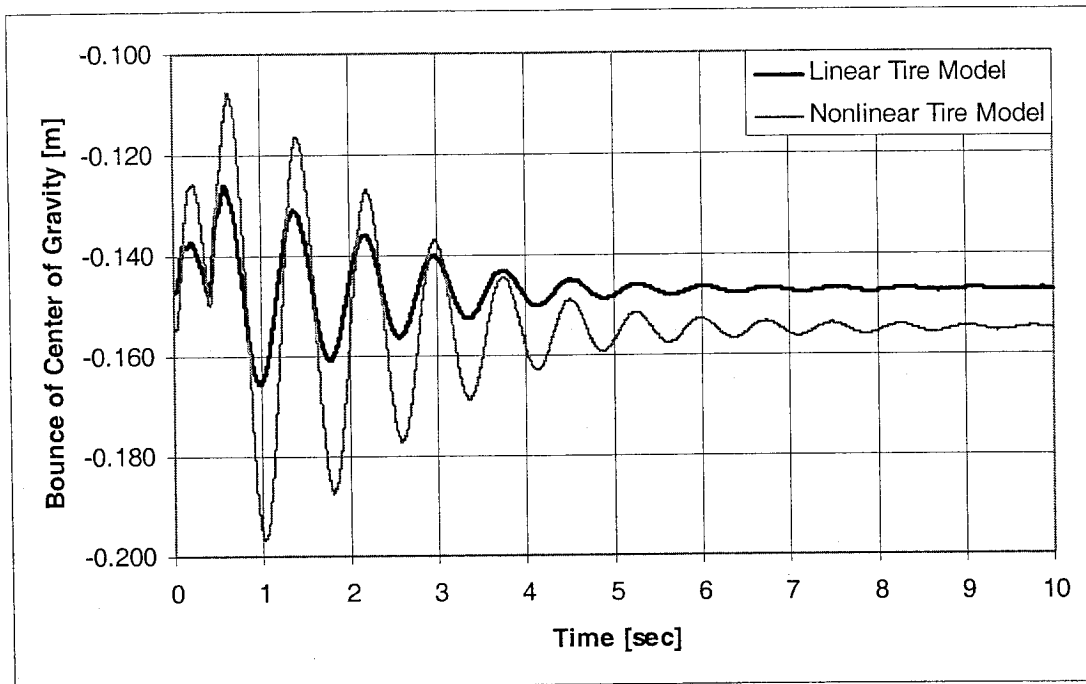


Fig. 3.25 Bounce of the center of gravity (amplitude of bulge: 0.1 m).

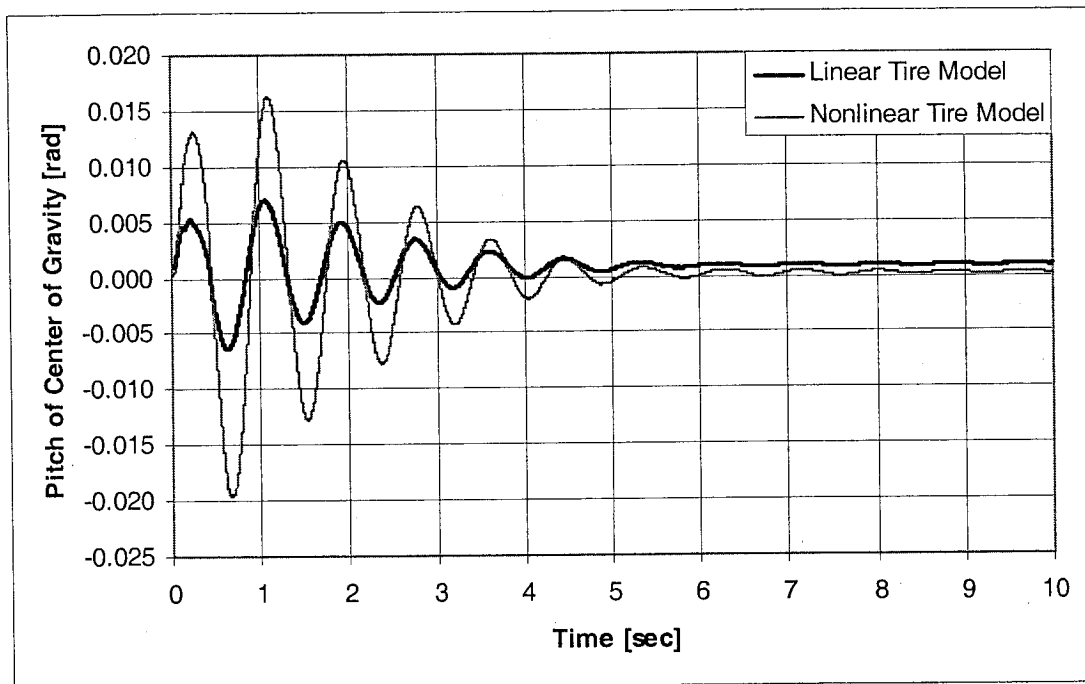


Fig. 3.26 Pitch of the center of gravity (amplitude of bulge: 0.1 m).

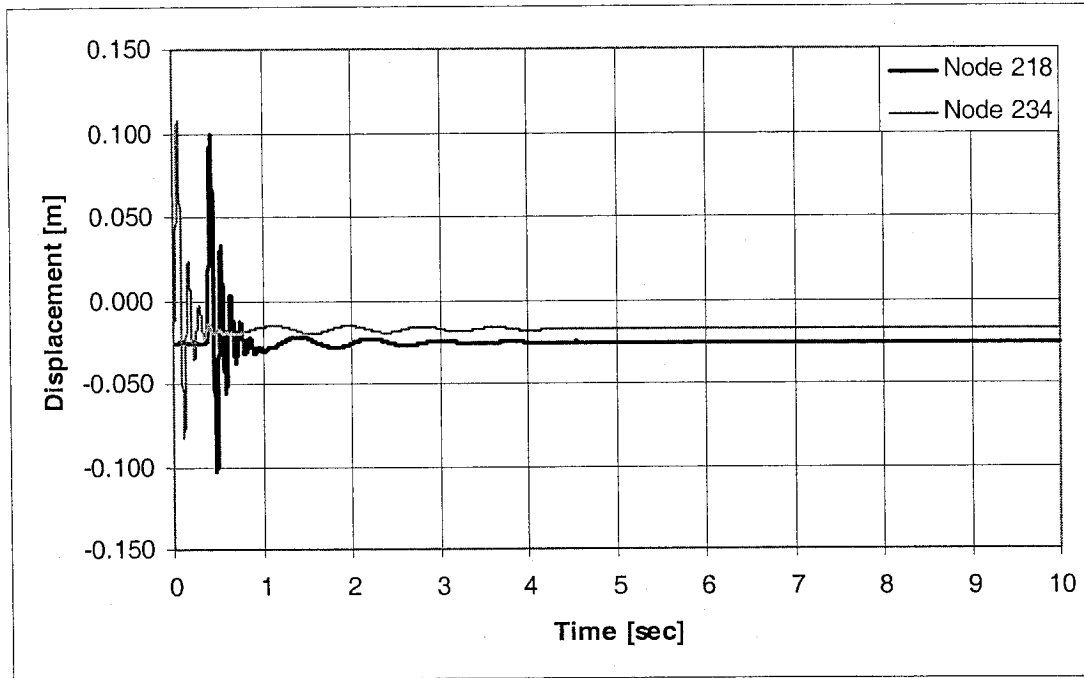


Fig. 3.27 Vertical displacements of node No. 218 and node No. 234 for linear tire model (amplitude of bulge: 0.1 m).

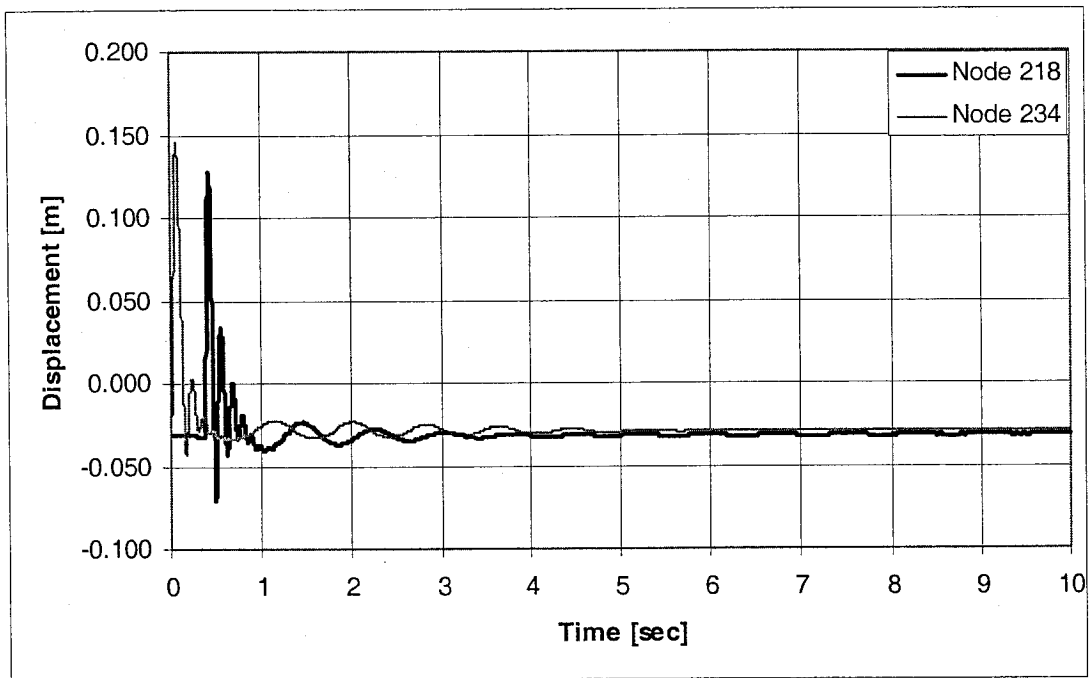


Fig. 3.28 Vertical displacements of node No. 218 and node No. 234 for nonlinear tire model (amplitude of bulge: 0.1 m).

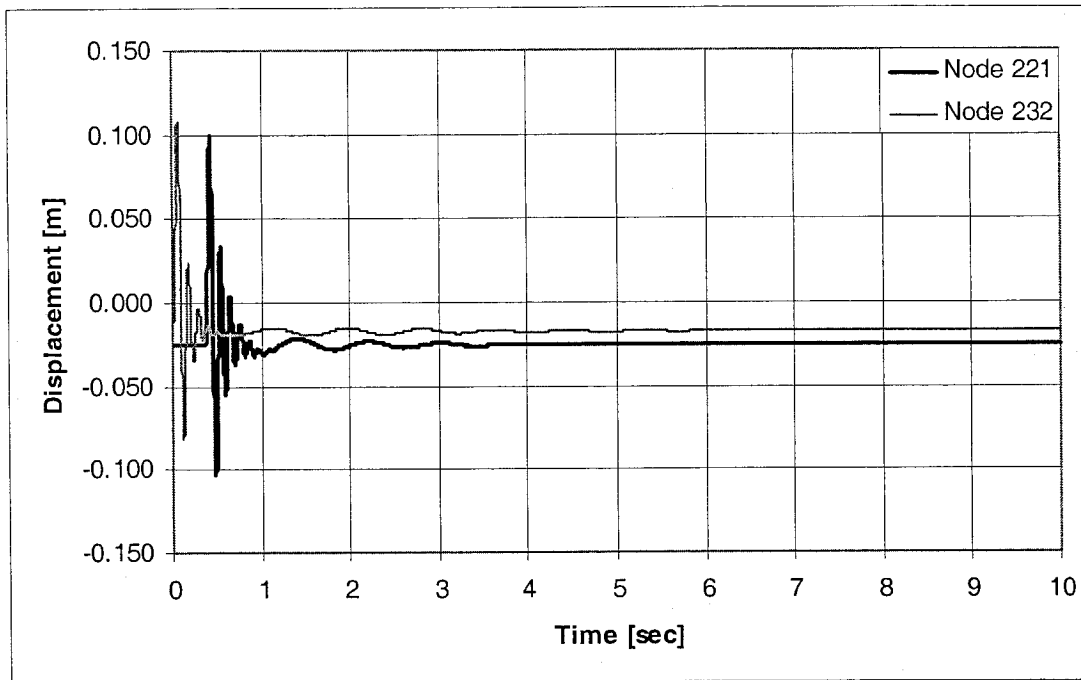


Fig. 3.29 Vertical displacements of node No. 221 and node No. 232 for linear tire model (amplitude of bulge: 0.1 m).

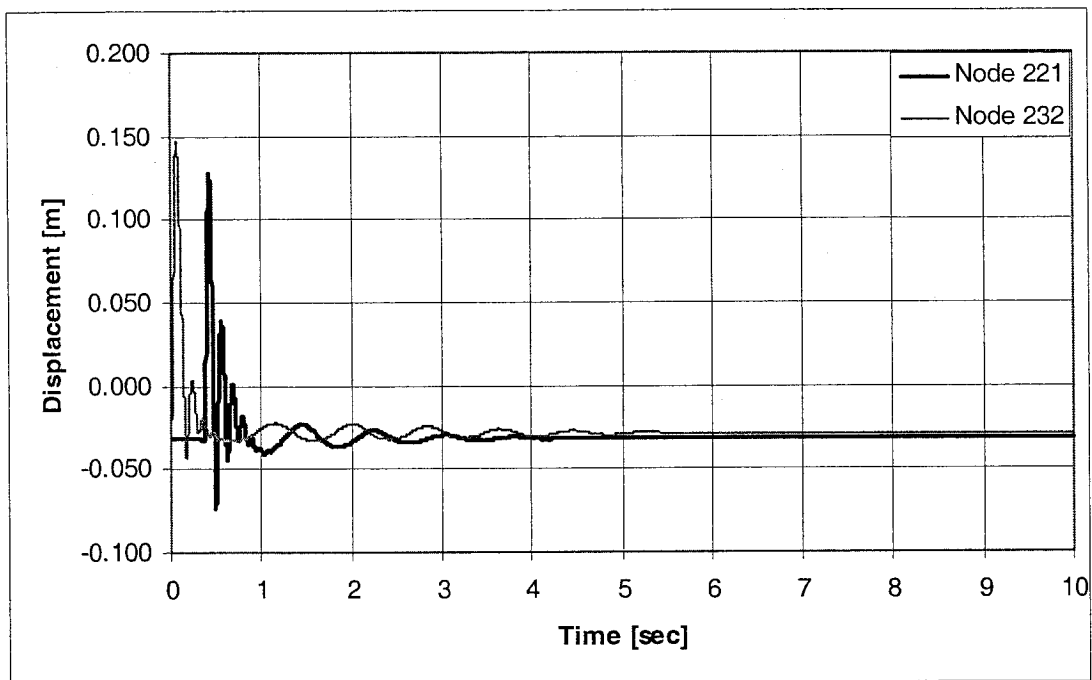


Fig. 3.30 Vertical displacements of node No. 221 and node No. 232 for nonlinear tire model (amplitude of bulge: 0.1 m).

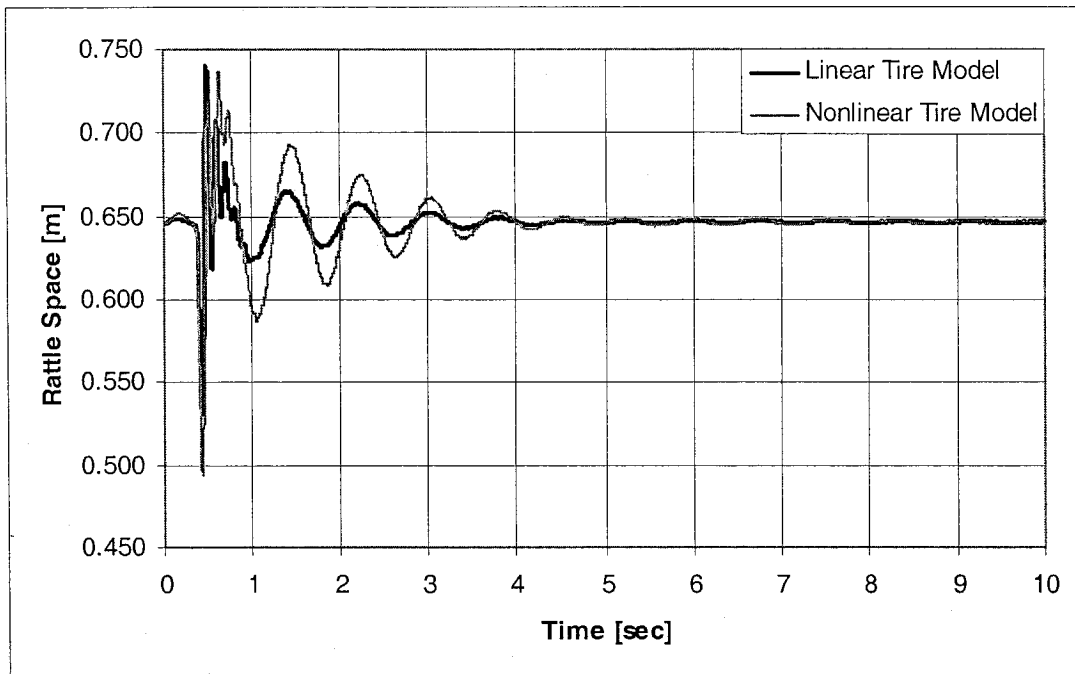


Fig. 3.31 Rattle space at rear right wheel (amplitude of bulge: 0.1 m).

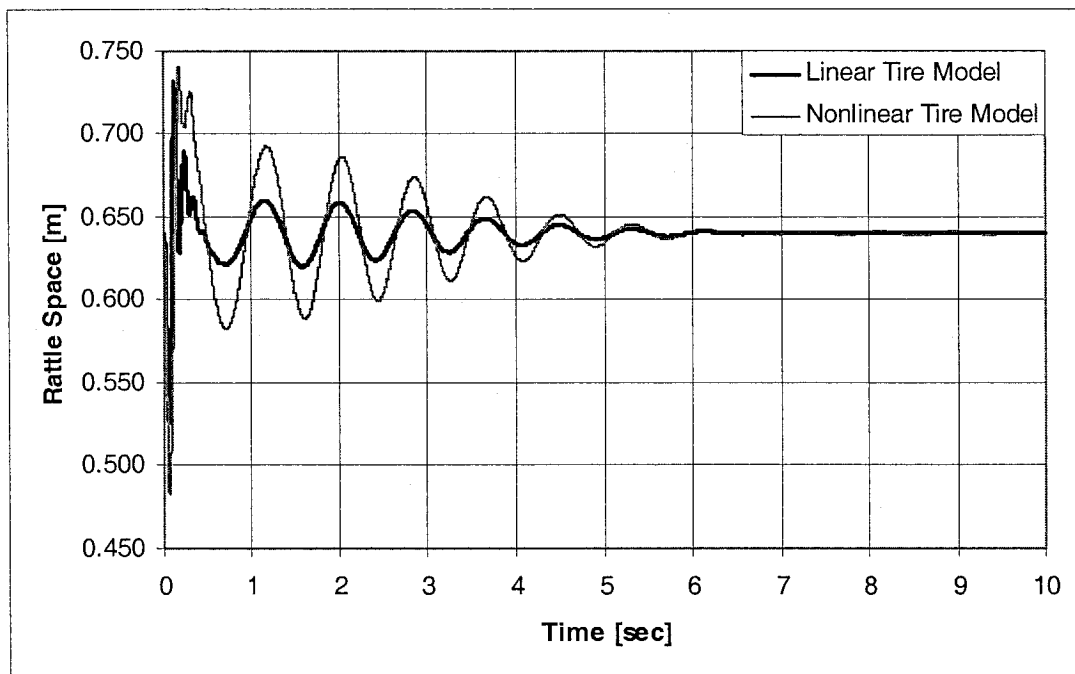


Fig. 3.32 Rattle space at front right wheel (amplitude of bulge: 0.1 m).

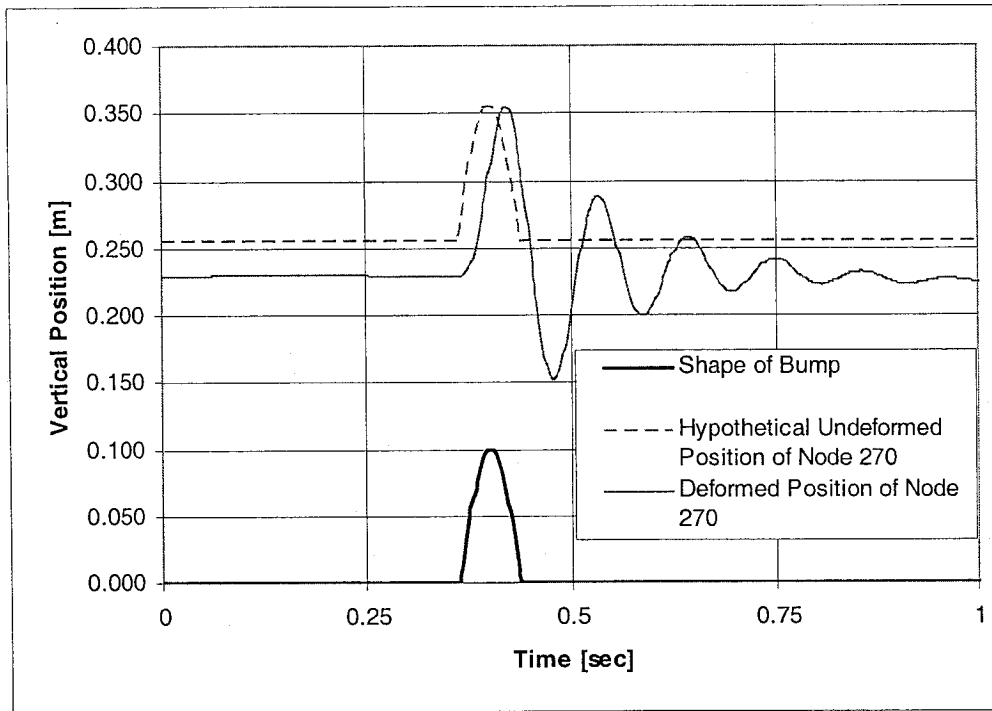


Fig. 3.33 Bounce of the right hand side rear wheel for linear tire model (amplitude of bulge: 0.1 m).

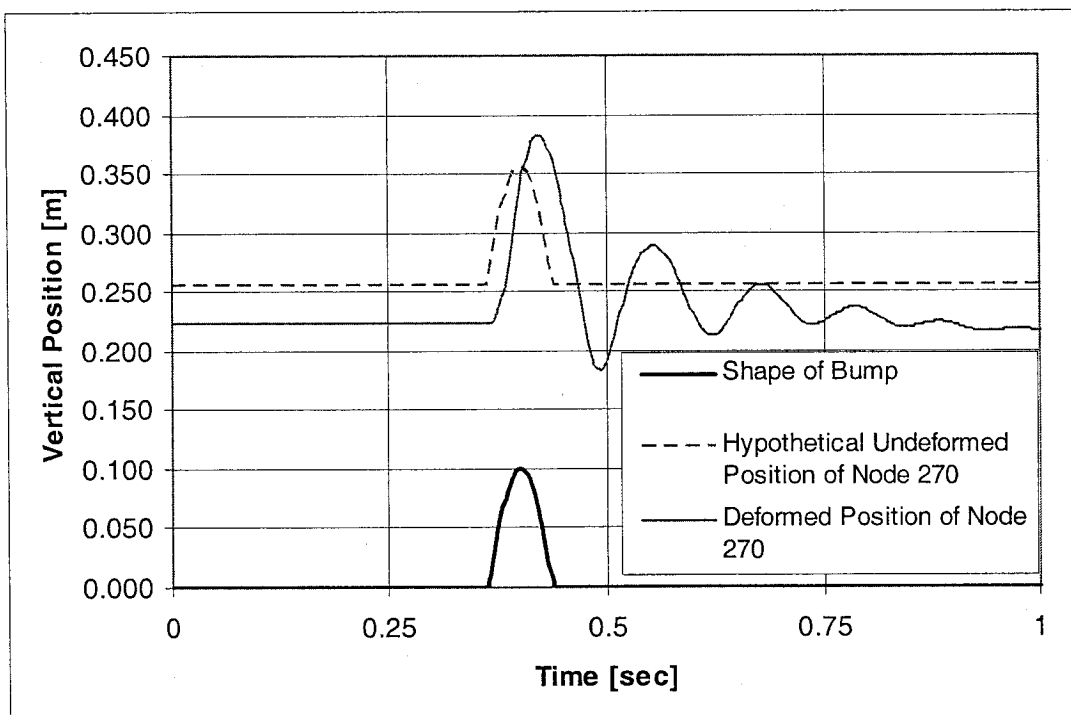


Fig. 3.34 Bounce of the right hand side rear wheel for nonlinear tire model (amplitude of bulge: 0.1 m).

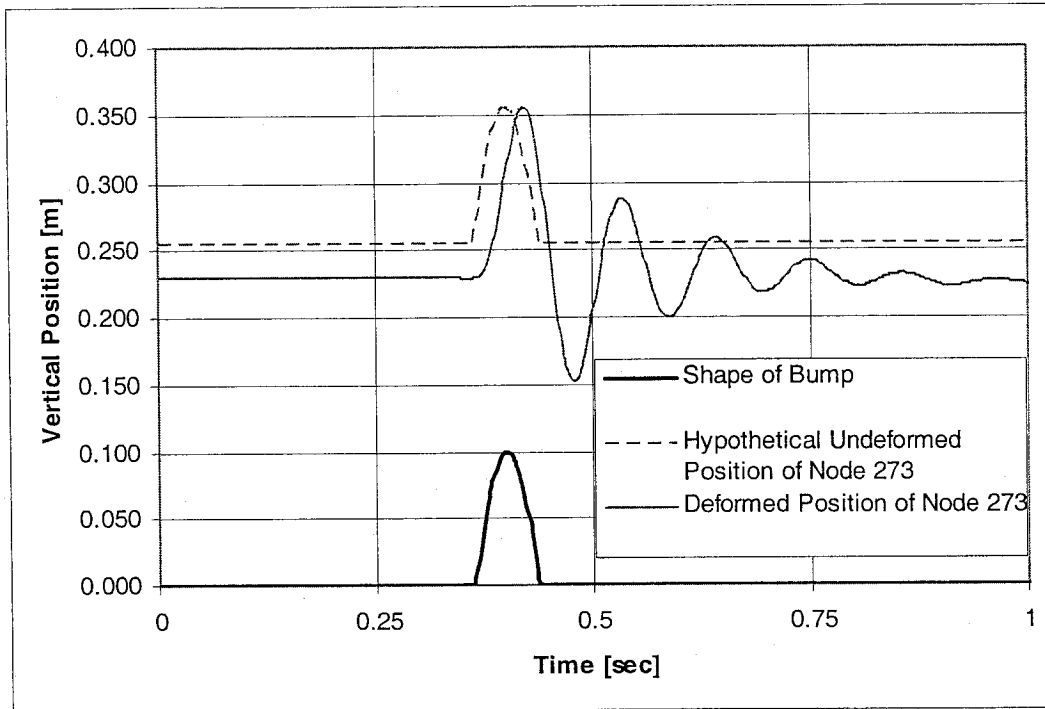


Fig. 3.35 Bounce of the left hand side rear wheel for linear tire model (amplitude of bulge: 0.1 m).

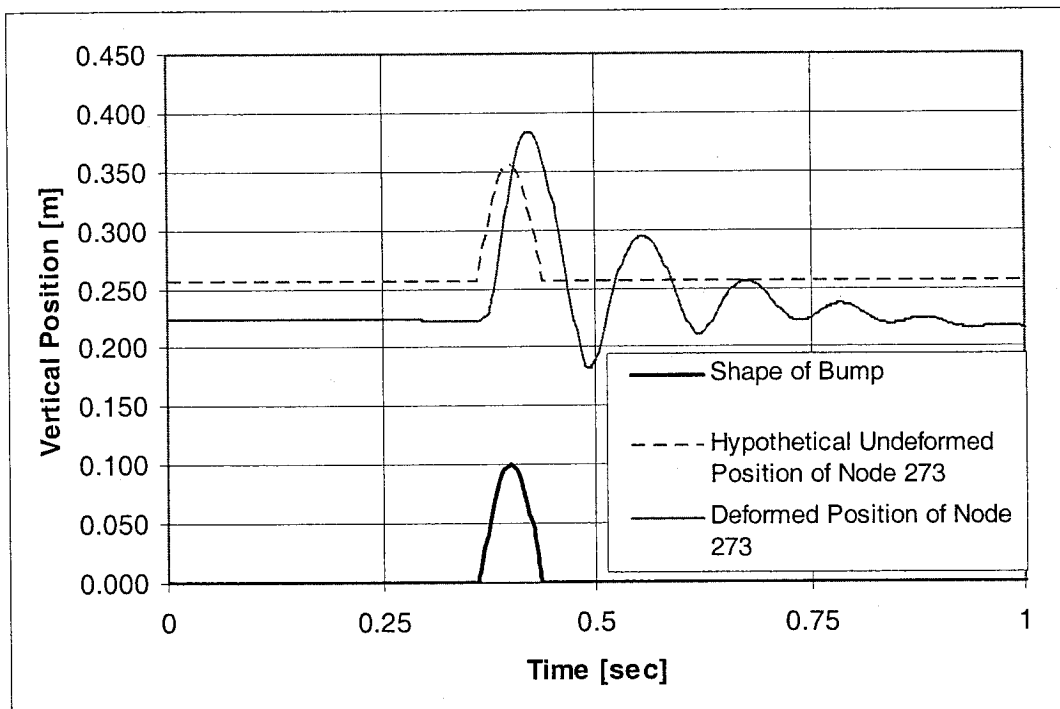


Fig. 3.36 Bounce of the left hand side rear wheel for nonlinear tire model (amplitude of bulge: 0.1 m).

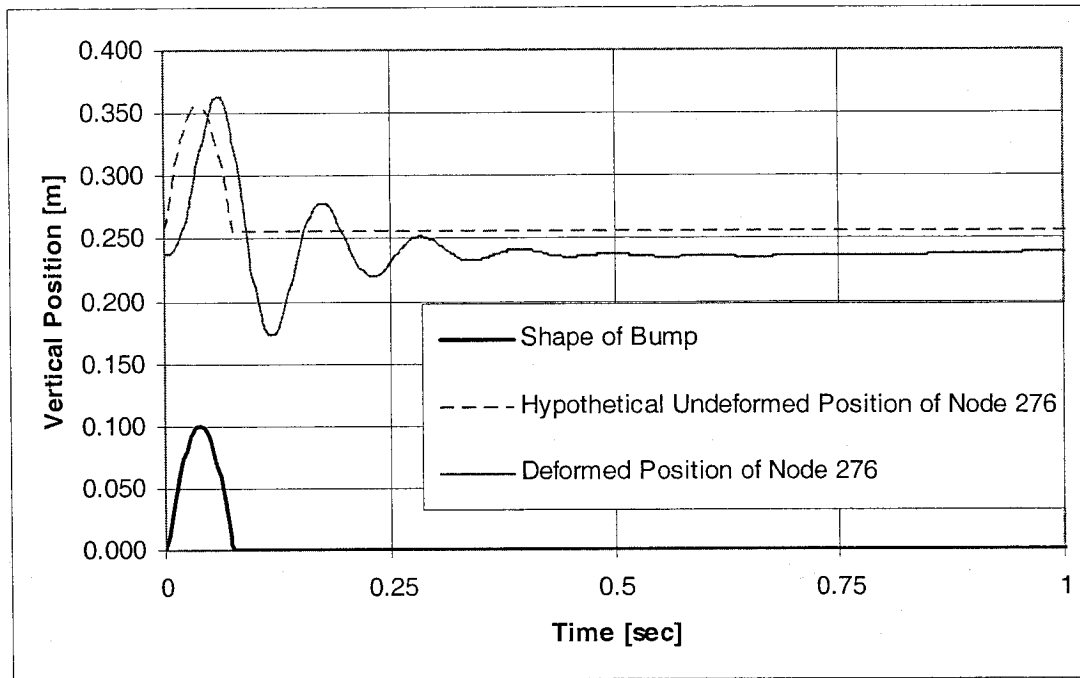


Fig. 3.37 Bounce of the right hand side front wheel for linear tire model (amplitude of bulge: 0.1 m).

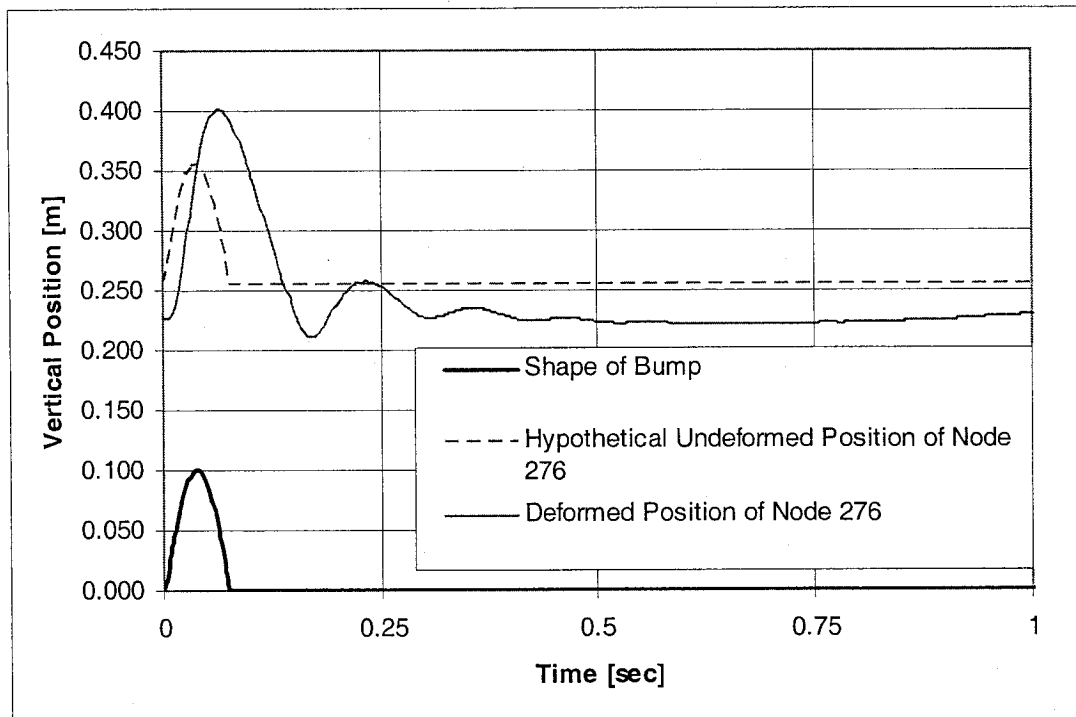


Fig. 3.38 Bounce of the right hand side front wheel for nonlinear tire model (amplitude of bulge: 0.1 m).

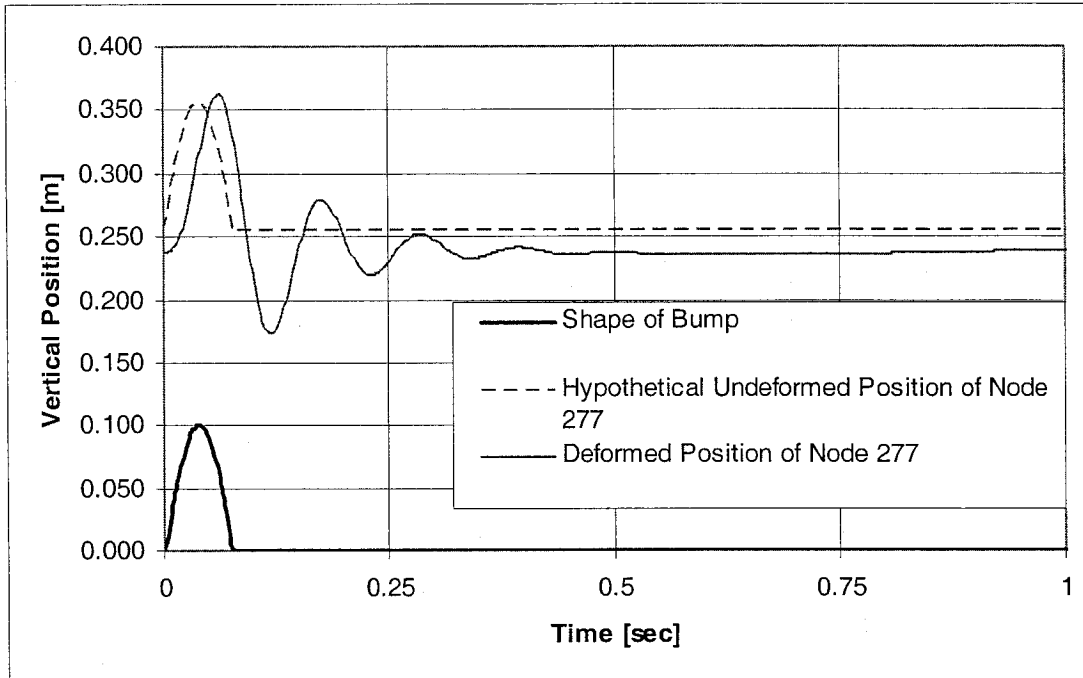


Fig. 3.39 Bounce of the left hand side front wheel for linear tire model (amplitude of bulge: 0.1 m).

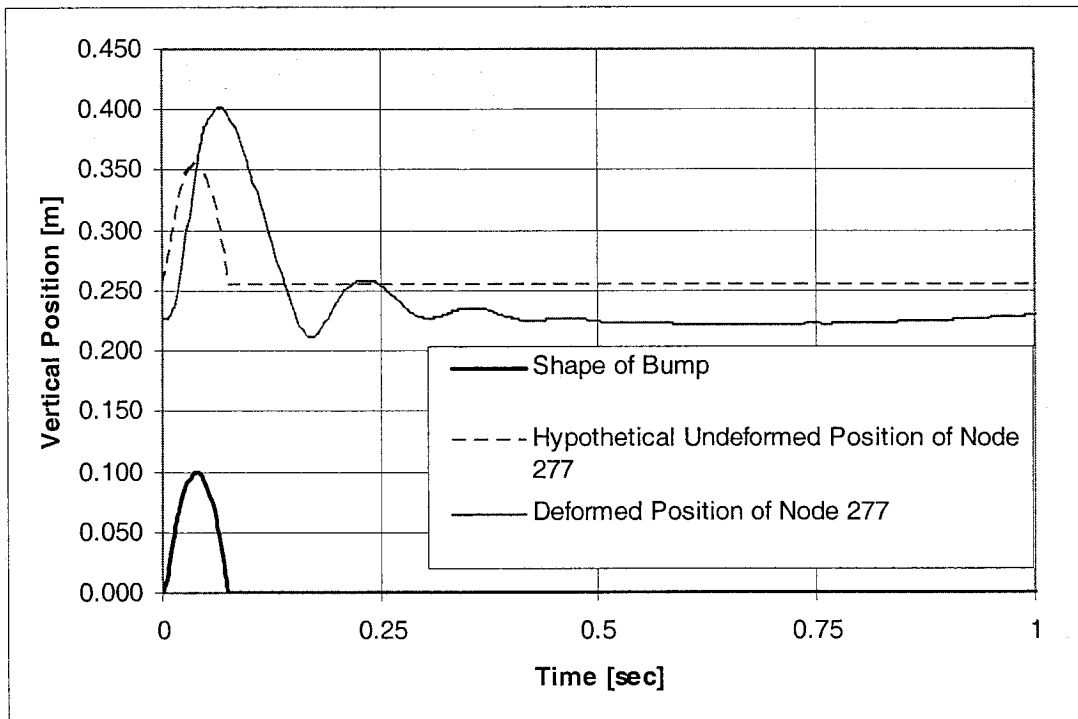


Fig. 3.40 Bounce of the left hand side front wheel for nonlinear tire model (amplitude of bulge: 0.1 m).

Comparison between Rigid Body and Flexible Body:

In this study, flexible and rigid body models are compared when the candidate buss passes over a bulge ($A = 0.1\text{m}$, $\lambda = 1.5\text{m}$). Only linear tire model is used as the influence of flexible structure on the responses is the main concern. The bounce and pitch of the center of gravity for both rigid and flexible body are shown in Figs. 3.41 and 3.42, respectively. Also Figs. 3.43 and 3.44 demonstrate the bounces or vertical responses of rear right chassis and rear right wheel, respectively for both rigid and flexible body (node No. 214 is located on the chassis at the right side of the rear axle, and node No. 218 is located on the rear right wheel center). According to the Figs. 3.41-3.44, there is no difference in the bounce and pitch responses of the center of gravity (c.g.) and the bounce responses of chassis and wheels between rigid body and flexible body. Bending mode of chassis and axles was not within the first twenty two natural frequencies considered in the mode superposition method. This may be the reason for no effect of flexibility on the ride response results of c.g., chassis and axles. However, very little differences are observed in the vertical responses for the nodes in the roof (node Nos. 191 and 166) between rigid and flexible body as shown in Figs. 3.45 and 3.46. This is mainly due to the fact that roof of the bus is more flexible compared to its chassis and axles. Moreover, there are significant differences in the lateral vibrations of the right sidewall (node Nos. 12 and 258) between rigid and flexible body as shown in Figs. 3.47 and 3.48. The lateral oscillation frequencies of node Nos. 12 and 258 of flexible body are approximately 11Hz and 13.5Hz, respectively, which completely comply with the 10th mode shape (natural frequency: 11.229Hz) and 13th mode shape (natural frequency: 13.91Hz) of flexible body. On the contrary, the lateral oscillation frequencies of node Nos. 12 and 258 of rigid

body are approximately 1Hz. The lateral oscillation frequencies of node Nos. 12 and 258 of flexible body could be reduced to about 1Hz if bottom part of the sidewall were made inward tapered. In reality, bottom parts of the sidewall of all vehicles are inward tapered.

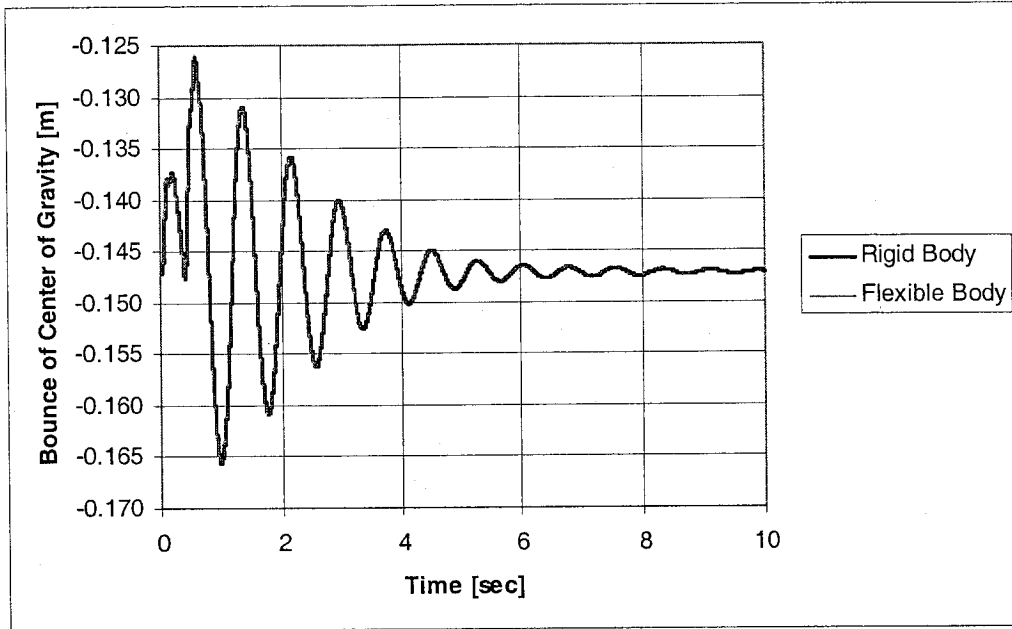


Fig. 3.41 Bounce of the Center of Gravity for linear tire model (amplitude of bulge: 0.1 m).

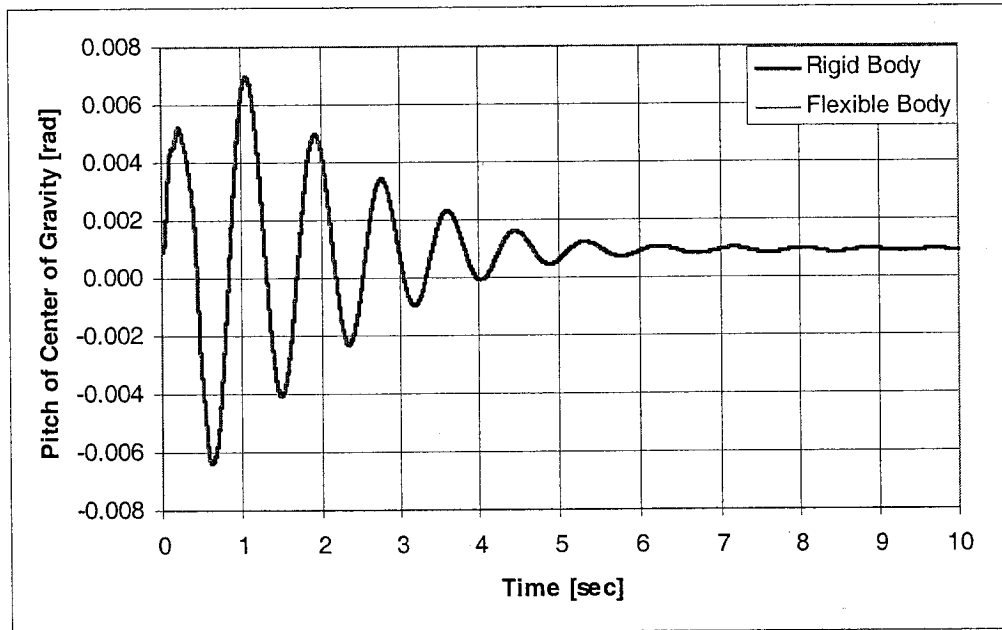


Fig. 3.42 Pitch of the Center of Gravity for linear tire model (amplitude of bulge: 0.1 m).

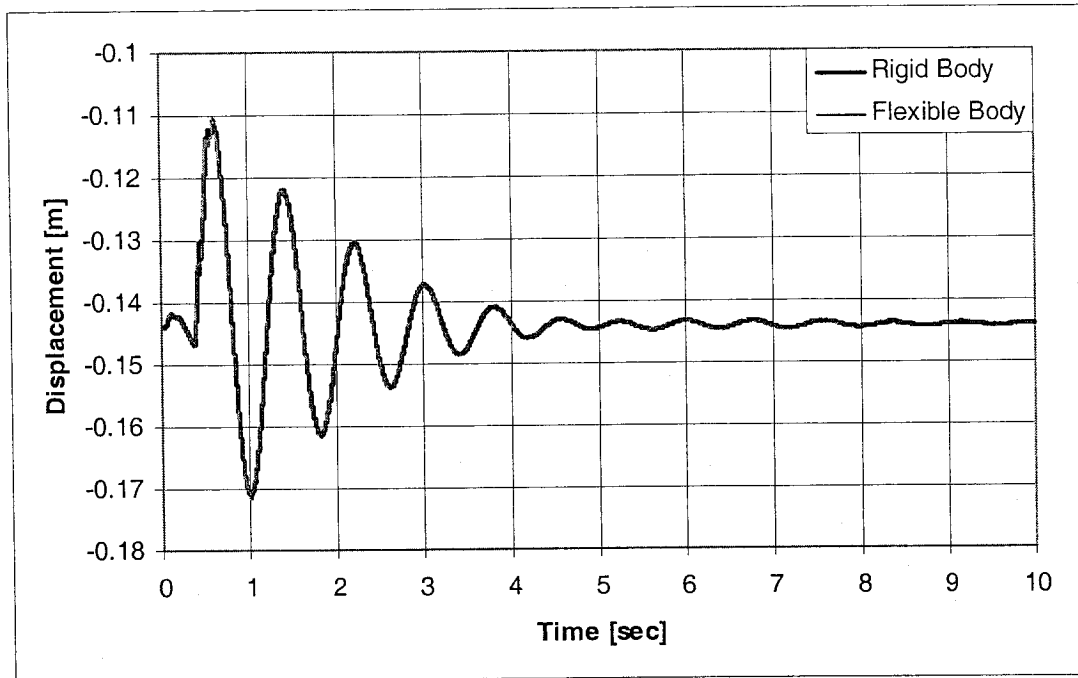


Fig. 3.43 Vertical displacement of node No. 214 for linear tire model (amplitude of bulge: 0.1 m).

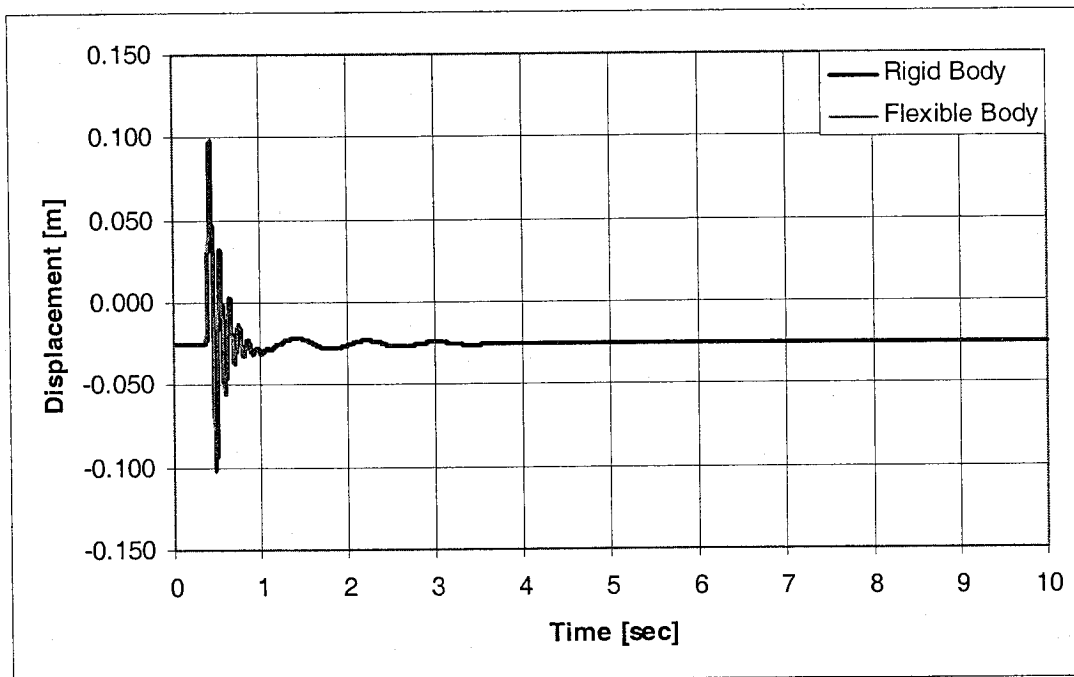


Fig. 3.44 Vertical displacement of node No. 218 for linear tire model (amplitude of bulge: 0.1 m).

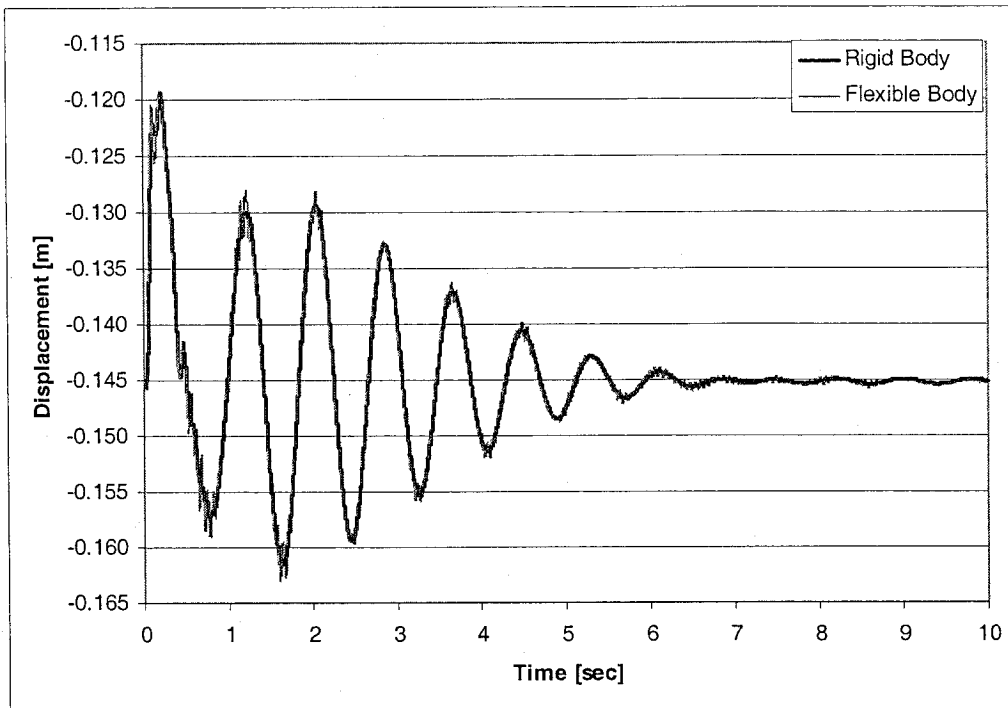


Fig. 3.45 Vertical displacement of node No. 191 for linear tire model (amplitude of bulge: 0.1 m).

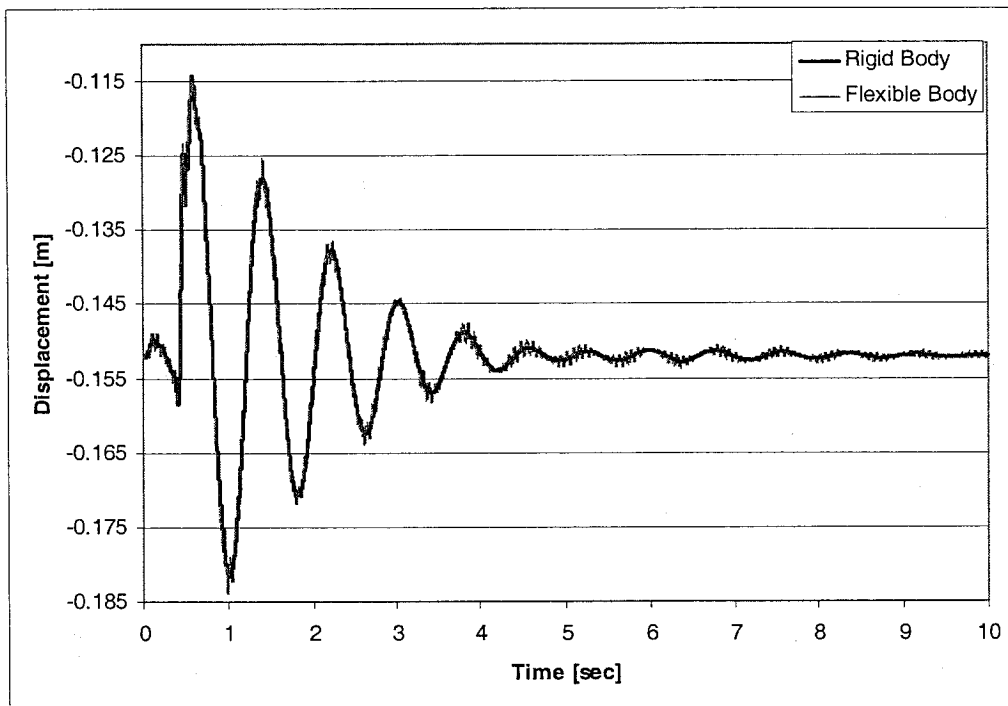


Fig. 3.46 Vertical displacement of node No. 166 for linear tire model (amplitude of bulge: 0.1 m).

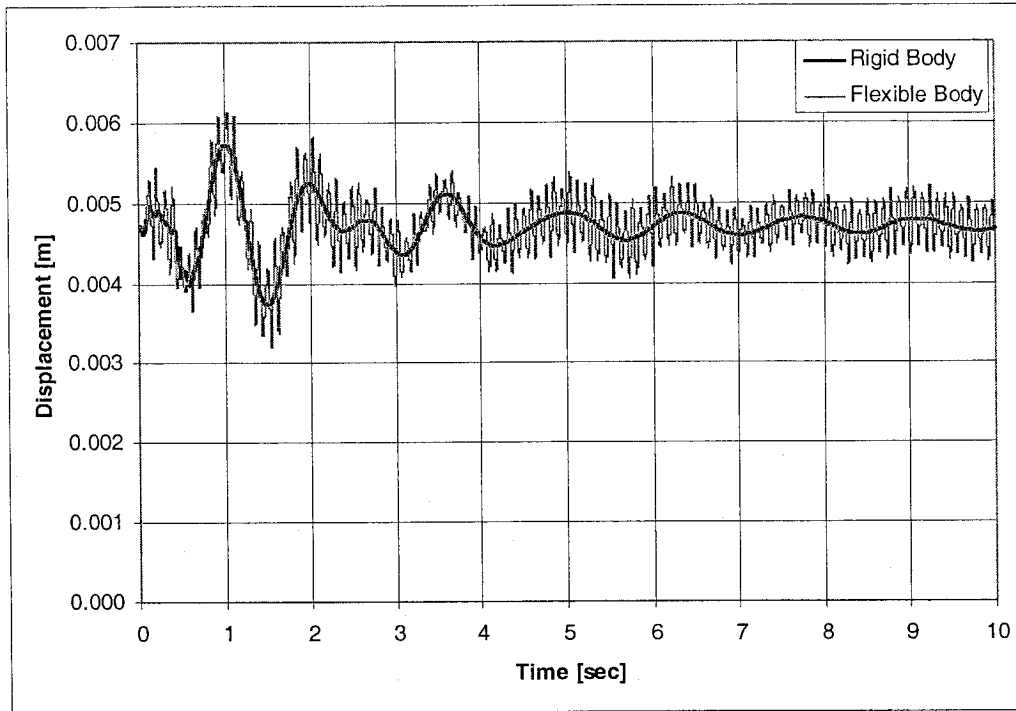


Fig. 3.47 Lateral displacement of node No. 12 for linear tire model (amplitude of bulge: 0.1 m).

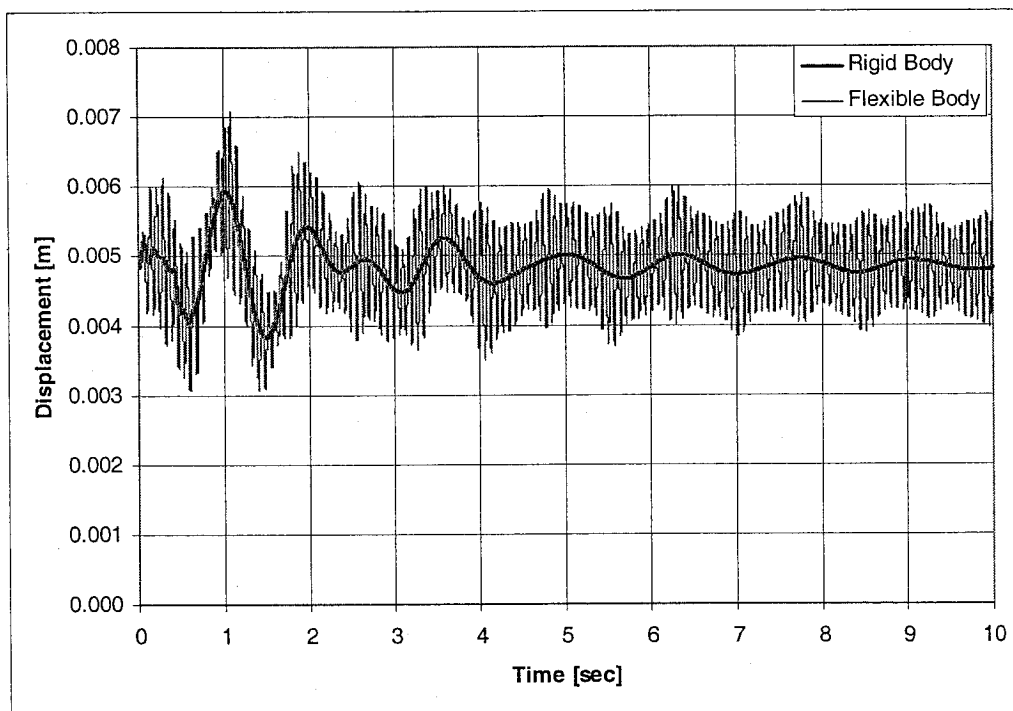


Fig. 3.48 Lateral displacement of node No. 258 for linear tire model (amplitude of bulge: 0.1 m).

3.3 RIDE ANALYSIS USING RANDOM ROAD INPUT

Experimental data of a Montréal city road 'Cote-Des-Neiges' shown in Fig. 3.49(a) has been taken as random road input [26]. The maximum amplitude of road roughness is 0.058 m. According to the simulation results described in the previous example, the linear tire model is capable of capturing the correct response in a desired range for small amplitude of excitations. Therefore, linear tire model and linear ground spring are considered for this example. Moreover, the flexible damped model is used for this example. Initial displacements arising from the total weight of the bus are involved in the analysis. The velocity of the bus is assumed to be equal to 20 m/s (72 km/h). It is important to note that initial distance coordinates are different for rear and front wheels. Simulation is carried out in time domain, and then outputs are converted into PSD (Power Spectral Density) units as the time domain response for random input is not useful. Figs. 3.49(b) and 3.49(c) demonstrate vertical displacements of node No. 218 (a node on the rear right wheel center) and node No. 214 (a node on the chassis at rear right axle), respectively. Figs. 3.50(a) and 3.50 (b) illustrate lateral displacement and lateral acceleration of node No. 304 (a node on the roof), respectively, which have been produced due to the track height difference between left and right track and the flexibility of the structure. The results show that maximum lateral acceleration of roof is 0.67 m/sec^2 . Finally, Figs. 3.51 and 3.52 show the damping forces exerted on the chassis for the dampers positioned in the front-right suspension and rear-right suspension, respectively.

PSD of left track height and right track height are shown in Figs. 3.53 and 3.54, and are obtained using the time history data presented in Fig. 3.49(a). MATLAB

subroutine using Welch's averaged modified periodogram method was used for the generation of the PSD as a function of circular frequency. The all PSD inputs and responses are obtained from raw time history data and were not filtered to remove low frequency unevenness of the road. According to the frequency analysis of the undamped linear candidate bus discussed in section 2.3.2, the undamped rolling, pitch and bounce natural frequencies of chassis and body are 0.73 Hz, 1.14 Hz and 1.31 Hz, respectively. On the other hand, the undamped bounce natural frequencies of front and rear axles are 9.16 Hz and 9.32 Hz, respectively. PSD of vertical acceleration of node No. 214 (a node on the chassis at rear right axle) is given in Fig. 3.55. The same responses are shown for node Nos. 264 (a node on the chassis at front right axle), 215 (a node on the chassis at rear left axle), and 262 (a node on the chassis at front left axle) in Figs. 3.56, 3.57 and 3.58, respectively. As the results indicate, the first highest pick of PSD of vertical acceleration of node No. 214 is at around 0.65 Hz (damped natural frequency), and the second highest pick is attained at around 9 Hz (damped natural frequency), which comply with the frequency responses of the undamped candidate bus as the damped natural frequency is smaller than the undamped natural frequency when the value of damping ratio is less than 1. On the contrary, the first highest pick of PSD of vertical acceleration of node Nos. 264, 215, and 262 are at around 9 Hz, and the second highest picks are attained at around 0.65 Hz. At first sight, the results seem contradictory with the frequency responses of the candidate bus, but it is possible to transmit vibrations from axles to the chassis local points through suspensions. It is important to note that the chassis of the candidate bus is connected with the axles at those nodes (node Nos. 214, 264, 215 and 262) through dampers. PSD of bounce and pitch acceleration of the center

of gravity are shown in the Figs. 3.59 and 3.60. As the results indicate, the first damped bounce and pitch natural frequency of the body is 0.68 Hz and 0.61 Hz, respectively. It also indicates the value of damping ratio is 0.45, which is less than 1.

PSD of vertical acceleration of rear right wheel is given in Fig. 3.61. The same responses are given for front right wheel, rear left wheel, and front left wheel in Figs. 3.62, 3.63 and 3.64, respectively. The bounce acceleration responses for all wheels are found maximum at around 8 Hz as shown in Figs. 3.61-3.64. The results indicate the damped bounce natural frequency of the wheels are 8 Hz, which is less than the undamped bounce natural frequency of the wheels. This reveals that the value of damping ratio is less than 1.

PSD of vertical load on front left tire is given in Fig. 3.65. The same responses are shown for front right tire, rear left tires, and rear right tires in Figs. 3.66, 3.67 and 3.68, respectively. The results demonstrate that tire loads are mainly dominated by the bounce of the body as the first highest picks are seen at around 0.62 Hz, which is nearly equal to the damped bounce natural frequency of the body. The fundamental reason of this phenomenon is that inertia of body is significantly greater than that of axles and wheels assembly as the weight of the body is 86.9 % of the total bus weight. On the other hand, PSD of damping forces in rear left and rear right suspension systems and front left and front right suspension systems are found maximum at around 0.65 Hz as shown in Figs. 3.69-3.72. This also indicates that the damping force is mostly dominated by the vertical motion of chassis and body as the weight of the axles is only 13.1 % of the total bus weight. Fig. 3.73 illustrates the PSD of the lateral acceleration response of node. No. 304, and the maximum amplitude is found at 6 and 8 Hz, which indicates the roof of the bus is

sensitive between 6 and 8 Hz.

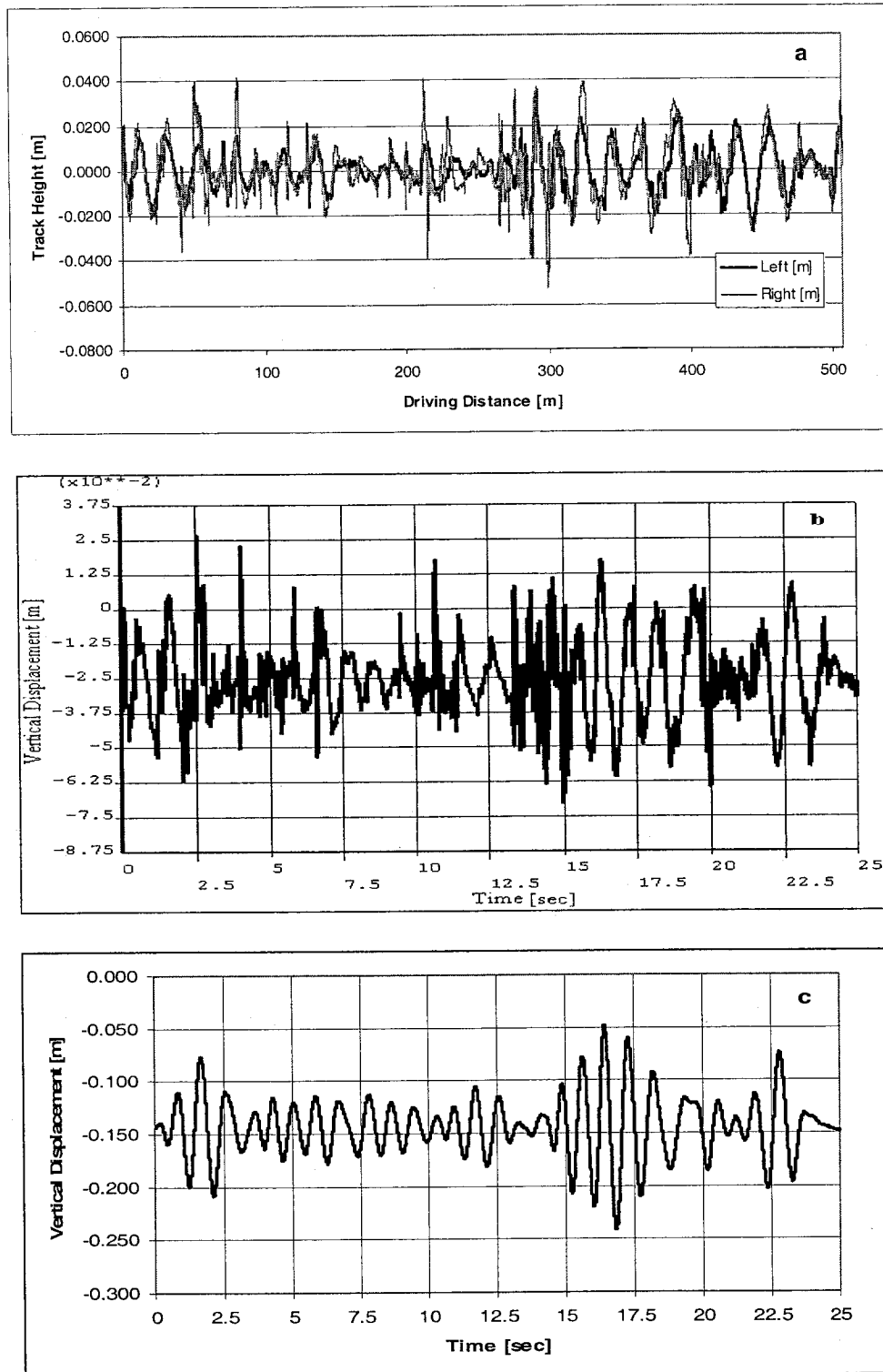


Fig. 3.49 Road profile (a) vertical displacement of node No. 218 (b) and node No. 214 (c).

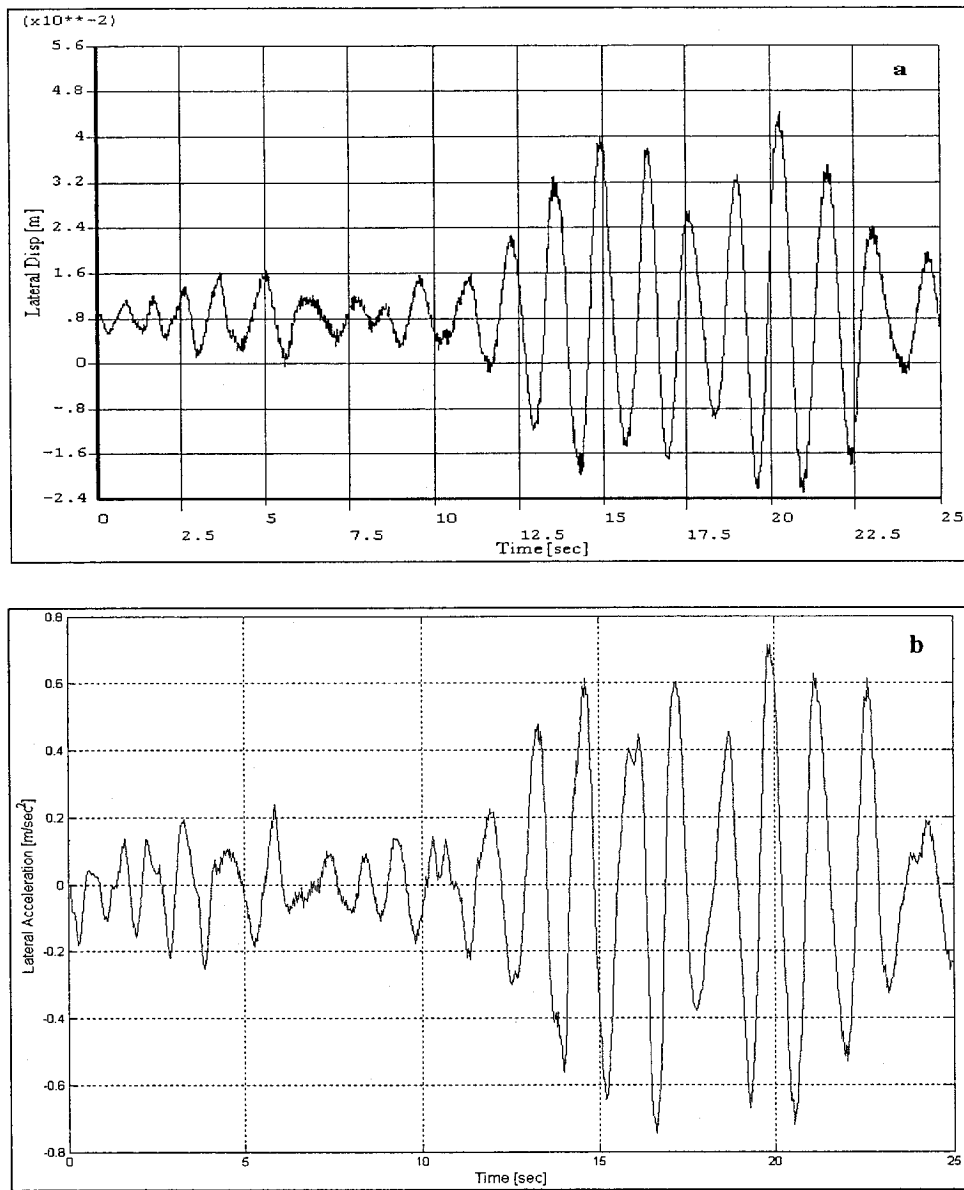


Fig. 3.50 lateral displacement (a) and lateral acceleration (b) of node No. 304.

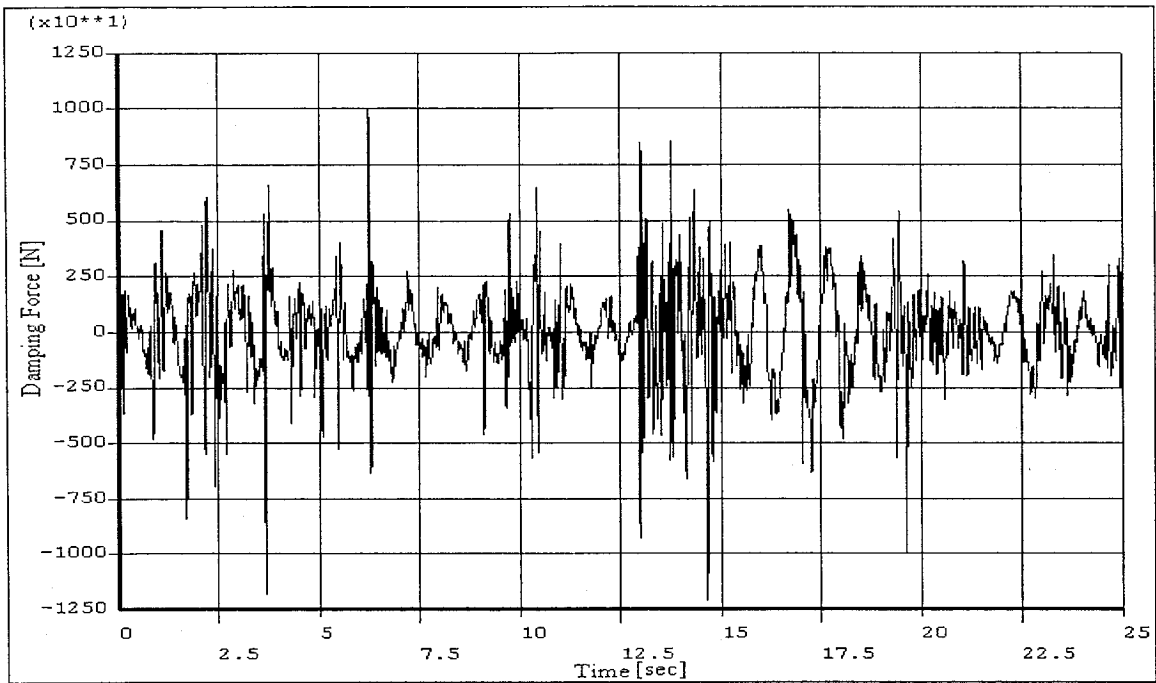


Fig. 3.51 Damping force in front-right suspension.

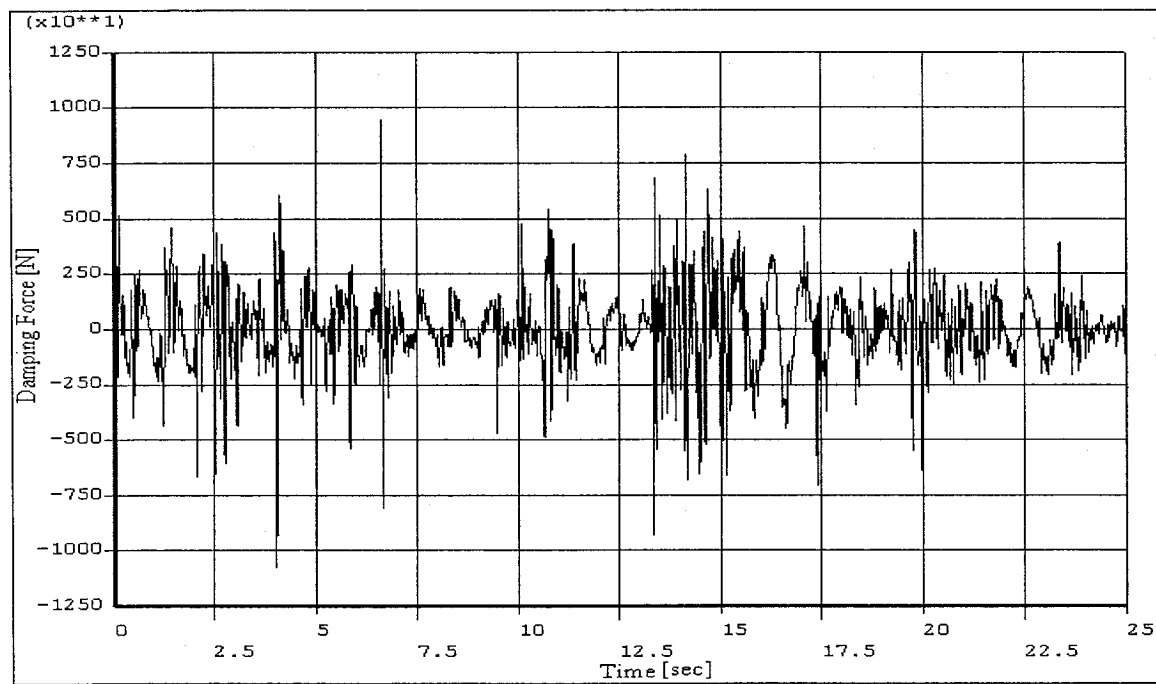


Fig. 3.52 Damping force in rear-right suspension.

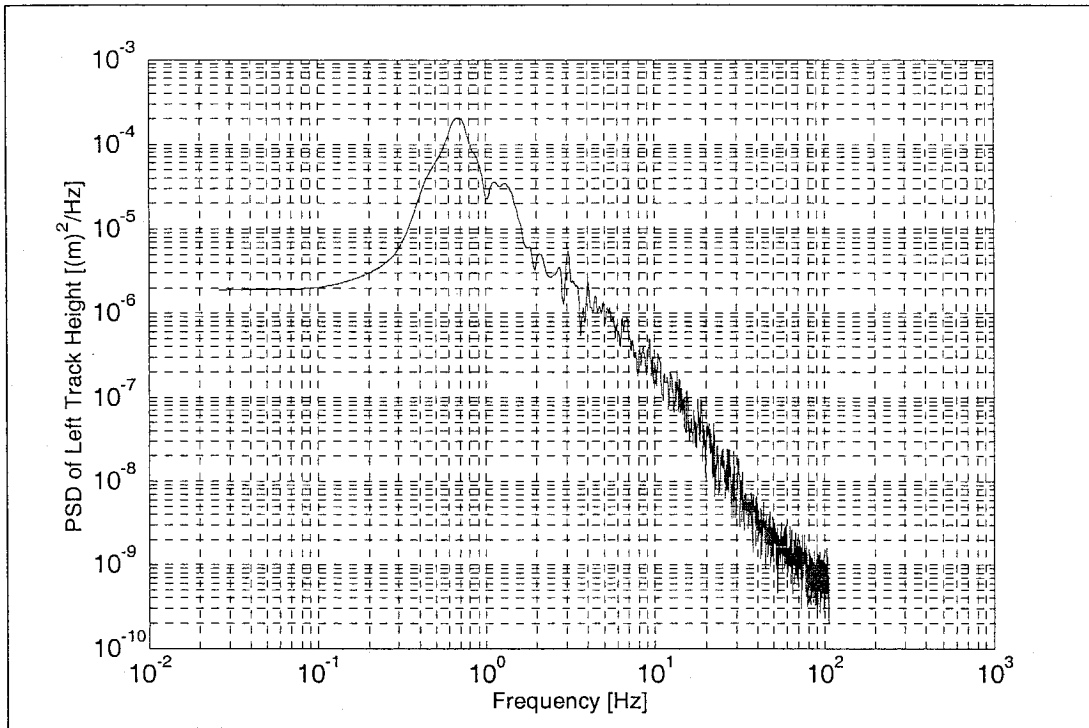


Fig. 3.53 PSD of left track height.

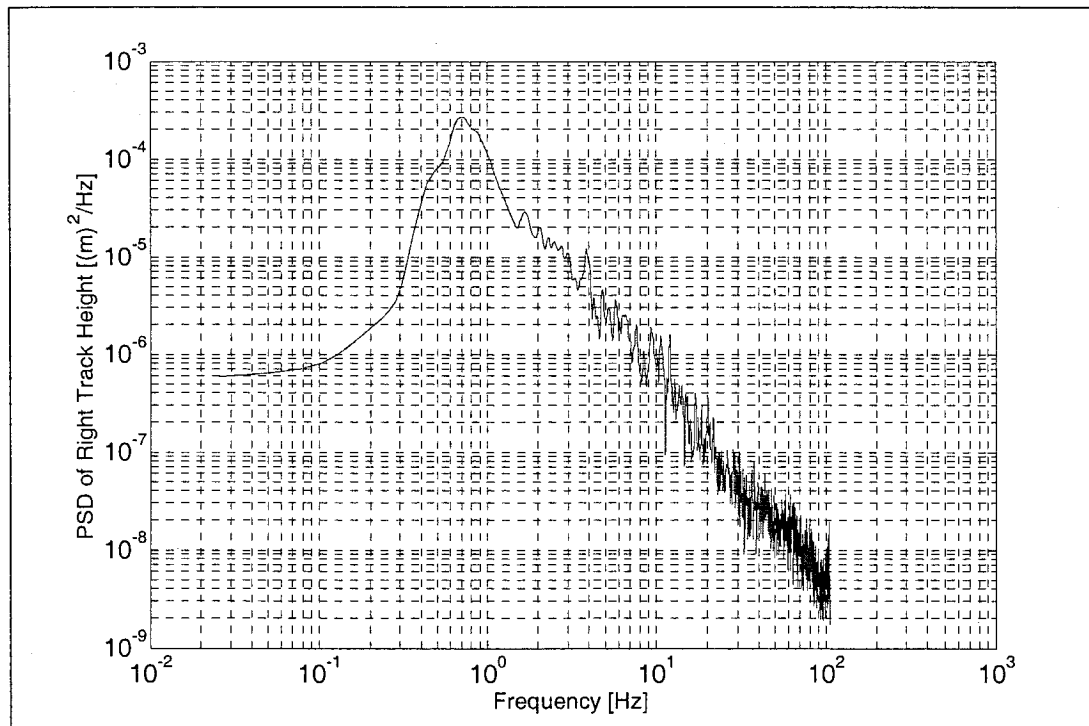


Fig. 3.54 PSD of right track height.

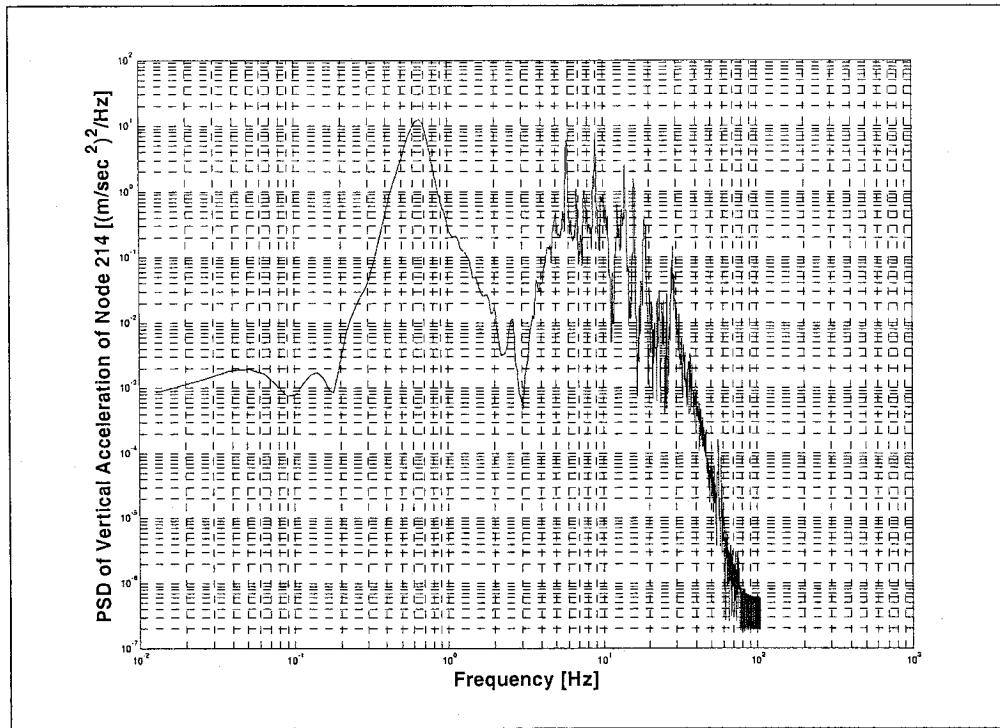


Fig. 3.55 PSD of vertical acceleration of node No. 214.

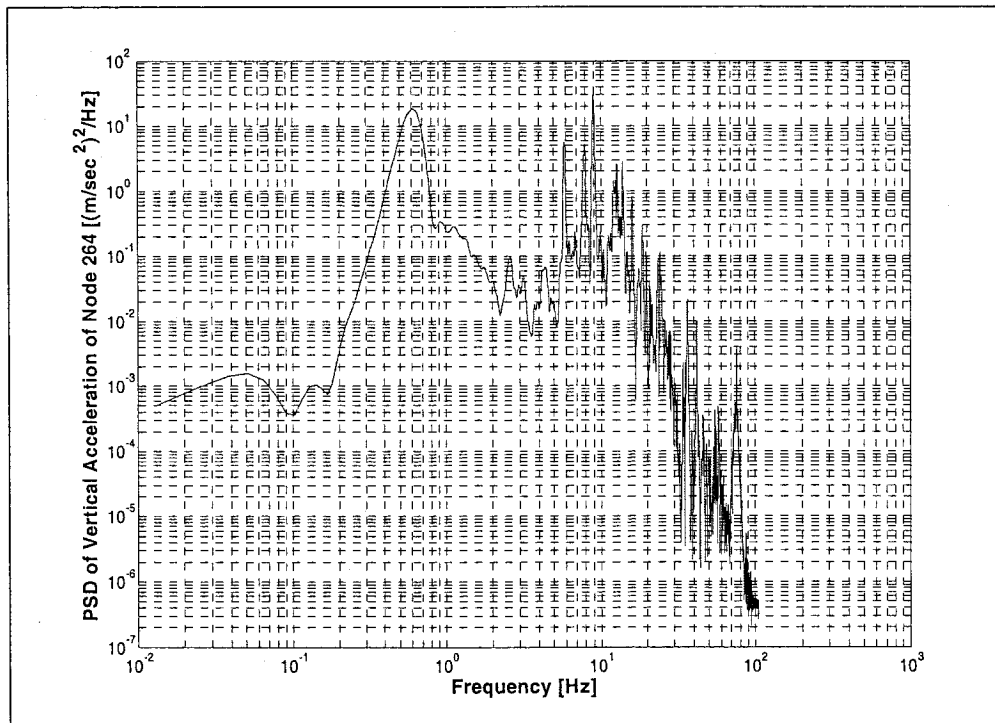


Fig. 3.56 PSD of vertical acceleration of node No. 264.

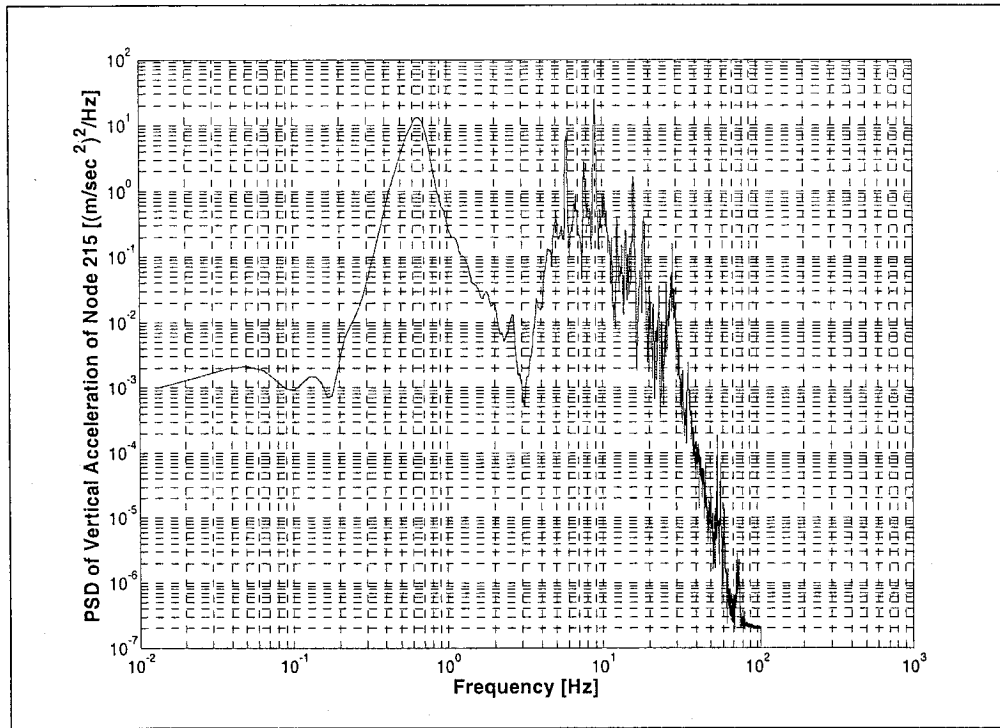


Fig. 3.57 PSD of vertical acceleration of node No. 215.

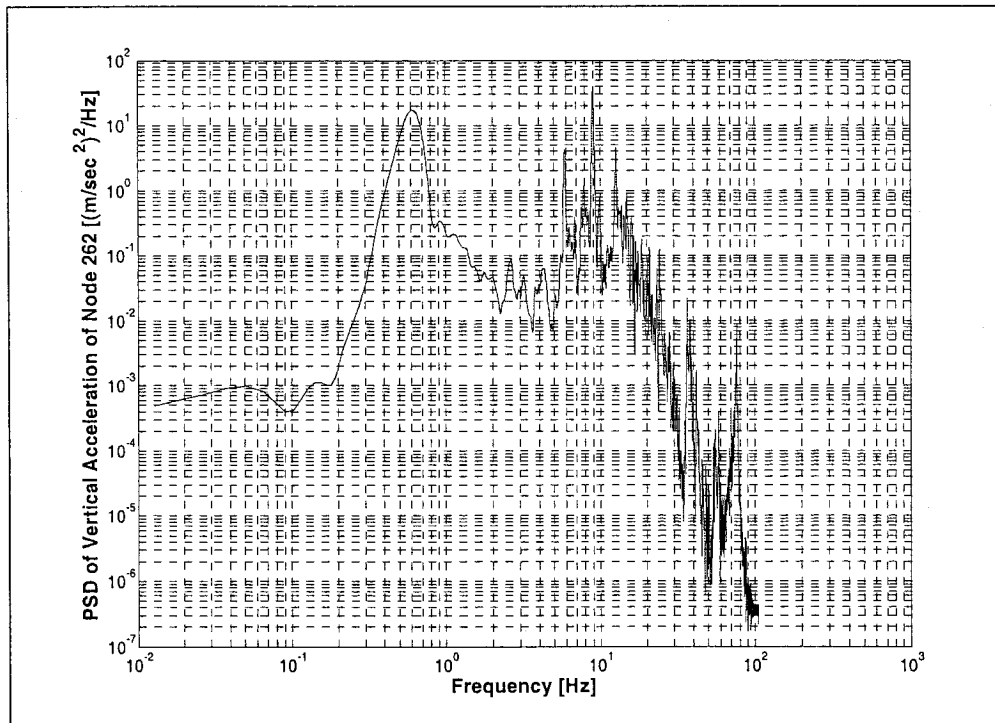


Fig. 3.58 PSD of vertical acceleration of node No. 262.

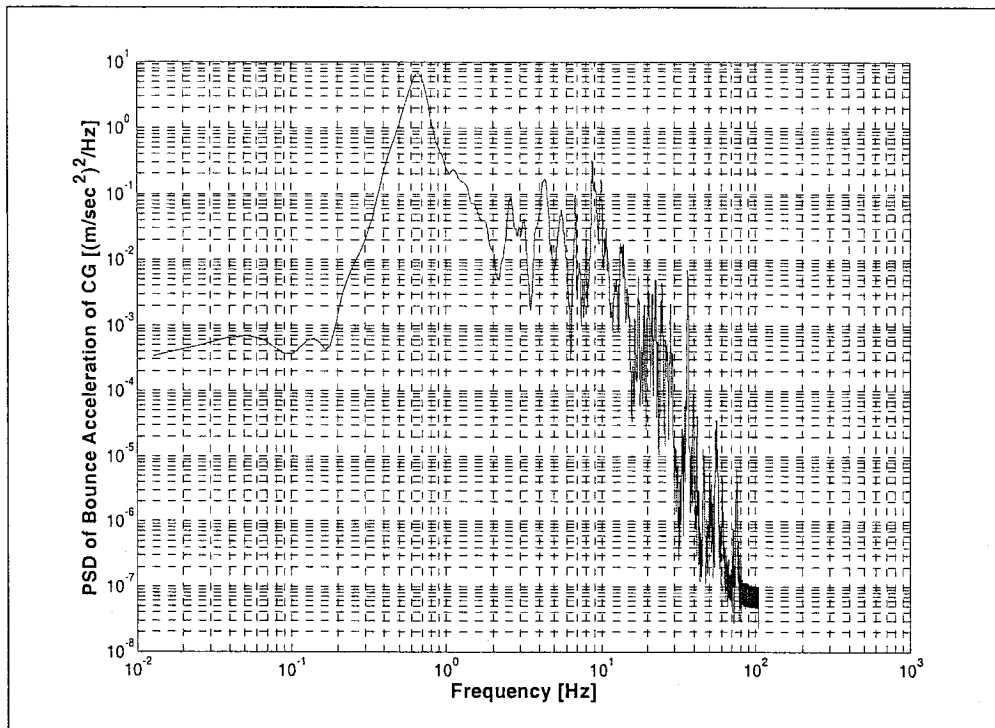


Fig. 3.59 PSD of bounce acceleration of the center of gravity.

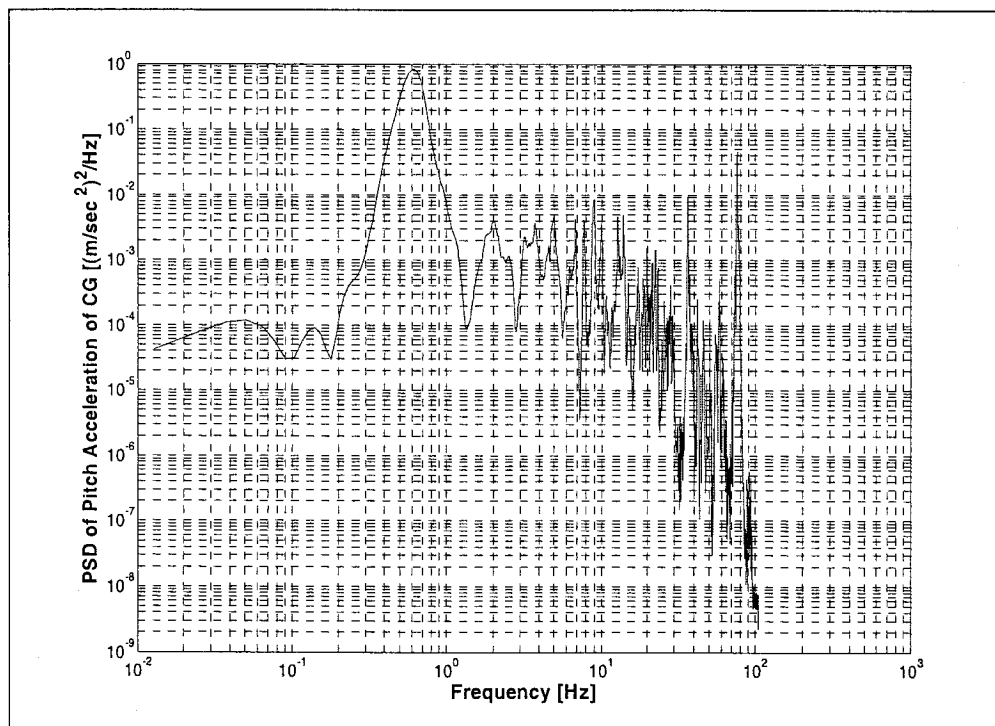


Fig. 3.60 PSD of pitch acceleration of the center of gravity.

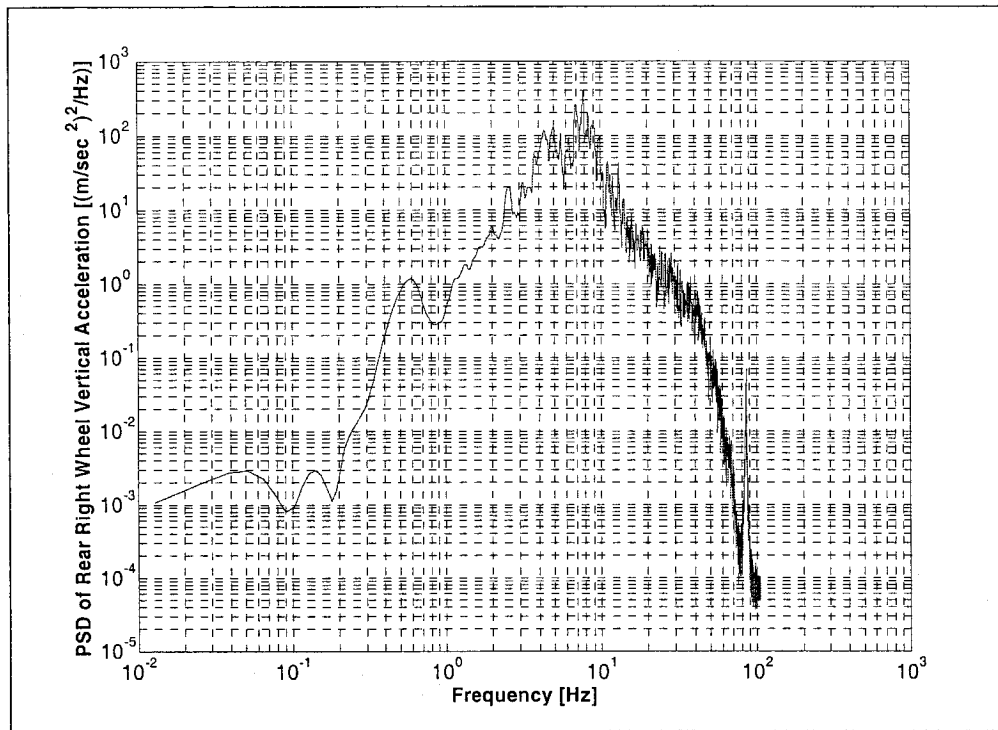


Fig. 3.61 PSD of rear right wheel vertical acceleration.

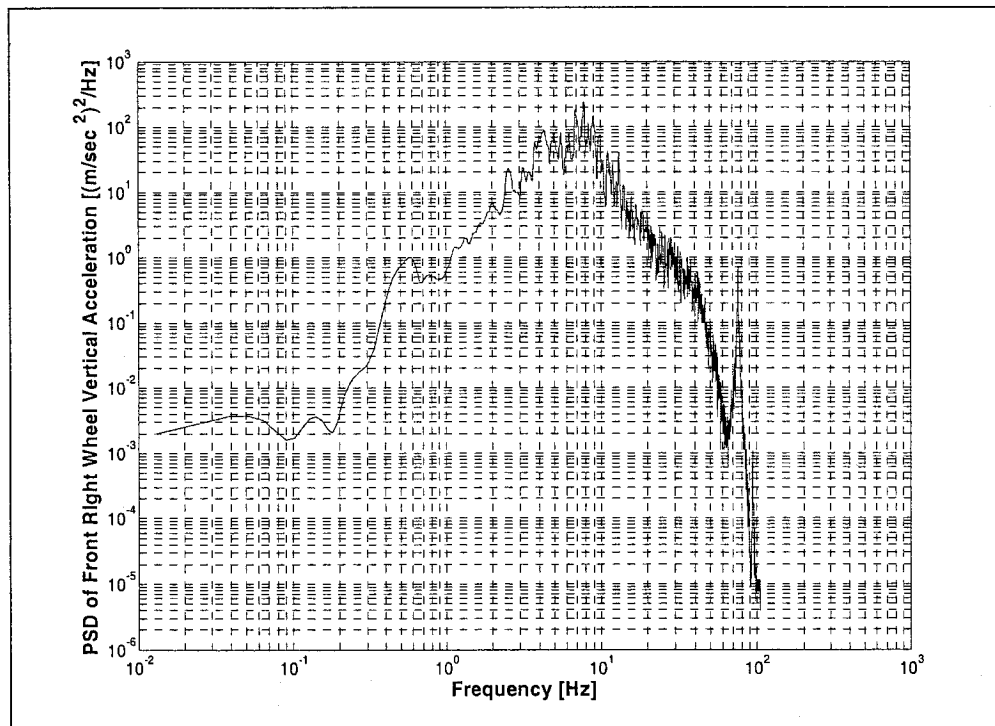


Fig. 3.62 PSD of front right wheel vertical acceleration.

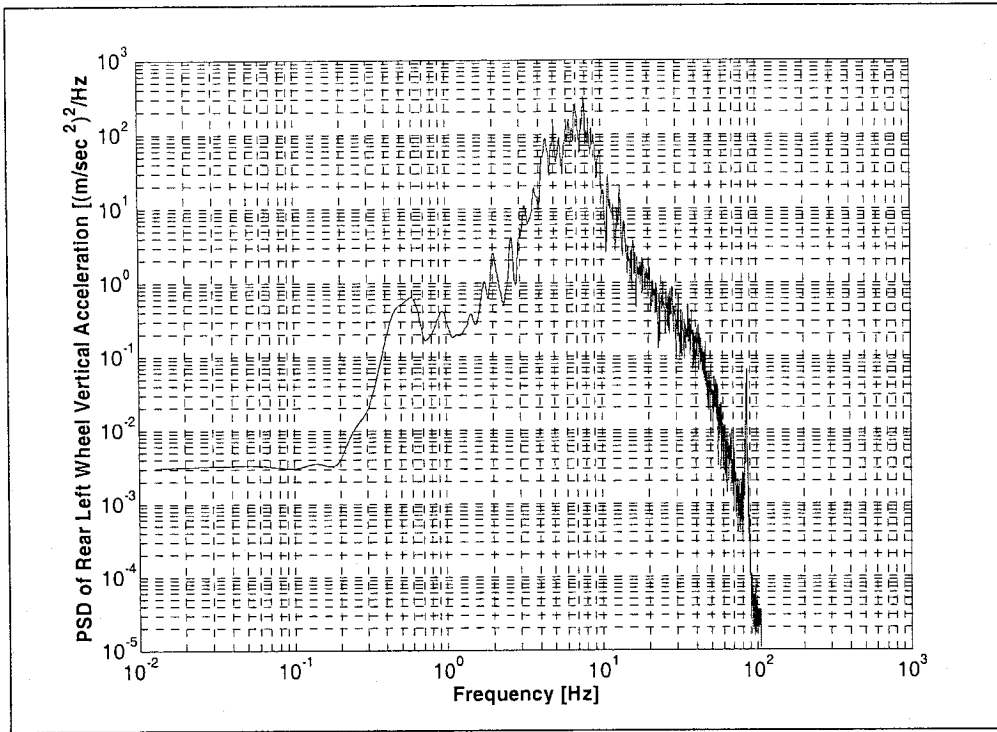


Fig. 3.63 PSD of rear left wheel vertical acceleration.

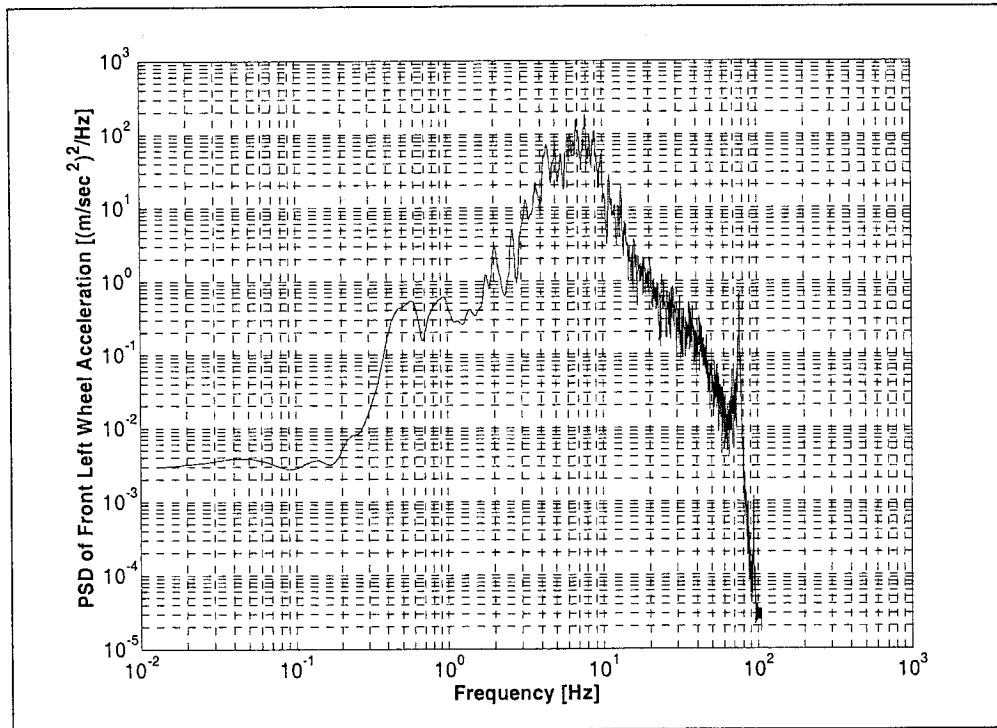


Fig. 3.64 PSD of front left wheel vertical acceleration.

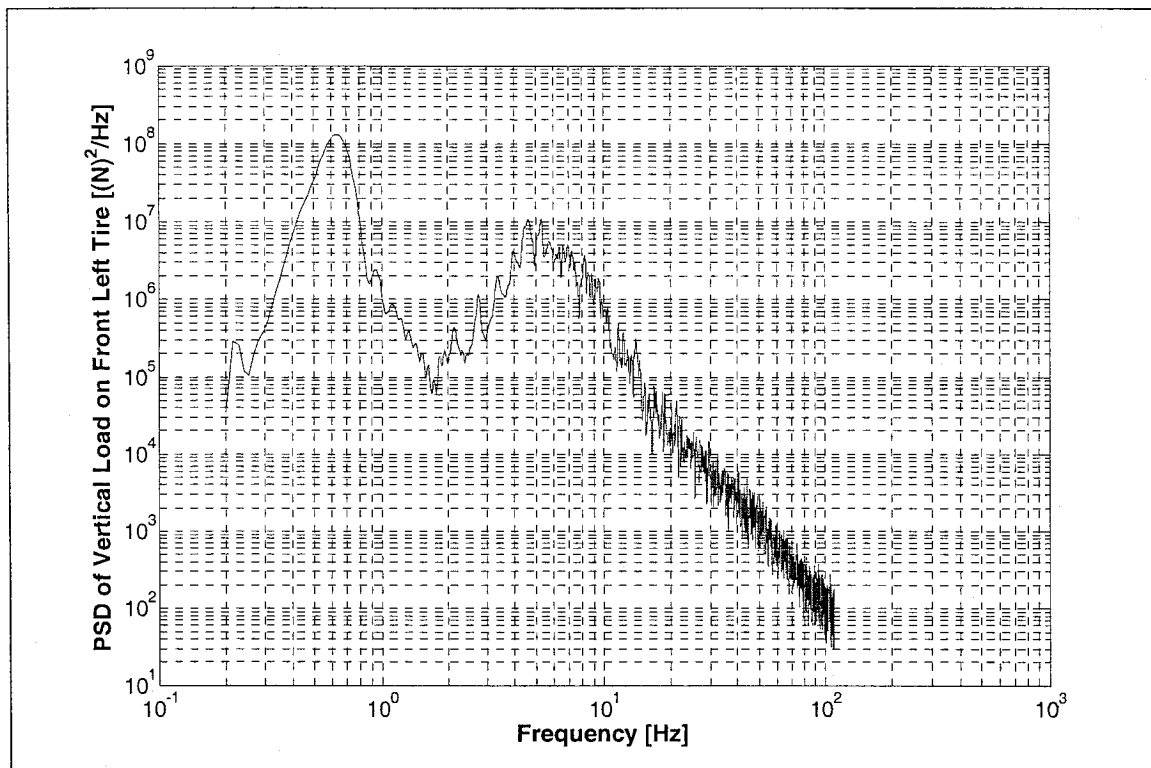


Fig. 3.65 PSD of vertical load on front left tire.

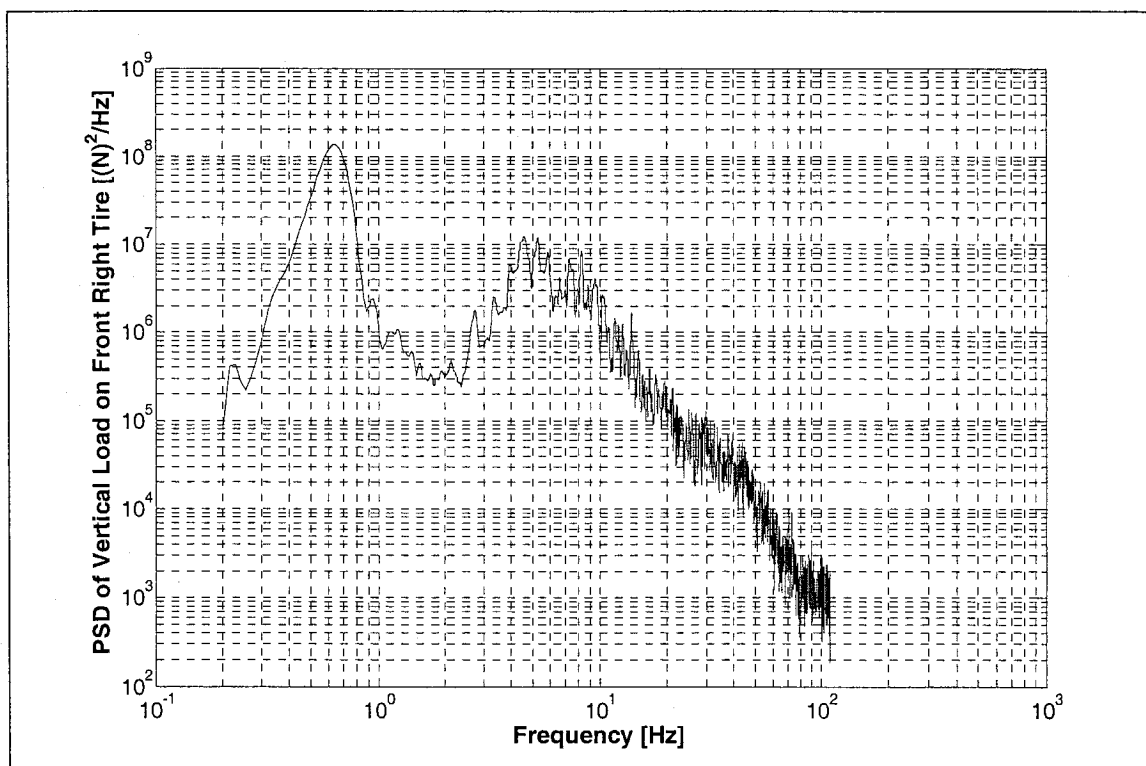


Fig. 3.66 PSD of vertical load on front right tire.

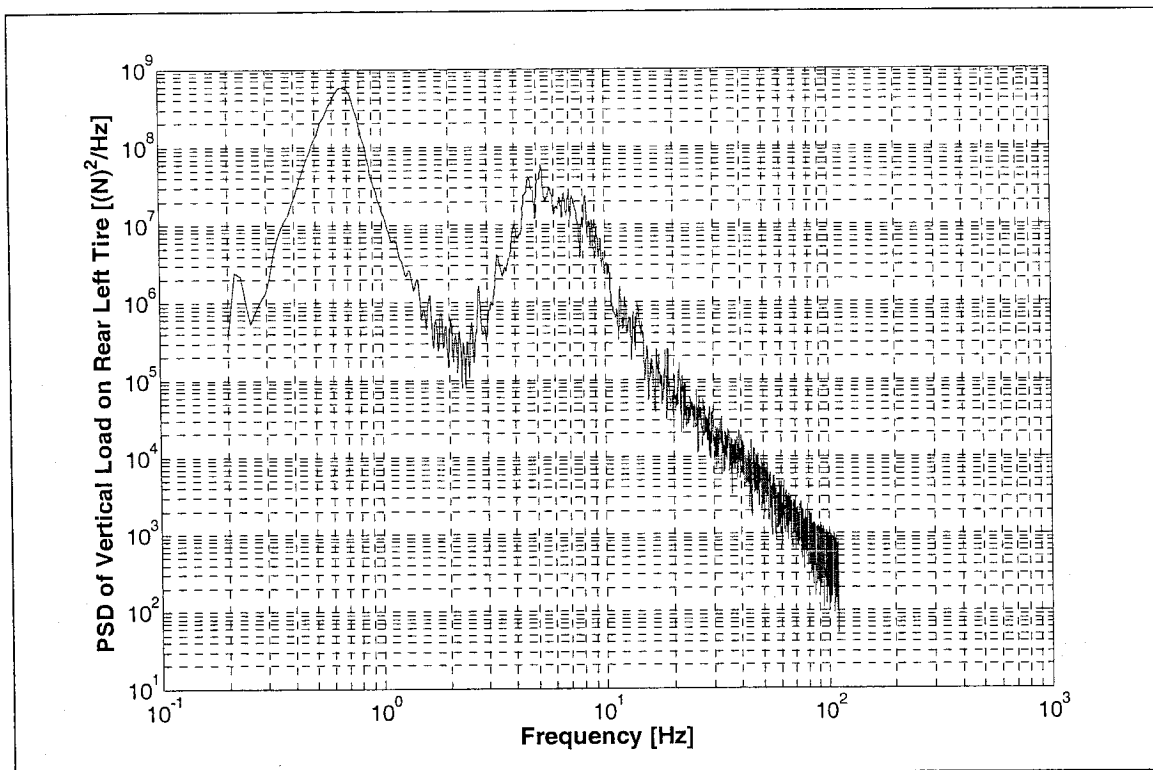


Fig. 3.67 PSD of vertical load on rear left tire.

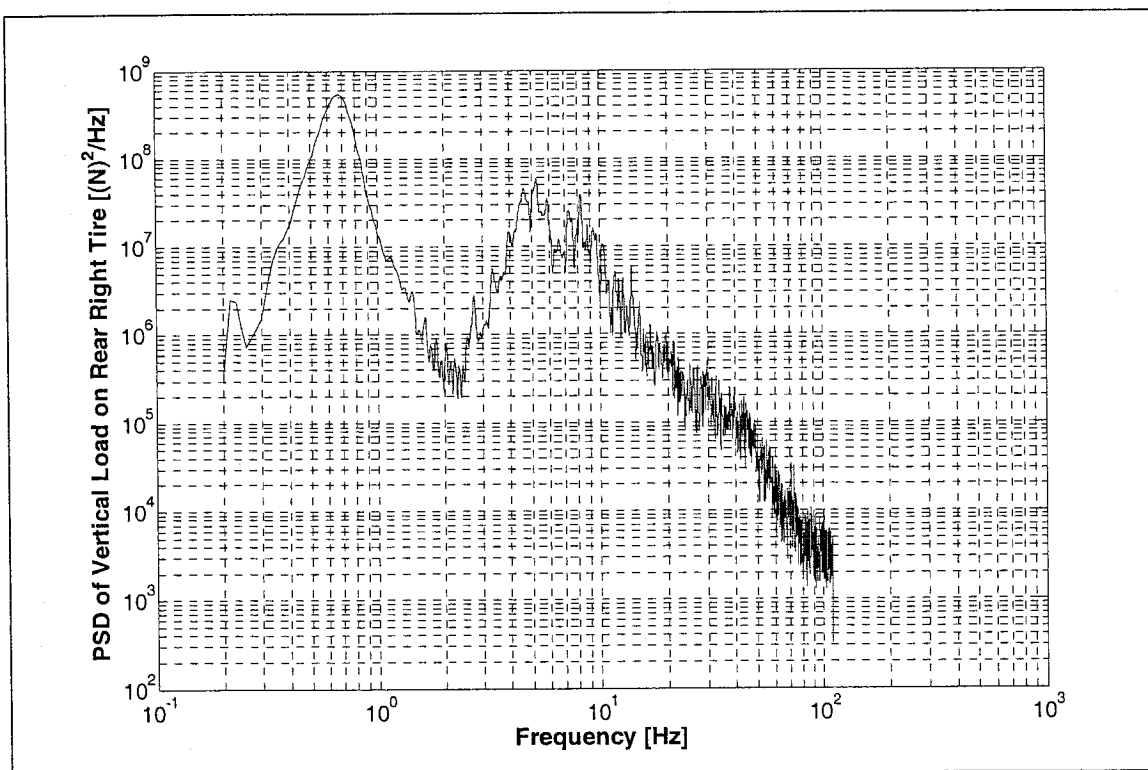


Fig. 3.68 PSD of vertical load on rear right tire.

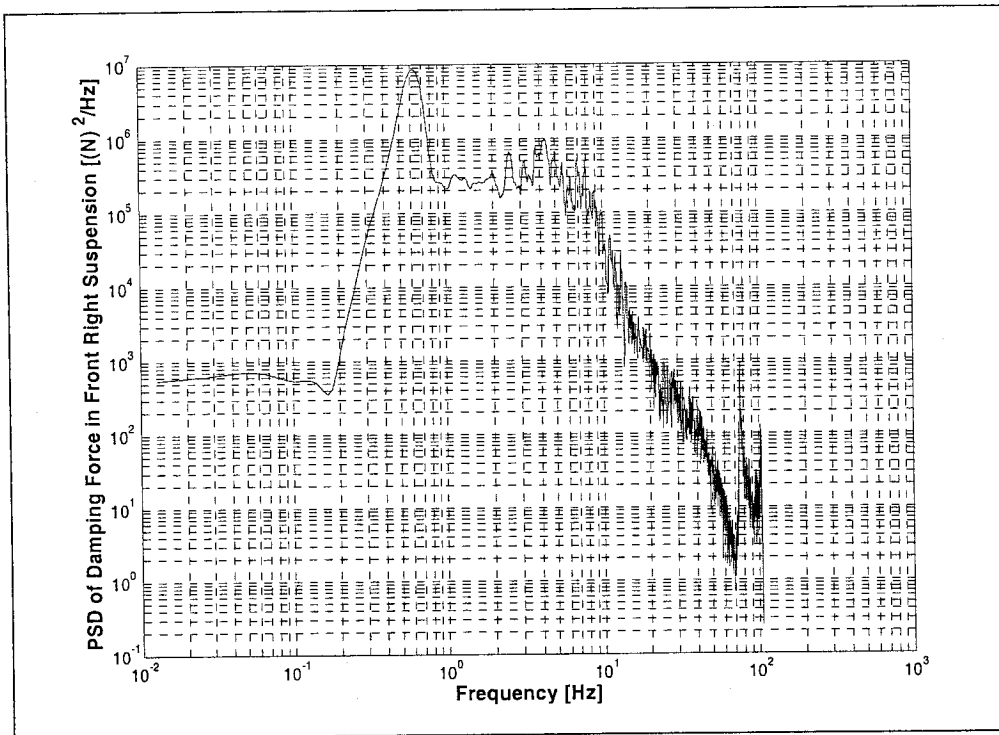


Fig. 3.69 PSD of damping force in front right suspension.

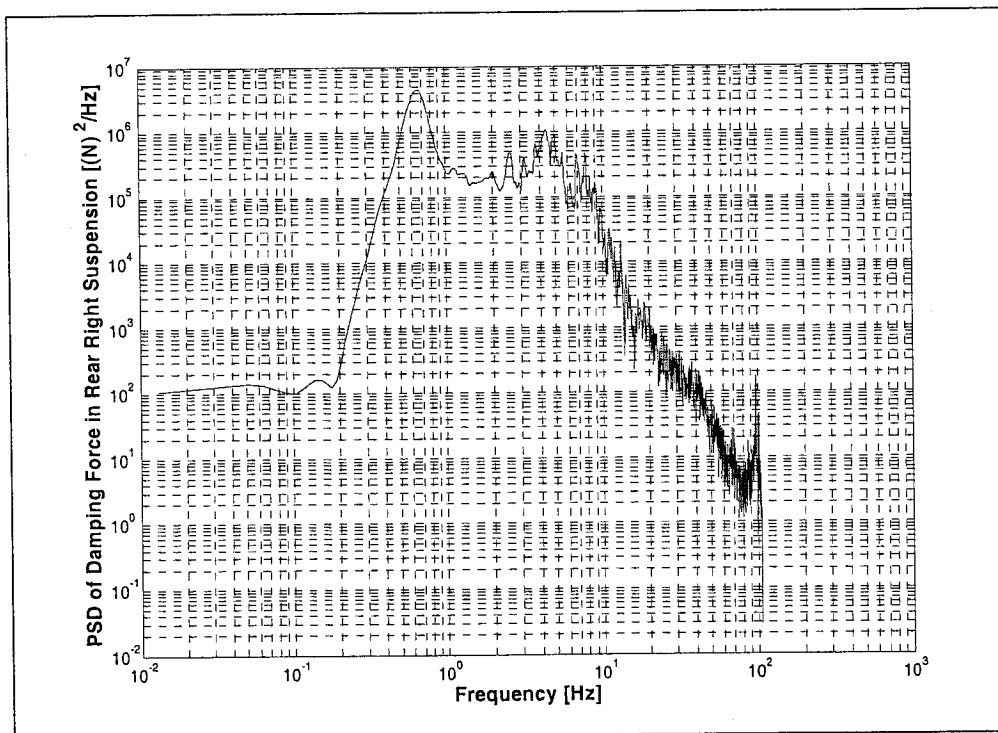


Fig. 3.70 PSD of damping force in rear right suspension.

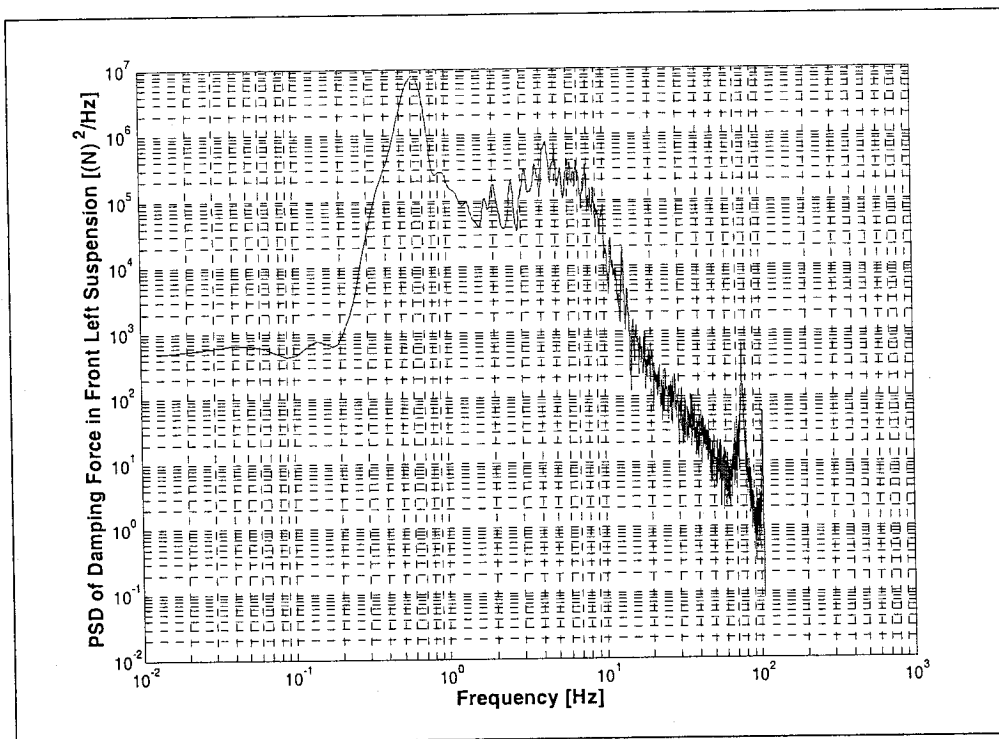


Fig. 3.71 PSD of damping force in front left suspension.

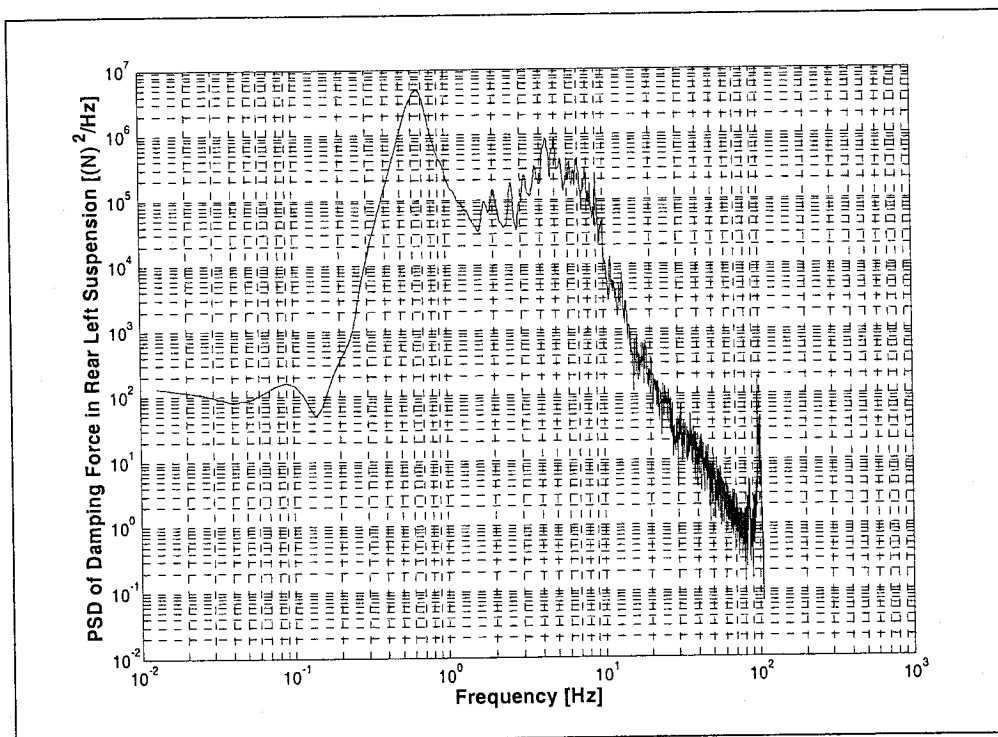


Fig. 3.72 PSD of damping force in rear left suspension.

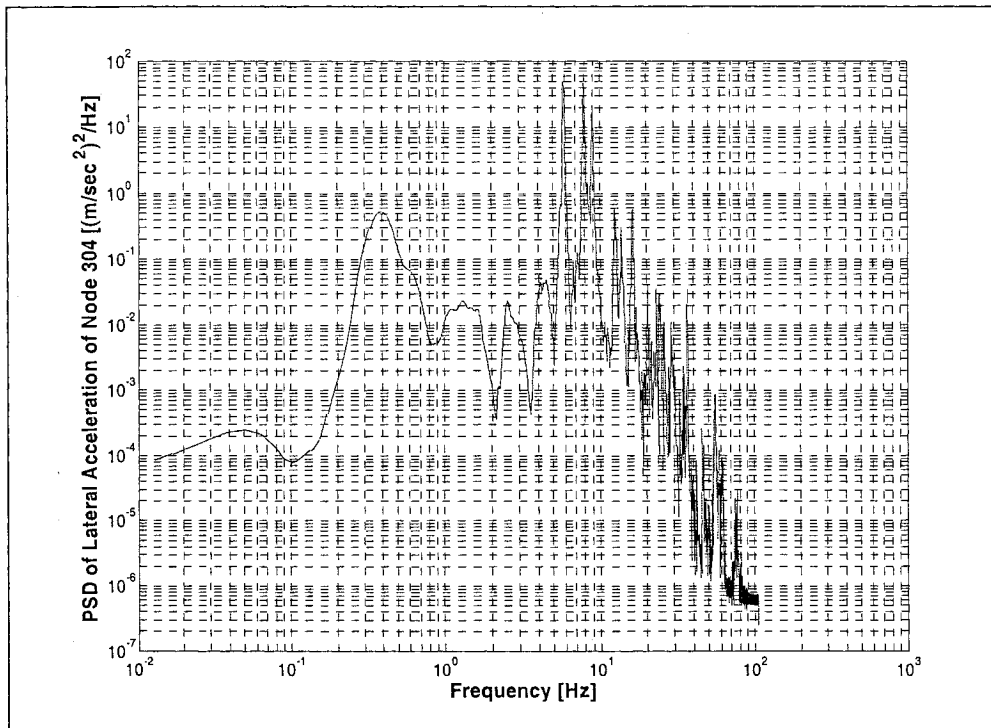


Fig. 3.73 PSD of lateral acceleration of node No. 304.

CHAPTER 4

HANDLING AND LONGITUDINAL ANALYSIS OF VEHICLE

4.1 INTRODUCTION

The handling characteristics of a road vehicle usually indicate its response to steering commands and to environmental inputs, such as thrust of wind and road disturbances. The control of the direction of motion of the vehicle and its ability to stabilize its direction of motion against external disturbances are two basic issues in vehicle handling. On the other hand, longitudinal characteristics of a road vehicle indicate its capability to accelerate, decelerate, and negotiate grades in a straight line motion [8]. Different types of handling and longitudinal analyses, such as pure cornering (steering input only), combined cornering and braking, pure symmetric or asymmetric braking, μ -split test (cornering on asymmetric frictional road surface), and wheel locking, are performed for this purpose in practice. In this chapter, pure cornering and combined cornering and braking analyses of the candidate bus model carried out using ANSYS have been presented. Since among other vehicle design and operational parameters like location of the center of gravity, vehicle's forward speed, tire properties have great influence on handling and longitudinal behavior of a vehicle, the capability of the presented finite element model of tire to represent the complex tire dynamic characteristics is investigated in both cases. It is important to note that longitudinal and/or lateral forces are generated between tires and road surface to keep the vehicle in dynamically equilibrium during its motion. Longitudinal tire forces, lateral tire forces and steering angle input on front wheels as external loads are applied to the bus model to carry out the analyses. In both cases, in order to calculate the longitudinal and lateral

forces, a proper four wheel mathematical model has been derived and simulated in MATLAB with the finite element highway bus model parameters and with the corresponding operational conditions. Moreover, in order to demonstrate the effectiveness and applicability of the large finite element model, comparison between elastic and rigid chassis performance is presented in this study for both types of analyses. The transient simulation of four wheel mathematical model in MATLAB is used to establish rigid body performance of the bus model. In pure cornering analysis, the longitudinal tire forces are neglected as constant forward speed is considered throughout the analysis, and the lateral tire forces are calculated using the *Elastic-Band Theory*. On the contrary, in combined cornering and braking analysis, the lateral tire forces are determined by the *friction ellipse*, instead of using the *cosine version of magic formula tire model* developed by Michelin [7]. The total weight of the bus and initial displacements arising from this total weight are involved in the analyses. In both types of analyses, the 3D FEM bus model developed for ride analysis is utilized with modifications to change in the tire model. In this case, the ground spring is removed, and the motion of the contact patches is constrained only in vertical direction so that the complete bus model can move and rotate freely in horizontal directions and about the vertical axis, respectively. Mode superposition method is chosen for both types of transient analyses in ANSYS to minimize the simulation time.

4.2 CORNERING ANALYSIS

Cornering analyses of the applied bus model are performed considering two cases - extensive and intensive trapezoidal steering angle inputs discussed in section 4.2.2. It is assumed that vehicle moves with constant forward speed 20 m/s. Tractive efforts or

longitudinal tire forces are thus neglected. Lateral tire forces are calculated using *Elastic-Band Theory*. For this purpose mathematical modeling of a proper four wheel vehicle has been derived at first. Simulation of the four wheel model has been carried out in MATLAB with finite element highway bus model parameters and with same steering angle input to find out the lateral tire forces. These lateral tire forces can be termed as pure lateral tire forces as tractive efforts have been neglected. Finally, considering that vehicle performs large rotations about the vertical axis during cornering, the lateral tire forces as external excitations have been applied carefully to the instantaneous position of the wheels of the finite element Highway-Bus model, as indicated in Fig. 4.1. The transient simulation of four wheel model in MATLAB is used to establish rigid body performance of the model during cornering. It must, however, be noted that the rigid body model was simplified and can not simulate all aspect of handling responses that can be performed by the 3D FEM model developed in this investigation. The assumptions made in developing the rigid body model are identified in the following subsection.

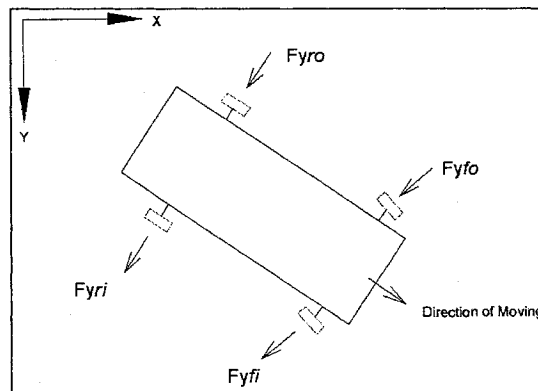


Fig. 4.1 Current position of the vehicle in turning.

4.2.1 Mathematical Modeling

The vehicle undergoes in a transient state between the application of steering input and the attainment of steady state motion. To examine the transient response, the

inertia properties of the vehicle is taken into consideration. During a turning maneuver, the vehicle is in translation as well as in rotation. To describe its motion, it is convenient to use a set of axes fixed to and moving with the vehicle body. With respect to the axes fixed to the body, the mass moments of inertia of the vehicle are constant, whereas with respect to the axes fixed to earth, the mass moments of inertia vary as the vehicle change its position. With reference to Fig. 4.2, let ox and oy be the longitudinal and lateral axes fixed to the vehicle body with origin at the center of gravity, and let V_x and V_y be the components of the velocity V of the center of gravity along the axes ox and oy , respectively, at time t . As the vehicle is in both translation and rotation during a turn, at time $t + \Delta t$, the direction and magnitude of the velocity of the center of gravity as well as the orientation of the longitudinal and lateral axes of the vehicle change, as shown in Fig. 4.2.

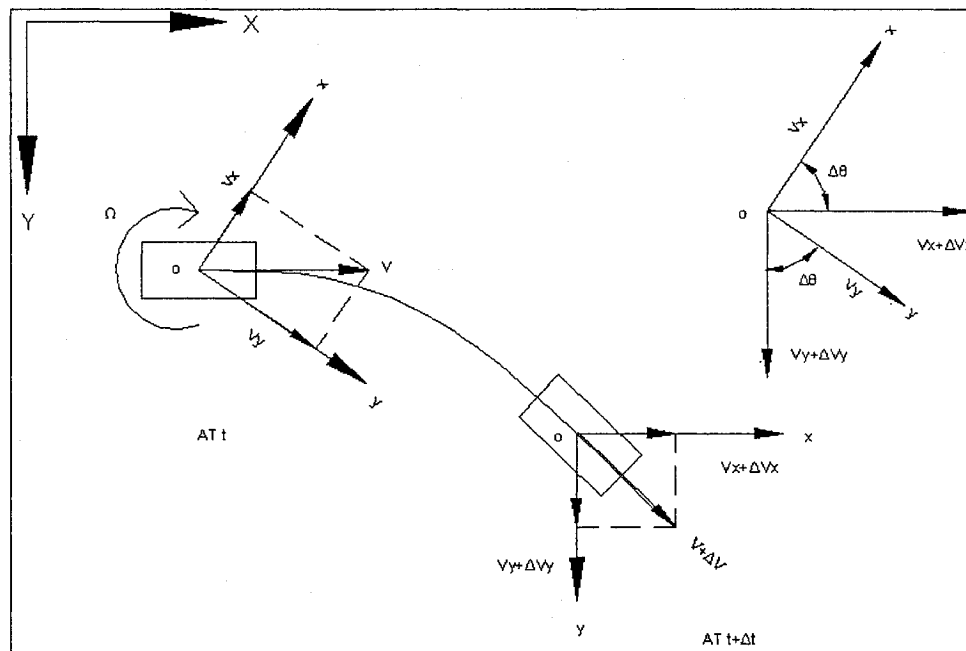


Fig. 4.2 Change of velocity component.

The change in velocities in each direction can now easily be expressed as [8]:

Change in Velocity along x -axis,

$$(V_x + \Delta V_x)\cos\Delta\theta - V_x - (V_y + \Delta V_y)\sin\Delta\theta$$

Change in velocity along y - axis,

$$(V_y + \Delta V_y)\cos\Delta\theta - V_y + (V_x + \Delta V_x)\sin\Delta\theta$$

For small angle, $\cos\Delta\theta \cong 1$ & $\sin\Delta\theta \cong \Delta\theta$. Moreover, neglecting $\Delta V_y \times \Delta\theta$ as small higher order term, change in velocity along x -axis simplifies to:

$$\Delta V_x - V_y \Delta\theta \tag{4.1}$$

Similarly, change in velocity along y -axis is:

$$\Delta V_y + V_x \Delta\theta \tag{4.2}$$

Differentiating (4.1) with respect to time, t , gives:

$$a_x = dV_x / dt - V_y d\theta / dt \tag{4.3}$$

Differentiating (4.2) with respect to time, t , gives:

$$a_y = dV_y / dt + V_x d\theta / dt \tag{4.4}$$

In order to derive the mathematical model of a four wheel vehicle, it is assumed that the vehicle body is symmetric about the longitudinal vertical plane, and that roll motion of the vehicle body is negligible. Referring to Fig. 4.3, for a vehicle having plane motion, the equations of motion with respect to the axes fixed to the vehicle body are given by:

Yaw equation of motion is obtained by taking the moment about C.G or z-axis (\curvearrowright + ve):

$$\begin{aligned}
 I_z \dot{\Omega} = & -(Fy_{ro} + Fy_{ri})c + Fx_{ro}t_r / 2 - Fx_{ri}t_r / 2 + Fx_{fo}Cos\delta_{fo}t_f / 2 - Fy_{fo}Sin\delta_{fo}t_f / 2 \\
 & - Fx_{fi}Cos\delta_{fi}t_f / 2 + Fy_{fi}Sin\delta_{fi}t_f / 2 + (Fx_{fi}Sin\delta_{fi} + Fy_{fi}Cos\delta_{fi})b + (Fx_{fo}Sin\delta_{fo} \\
 & + Fy_{fo}Cos\delta_{fo})b \\
 \Rightarrow \dot{\Omega} = & \frac{1}{I_z} [-(Fy_{ro} + Fy_{ri})c + (Fx_{ro} - Fx_{ri})t_r / 2 + (Fx_{fo}Cos\delta_{fo} - Fx_{fi}Cos\delta_{fi} + Fy_{fi}Sin\delta_{fi} \\
 & - Fy_{fo}Sin\delta_{fo})t_f / 2 + (Fx_{fi}Sin\delta_{fi} + Fx_{fo}Sin\delta_{fo} + Fy_{fi}Cos\delta_{fi} + Fy_{fo}Cos\delta_{fo})b] \quad (4.7)
 \end{aligned}$$

where: Fx_{fi} is the longitudinal force on the front-inner tire,

Fx_{fo} is the longitudinal force on the front-outer tire,

Fx_{ri} is the longitudinal force on the rear-inner tire,

Fx_{ro} is the longitudinal force on the rear-outer tire,

Fy_{fi} is the lateral tire force on the front-inner tire,

Fy_{fo} is the lateral tire force on the front-outer tire,

Fy_{ri} is the lateral tire force on the rear-inner tire,

Fy_{ro} is the lateral tire force on the rear-outer tire,

I_z is the mass moment of inertia of the vehicle about the z-axis,

Ω is the angular or yaw velocity about the z-axis,

δ_{fi} is the steering angle, δ_f distribution on front-inner wheel,

δ_{fo} is the steering angle, δ_f distribution on front-outer wheel,

t_f is the front track width,

t_r is the rear track width,

b is the distance from front tires to center of gravity,

c is the distance from rear tires to center of gravity.

Using the assumption of small average steering angle, δ_f , the following terms in the Eqs. 4.5-4.7 can be written as follows:

$$\text{Sin}\delta_{fi} \cong \delta_{fi}, \text{Cos}\delta_{fi} \cong 1, \text{Sin}\delta_{fo} \cong \delta_{fo} \text{ and } \text{Cos}\delta_{fo} \cong 1$$

Hence, the equations of motions of the vehicle (Eqs. 4.5-4.7) becomes:

$$\dot{V}_x = V_y \Omega + \frac{1}{m} (Fx_{fo} + Fx_{fi} + Fx_{ro} + Fx_{ri} - Fy_{fo} \delta_{fo} - Fy_{fi} \delta_{fi}) \quad (4.8)$$

$$\dot{V}_y = -V_x \Omega + \frac{1}{m} (Fy_{fo} + Fy_{fi} + Fx_{fo} \delta_{fo} + Fx_{fi} \delta_{fi} + Fy_{ro} + Fy_{ri}) \quad (4.9)$$

$$\begin{aligned} \dot{\Omega} = \frac{1}{I_z} [& -(Fy_{ro} + Fy_{ri})c + (Fx_{ro} - Fx_{ri})t_r / 2 + (Fx_{fo} - Fx_{fi} + Fy_{fi} \delta_{fi} - Fy_{fo} \delta_{fo})t_f / 2 \\ & + (Fx_{fi} \delta_{fi} + Fx_{fo} \delta_{fo} + Fy_{fi} + Fy_{fo})b] \end{aligned} \quad (4.10)$$

The trajectory of the vehicle can be determined by solving the following differential equations along with the Eqs. 4.8-4.10:

$$\dot{X}_t = V_x \text{Cos}(\psi) - V_y \text{Sin}(\psi) \quad (4.11)$$

$$\dot{Y}_t = V_x \text{Sin}(\psi) + V_y \text{Cos}(\psi) \quad (4.12)$$

$$\dot{\psi} = \Omega \quad (4.13)$$

For a given steering angle δ_f , the steer angles of inner and outer wheels, δ_{fi} and δ_{fo} are based on Ackermann steering geometry. These angles can be computed as a function of δ_f as follows. Using the geometry shown in Fig. 4.4, for a radius of curvature R :

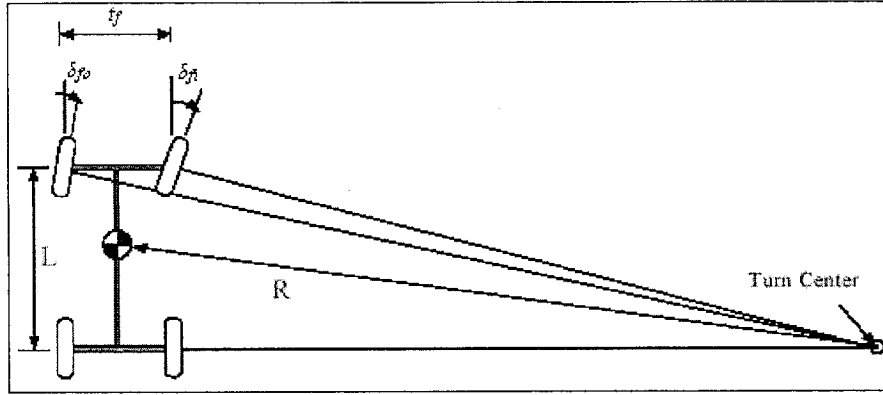


Fig. 4.4 Steering Geometry.

$$\delta_{fi} = \frac{L}{R - \frac{t_f}{2}} \quad (4.14)$$

$$\delta_{fo} = \frac{L}{R + \frac{t_f}{2}}; \text{ where: } L \text{ is the wheel base and } t_f \text{ is the front track width.} \quad (4.15)$$

Assuming $\frac{t_f}{2} \ll R$, average steering angle, $\delta_f = \frac{(\delta_{fi} + \delta_{fo})}{2} = \frac{L}{R} \Rightarrow R = \frac{L}{\delta_f}$

Substituting for R in the Eqs. 4.14 and 4.15, δ_{fi} and δ_{fo} can be expressed in terms of steering angle:

$$\delta_{fi} = \frac{2L\delta_f}{2L - t_f \times \delta_f} \quad (4.16)$$

$$\delta_{fo} = \frac{2L\delta_f}{2L + t_f \times \delta_f} \quad (4.17)$$

For constant speed turning, the longitudinal equation (Eq. 4.8) as well as F_x term in the lateral and yaw equations (Eq. 4.9 and 4.10) can be dropped to yield a 2 DOF rigid body handling model. The tire lateral forces, F_y can be further expressed by cornering stiffness and slip angle:

$$F_y = C_\alpha \alpha; \text{ where: } C_\alpha \text{ is the cornering stiffness of tire,}$$

α is the slip angle of tire.

Since two tires on each side of rear axle are considered in the applied finite element bus model, the lateral tire forces in the Eqs. 4.9-4.10 can be written as follows:

$$Fy_{fi} = C_{afi} \alpha_{fi} \quad (4.18)$$

$$Fy_{fo} = C_{afo} \alpha_{fo} \quad (4.19)$$

$$Fy_{ri} = 2C_{ari} \alpha_{ri} \quad (4.20)$$

$$Fy_{ro} = 2C_{aro} \alpha_{ro} \quad (4.21)$$

A number of factors affect the cornering stiffness, C_a of pneumatic tires. The normal load on the tire strongly influences the cornering stiffness and the relation between them is nonlinear as shown in Fig. 2.12. During turning, lateral load shift occurs from inner side to outer side of the vehicle owing to the lateral acceleration. As a result, the normal load on the outer tires increases while that on the inner tires decreases in turning. In order to calculate the cornering stiffness, C_a of inner and outer tires with respect to the instantaneous normal load on the corresponding tires, the following empirical relation constructed from the curve fitting of experimental data as shown in Fig. 2.12 can be used:

$$C_a = 1e^{-09} N^3 - 0.0003 N^2 + 16.707 N$$

In the above equation, N represents instantaneous normal load on a tire. Thus, it gives:

$$C_{afi} = 1e^{-09} N_{fi}^3 - 0.0003 N_{fi}^2 + 16.707 N_{fi} \quad (4.22)$$

$$C_{afo} = 1e^{-09} N_{fo}^3 - 0.0003 N_{fo}^2 + 16.707 N_{fo} \quad (4.23)$$

$$C_{ari} = 1e^{-09} (N_{ri}/2)^3 - 0.0003 (N_{ri}/2)^2 + 16.707 (N_{ri}/2) \quad (4.24)$$

$$C_{aro} = 1e^{-09} (N_{ro}/2)^3 - 0.0003 (N_{ro}/2)^2 + 16.707 (N_{ro}/2) \quad (4.25)$$

In the Eqs. 4.22-4.25, N_{fi} , N_{fo} , N_{ri} and N_{ro} indicate instantaneous normal load on the front-

inner tire, the front-outer tire, the rear-inner tires and the rear-outer tires, respectively. Referring to Fig. 4.5(a) and 4.5(b), the instantaneous normal loads on tires N_{fi} , N_{fo} , N_{ri} and N_{ro} are calculated by the following relations obtained by taking moment about B, A, D and C, respectively:

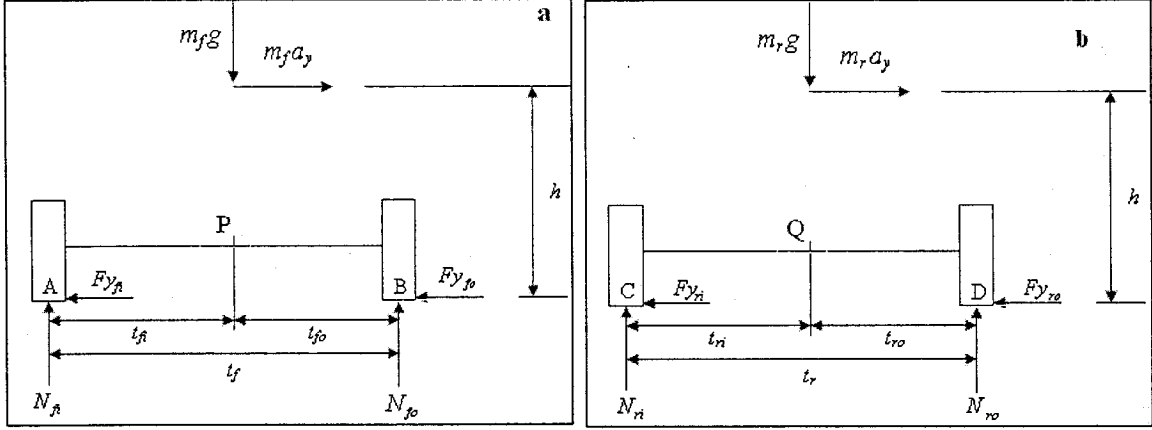


Fig. 4.5 Normal load on front tires (a) and rear tires (b).

$$N_{fi} = n_{fi} - \frac{m_f \times a_y \times h}{t_f}; \text{ where } n_{fi} = \text{static load on front - inner tire} = \frac{m_f g t_{fo}}{t_f}, N_{fi} \geq 0 \quad (4.26)$$

$$N_{fo} = n_{fo} + \frac{m_f \times a_y \times h}{t_f}; \text{ where } n_{fo} = \text{static load on front - outer tire} = \frac{m_f g t_{fi}}{t_f}, N_{fo} \leq m_f g \quad (4.27)$$

$$N_{ri} = n_{ri} - \frac{m_r \times a_y \times h}{t_r}; \text{ where } n_{ri} = \text{static load on rear - inner tire} = \frac{m_r g t_{ro}}{t_r}, N_{ri} \geq 0 \quad (4.28)$$

$$N_{ro} = n_{ro} + \frac{m_r \times a_y \times h}{t_r}; \text{ where } n_{ro} = \text{static load on rear - outer tire} = \frac{m_r g t_{ri}}{t_r}, N_{ro} \leq m_r g \quad (4.29)$$

The values of n_{fi} , n_{fo} , n_{ri} and n_{ro} can be determined by the static analysis of the vehicle due to the gravitational weight. m_f and m_r represents the front and rear wheel loads, and those are calculated by the following relations:

$$m_f = \frac{m \times c}{b + c} \quad (4.30)$$

$$m_r = \frac{m \times b}{b + c}; \text{ where } m = \text{gross vehicle mass.} \quad (4.31)$$

In the Eqs. 4.18-4.21, α_{fi} , α_{fo} , α_{ri} and α_{ro} indicate slip angle of front-inner tire, front outer tire, rear-inner tires and rear-outer tires, respectively. Referring to the velocity diagram of the vehicle as shown in Fig. 4.6 and using the small steering angle assumptions, slip angles of different positioned tires can be defined in terms of the vehicle motion variables V_x , V_y and Ω as follows:

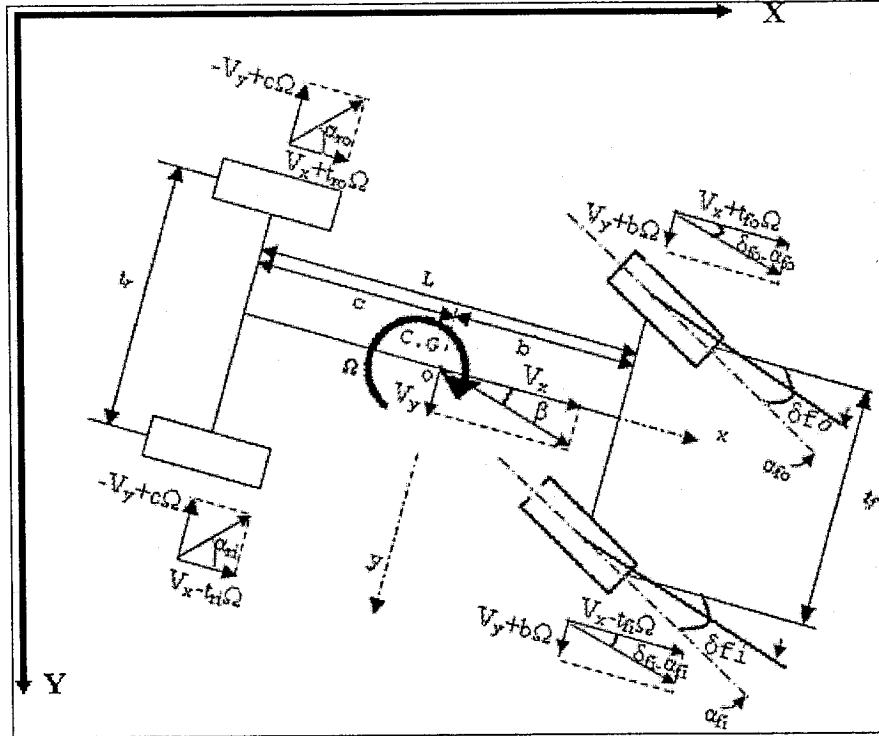


Fig. 4.6 Velocity diagram of vehicle.

$$\delta_{fi} - \alpha_{fi} = \frac{V_y + b \times \Omega}{V_x - t_{fi} \times \Omega} \quad (4.32)$$

$$\delta_{fo} - \alpha_{fo} = \frac{V_y + b \times \Omega}{V_x + t_{fo} \times \Omega} \quad (4.33)$$

$$\alpha_{ri} = \frac{-V_y + c \times \Omega}{V_x - t_{ri} \times \Omega} \quad (4.34)$$

$$\alpha_{ro} = \frac{-V_y + c \times \Omega}{V_x + t_{ro} \times \Omega} \quad (4.35)$$

4.2.2 Transient Response of the Bus with Rigid and Elastic Body

4.2.2.1 Extensive Cornering

Bus response under extensive cornering is obtained for a trapezoidal steering input (max. amplitude, 2.2 degree) that lasts for 5.5 sec is presented as average front wheel steer angle in Fig. 4.7(a). The corresponding steer angles for inner and outer front wheels are obtained on the basis of Eqs. 4.16 and 4.17, respectively and shown as Figs. 4.7(b) and (c). During turning or cornering, lateral inertial load is generated because of the time varying lateral acceleration, and the lateral inertial load causes lateral load shift from inner to outer wheels. As a result, the normal load on inner tires is decreased and that on outer tires is increased. The variations of the cornering stiffness on different positioned tires throughout the simulation of the designed bus with rigid body, illustrated in the Fig. 4.8, are caused by the nonlinear characteristics of the applied cornering stiffness with respect to the normal load (Fig. 2.12). Consequently, the variations of cornering forces developed on different positioned tires and ground interface throughout the simulation of the designed bus with rigid body are nonlinear as shown in Fig. 4.9. These cornering or lateral tire forces as external excitations have been applied carefully to the instantaneous position of the wheels (Fig. 4.1) to carry out the simulation of the candidate bus with elastic body in cornering. The lateral velocities, the lateral accelerations and the yaw velocities of the centers of gravity of the rigid and elastic bus models are given in Fig. 4.10, where the thin and thick lines refer to the bus with the elastic body and with the rigid body, respectively. As these results show, both the models

produce identical response for the center of gravity, where only small deviation is observed for lateral velocity.

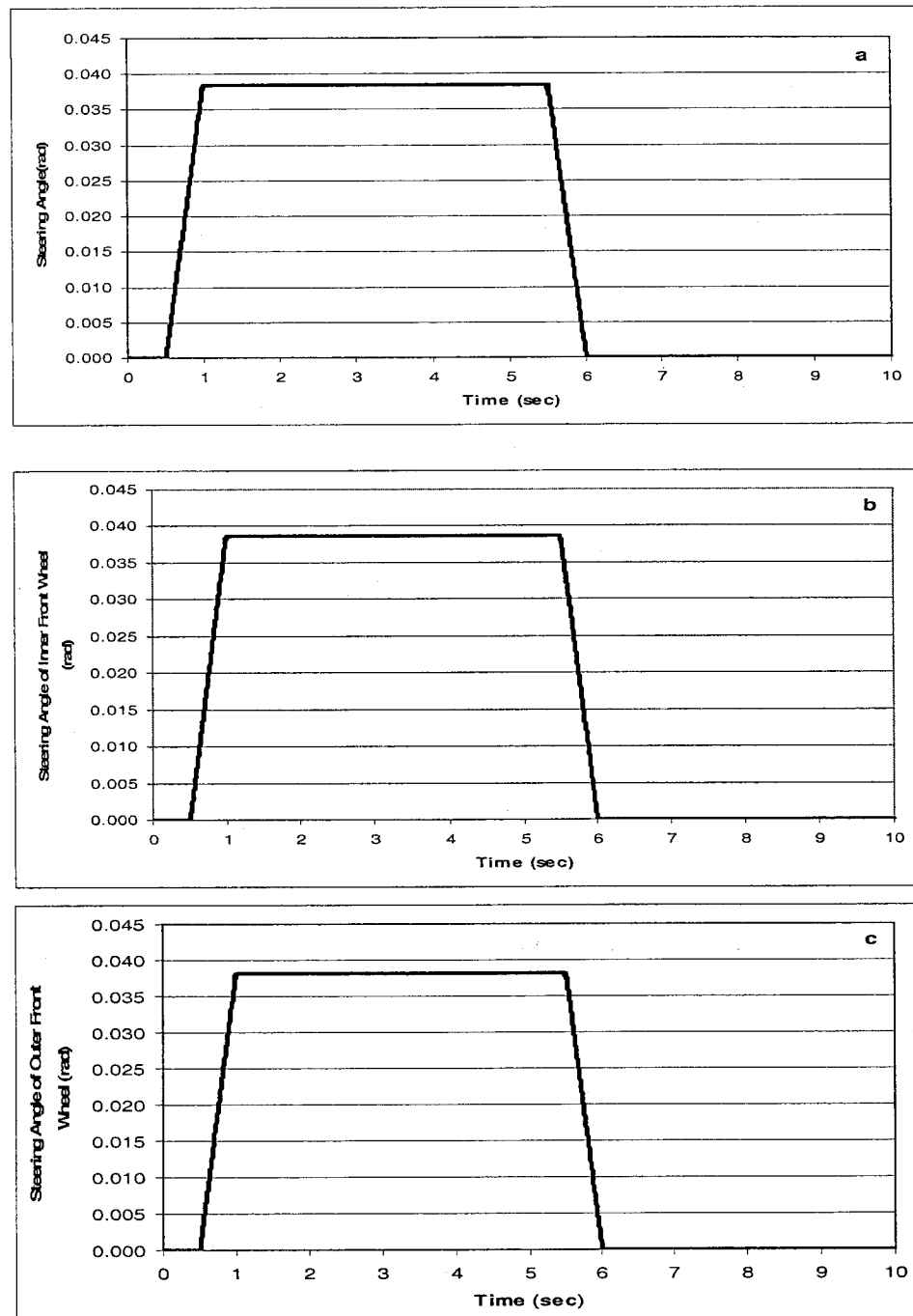


Fig. 4.7 Steering angle input (a), steering angle input distribution on inner front wheel (b) and on outer front wheel (c).

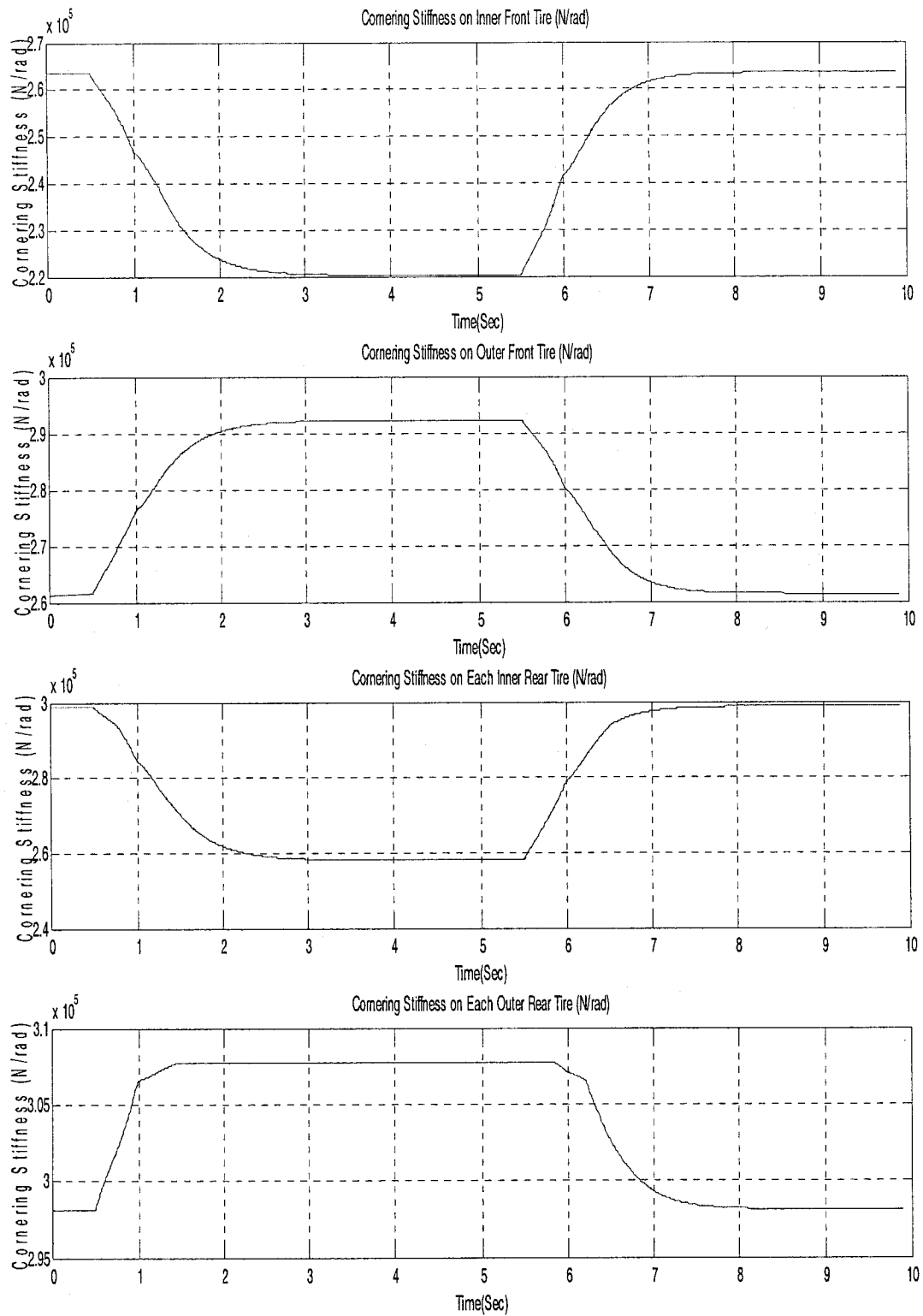


Fig. 4.8 Change in cornering stiffness during the maneuver.

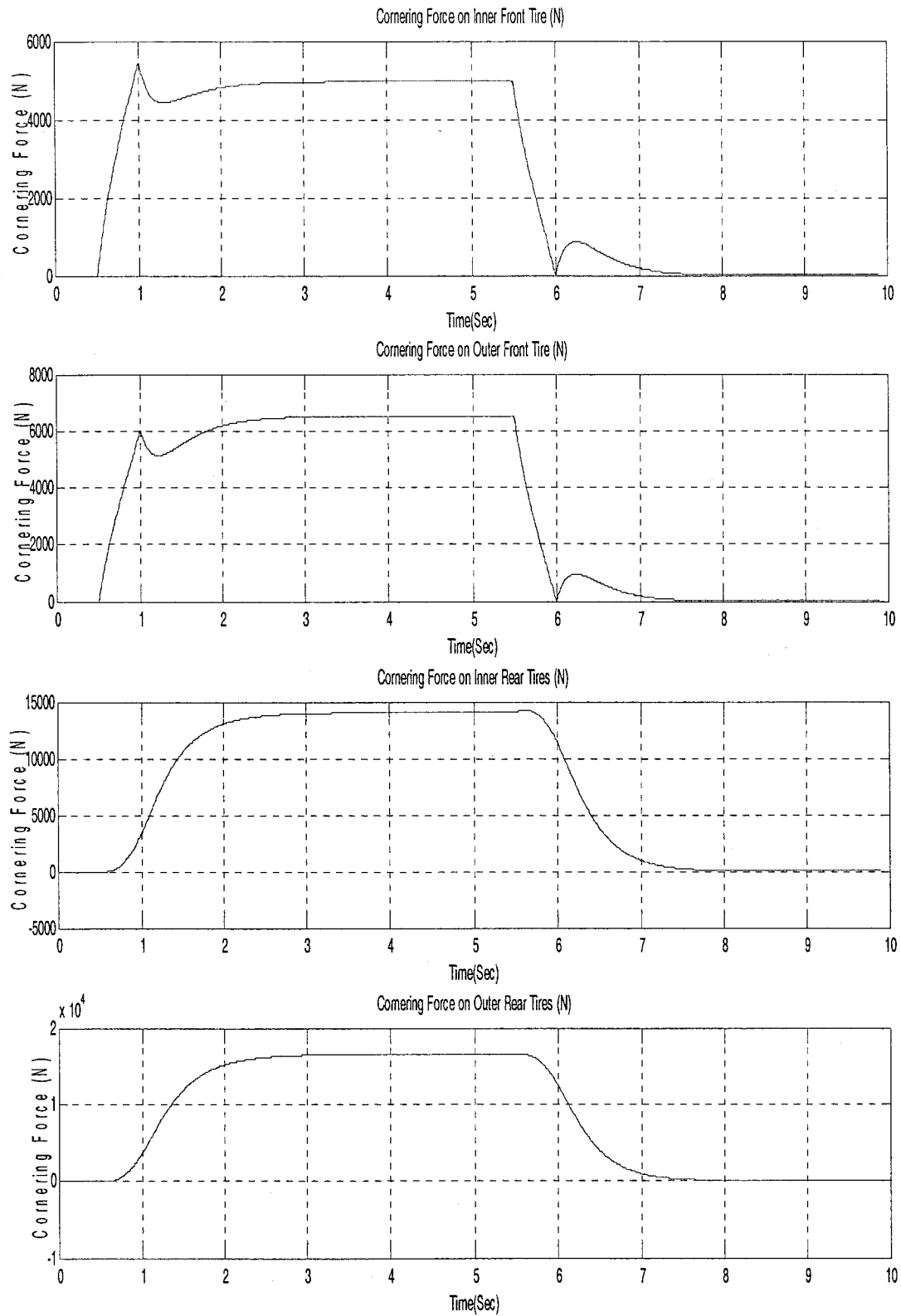


Fig. 4.9 Change of developed cornering forces at different tires.

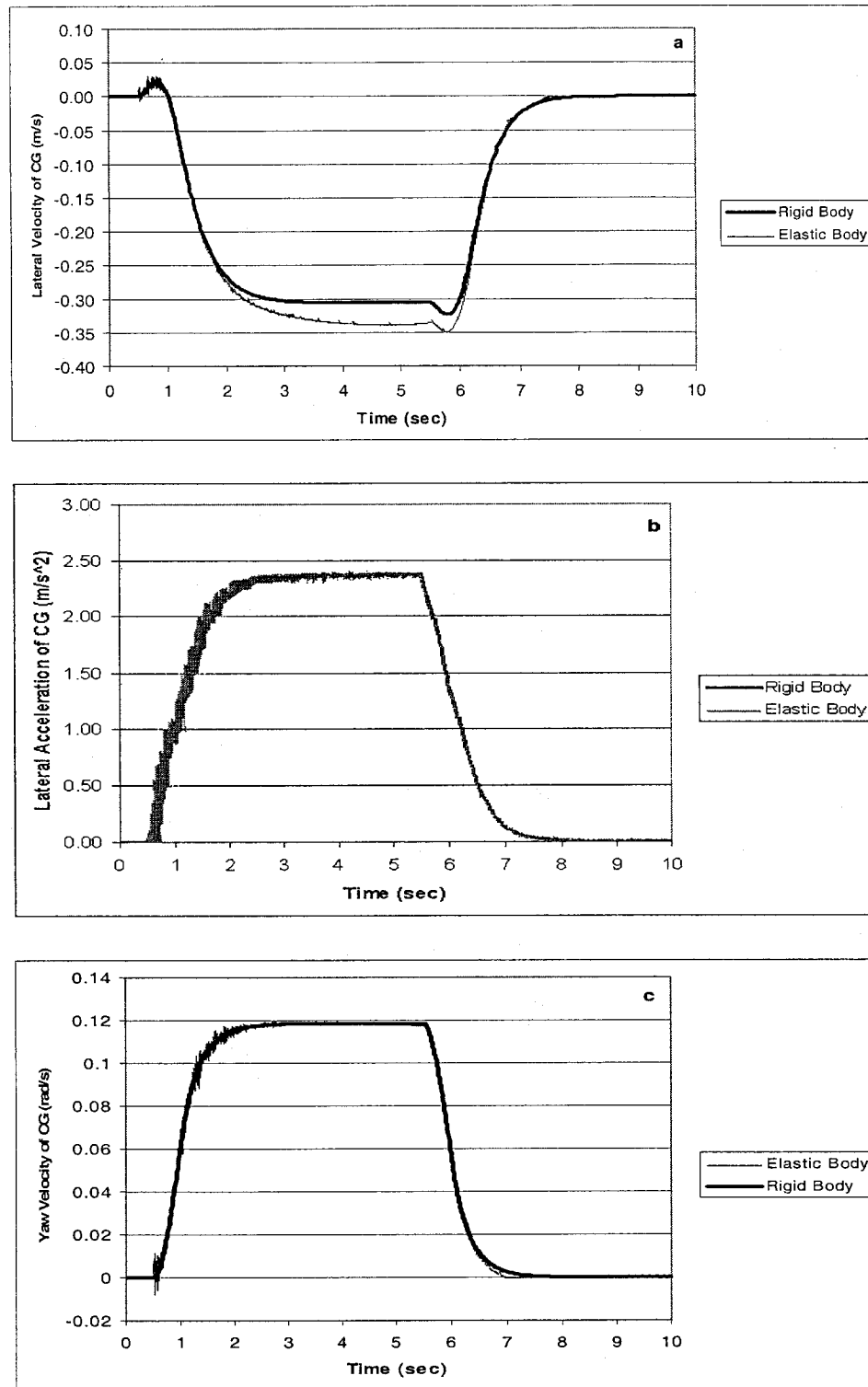


Fig. 4.10 Lateral velocity (a), lateral acceleration (b) and yaw velocity (c) of center of gravity.

During turning normal loads on the inner tires decrease, while those on the outer tires increase in both rigid body and elastic body bus models. However, there is significant deviation in the normal loads on the inner and outer tires of the front and rear axles between the bus models with rigid body and elastic body. The results for the front tires are shown in Fig. 4.11. These results show that for axle load over 23.5 KN, there is around 6 KN difference in the load shift predicted by the two models. The elastic model consistently show lower load shift. Similar trend in a similar study was reported in [1].

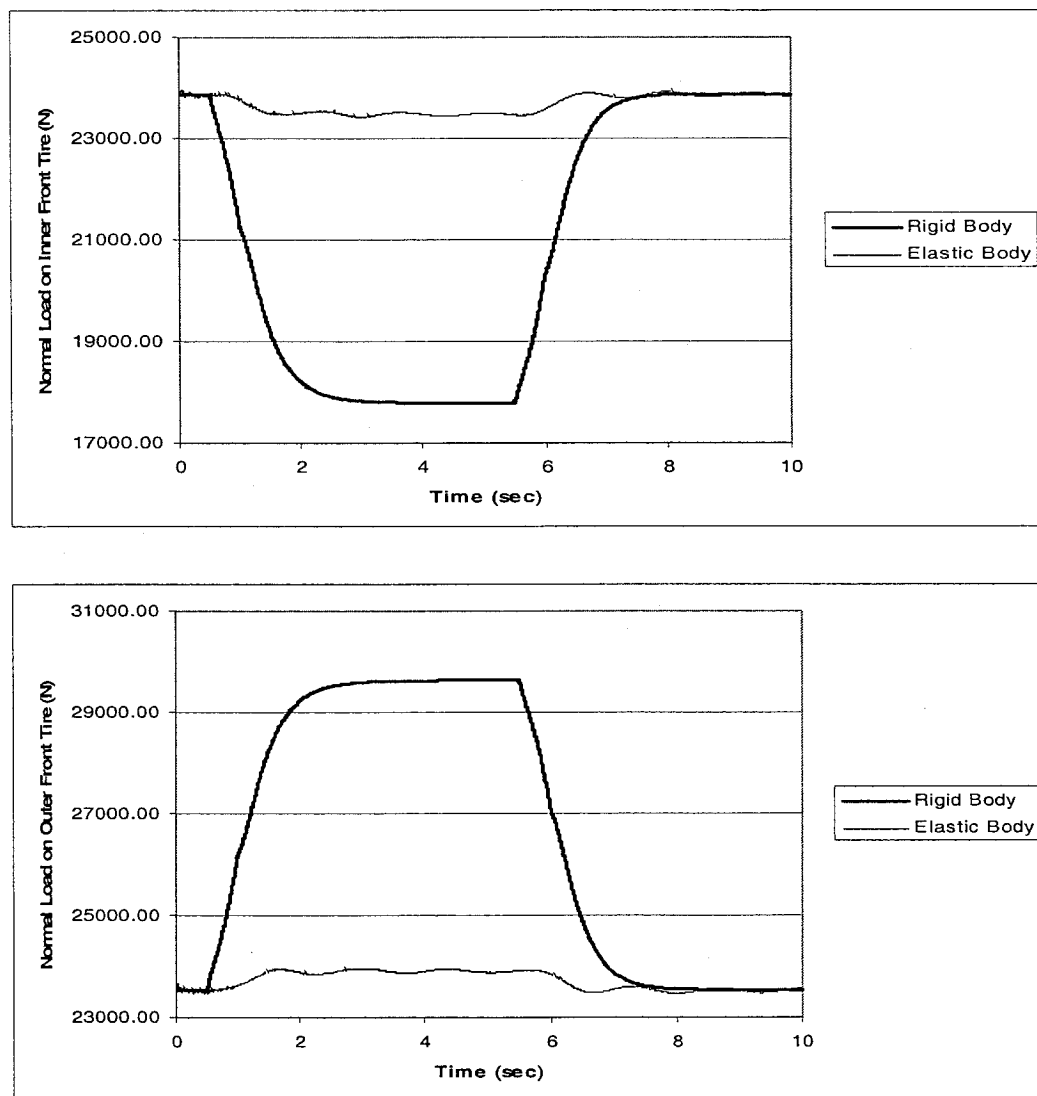


Fig. 4.11 Normal load distribution on inner and outer front tires.

This perhaps can be partially attributed to the distribution of mass over a wide area for the case of flexible model. Same results for the rear axles are shown in Fig. 4.12. In this case, for axle load over 63 KN, the rigid model tends to predict a load shift of 16 KN larger than that of the flexible model. In both cases (front and rear), the flexible model predicts 25 % less load shift than that of the rigid model. This, in turn, affects the tire characteristics under handling and corresponding responses.

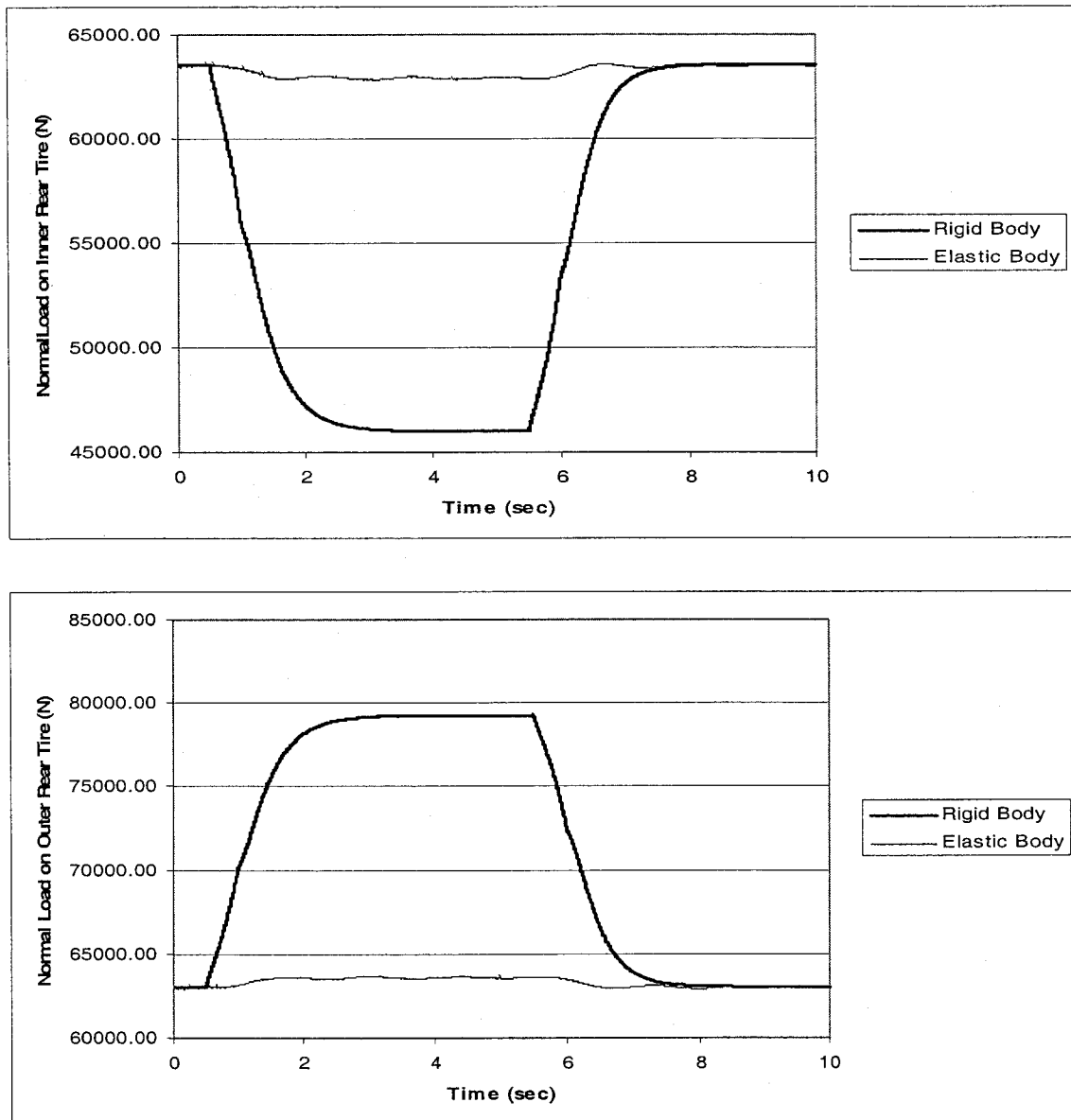


Fig. 4.12 Normal load distribution on inner and outer rear tires.

Another interesting result that can be evaluated is the development of slip angles at each wheel under the given steering input. For the rigid body model, slip angle is calculated on the basis of Eqs. 2.32-2.35 derived from velocity diagram of the bus. In the case of elastic body model, on the other hand, the slip angle is established based on Eq. 2.2, which is mostly dominated by the tire contact length parameter, l_t . In this case, the tire contact length value corresponding to instantaneous vertical load is considered throughout the simulation and is calculated using Eqs 2.3-2.5. It is important to note that as linear vertical tire stiffness is considered for the flexible body model, the magnitude of the tire contact lengths of different positioned tires vary linearly with respect to the vertical loads on corresponding tires. The slip angle time history for each tire of rigid and flexible bus model is presented in Figs. 4.13 and 4.14. As the results show, both results predict similar trend for slip angle for each wheel location. The results further reveal that the difference in the magnitude of slip angle for the outer tires is considerably more than that of the inner tires. The flexible body model exhibits larger values for outer tires and smaller values for inner tires compare to the rigid body model.

The trajectory of the bus models for the given input is finally presented in Fig. 4.15. Due to the difference in slip angle predicted by rigid and flexible model, it is expected that there will be a deviation in the path of the two models. It is important to note that as the results indicate in the Fig. 4.13, the average slip angle of front tires in case of rigid body model is smaller than that of flexible body. Consequently, the results show that the rigid body model predicts a tighter curve response when compared to that of the flexible model.

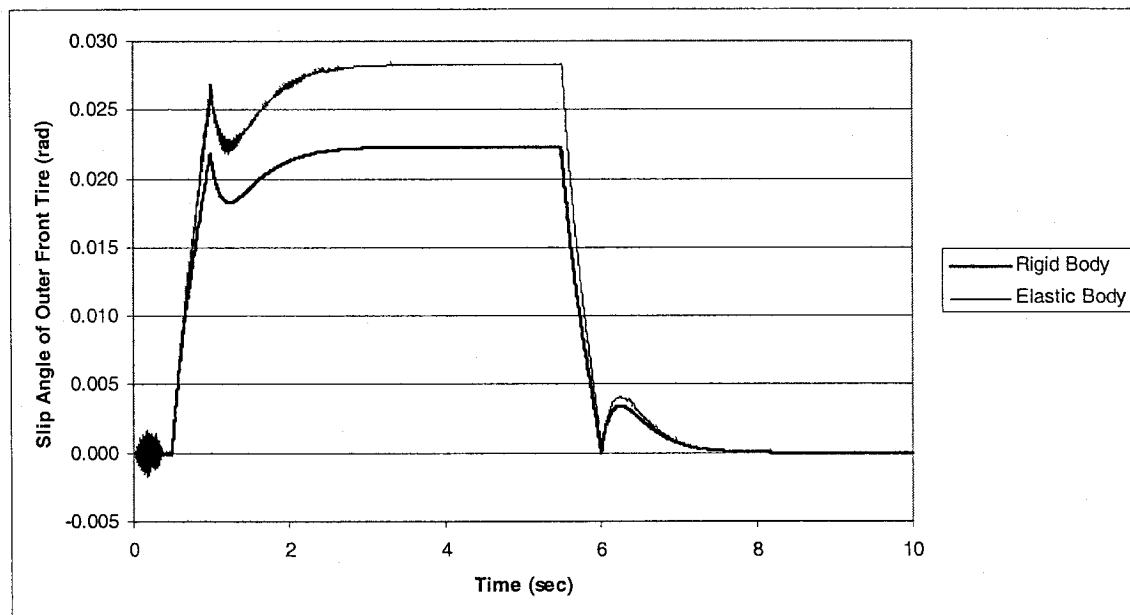
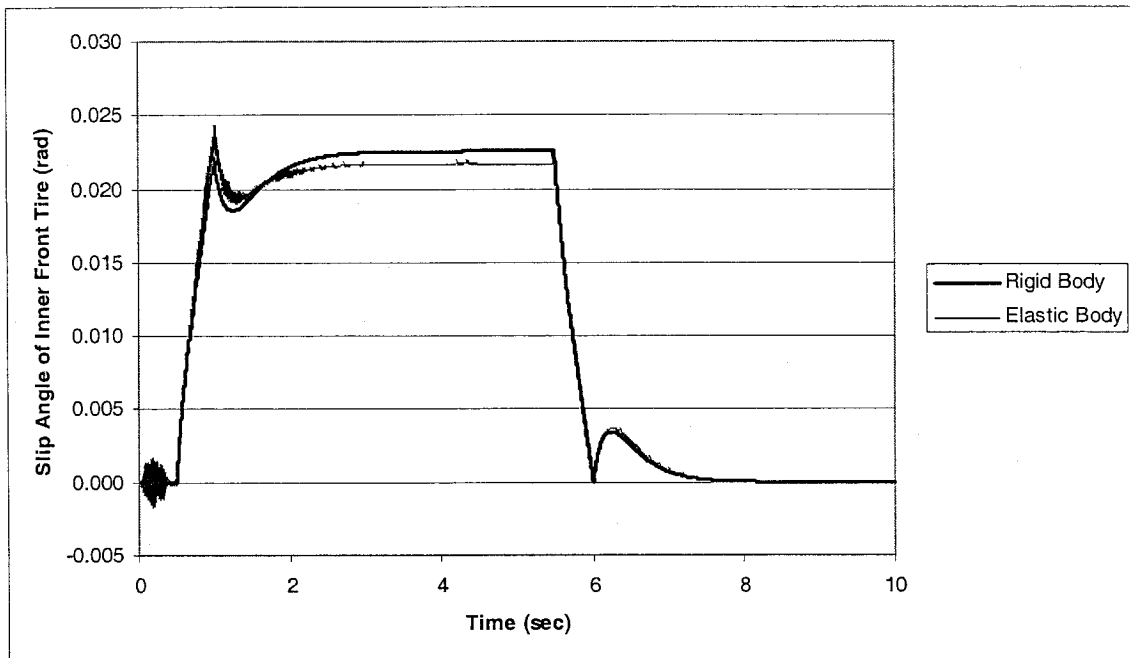


Fig. 4.13 Slip angle generation on inner and outer front tires.

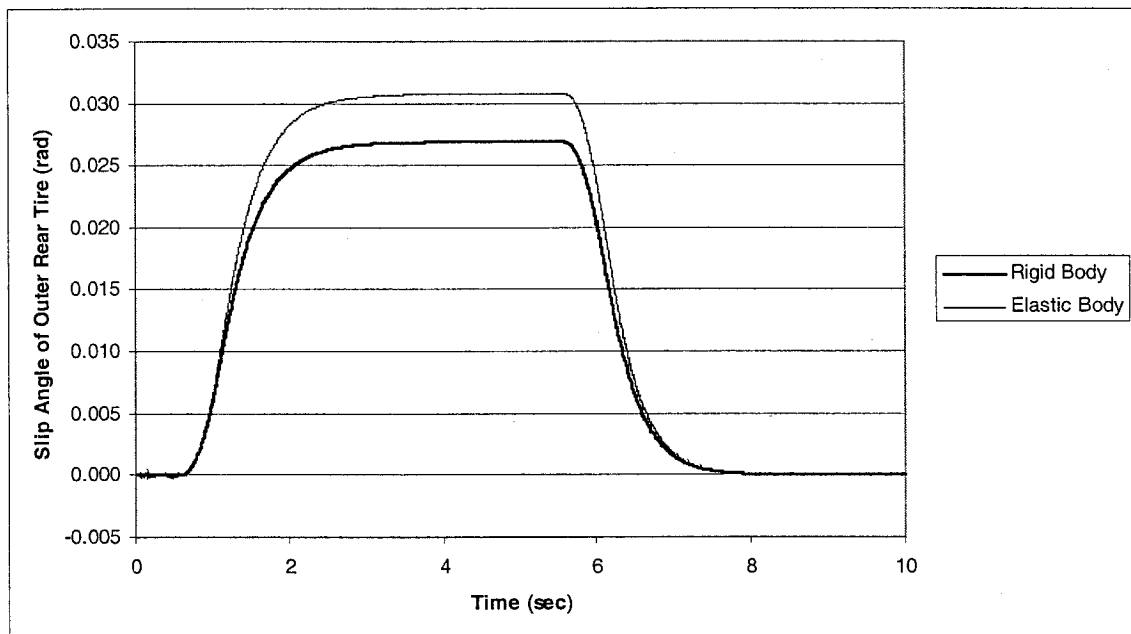
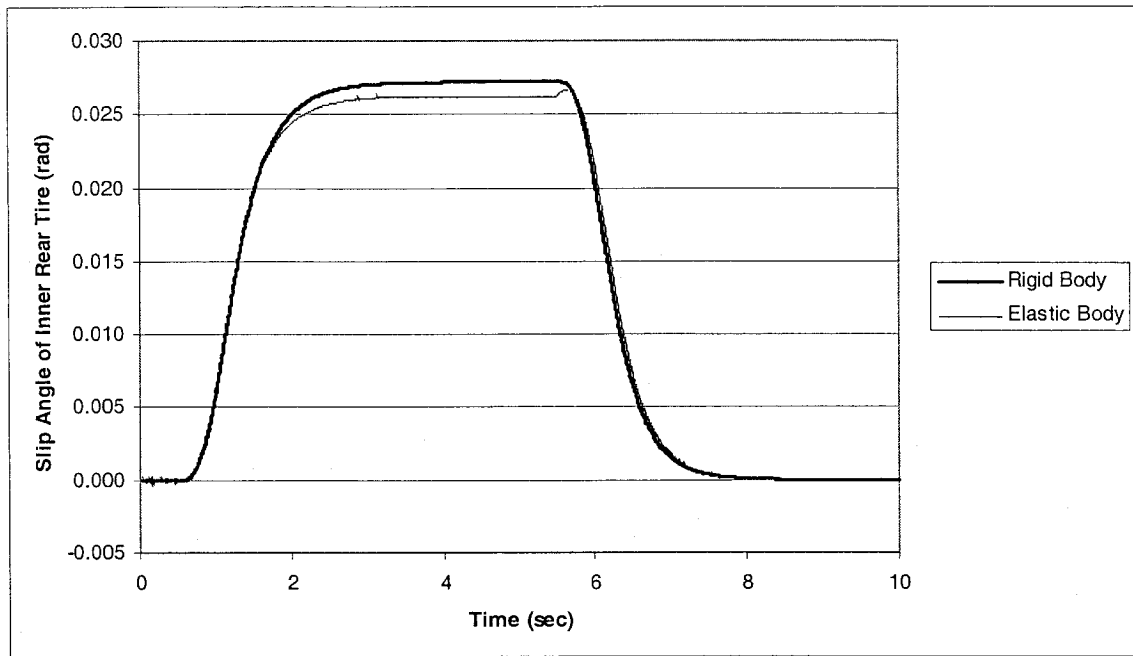


Fig. 4.14 Slip angle generation on inner and outer rear tires.

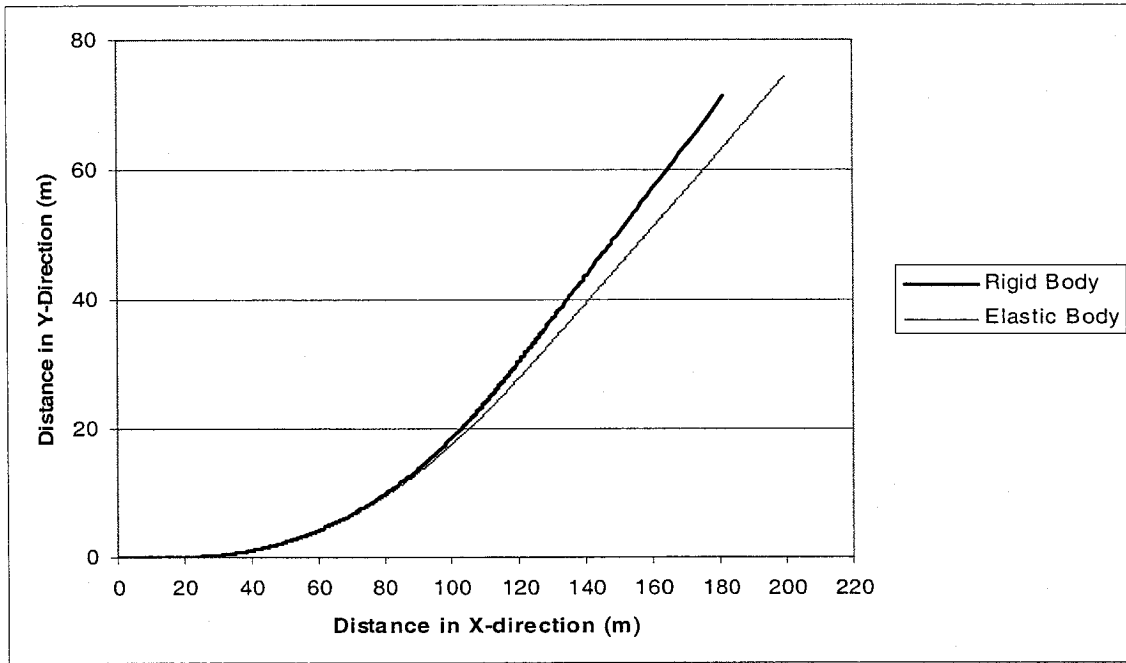


Fig. 4.15 Trajectory of the bus.

4.2.2.2 Intensive Cornering

The results presented above are responses to an extensive cornering at 72 km/hr subjected to average steer angle of 2.2 degree over period of 5.5 seconds. In order to examine the effect of more severe input the simulations were repeated for a steer angle input of 3.2 degree at the same forward velocity, and is referred to as intensive cornering. The average steer angle input along with the corresponding inner and outer wheel steer angles are shown in Fig. 4.16.

The time history of cornering stiffness for each tire during the simulation is presented in Fig. 4.17. These results show the expected increase in cornering stiffness of outer tires while that of inner tires reduces with the load shift. Comparison of these results with those obtained for extensive cornering (Fig. 4.8) clearly reveals same trend with noticeable difference at the end of 6 seconds when steering input reduces to zero. The smooth transition of dynamic stiffness value to the static value observed in the case

of extensive cornering is not present in the case of intensive cornering. In the case of intensive cornering, the stiffness value tends to oscillate and over shoot prior to returning to its static levels. This can be easily attributed to the roll dynamics (lateral oscillation) of the sprung mass.

The time history of cornering forces developed at the tire-road interface of each tire are shown in Fig. 4.18. The trends of cornering forces correspond well with the cornering stiffness trends obtained in Fig. 4.17. The lateral oscillation of the sprung mass is also evident in the lateral and yaw response plots for the intensive steering input as presented in Fig. 4.19. Fig. 4.19 also presents the simulated responses for the flexible bus model. As shown, both the models predict very comparable results both in trend and magnitude, where same deviation is noticed for the lateral velocity responses only.

The slip angles generated at each tire of the rigid body and flexible body models under the intensive cornering input are shown in Figs. 4.20 and 4.21. Similar to extensive cornering response, the slip angle response over the entire maneuver is very similar for both rigid and flexible body models. Again the noticeable deviation is only observed for outer wheels, where flexible body model exhibits larger values.

Finally, the trajectory of the bus models under the intensive steering input is shown in Fig. 4.22. The results obtained are very similar to those of under extensive steering input. As the results indicate in Fig. 4.20, the average slip angle of front tires in case of rigid body model is smaller than that of flexible body and the difference is little more compare to extensive cornering. Consequently, in this case, also the rigid body model tends to follow a tighter curve than that of flexible body model. Moreover, the

radius of turn for intensive cornering is smaller compare to extensive cornering for both models.

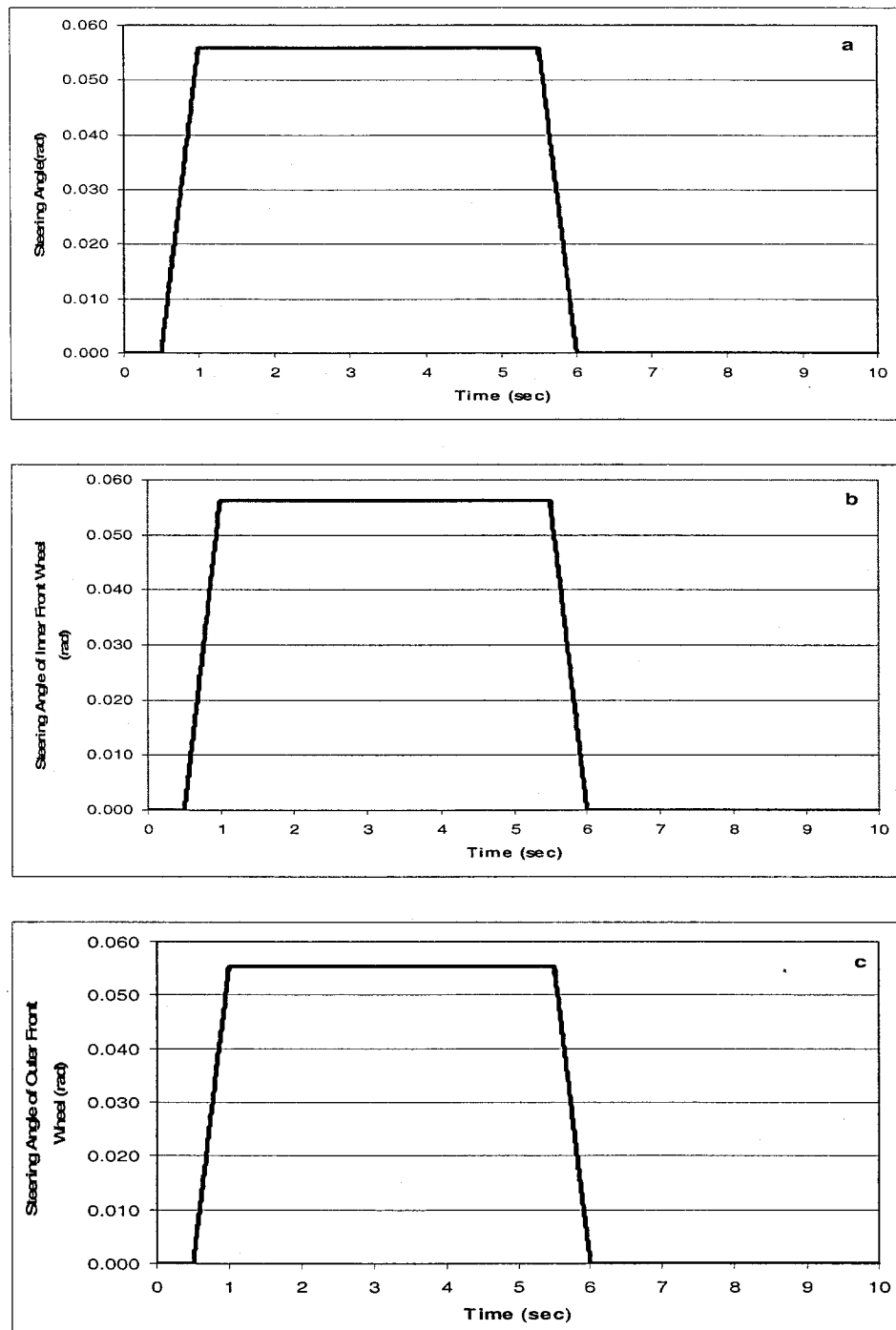


Fig. 4.16 Steering angle input (a), steering angle input distribution on inner front wheel (b) and on outer front wheel (c).

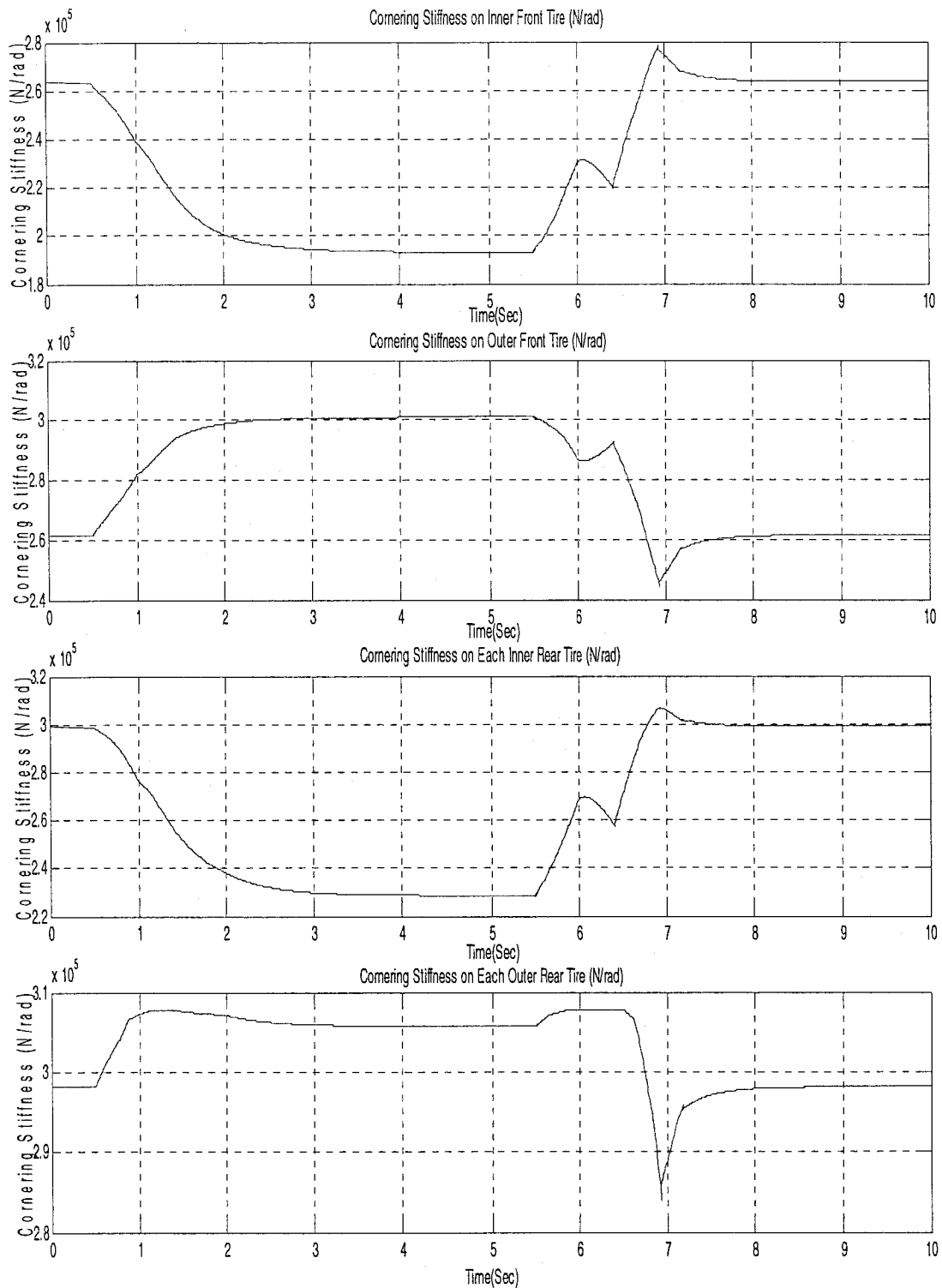


Fig. 4.17 Change of cornering stiffness at different tires.

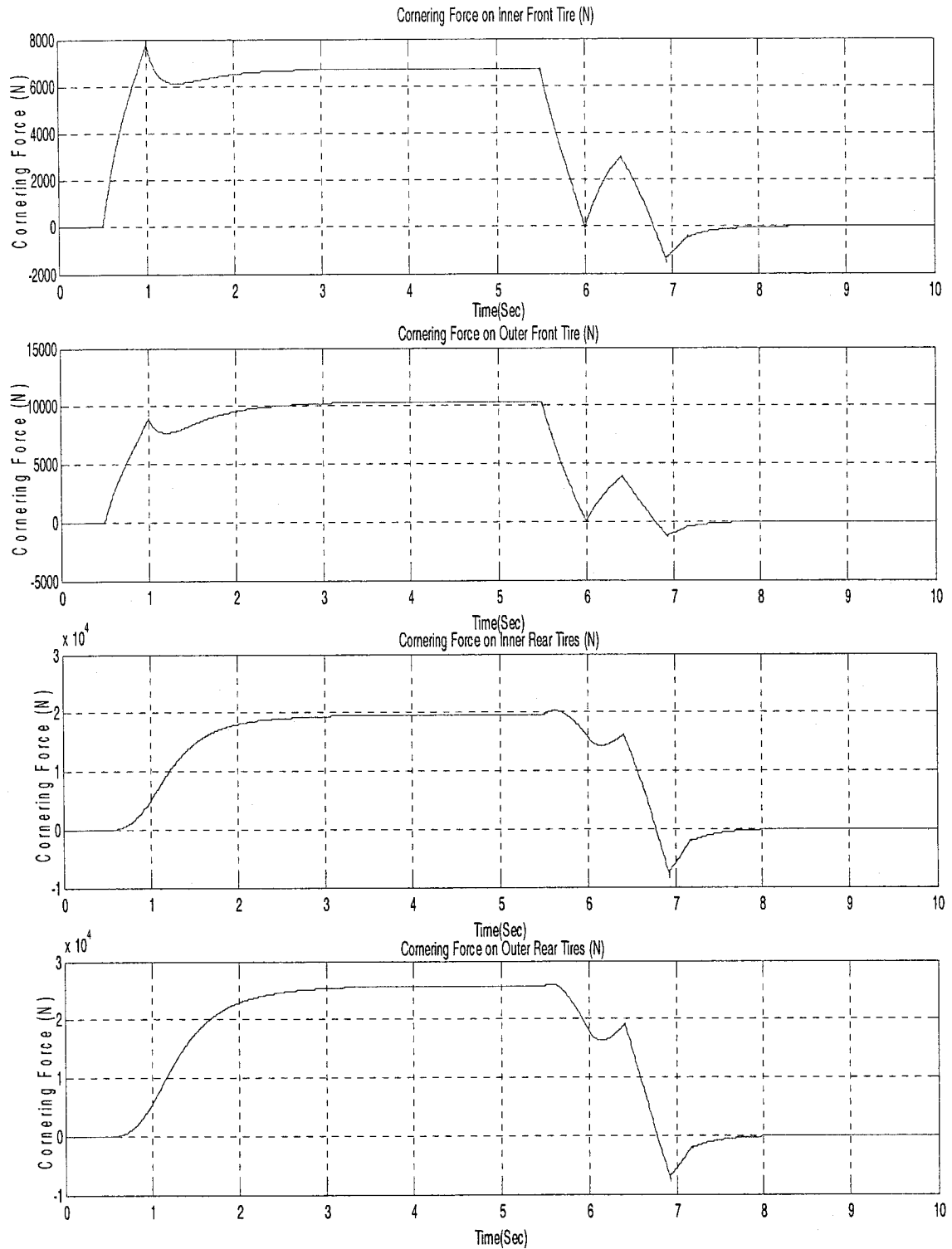


Fig. 4.18 Change of developed cornering force at different tires.

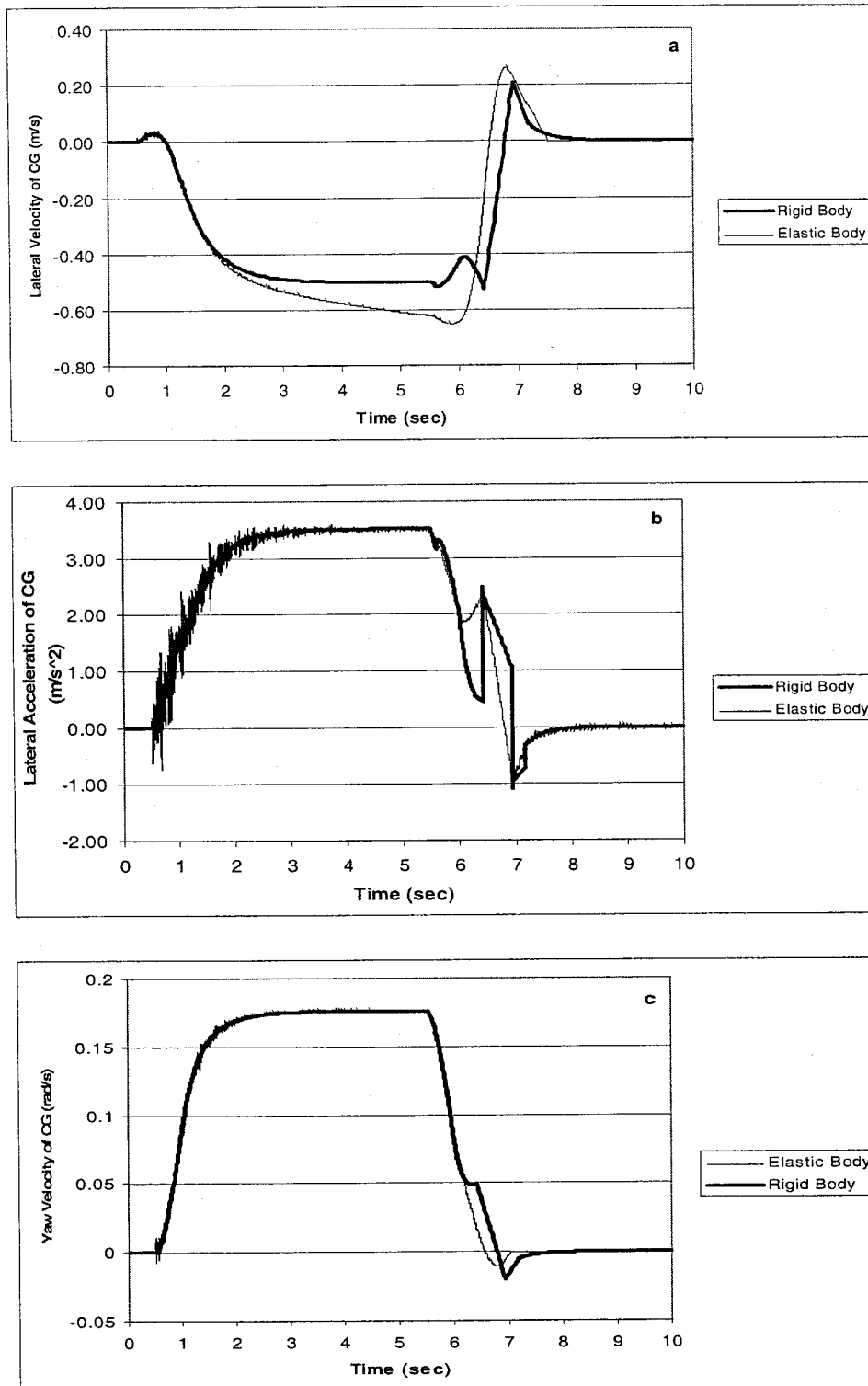


Fig. 4.19 Lateral velocity (a), lateral acceleration (b) and yaw velocity (c) of center of gravity.

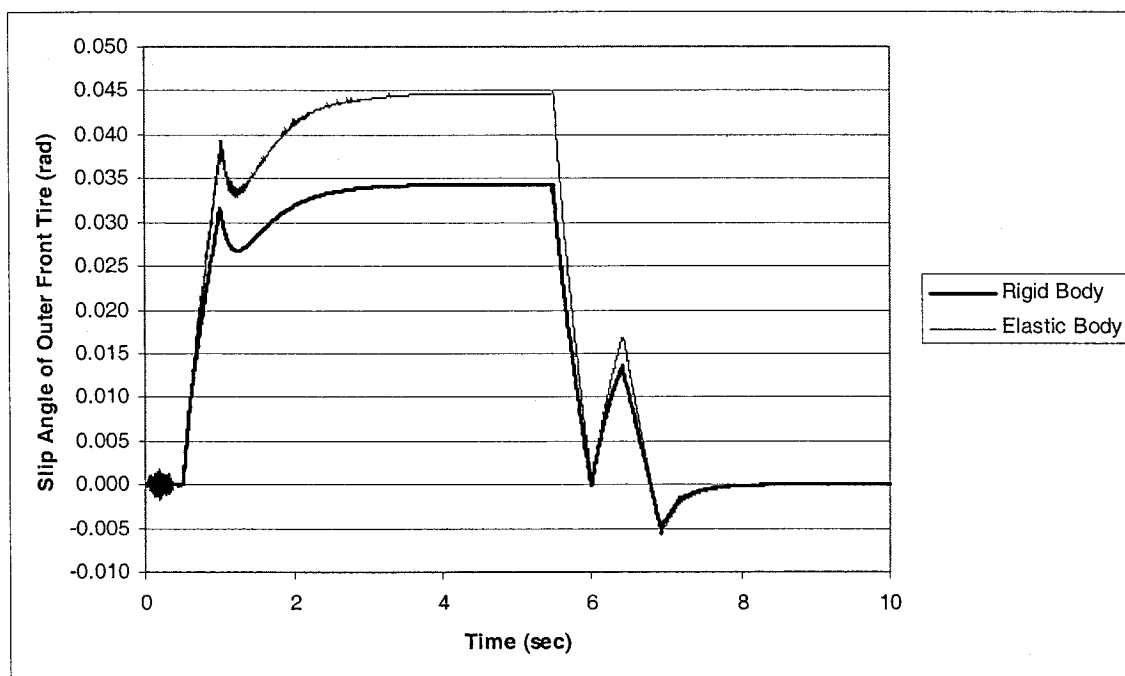
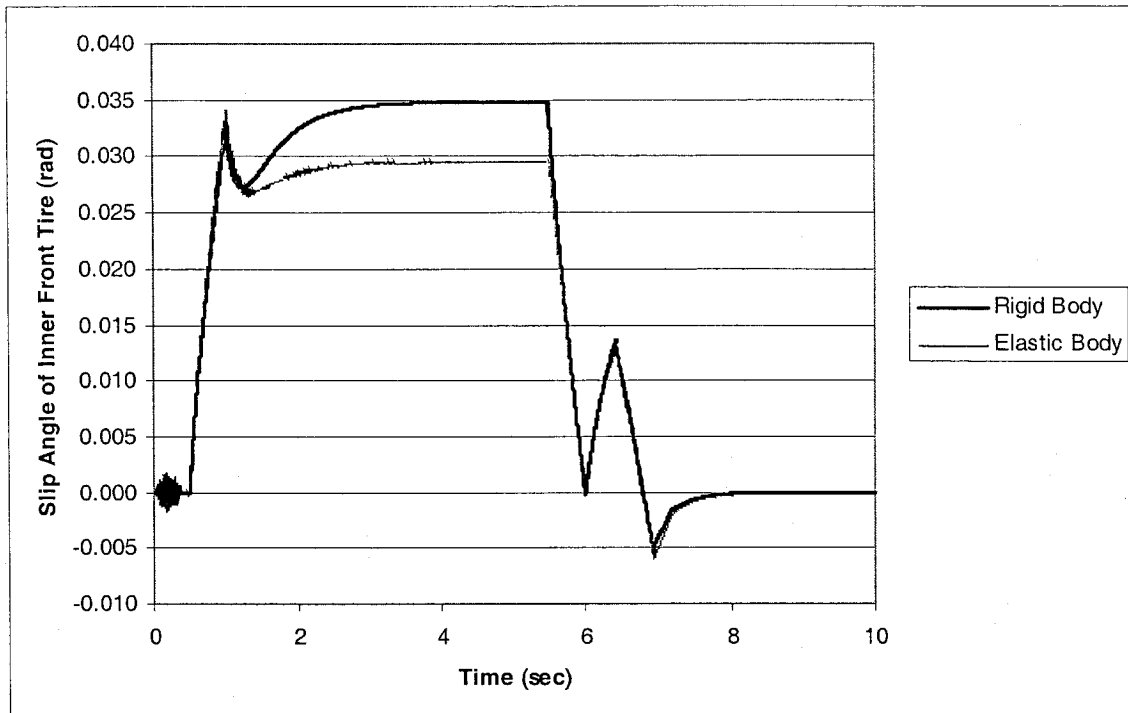


Fig. 4.20 Slip angle generation on inner and outer front tires.

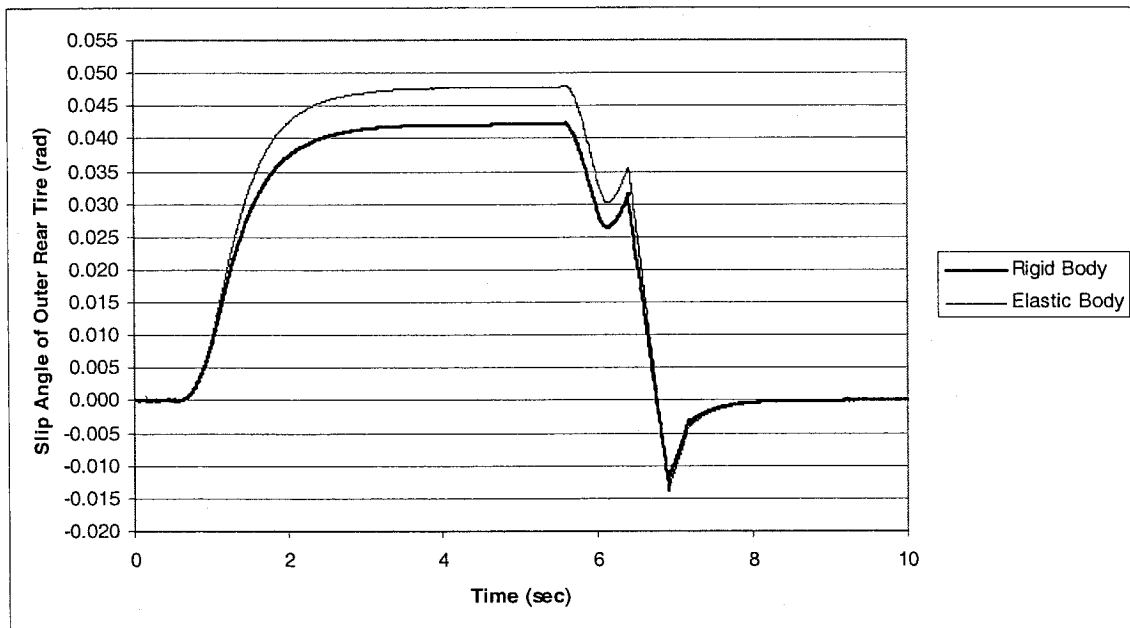
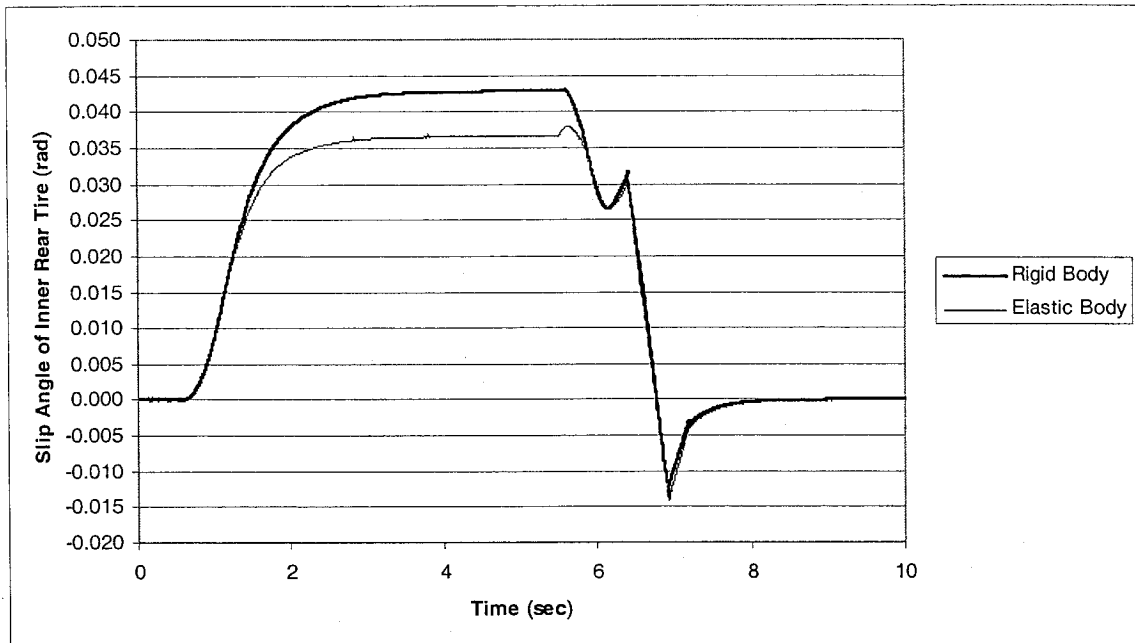


Fig. 4.21 Slip angle generation on inner and outer rear tires.

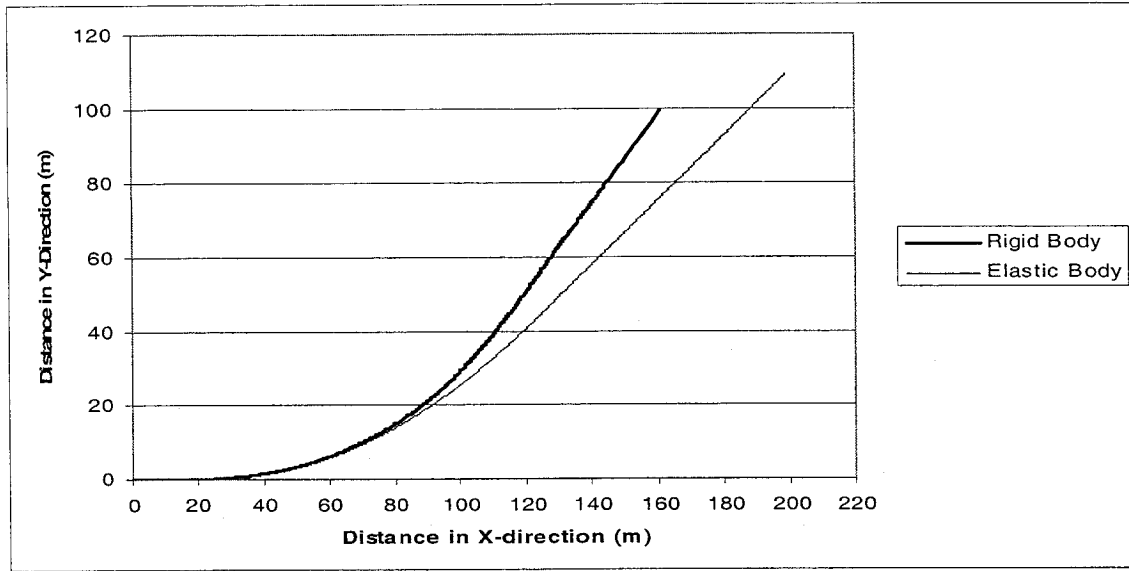


Fig. 4.22 Trajectory of the bus.

4.3 COMBINED CORNERING AND BRAKING ANALYSIS

The bus models developed in this investigation is finally evaluated for simulation under combined cornering and braking maneuver. For this, the steer angle used is the trapezoidal input presented in the Fig. 4.7, while identical braking moment presented in Fig. 4.23 is applied to each wheel of the bus. The braking moment is applied slightly after the steering input initiated and is released slightly before the end of steering input, as shown in Fig. 4. 23.

In order to simulate responses to combined steering and braking maneuver, the models are modified to include both longitudinal and lateral (cornering) tire forces. It is assumed that vehicle's initial forward speed is 20 m/s. The influence of breaking on cornering forces of tires is considered according to *friction ellipse*. In general, braking (or tractive) force reduces the cornering force that can be generated at a given slip angle. This longitudinal and lateral tire force can be termed as combined longitudinal and lateral tire force, respectively. Finally, considering that vehicle performs large rotations about

the vertical axis during combined cornering and braking, combined Longitudinal tire forces, combined lateral tire forces and steering angle input on front wheels as external loads have been applied carefully to the instantaneous position of the wheels of the finite element Highway-Bus model as illustrated in Fig. 4.24. In order to calculate required

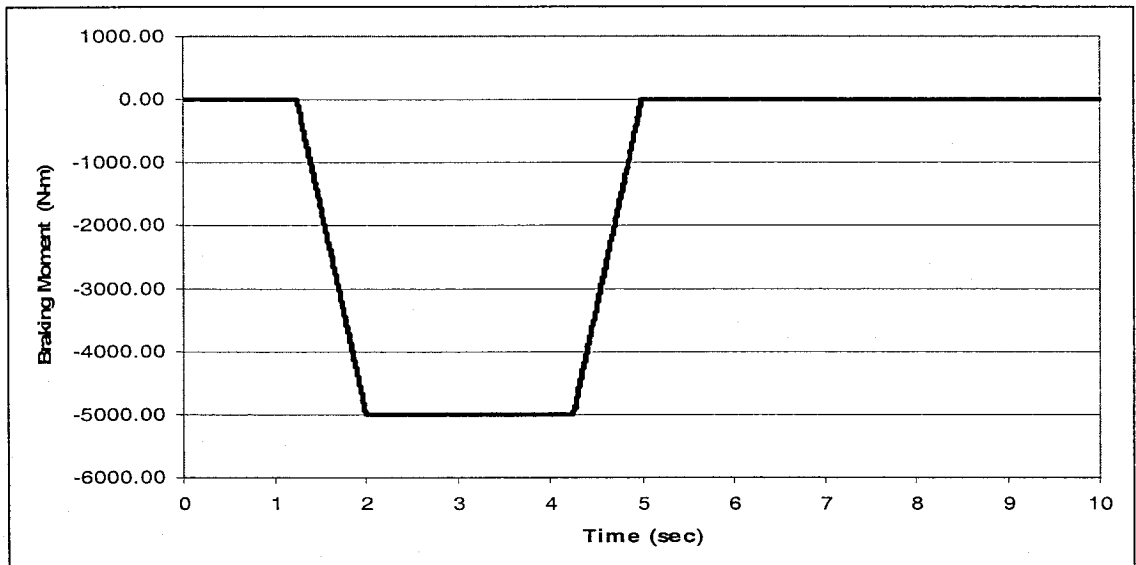


Fig. 4.23 Applied breaking moment on each wheel.

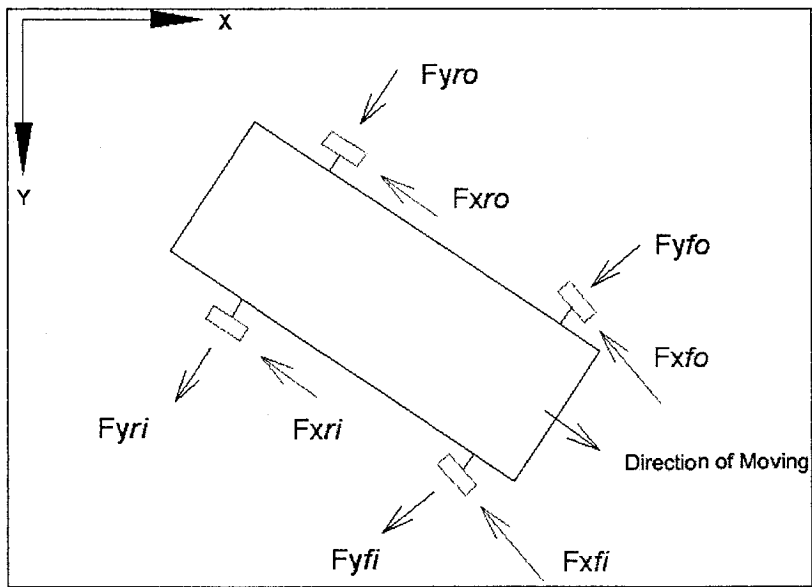


Fig. 4.24 Current position of the vehicle in combined turning and braking.

external loads, a proper four wheel mathematical model has been derived and simulated in MATLAB with the finite element highway bus model parameters and with the corresponding operational conditions. The simulation is performed in two phases. In the first phase, pure cornering analysis is carried out in order to predict the relationship between the cornering force and the slip angle under free rolling conditions (i.e., in the absence of tractive or braking effort). In the second phase combined cornering and braking analysis is carried out. The relationship developed in the first phase between the pure cornering force and the slip angle under free rolling conditions along with *friction ellipse* is utilized in the second phase. The transient simulation of four wheel model in MATLAB serves the rigid body performance of the candidate bus model during combined cornering and braking. The modeling considerations for braking and the comparison between elastic and rigid chassis performance in combined cornering and braking is illustrated in the following sub sections.

4.3.1 Mathematical Modeling

The mathematical modeling for the first phase or pure cornering analysis is already described in the section 4.2.1. The purpose of the first phase is to make a data table of the relationship between the cornering force and the slip angle under free rolling conditions for each wheel. The relationship between the pure cornering force and the slip angle under free rolling conditions helps to calculate the combined lateral tire force on each wheel using the *friction ellipse* in the second phase. In order to carry out the second phase or the combined cornering and braking analysis of the rigid bus model, the longitudinal equation of motion (Eqs. 4.8) must be considered along with lateral and yaw equations (Eqs. 4.9 and 4.10). The trajectory of the vehicle can be determined by solving

the differential equations, Eqs. 4.11- 4.13 along with the equations of motion. The value of steer angles of front-inner wheel and front-outer wheel δ_{fi} and δ_{fo} in the equations of motion can be calculated using Eqs. 4.16 and 4.17. In the equations of motion Fx represents the Braking or longitudinal tire force on each wheel as the braking moment, b_m is applied on each wheel. Braking forces can be calculated, using a simple approximation that dynamic loaded radius of tire is nearly equal to the effective rolling radius of tire, from the following relations:

$$Fx_{fi} = \frac{b_m}{R_{d_fi}} ; \text{ where } R_{d_fi} = \text{dynamic radius of front-inner tire} \quad (4.36)$$

$$Fx_{fo} = \frac{b_m}{R_{d_fo}} ; \text{ where } R_{d_fo} = \text{dynamic radius of front-outer tire} \quad (4.37)$$

$$Fx_{ri} = \frac{b_m}{R_{d_ri}} ; \text{ where } R_{d_ri} = \text{dynamic radius of rear-inner tires} \quad (4.38)$$

$$Fx_{ro} = \frac{b_m}{R_{d_ro}} ; \text{ where } R_{d_ro} = \text{dynamic radius of rear-outer tires} \quad (4.39)$$

Dynamic radii of different positioned tires can be calculated from the following relations:

$$R_{d_fi} = -N_{fi} / k_{tf} + R_{of} ; \text{ where } k_{tf} = \text{vertical stiffness of front tire} \quad (4.40)$$

$$R_{d_fo} = -N_{fo} / k_{tf} + R_{of} \quad (4.41)$$

$$R_{d_ri} = -N_{ri} / k_{tr} + R_{or} ; \text{ where } k_{tr} = \text{vertical stiffness of rear tires} \quad (4.42)$$

$$R_{d_ro} = -N_{ro} / k_{tr} + R_{or} \quad (4.43)$$

In the Eqs. 4.40-4.43, R_{of} and R_{or} is the unloaded radius of front and rear tire, respectably and N_{fi} , N_{fo} , N_{ri} and N_{ro} indicate instantaneous normal load on the front-inner tire, the front-outer tire, the rear-inner tires and the rear-outer tires, respectively. Referring to Figs. 4.25(a) and 4.25(b), the instantaneous normal loads on tires N_{fi} , N_{fo} , N_{ri} and N_{ro} are

calculated by the following relations obtained by taking moment about B, A, D and C, respectively:

$$N_{fi} = n_{fi} - \frac{(m_f + L_x) \times a_y \times h}{t_f}; \text{ where } n_{fi} = \text{static load on front - inner tire} = \frac{m_f g t_{fo}}{t_f},$$

$$N_{fi} \geq 0 \quad (4.44)$$

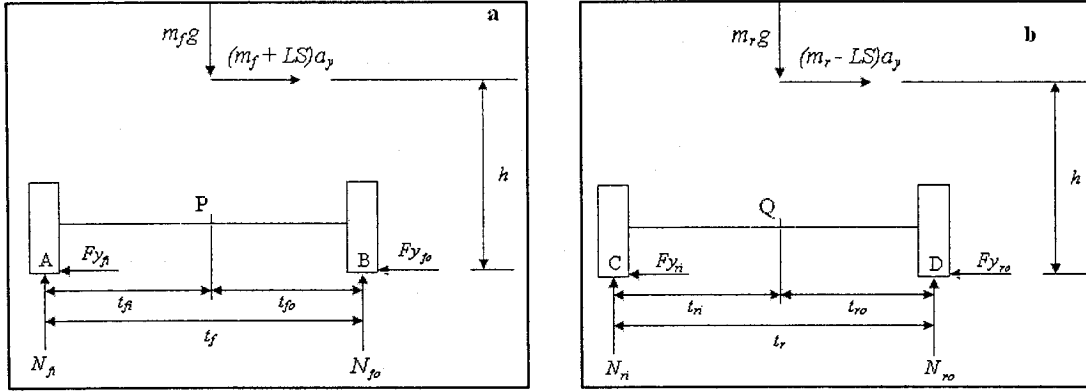


Fig. 4.25 Normal load on front tires (a) and rear tires (b).

$$N_{fo} = n_{fo} + \frac{(m_f + L_x) \times a_y \times h}{t_f}; \text{ where } n_{fo} = \text{static load on front - outer tire} = \frac{m_f g t_{fi}}{t_f},$$

$$N_{fo} \leq m_f g \quad (4.45)$$

$$N_{ri} = n_{ri} - \frac{(m_r - L_x) \times a_y \times h}{t_r}; \text{ where } n_{ri} = \text{static load on rear - inner tires} = \frac{m_r g t_{ro}}{t_r},$$

$$N_{ri} \geq 0 \quad (4.46)$$

$$N_{ro} = n_{ro} + \frac{(m_r - L_x) \times a_y \times h}{t_r}; \text{ where } n_{ro} = \text{static load on rear - outer tires} = \frac{m_r g t_{ri}}{t_r},$$

$$N_{ro} \leq m_r g \quad (4.47)$$

The values of n_{fi} , n_{fo} , n_{ri} and n_{ro} can be determined by the static analysis of the vehicle due to the gravitational weight as discussed section 2.3.1. m_f and m_r represents the front

and rear wheel loads, and those are calculated by the Eqs. 4.30 and 4.31. In Eqs. 4.44-4.47, the term L_x represents the longitudinal load shift from rear axle to front axle due to the braking. Referring to Fig. 4.26, the instantaneous load transfer, L_x (in kg) from rear axle to front axle are calculated by the following relation obtained by taking moment about the front wheel:

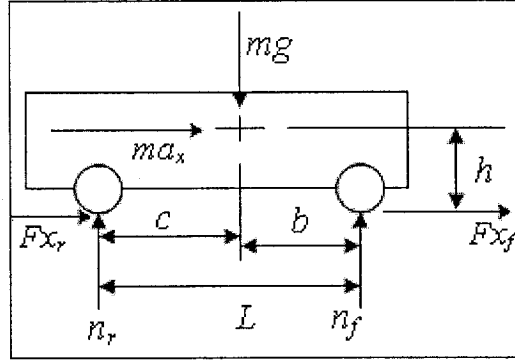


Fig. 4.26 Load shift during braking.

$$L_x = \left| \frac{m \times a_x \times h}{L \times g} \right|; \text{ where: } a_x \text{ is the braking deceleration} \quad (4.48)$$

The combined lateral tire forces, F_y in the equations of motion can be determined using the *friction Ellipse* method as follows:

$$F_{y_{fi}} = F_{y_{\alpha_{fi}}} \sqrt{1 - \left(\frac{F_{x_{fi}}}{F_{x_{\max_{fi}}}} \right)^2} \quad (4.49)$$

$$F_{y_{fo}} = F_{y_{\alpha_{fo}}} \sqrt{1 - \left(\frac{F_{x_{fo}}}{F_{x_{\max_{fo}}}} \right)^2} \quad (4.50)$$

$$F_{y_{ri}} = 2 \times F_{y_{\alpha_{ri}}} \sqrt{1 - \left(\frac{F_{x_{ri}}}{F_{x_{\max_{ri}}}} \right)^2} \quad (4.51)$$

$$F_{y_{ro}} = 2 \times F_{y_{\alpha_{ro}}} \sqrt{1 - \left(\frac{F_{x_{ro}}}{F_{x_{\max_{ro}}}} \right)^2} \quad (4.52);$$

where Fy_α is the pure lateral tire force at instantaneous slip angle generated on a tire, and Fx_{max} is possible maximum braking force that can be generated on each wheel. Possible maximum braking force, Fx_{max} can be calculated by the following relations:

$$Fx_{max_{fi}} = \mu \times N_{fi} \quad (4.53)$$

$$Fx_{max_{fo}} = \mu \times N_{fo} \quad (4.54)$$

$$Fx_{max_{ri}} = \mu \times N_{ri} \quad (4.55)$$

$$Fx_{max_{ro}} = \mu \times N_{ro} \quad (4.56);$$

where μ is the co-efficient of road adhesion. The value of μ is 0.95 as the asphalt and concrete (dry) type of road is considered in this analysis. The pure lateral tire force, Fy_α at instantaneous slip angle generated on a tire can be calculated by interpolating pure lateral force versus slip angle data table (constructed from the first phase simulation, i.e. pure cornering analysis). Instantaneous slip angle can be calculated with the help of Eqs. 4.32-4.35.

4.3.2 Transient Response of the Bus with Rigid and Elastic Body

The applied longitudinal tire forces or breaking forces, computed from the combined cornering and braking simulation of the four wheels rigid body model are given in Fig. 4.27, and the corresponding longitudinal slips on each side of axle for flexible body model are presented in Fig. 4.28. Results show that inner rear wheel tires develop less than the half of the longitudinal slip of inner front wheel tire. The same trend is found between outer rear wheel tires and outer front wheel tire. This is expected since there are two tires on each side of the rear axle, and vertical loads on rear tires are greater than that of front tire. Because of two tires, the longitudinal tire stiffness on each side of the rear axle is just double compare to that on each side of front axle. Moreover, slip

decreases with the increase of vertical load as frictional force increases with the increases of vertical load. It should be noted that load shift for the flexible body as seen in Figs. 4.11 and 4.12, between inner and outer wheel tire is very little; consequently, there is almost no difference between the inner and outer tire slip responses of same axle. The cornering force developed by the tires on each side of axles under combined braking and steering maneuver is shown in Fig. 4.29. These results can be readily compared with those of pure cornering under same steering input presented earlier in Fig. 4.9. The results show that the available cornering force under the braking effort reduces significantly as expected. Similar trend can also be observed from the time history slip angle response at each tire presented in Figs. 4.30 and 4.31. These results further show a comparison of slip angle developed by the tires of elastic body and rigid body models. Similar to pure cornering, the noticeable deviation is only observed for outer wheels, where flexible body model exhibits larger values. However, the difference is continually decreasing throughout the application of brake. Again the results further reveal that the flexible body model exhibits very little larger values for inner tires compare to the rigid body model, which is opposite to the slip angle time response for pure cornering.

Various vehicle responses to combined braking and steering maneuver are next presented for both rigid body model and flexible body model in this section. Figs. 4.32(a) and 4.32(b) show longitudinal velocities and longitudinal decelerations of the centers of gravity of the bus model versions. It is necessary to mention that rolling resistance of wheels is not considered in this example, and it is evident from the results presented in Fig. 4.32.

Figs. 4.33(a)-(c) show lateral velocities, lateral decelerations and yaw velocities of the centers of gravity of the bus model versions, respectively. These results can be readily compared with those obtained in Fig. 4.10 for pure cornering in order to examine the braking effort. These results presented in Fig. 4.33 show that both the rigid body and flexible body models predict identical responses to combined braking and steering maneuver.

The trajectory of the center of gravity for the given combined maneuver for the two models is shown in Fig. 4.34. As the result shows, under combined maneuver, the flexible body model tends to follow a tighter curve than that of the rigid body. This when compared to pure cornering trajectory presented in Fig. 4.15 clearly show the opposite trend. Since the average slip angle of front tires for the flexible body model is little larger than that for rigid body model, it apparently seems rigid body model should follow a tighter curve than that of the flexible body model. However, the fact is that load shift between inner and outer wheels in case of rigid body is significant, whereas in case of flexible body, load shift is very small as shown in Figs. 4.11 and 4.12. As a result, the braking force shown in Fig. 4.27 can be regarded as asymmetric braking in case of rigid body model, whereas it can be regarded as symmetric braking in case of flexible body model. The asymmetric braking causes the rigid body model moves outward.

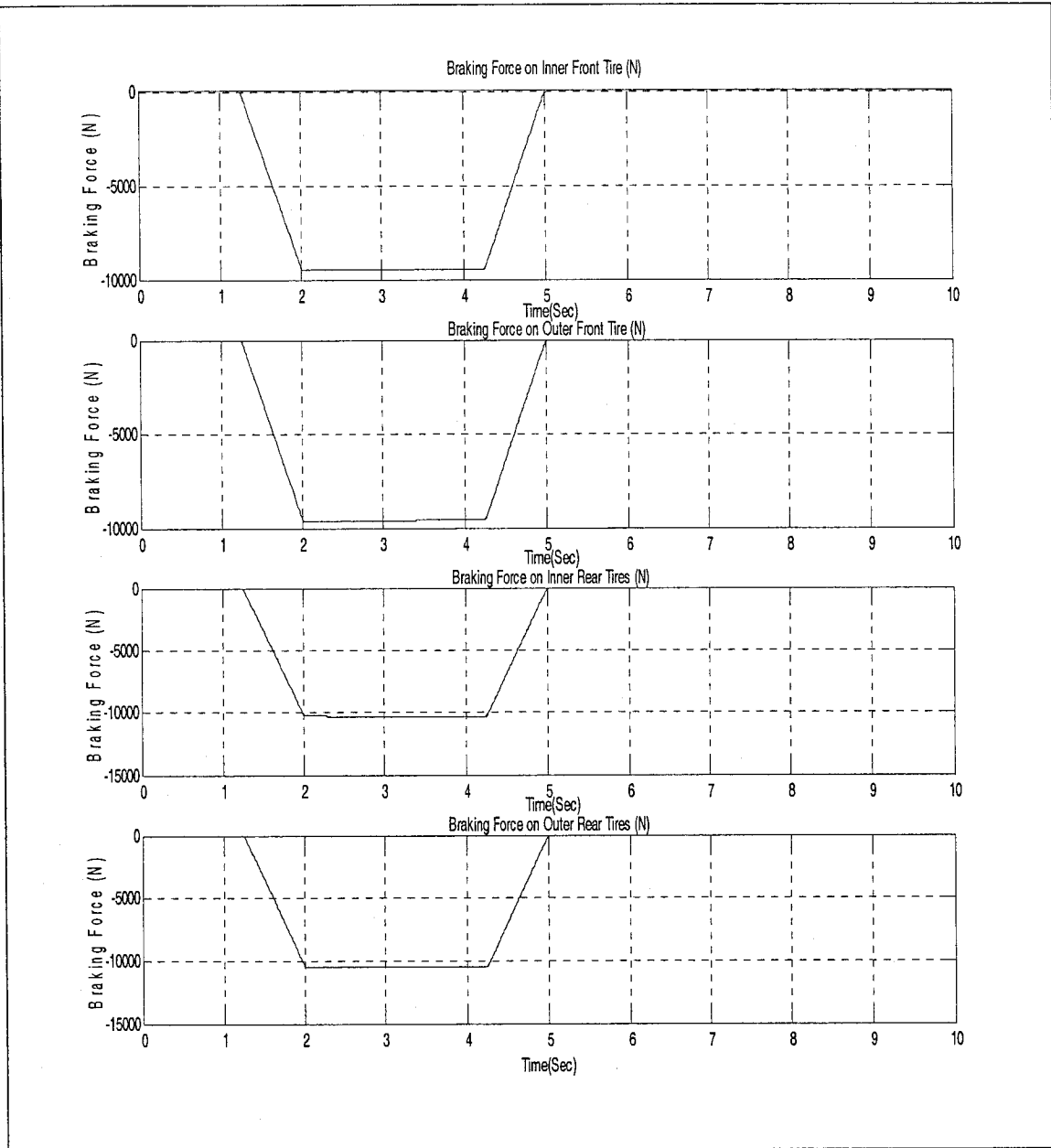


Fig. 4.27 Braking forces at different tires.

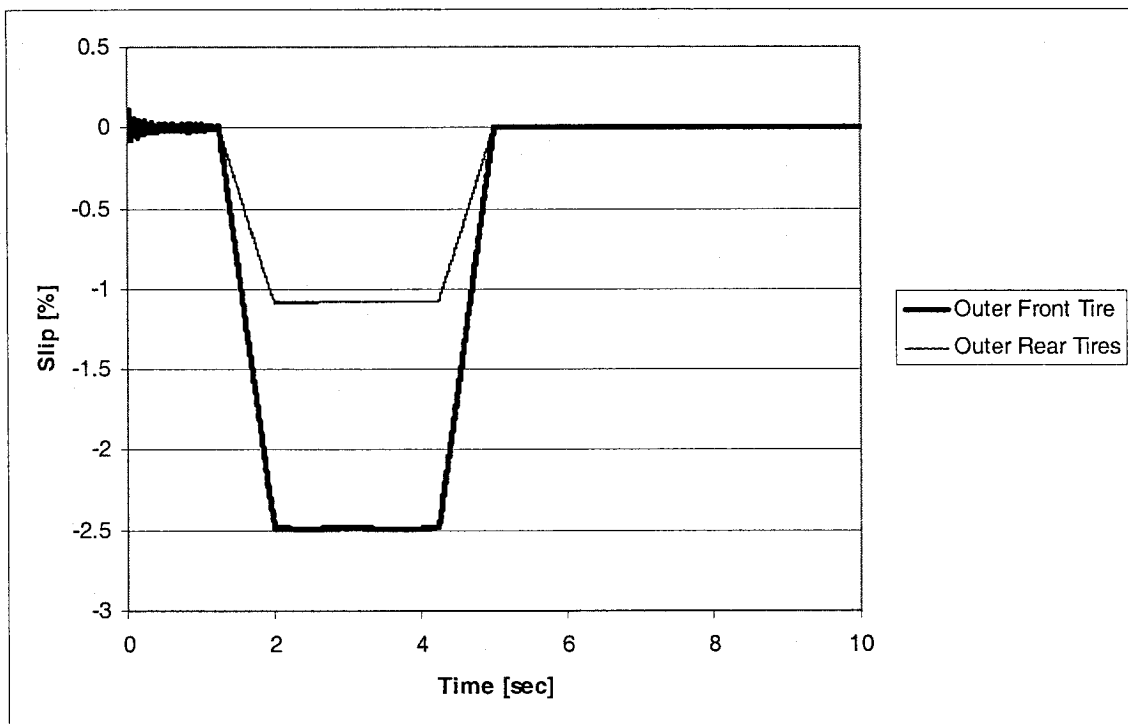
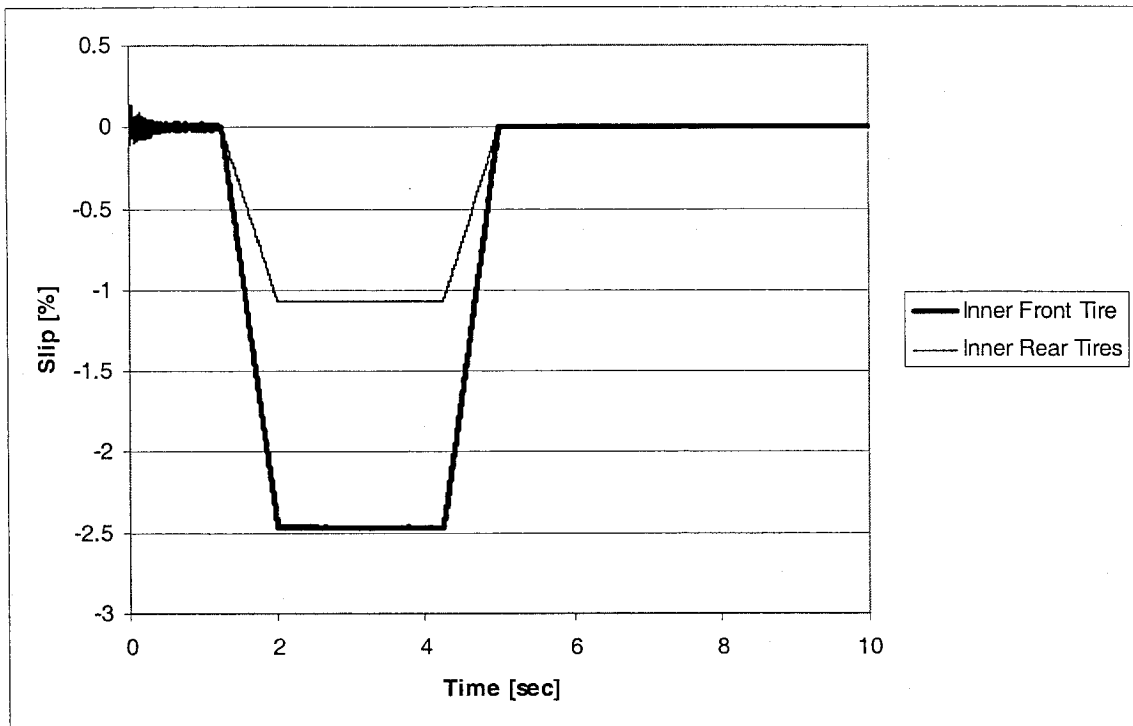


Fig. 4.28 Longitudinal slip of tires of the flexible body model.

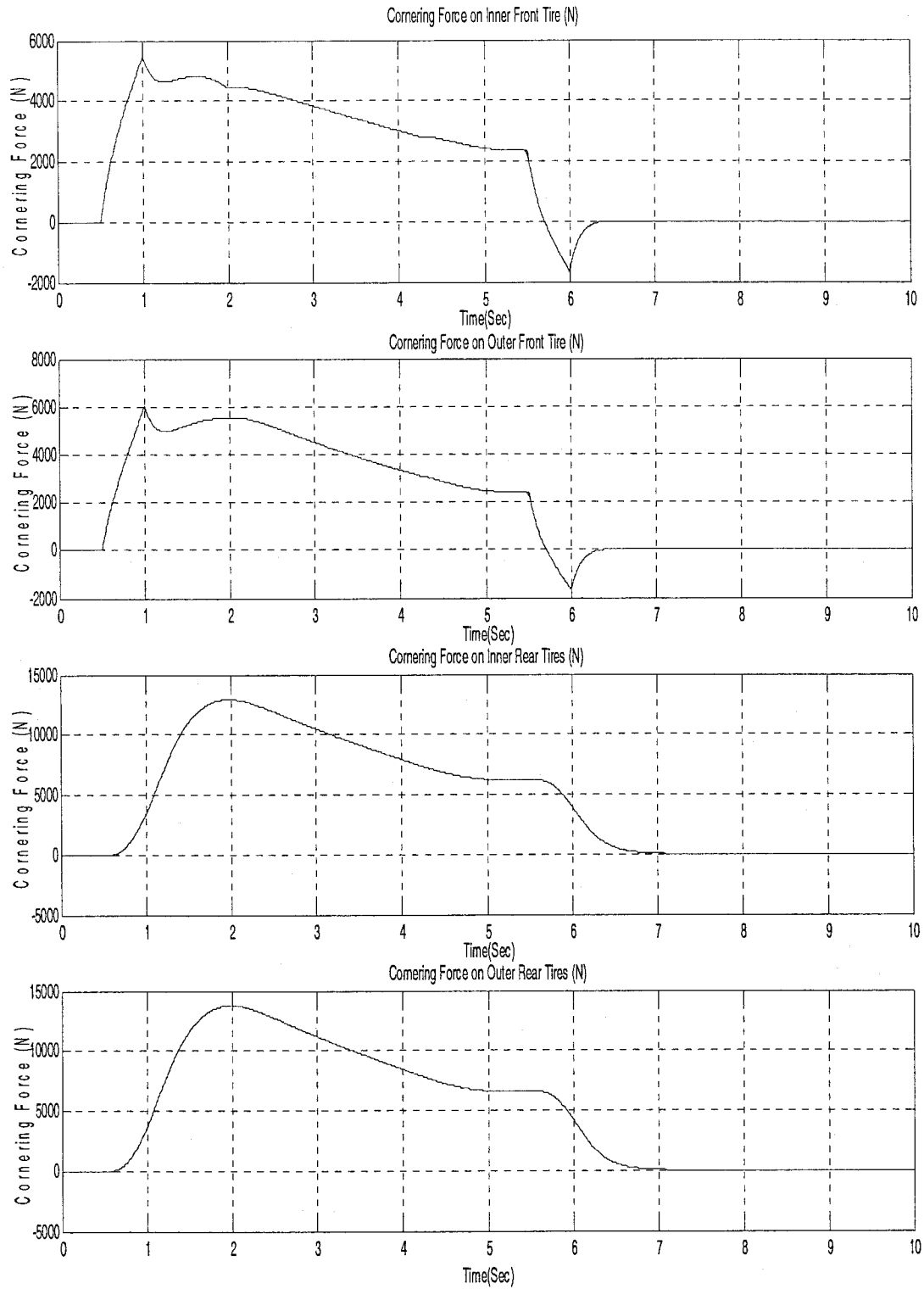


Fig. 4.29 Change of developed cornering forces at different tires.

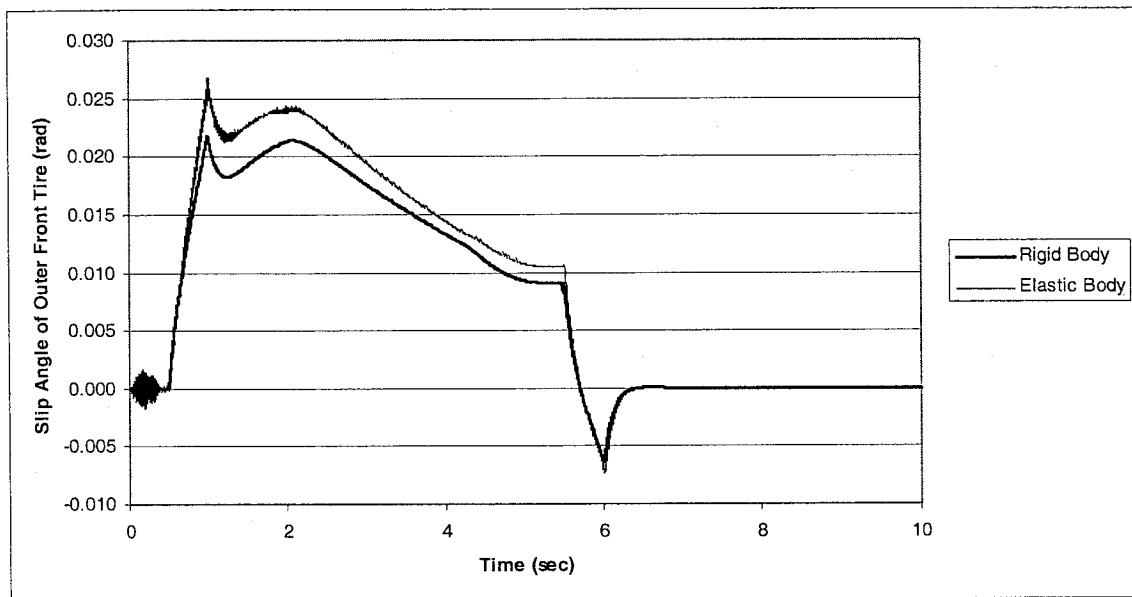
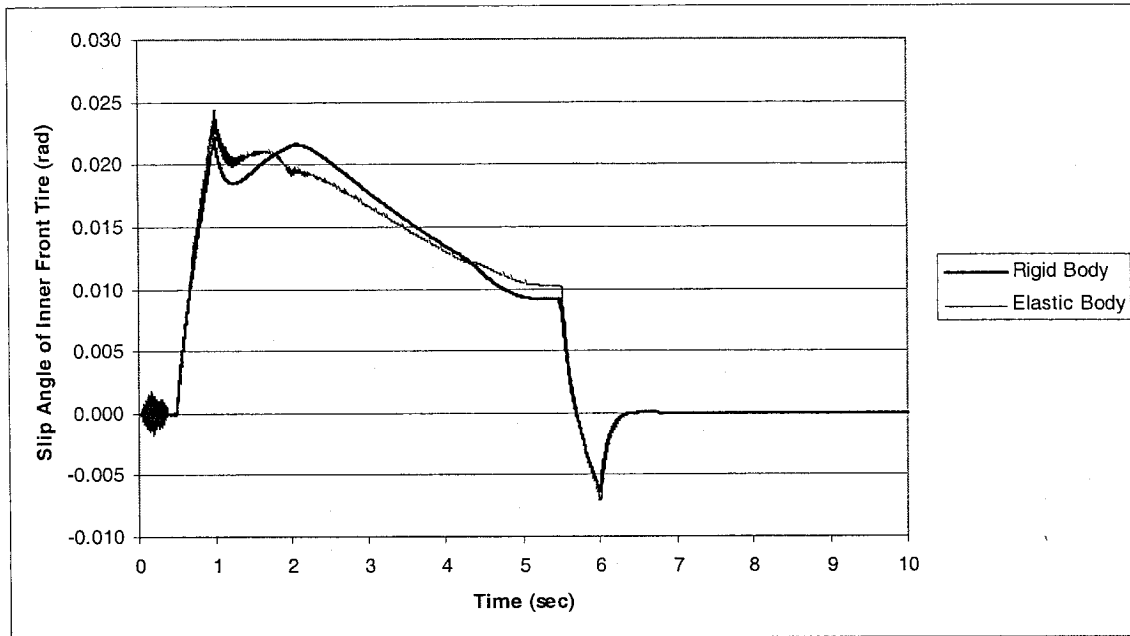


Fig. 4.30 Slip angle generation on inner and outer front tires.

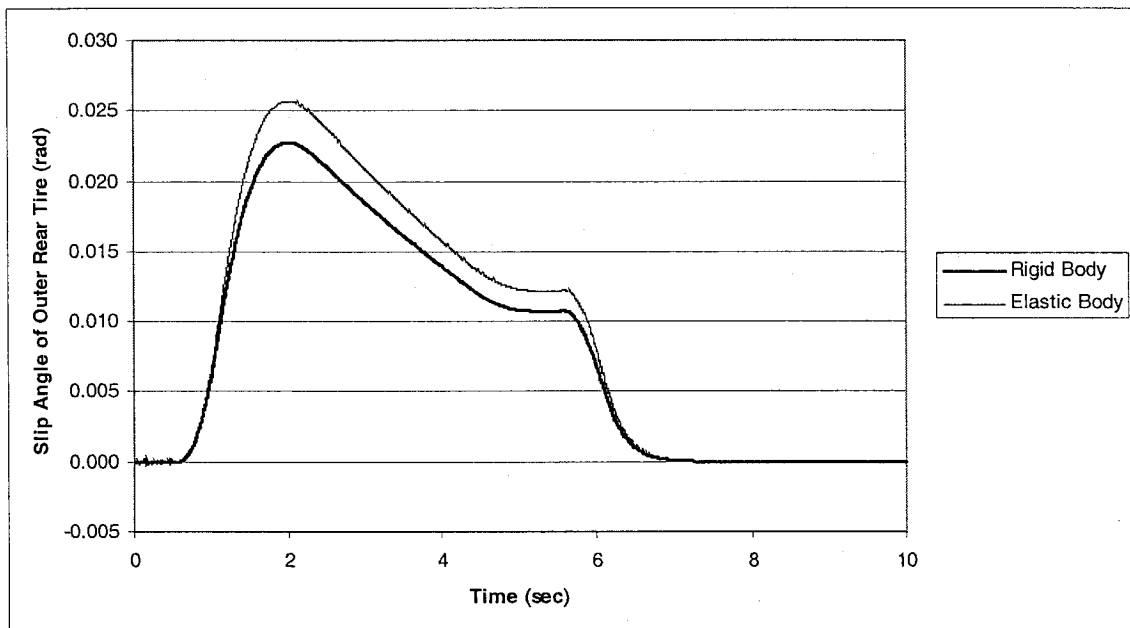
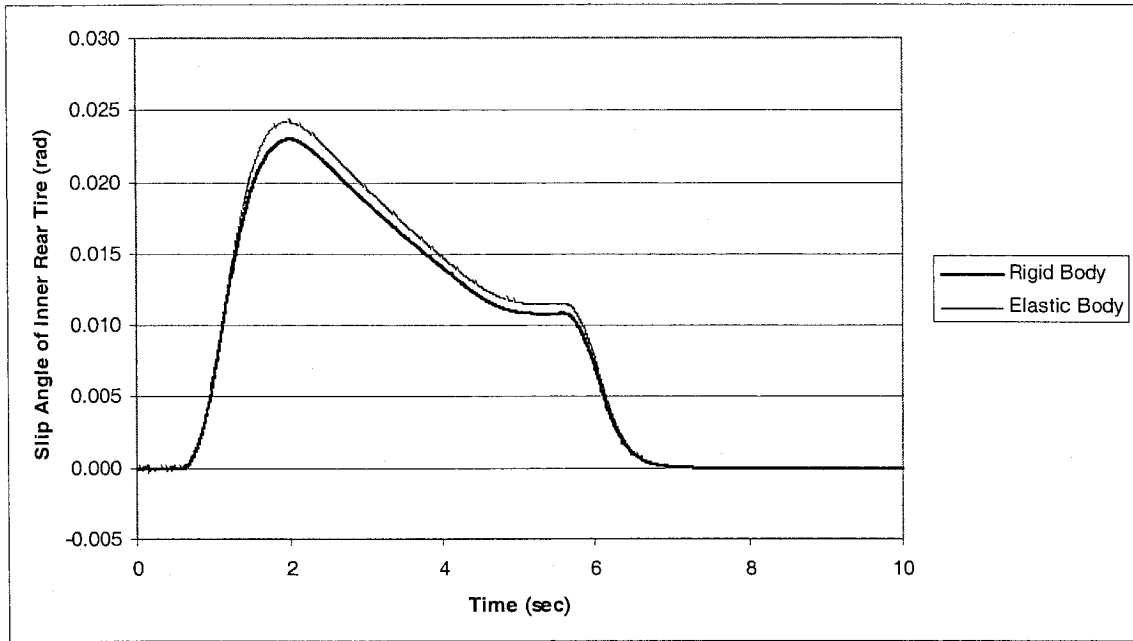


Fig. 4.31 Slip angle generation on inner and outer rear tires.

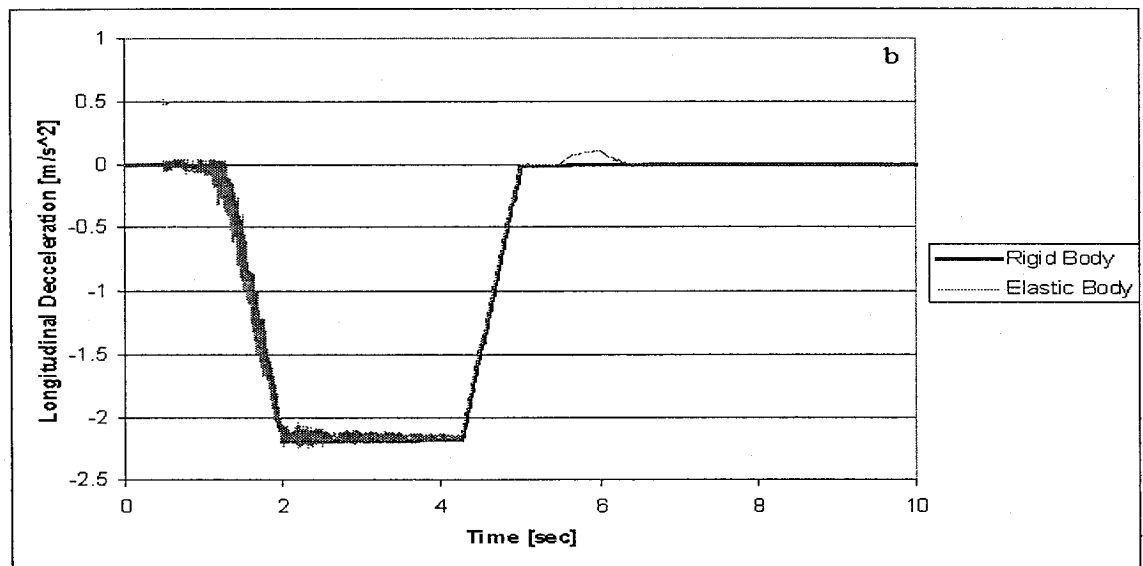
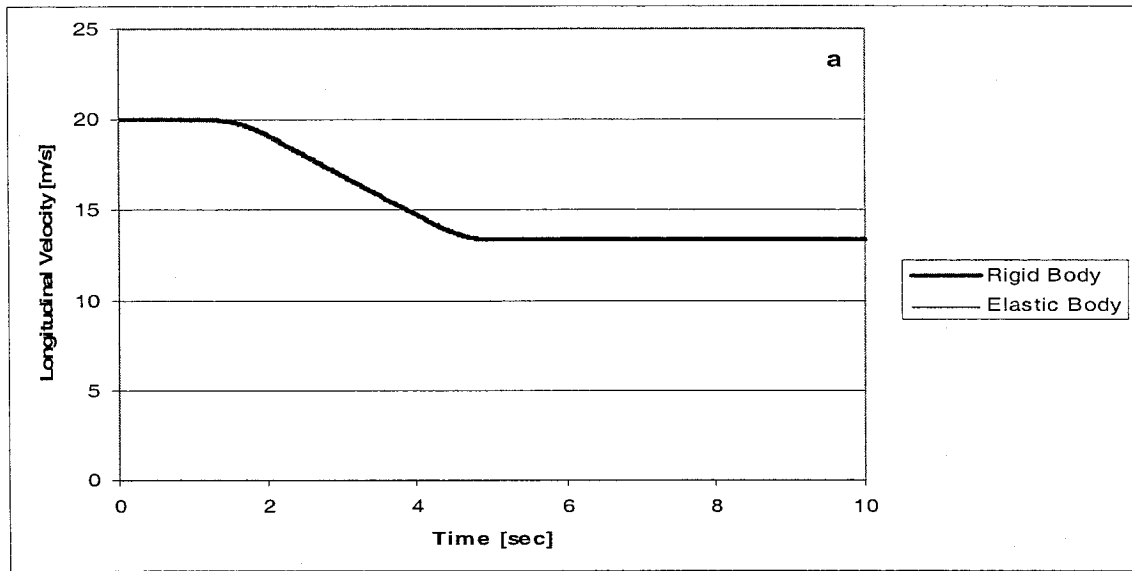


Fig. 4.32 Longitudinal velocities (a) and longitudinal decelerations (b) of center of gravity.

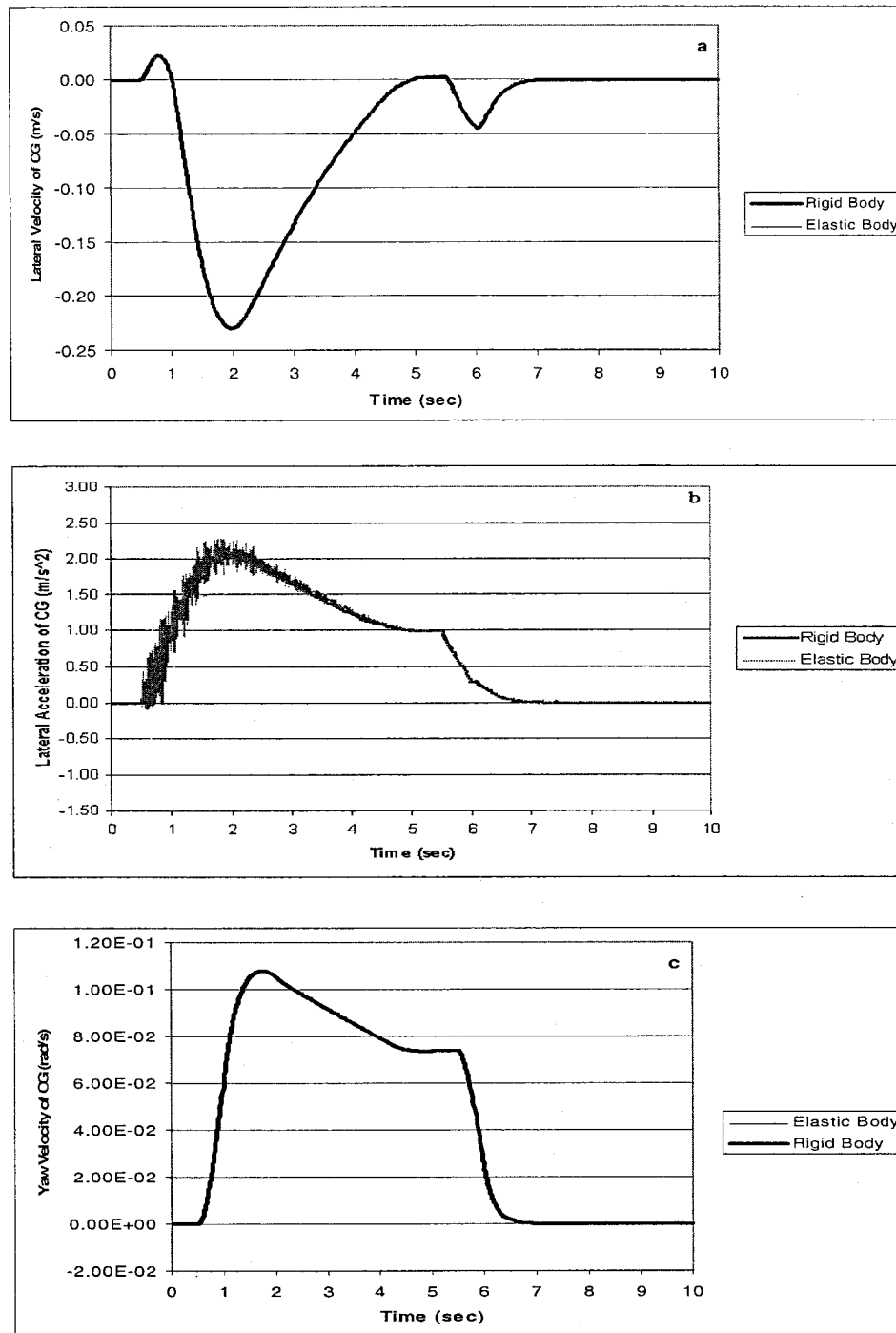


Fig. 4.33 Lateral velocity (a), lateral acceleration (b) and yaw velocity (c) of center of gravity.

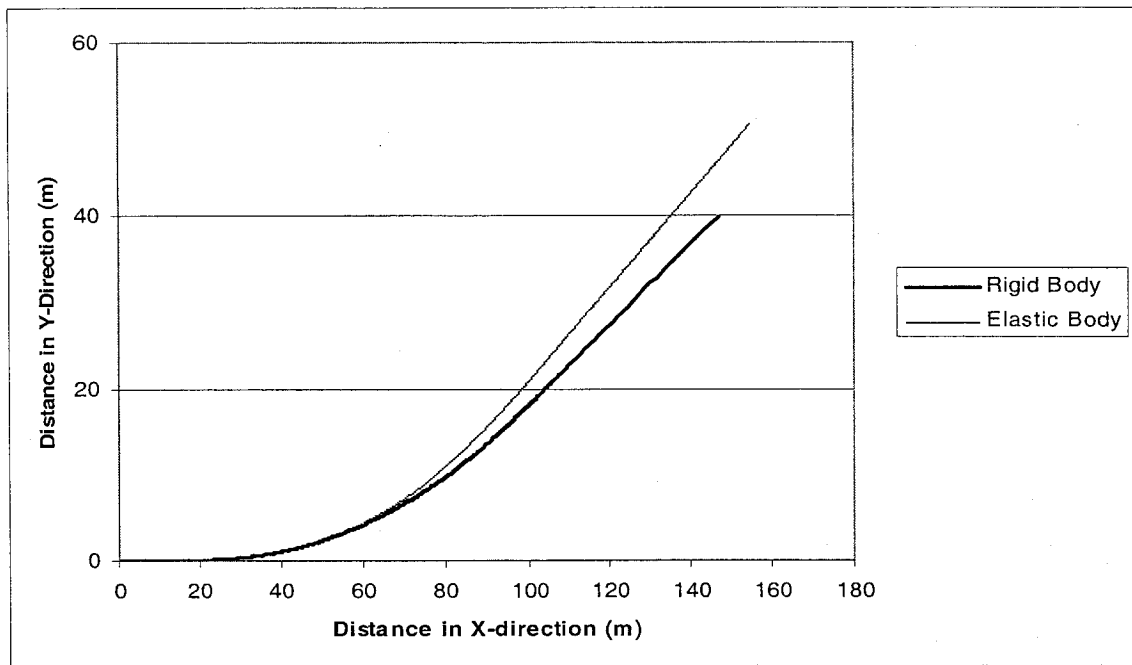


Fig. 4.34 Trajectory of the bus.

CHAPTER 5

CONCLUSIONS AND FUTURE WORK

5.1 CONCLUSIONS

The four-wheel rigid body model developed for this investigation is capable of simulating longitudinal, lateral and yaw responses to various steering and braking inputs. The proposed FEM model, on the other hand, can be used to predict very wide range of responses in 3-D environment for a wide range of single or combined inputs. The present limited study has shown that the influence of body flexibility has little effect on the responses to the inputs considered. It, however, provides a powerful tool for examining combined integrity of structural and dynamic performances.

The following important conclusions can be drawn from the analytical studies undertaken in this research:

1. The developed finite element bus model is effective in the dynamic simulations of its motions as it is validated by static weight balance check and frequency analysis. Sprung mass and unsprung mass mode shapes are successfully uncoupled. The found rolling, pitch and bounce frequency of the sprung mass are 0.73 Hz, 1.1 Hz and 1.3 Hz, respectively; whereas front and rear unsprung bounce frequencies are 9.1 Hz and 9.3 Hz, respectively.
2. A new definition is suggested for longitudinal and lateral slips for the finite element tire model based on the tire contact length, the value of which directly varies with vertical tire load, and the proposed definition is justified by comparing the elastic body responses with the rigid body responses.

3. Excitation frequency and vehicle dynamics studies are typically limited to 20 Hz. Thus, employing Mode Superposition method drastically reduces the solution time even though large degrees of freedom bus model is used.
4. The methodology applied to identify the low frequency range i.e. the considered low frequency range of the applied finite element bus model for employing mode superposition method is well adequate to capture the response of the bus with regards to the given excitations, and this is verified by comparing the responses in ride analysis with mode superposition method and full method.
5. Attached ground spring with tire in ride analysis provides accurate response. Moreover ground spring provide effective means to give the road excitations on the tire ground contact patch.
6. The mathematical model developed for four-wheel rigid body vehicle is well capable to capture the responses to combined slip conditions (braking-in-a-turn) as well as pure slip conditions, and good correlation is found between the responses of rigid body bus model and elastic body bus model in handling and longitudinal studies.
7. The application of *friction ellipse* tire model over *cosine version of magic formula* tire model is found to be extremely useful and efficient for vehicle handling and longitudinal performance analysis as *magic formula* tire model requires the determination of increased number of parameters, around 42. On the contrary, *friction ellipse* tire model requires only a few numbers of experimental data sets. Moreover, the determination of increased number of parameters raises the total percentage of errors.

8. In case of pure turning and braking-in-a-turn analyses, the developed rigid body and elastic body models are found to predict almost same results for the responses of the center of gravity to the inputs considered.
9. For the ride analysis, both rigid and flexible models predict same responses, where there is little or no effect of body flexibility. The elastic model is, however, capable of simulating three dimensional responses under vertical input.

5.2 FUTURE WORK

Although this thesis has taken an important step towards the non-conventional efficient application of the finite element method for three dimensional dynamic analysis of road vehicles, it only presents limited results and analysis needed to explore its full potential. Significant more work may be identified as follows that will enhance the model and its usefulness for analysis and simulation of vehicle dynamics:

1. To correlate the finite element bus model in terms of structural stiffness and mass distribution with a real bus in order to obtain a more accurate set of results. This can be accomplished by comparing finite element static analysis results with the experimental results obtained for a real bus.
2. To improve the finite element bus model, namely inclusion of non-linear damper characteristics in suspension and yaw frequency of tire.
3. To improve the four-wheel rigid body bus model, namely inclusion of linear or nonlinear suspension effects, roll motion, nonlinear vertical tire stiffness, effective rolling radius of tire, rolling resistance, and road roughness in pure turning and combined turning and braking analyses.

4. To validate the four-wheel rigid body and finite element bus model using time transient road test data for pure turning and combined turning and braking analyses.
5. To explore the full potential of the four-wheel rigid body and finite element bus model, μ -split cornering, wheel locking and asymmetric braking can also be investigated and further can be checked against the time transient experimental data sets.

REFERENCES

- [1] Kuti, I., "Simulation of Vehicle Motions on the Basis of the Finite Element Method", *Vehicle System Dynamics*, Vol. 36, No. 6 (2001), pp. 445-469.
- [2] Kuti, I., "A Computational Procedure for Non-Linear Dynamic Analysis of Vehicles", *Vehicle System Dynamics*, Vol.30 (1998), pp. 37-54.
- [3] Kuti, I., "Dynamic Analysis of Vehicle Manoeuvres on the Basis of the Finite Element Method", *Periodica Polytechnica Ser. Transp. Eng.*, Vol. 29. No. 1-2 (2001), pp. 47-58.
- [4] Balasa, B., Nicolae, G., and Tircomnicu, R., "Bus expert system for dynamic simulations design and quality control", *COPERNICUS Project No. CP94-0520*.
- [5] Specifications of Prevost XLII-40 Model 2005, Prevost Car Inc, http://www.prevostcar.com/cgi-bin/pages.cgi?page=xl2c_chara.
- [6] Ahmed, A.K.W., "Ground Transportation Systems", *Encyclopedia of Vibrations*, Editor: S.G. Brann, D.J. Ewins, S.S. Rao, Academic Press, London, U.K., 2002, pp. 603-620.
- [7] Bayle, P., Forissier, J. F., and Michelin, L.S., "A New Tyre Model for Vehicle Dynamics Simulations", *Automotive Technology International '93*, pp. 193-198.
- [8] Wong, J.Y., "Theory of Ground Vehicle", Third Edition, John Wiley & Sons, Inc, New York, 2001.
- [9] Segel, L., "The Mechanics of Heavy-Duty Trucks and Truck Combinations", presented at the Engineering Summer conferences, University of Michigan, Ann Arbor, 1984.

- [10] Pacejka, H.B., and Bakker, E., "The Magic Formula Tyre Model", *Vehicle System Dynamics*, 21(1993), pp. 1-18.
- [11] Osten, J.J.M., and Bakker, E., "Determination of Magic Tyre Model Parameters", *Vehicle System Dynamics*, 21 (1993), pp. 19-29.
- [12] Cabrera, J.A., Ortiz, A., Carabias, E., and Simon, A., "An Alternative Method to Determine the Magic Tyre Model Parameters Using Genetic Algorithms", *Vehicle System Dynamics*, Vol.41, No.2, (2004), pp.109-127.
- [13] Pacejka, H.B., and Besselink, I.J.M., "Magic Formula Tyre Model with Transient Properties", *Vehicle System Dynamics Supplement*, 27(1997), pp.234-249.
- [14] Mastinu, G., Gaiazzi, S., Montanaro, F., and Pirola, D., "A Semi-Analytical Tyre Model for Steady-and-Transient-State Simulations", *Vehicle System Dynamics Supplement*, 27(1997), pp.2-21.
- [15] Maurice, J.P., Zegelaar, P.W.A., and Pacejka, H.B., "The Influence of Belt Dynamics on Cornering and Braking Properties of Tyres", *Vehicle System Dynamics Supplement*, 28 (1998), pp.299-311.
- [16] Kuti, I., "Transient Analysis of the Horizontal Motion of Road Vehicles using Large Finite Element Models", 6th Mini Conf. on Vehicle System Dynamics, Identification and Anomalies, Hungary, Budapest, Nov. 9-11, 1998.
- [17] Oueslati, F., and Sankar, S., "Optimization of a Tractor-Semitrailer Passive Suspension Using Covariance Analysis Technique", SAE paper 942304, 1994.
- [18] Wong, J.Y., and El-Gindy, M., 'Computer Simulation of Heavy Vehicle Dynamic Behavior –User Guide to UMTRI Models', no. 3, Road and Transportation Association of Canada, 1985.

- [19] Raju, S.I., "Influence of Road Roughness and Directional Maneuvers on the Dynamic performance of Heavy Vehicles", Concorcordia Master's Thesis, Canada, 1989.
- [20] Kuti, I., "A Theoretical Description of Vehicle Motions including Elastic Vibrations", 7th Mini Conf. on Vehicle System Dynamics, Identification and Anomalies, Hungary, Budapest, Nov. 6-8, 2000.
- [21] Crocker, J., Zgela, M., Desrocher, C., et al., "Intercity Bus Weight Reduction Program-Phase 1", Transport Canada Publication, No. TP 13560E, Jan 2000.
- [22] Specifications of Material, Automation Creations, Inc., <http://www.matweb.com>.
- [23] Mousseau, C.W., Hulbert, G.M., and Clark, S.K., "On the Modeling of Tires for the Prediction of Automotive Durability Loads", Vehicle System Dynamics Supplement 25 (1996), pp.466-488.
- [24] Kim, S.J., and Savkoor, R.A., "The Contact Problem of In-Plane Rolling of Tires on a Flat Road", Vehicle System Dynamics Supplement, 27 (1997), pp. 189-206.
- [25] Fancher, P., Bernard, J., Clover, C., And Winkler, C., "Representing Truck Tire Characteristics in Simulations of Braking and Braking-In-A-Turn Maneuvers", Vehicle System Dynamics Supplement, 27 (1997), pp.207-220.
- [26] Rakheja, S., and Wong, Zhanqi, "Roughness Characteristics of Urban Roads (Montreal and Longueuil)", CONCAVE Report 15-99, Oct 1999.